Numerical Modelling of the Effect of Fretting Wear on Fretting Fatigue

Jason John Madge, MEng(Hons).

Thesis submitted to the University of Nottingham
for the degree of Doctor of Philosophy

June 2008

Contents

Abstract

This thesis reports the development of a method for predicting the fretting fatigue life of a system which takes into consideration the material removed as a result of fretting wear.

The first implementation is based on a critical plane, multiaxial fatigue model and a damage accumulation framework. The model is applied to both 'cylinder on flat' and 'rounded edge punch on flat' geometries, for which experimental data from the literature is used for comparison..

The method is able to predict a number of key experimentally observed phenomena, which existing approaches are unable to do. The dependence of fretting fatigue life on slip amplitude is captured demonstrating a critical range of slip amplitudes, relating to the partial slip regime, for which a minimum in life is predicted. The method is also shown to predict the occurrence of cracking at specific locations in the slip region. The method indicates that these phenomena are dependent on the relative rates of wear and fatigue damage occurring across the contact.

The second implementation treats the nucleation and propagation fatigue phases separately. The fatigue model adopted above is reformulated to serve as a nucleation model, whilst the crack propagation phase is based on a fracture mechanics perspective. The method is used to study the effect of wear on both the propagation and nucleation aspects of fatigue. The method is also employed to investigate the role of fretting wear in fretting fatigue crack arrest.

Publications

Madge, J. J., I. R. McColl and S. B. Leen (2006). A computational study on the wear induced evolution of fatigue damage parameters in fretting fatigue specimens. Fatigue 2006, GA, Atlanta, Elsevier.

Ding, J., J. J. Madge, S. B. Leen and E. J. Williams (2006). Towards the Modelling of Fretting Wear and Fatigue Interaction in Spline Couplings. Journal of applied mechanics and materials 5-6: 165-172.

Madge, J. J., S. B. Leen, I. R. McColl and P. H. Shipway (2007). Contact-evolution based prediction of fretting fatigue life: Effect of slip amplitude Wear 262(9-10): 1159-1170.

Madge, J. J., S. B. Leen and P. H. Shipway (2007). The critical role of fretting wear in the analysis of fretting fatigue. Wear 263(1-6), 542-551

Madge, J. J., S. B. Leen and P. H. Shipway (2008). A combined wear and crack nucleation-propagation methodology for fretting fatigue prediction. International Journal of Fatigue: 30(9). 1509-1528

Acknowledgements

Firstly I would like to thank my supervisors, Dr Sean Leen and Prof. Philip Shipway. Their support, patience, enthusiasm and encouragement throughout my Ph.D has made the process a very valuable, interesting and enjoyable experience.

I must also mention the late Dr Ian McColl, who initially co-supervised my research with Dr Leen. His desire to investigate wear modelling showed great foresight, and he offered unique insights and guidance to the project during my first year. Unfortunately, Dr McColl passed away in late 2005; he is still greatly missed.

I extend special thanks to Dr Jian Ding and Dr Ed Williams at the Nottingham Transmissions UTC, and Scott Wood and Nina Bannerjee at Rolls-Royce plc for helpful guidance and discussion. There are many others I would like to thank for their help throughout my research, but cannot be mentioned here for brevity; thank you all.

I am also grateful for the financial support of both the Engineering and Physical Sciences Research Council, and Rolls-Royce plc.

I would like to thank my parents who have supported me throughout my studies and in life generally. Together they are responsible for sparking my interest in engineering science.

Finally I give my thanks to my wife Yin Yee Ng. Without whom I simply could not have finished this thesis.

Nomenclature

γ	Shear strain
δ	Maximum slip observed across a contact surface over one fretting cycle (mm)
δ_{app}	displacement amplitude applied remote from contact surface (mm).
ε	*S*train
ε_f'	Coffin-Manson fatigue ductility exponent
$\Delta\varepsilon$	Strain range over one fatigue cycle
μ	Coefficient of friction
ν	Poisson's ratio
σ	Stress (MPa)
σ_e	Fatigue endurance strength (MPa)
σ_f'	Basquins fatigue strength exponent
τ	Shear stress (MPa), pseudo time within cycle jump ΔN
ω	Accumulated damage
b	Basquins fatigue strength exponent (MPa), specimen width (mm)
c	Coffin-Manson fatigue ductility exponent
C	Paris law coefficient
d	Marco-Starkey damage model exponent
E	Youngs Modulus (MPa)
E^*	Combined Young's modulus (MPa)
h	Nodal wear depth
H	Hardness (MPa)
k	Wear coefficient (mm^3MPa^{-1})
K_I	Opening mode stress intensity factor(MPa√mm)
K_{II}	In-plane shearing mode stress intensity factor (MPa√mm)
ΔK_{eff}	Effective stress intensity factor range
ΔK_{th}	Threshold stress intensity factor range (MPa√mm)
l	Crack length (mm)
l_0	El-Haddad intrinsic crack length (mm)
m	Paris law exponent
n	Number of cycles
N_f	Total number of cycles to failure
N_i	Number of cycles to crack initation
N_p	Number of propagation cycles (from initiation to failure)
P	Normal load (N)
p	Normal pressure (MPa)
$p(x)$	Normal pressure at distance x from centre of contact (MPa)
Q	Shear load (N), Geometric form factor
$q(x)$	Shear traction at distance x from centre of contact (MPa)
V	Worn volume (mm^3)
R	Radius of contact surface (mm), Stress ratio
R^*	Combined radius of curvature (mm)
S	Slid distance (mm)
x	Distance from centreline of contact (mm)
y	Depth below the contact surface (mm)

Acronyms

COF	Coefficient of Friction
FDP	Fatigue Damage Parameter
SWT	Smith-Watson-Topper (fatigue parameter)
FS	Fatemi-Socie (fatigue parameter)
M-P	Miner-Palmgren (linear damage rule)

Chapter 1

Introduction

1.1 Air Travel

Turbo fan engines such as the Rolls-Royce Trent 1000 shown in Figure 1.1 have become the standard for aero-engine architecture in civilian aircraft. Their construction divides the air flow passing through the engine compressor so the minimum quantity is processed in the high pressure engine core; the remainder bypasses the core to maximize the low pressure, low velocity, mass flow and generate high propulsive efficiencies.

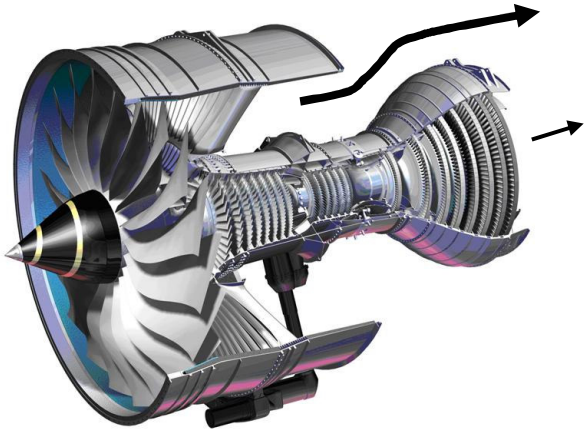

Figure 1.1. Roll-Royce Trent 1000 turbofan engine

1.2 Socio-Economic Drivers for Efficient Engine Design

Competition between engine manufacturers, rising oil prices and increasing evidence linking exhaust emissions, such as CO_2, to climate change are major driving forces for developing more efficient aero-engines.

1.3 A Future Perspective

A study by the Intergovernmental Panel for Climate Change (Penner et al, 2000) into the environmental impact of aircraft highlighted the need to improve further the efficiency of civil aero-engines and this will influence development in all areas of engine operation. The study suggested that a potential 25% increase in propulsive efficiency was achievable by increases in the bypass ratio representing a healthy opportunity for development.

Increasing the bypass ratio can be achieved in two ways; by increasing the fan diameter or by reducing the core diameter. The former approach has the disadvantages of increasing engine size and weight with the associated complications of structural vibration, increased gyroscopic loads and ground clearance issues. Conversely, any reduction of the core diameter to increase the bypass ratio provides a potential to reduce engine weight which in turn could lead to additional weight reductions in the airframe of between 1.5 and 4 times those achieved in the engine itself. (Penner et al, 2000). This indicates the potential contribution that reducing the diameter of an engine's core can make towards improving the efficiency of aircraft in the future.

The transmission shaft set that transmits the torque from the turbines at the rear of the engine to the compressors at the front. As these components are located at the centre of the engine, reductions in their diameters will allow all other systems around them to become smaller (Figure 1.2).

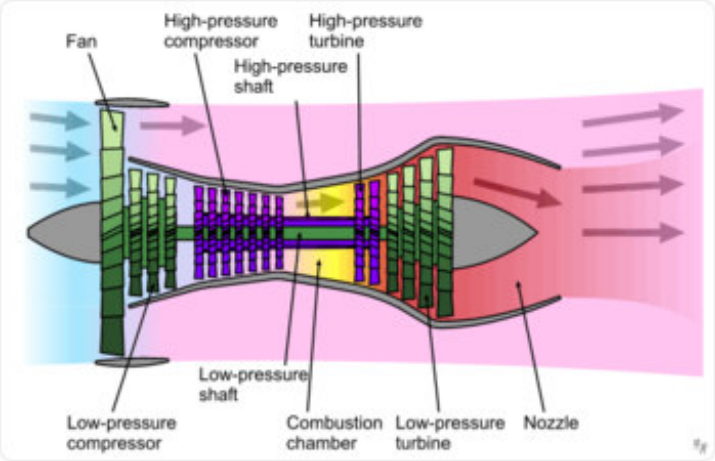

Figure 1.2. Simplified section of a twin spool turbofan engine
(courtesy of www.Wikipedia.com)

However, increasing an engine's propulsive efficiency by reducing core size generates larger stresses in the transmission components which are already highly stressed in modern configurations. Therefore to achieve the above potential efficiency benefits it is critical that transmission shaft performance is increased

1.4 Spline couplings

Spline couplings are often employed in the transmission shafts. These couplings provide an excellent solution for systems needing to transmit torque along a demountable shaft. They offer the ability to transmit torque, bending moment and axial load, and can accommodate small misalignments and moderate operating temperatures, all within compact dimensions. However, the result is a highly stressed component which must

cope with small amplitude movement imposed by cyclic misalignment, torque fluctuations, etc. Due to the critical importance of these components to safe aircraft operation, a high degree of confidence in the capability of these shafts is required. As such it is necessary that all potential failure modes are understood to mitigate the risk of failure.

Fatigue in the tooth root is generally the limiting factor on modern splines (Figure 1.3). However, the presence of small amplitude movement at the contact interface implies that the fretting phenomenon may potentially also occur. This complex failure mode is particularly dangerous as it is currently difficult to predict and can cause significant reductions in fatigue life. Fretting causes degradation of surfaces due to both wear and cracking. Figure 1.4 depicts examples of experimental spline coupling failures. Figure 1.4b highlights the complex failure characteristics of fretting fatigue with cracking occurring a significant distance away from the end of engagement where conventional analysis would predict failure. Additionally, fretting wear can result in significant material removal from the spline contact surfaces, ultimately compromising the tooth intergrity.

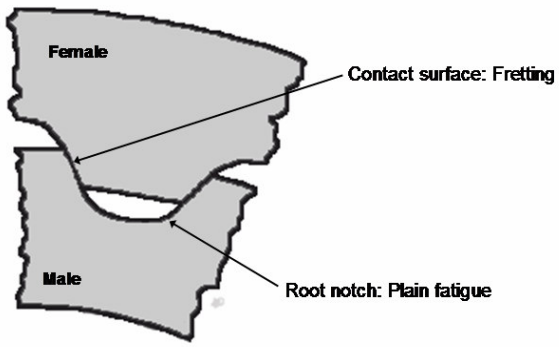

Figure 1.3. Spline cross section showing common failure locations

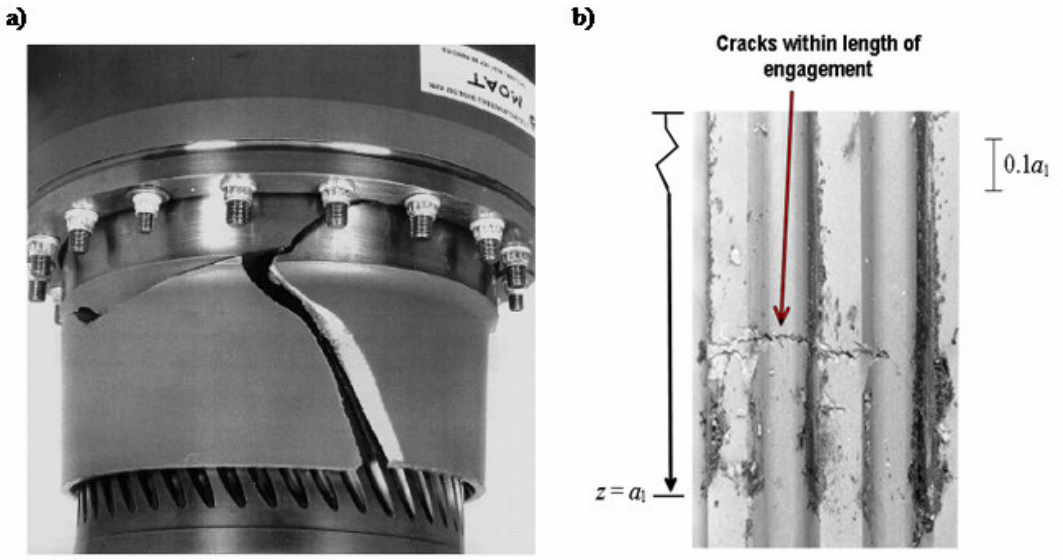

Figure 1.4. a) Example of a failed spline coupling, (Mugadu et al, 2002).
b) Fretting fatigue cracking for a laboratory scaled spline coupling under overload (Ratsimba et al, 2004).

In current aero-engine spline designs, fretting does not tend to be the life limiting factor. However, as splines become more highly stressed to meet the needs of future engines fretting is likely to become an issue. Therefore it will become increasingly important to understand the phenomenon more fully so that splines, and other components which experience fretting, are optimized from a fretting perspective. In particular, a method is required that is capable of assessing coupling performance in terms of both wear and fatigue behaviour. There is also evidence that the interaction between wear and fatigue is an important factor in fretting damage mechanisms

1.5 Aims

The aim of this study is to develop a methodology for predicting the effect of fretting wear induced stress evolution on fretting fatigue life. The work will provide the foundation for more accurate lifing of components subject to fretting.

1.6 Thesis scope

Chapter 2 will present a literature review of relevant works, discussing the state of the art in the fields relevant to the aims of this thesis i.e. contact mechanics, fatigue of metals, fracture mechanics, wear and friction and their application to fretting analysis are discussed.

Chapter 3 describes the development of a novel methodology which combines fretting wear modeling with a critical plane fatigue lifing model to allow the effect of fretting wear to be captured in fatigue lifing predictions. The Finite Element (FE) based implementation combines a modified version of the Archard wear equation, a critical plane fatigue damage model and a Miners rule damage accumulation framework.

Chapter 4 studies the application of the combined fretting wear/critical plane model to an experimental test series taken from the literature. The development of surface tractions with wear and hence cyclic fatigue damage in a cylinder on flat geometry is studied

Chapter 5 applies the combined fretting wear/critical plane model to a punch on flat contact configuration. The method is validated against experimental geometry. The impact of wear on fatigue life and failure position predictions are investigated.

Chapter 6 describes the development of a complimentary fretting fatigue/wear model which adopts a fracture mechanics perspective alongside the modified Archard wear model described previously. The critical plane and fracture mechanics models developed are then combined within the wear model approach to provide a 'total life' initiation-propagation fatigue model for fretting analysis.

Chapter 7 applies the fracture mechanics model to the cylinder on flat geometry studied in Chapter 5 to study the effect of wear on fretting fatigue crack propagation. Life predictions are made using the total-life model. A brief study of the impact of wear on crack arrest and crack reactivation is also conducted.

Chapter 8 describes the application of the fretting wear model to a novel type of rotor joint. The insight gained from the preceding chapters is applied to optimize the contact behaviour of the joint.

Chapter 9 outlines the conclusion from the thesis.

Chapter 10 makes recommendations for future work.

Chapter 2

Literature review

2.1 Introduction

This review will initially examine the relevant results of contact mechanics in order to explore the basic loading characteristics of two common analytical geometries. An overview of both fatigue and fretting is then given. The final section focuses on the analytical techniques that have been employed in fretting fatigue modelling

2.2 Contact mechanics

Contact mechanics considers the analysis of contacting bodies. The benchmark work Hertz (1882) considered the contact between normally loaded non-conforming bodies. Solutions were given for both two dimensional (2D) contact between a pair of elastic halfspaces, and the 3D case of contacting spheres. Here the 2D case, of the type depicted in Figure 2.1, is discussed.

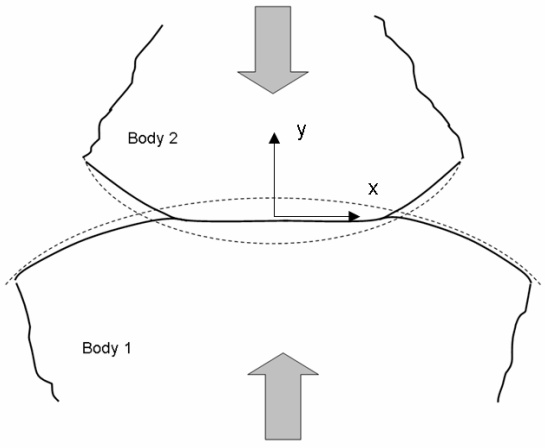

Figure 2.1 Schematic of Hertzian contact.

Elastic deformation within the bodies results in a contact with finite width $2a$:

$$a^2 = \frac{4PR^*}{\pi E^*} \tag{2.1a}$$

where P is the normal load, R^* is the combined radius of curvature and E^* is the combined modulus:

$$E^* = \frac{1}{\left(\frac{1-\nu_1^{\,2}}{E_1} + \frac{1-\nu_2^{\,2}}{E_2}\right)} \tag{2.1b}$$

$$R^* = \frac{1}{\left(\frac{1}{R_1} + \frac{1}{R_2}\right)} \tag{2.1c}$$

where E_i, R_i and ν_i are the Young's modulus, Radius of curvature and Poisson's ratio for contact body i respectively.

The contact pressure distribution is governed by the following equation

$$p(x) = \frac{2P}{\pi E^*}\sqrt{a^2 - x^2} \tag{2.2}$$

where x is the horizontal distance from the centre of contact. The resulting normal pressure distribution has an elliptical form: The maximum normal pressure p_0 occurs on the centreline

$$p_0 = \sqrt{\frac{PE^*}{\pi R}} \tag{2.3}$$

falling continuously to zero at the edges of contact. The subsurface stresses can now be obtained, the variation of stresses along the centreline of contact y is shown in Figure 2.2. The Hertzian pressure distribution is shown in Figure 2.3

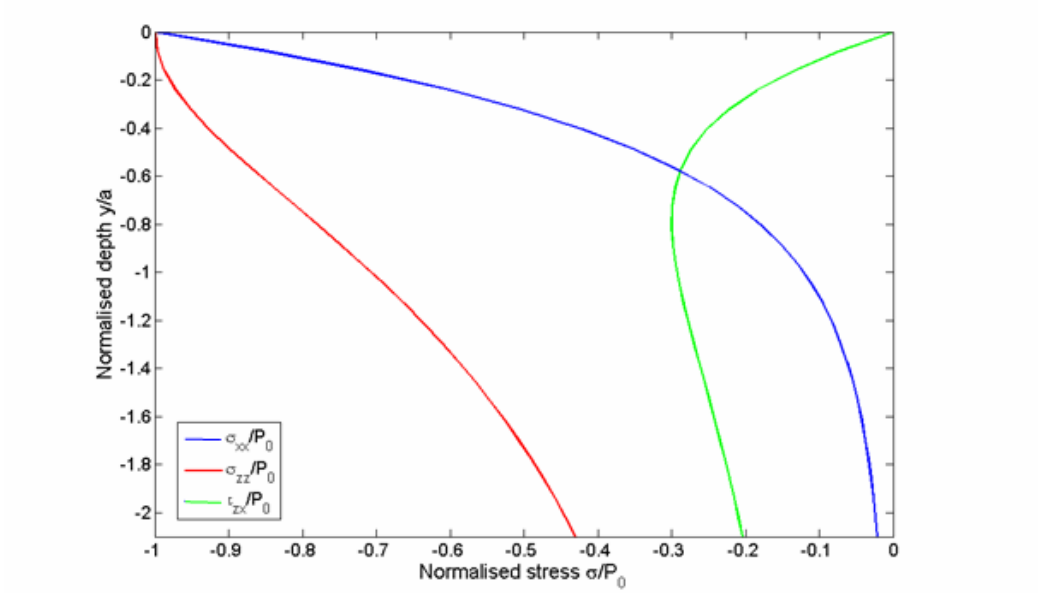

Figure 2.2. Subsurface distribution of stress components, x=0.

Under plane strain conditions (ε_z=0), the third stress component σ_z is found to be dependent on Poisson's ratio: $\sigma_{zz}=\nu(\sigma_{xx}+\sigma_{yy})$. Hence, for typical materials ($\nu\approx0.3$) the condition $\sigma_{zz}\approx\sigma_{xx}=\sigma_{yy}=-p_0$ creates a near hydrostatic stress state at the contact surface. It is found that the maximum shear stress occurs at a depth of approximately 0.3a. Therefore failure will occur below the contact surface under perpendicular load conditions.

The Hertzian 2D analysis, which considers the contact between two cylinders, is subject to the following assumptions:

i) negligible friction at the interface

ii) each body is a semi-infinite, elastic, 'half-space'

iii) The width of the contact is small compared to the body radii

iv) Profile is smooth, continuous and non-conforming

Hertz' original theory has been extended to cover the application of tangential loads and the presence of friction at the interface independently by Cattaneo (1938) and Mindlin & Deresiewicz (1953). The Coulomb friction model was employed:

$$q(x) \leq \mu p(x) \tag{2.4}$$

where $q(x)$ is the shear traction at point x, and μ is the coefficient of friction (COF). In this case the Coulomb friction law is applied on a local basis, i.e. if the shear traction at any point is less than the critical value μp, no relative displacement occurs. However, if the Coulomb limit is reached at any point along the surface, the shear traction at this point is essentially the pressure scaled by μ.

$$q'(x) = \mu p_0 \sqrt{1 - \frac{x}{a}} \tag{2.5}$$

If the global Coulomb limit is not exceeded, i.e, $Q<\mu P$, a central stick region will exist of width 2c:

$$\frac{c}{a} = \sqrt{1 - \frac{Q}{\mu P}} \tag{2.6}$$

A second shear traction in the region $-c<x<c$ is given by:

$$q''(x) = -\mu \frac{c}{a} p_0 \sqrt{1 - \frac{x^2}{c^2}} \tag{2.7}$$

The overall shear traction across the contact is given by the superposition of $q'(x)$ and $q''(x)$ (Figure 2.3).

Due to the nature of the Hertzian pressure distribution, the condition $Q<\mu P$ results in a stick region which is bounded by two slip regions. Therefore, although the contact appears to be stuck, the Coulomb friction limit has been exceeded locally at some points, which are sliding, referred to as the partial slip regime.

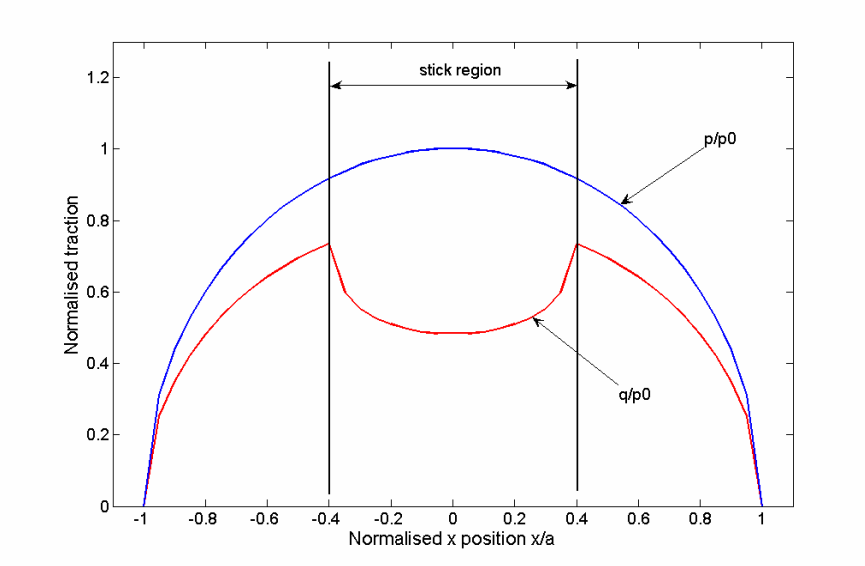

Figure 2.3. Surface tractions for Hertzian/Mindlin contacts.
(Q/P=0.46, μ=0.8)

Johnson (1961) conducted an experimental study of a spherical contact under such a partial slip condition. A clear slip annulus was observed over which wear was noted. Conversely, in the central stick region no obvious wear was noted. The frictional dissipation of the experiments showed good agreement with that predicted by the Cattaneo-Mindlin solution.

The Cattaneo-Mindlin solution has been extended by Nowell & Hills (1987) to include the effect of a bulk substrate load. The problem is depicted in Figure 2.4; being similar to the configurations used in many fretting fatigue experimental studies, it provides a useful benchmark solution.

The effect of the bulk stress is to create an eccentricity to the Mindlin-Cattaneo shear traction distribution:

$$q''(x) = -\mu \frac{c}{a} p_0 \sqrt{1-\left(\frac{x-e}{c}\right)^2} \qquad \text{where} \qquad e = \frac{\sigma_b a}{4\mu p_0} \qquad (2.8)$$

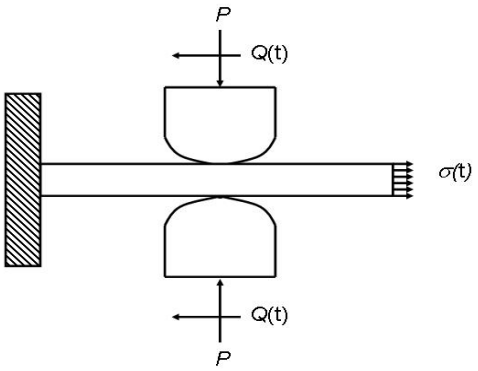

Figure 2.4. Schematic of fretting fatigue test configuration.

The resultant shear traction is then given by the superposition of *q'(x)* and *q''(x)* (from Equation 2.5 & 2.8); an example is shown in Figure 2.5.

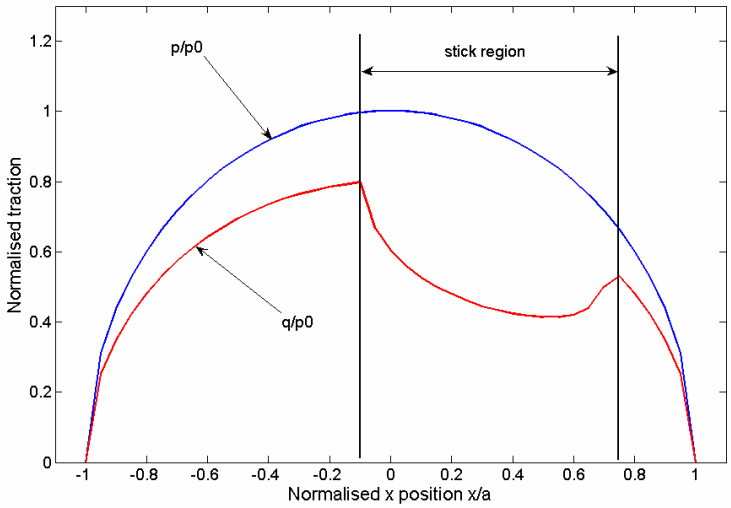

Figure 2.5 Effect of bulk load on shear traction distribution.
(Q/P=0.46, μ=0.8, σ_b/P_0=0.5)

This solution is still based on the elastic half-space assumption. This is found to be a reasonable approximation as long as the material response is dominated by elastic behaviour, and the specimen thickness is greater than 10 times the contact width. Fellows et al (1995) found that although the shear tractions are largely unaffected by specimen thickness, subsurface stresses are, which has implications for fatigue life prediction.

The cylinder on flat configuration creates a non-conforming contact. Another type of contact configuration is the 'punch on flat' (Figure 2.6). This creates a conforming contact, where the contact width is independent of normal load. The punch surface is also discontinuous, with sharp corners at the contact edges.

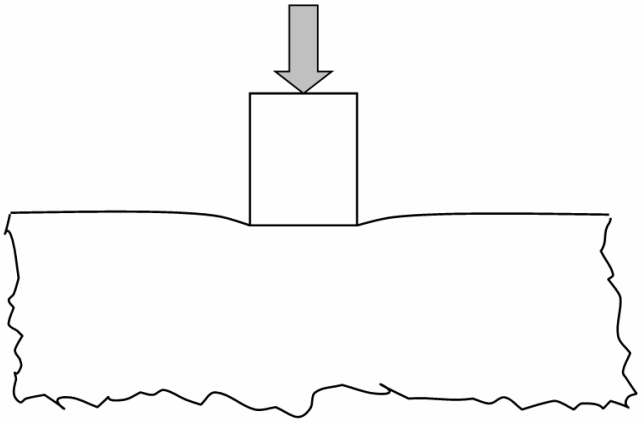

Figure 2.6. The punch on flat contact configuration.

The solution for a rigid punch indenting a plane elastic half-space shows that these discontinuities give rise to an asymptotic pressure distribution (e.g. Johnson 1985).

$$p(x) = \frac{P}{\pi\sqrt{a^2 - x^2}} \qquad (2.9)$$

The pressure peaks shown in Figure 2.7 indicate that these will create a theoretical pressure singularity at the contact edges ($x = \pm a$). The inclination of the punch, the relative modulus between the punch and half-space and the coefficient of friction at the contact affect the order of singularity at the contact edges (Giner et al, 2005).

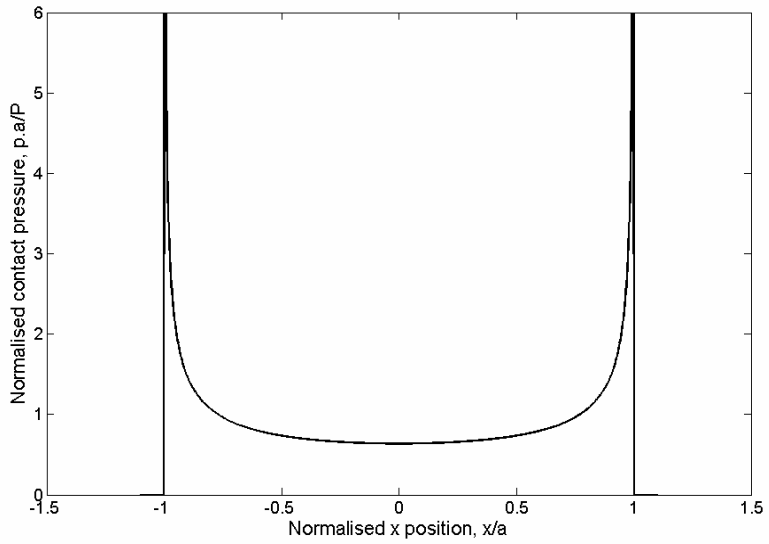

Figure 2.7. Pressure distribution for a rigid, frictionless punch on a flat elastic half-space.

The presence of contact pressure singularities at the edges of contact implies that a high stress singularity will also exist here. An obvious drawback in the adoption of an elastic half-space assumption is that non-physical infinite stresses are predicted. In reality plasticity would occur in these regions. Analytical techniques are generally limited to the rigid-perfectly plastic assumption when applied to problems involving plasticity. Numerical methods such as boundary elements (BE) and finite elements (FE) (e.g. Sum et al, 2005) have become popular where analysis must be extended to specific geometries or material models.

2.3 Tribology

2.3.1 Introduction

Tribology is the study of the interaction between contacting bodies and can be subdivided into three broad areas: friction, wear and lubrication. A brief overview of friction and wear is given below

2.3.2 Friction

Friction is the resistance created at a contact interface to a relative tangential displacement of the two bodies. Bushan & Gupta (1991) cite three main causes of friction:

i.) Adhesion

ii.) Ploughing

iii.) Asperity deformation.

The total friction can typically be approximated with sufficient accuracy by the sum of these components.

Adhesion relates to the galling tendency of some materials. Junctions formed at asperity contacts due to normal load are deformed and later fractured by relative motion. As such adhesive friction is a function of both the interfacial shear strength and the surface energy of the contacting pair of materials.

Ploughing occurs either when one body is much harder than the other, or when hard wear particles are present, for example oxides. As the hard asperity/particle is traversed across the softer surface, the softer material is forced to plastically deform out of the path of the hard 'plough'. This friction component is principally a function of the hard asperity geometry (Rabinowicz, 1965); however as wear progresses, the

geometry is altered by the build up of material on the plough. This partially explains why friction coefficient can change as wear progresses.

Asperity deformation generally forms the most significant portion of total friction in metallic contacts (Bhushan & Gupta, 1991). This component arises from the deformations in asperities as they slide across each other such that compatibility is maintained.

Plasticity is a key feature in the friction components mentioned above, explaining it's irreversible and dissipating nature. Plasticity itself is a complex subject. A material's response will be altered by the material structure, both in terms of its crystal structure (e.g. dislocations, crystal size and orientation), temperature and loading history. It is therefore apparent that friction coefficient will not only be a function of original material condition (material combination, heat treatment, surface roughness etc) but will also be dependent on a number of environmental variables, and their histories such as sliding velocity, distance slid, normal load and temperature.

From the above arguments it is clear that friction is complex phenomena. A model which can predict the behaviour of friction under a wide range of different conditions is not yet available. This is perhaps the justification for the enduring use of the Coulomb friction model, which is the most commonly used approximation of friction. The Coulomb law assumes that the maximum shear load that can be sustained across the contact is proportional to the normal load. In reality there is a maximum load that can be transmitted, as the shear strength of the material is reached, hence a maximum shear stress τ_{max} appears in some friction laws, e.g. Heilmann & Rigney (1981).

2.3.3 Wear

The deformation mechanisms associated with friction as mentioned above result in damage being sustained by material close to the contact interface. Eventually this results in particle detachment, which cumulatively is observed as wear. The mechanisms cited above with regard to friction generation are also found to be characteristic wear mechanisms. Bhushan & Gupta (1991) state that wear can be separated into six main categories: adhesion, abrasion, fatigue, erosion, corrosion and electrical arc. Fretting wear is typically a combination of adhesion, abrasion, fatigue and corrosion wear. Godet (1984) argued that in fact these mechanisms are only detachment mechanisms whereas in the actual wear process both particle detachment and ejection are important factors in the wear process. During the period between detachment and ejection, the particle becomes entrained in what Godet called the 'third body'. This is a compound layer of debris which occupies space within the contact itself, altering the tribo-system. Whilst Godet's theory offers an informative view into the wear process, it is yet to be treated quantitatively.

The Archard wear law was originally proposed by Archard (1953), and validated against a wide variety of materials undergoing sliding wear by Archard & Hirst (1956), with Rabinowicz (1965) later extending the law to abrasive wear. The relation is the most common wear model, based on the principle that the rate of wear for a given material is proportional to the contact pressure and the slid distance, and inversely proportional to the hardness:

$$V = K\frac{PS}{H} \qquad (2.10)$$

where V is the worn volume, P is the normal load, S is the total slid distance, H is the material Hardness and K is a non dimensional constant of proportionality, termed the wear coefficient.

By assuming that the friction force is proportional to the normal load P, via Coulomb friction, the Archard wear law can be interpreted as indirectly relating the wear to the energy dissipated at the surface. Fouvry et al (1996) have developed a modified wear law which is based on this interpretation whereby the wear coefficient is based on the dissipated energy. This is discussed further below.

Molecular dynamics simulations of sliding wear have shed light on the way that sliding surfaces interact, demonstrating mixing, wear particle formation and dislocation movement etc (e.g. Smith et al, 2005). They enable the tribological behaviour of a contact to be investigated at atomic scale interactions. The model is able to supply information on both friction and wear behaviour based on molecular behaviour and is thus quite general. However, currently these simulations are limited to the nanoscale. So that it is not feasible to apply them to real engineering assemblies.

2.4 Fatigue of Metals

2.4.1 General

Fatigue is defined by ASTM (1993) as "The process of progressive localised permanent structural change occurring in a material subjected to conditions which produce fluctuating stresses and strains at some point or points and which may culminate in cracks"

Interest in fatigue was spurred by the observation that failures occurred at loads below that of the material monotonic strength. Failures were noted to start at specific geometric features which presented stress concentrations.

2.4.2 Fatigue Mechanisms

Fatigue can be considered in four stages:

i) Nucleation

ii) Stage I crack growth

iii) Stage II crack growth

iv) Final fracture

Nucleation is a microstructural phenomenon. Metals generally have a polycrystalline structure i.e. they are made up of many adjoining grains. Each grain is a crystal lattice, whose form and size is dependent on the material and its manufacturing process. The atomic strength of a perfect crystal lattice is many times higher than that demonstrated on a macroscopic scale. The reason for the disparity is the presence of dislocations which exist in the lattice (Taylor, 1934). These imperfections can slip, one atomic spacing at a time, at shear stresses significantly below that required to break a perfect lattice (Figure 2.8).

In a poly-crystal the grain crystal structures are generally at random orientations with respect to each other, and contain a random distribution of dislocations. Some of the slip planes will be aligned with the principal shear stress plane, hence slip will tend to occur on these planes; this partially explains the stochastic nature of fatigue.

Eventually persistent slip bands form resulting in extrusions and intrusions forming at the surface. These extrusions act as microscopic stress concentrations at which stage I cracks initiate under shear loading. Further cycling results in these small cracks

coalescing into stage II growth which is dominated by tensile loading. Final fracture results in components failure arising either from ductile tearing or brittle fracture.

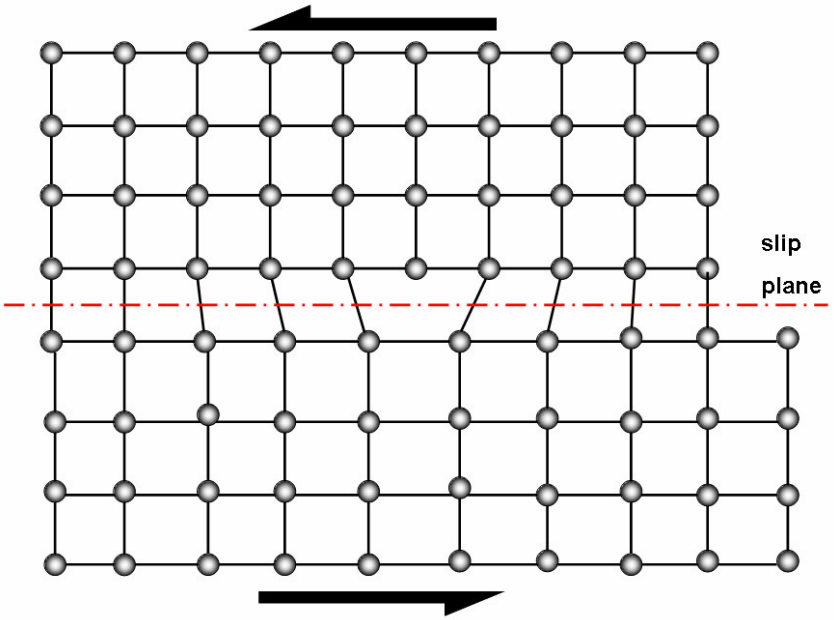

Figure 2.8. Edge dislocation in a crystal lattice structure

2.4.3 Relating Stress and Fatigue Life

The first systematic study into the relationship between stress and life was conducted by Wöhler (1870), observing that fatigue life was a stronger function of stress range than of peak stress. The ensuing S-N curve approach is still popular.

The stress-life approach was developed by Basquin (1910) with the observation of a log-log relationship between stress amplitude and life in high-cycle fatigue (Equation 2.11).

$$\frac{\Delta\sigma}{2} = \sigma_f' \left(2N_f\right)^b \qquad (2.11)$$

where $\Delta\sigma$ is the stress range, σ_f' is the fatigue strength coefficient, b is the fatigue strength exponent.

As the stress amplitude passes above the elastic limit of the material, the low-cycle, high strain fatigue regime becomes dominant. In low cycle fatigue the stress is no longer effective at characterising material damage. However, a similar relationship to Equation 2.11 is found to exist in the low cycle fatigue domain between the plastic strain amplitude and the number of cycles to failure (Manson & Hirschberg, 1964):

$$\frac{\Delta\varepsilon_p}{2} = \varepsilon_f'(2N_f)^c \qquad (2.12)$$

where ε_f' is the fatigue ductility coefficient and c is the fatigue ductility exponent. Later the Basquin and Coffin-Manson relations were combined to provide a total strain-life approach. By using Hooke's law the stress range of Equation 2.11 can be expressed in terms of the elastic strain range $\Delta\varepsilon_e$. The total strain range can then be found and related to fatigue life as follows:

$$\frac{\Delta\varepsilon}{2} = \frac{\Delta\varepsilon_e}{2} + \frac{\Delta\varepsilon_p}{2} = \frac{\sigma_f'}{E}(2N_i)^b + \varepsilon_f'(2N_i)^c \qquad (2.13)$$

where $\Delta\varepsilon$ is the total strain range. A myriad of different parameters have since been correlated to fatigue life. Generally these consist of functions of stress and strain, although a number of energy based approaches have been reported.

The Smith-Watson-Topper (SWT) parameter proposed by Smith et al (1970) is a direct development of the strain-life equation which seeks to address the effect of mean stress on fatigue life which is neglected in Equation 2.13:

$$SWT = \sigma_{\max}\frac{\Delta\varepsilon}{2} = \frac{\sigma_f'^2}{E}(2N_f)^{2b} + \sigma_f'\varepsilon_f'(2N_f)^{b+c} \qquad (2.14)$$

where σ_{max} is the maximum normal stress in a fatigue cycle.

The above approaches were developed on the basis of uniaxial fatigue, i.e. where the largest principal stress is large compared to remaining principal stresses. Most

engineering structures are in fact subject to multiaxial loading, where both normal and shear stresses may be significant. A great deal of research has been conducted in relating the multiaxial fatigue case to its uniaxial counterpart. The critical plane approach has emerged as a popular method to achieve this. The approach is based on physical observations that fatigue cracks initiate and grow within a material on certain planes, where the growth and orientation depends on the stresses and strains on these planes. Dominant fatigue damage occurs on a plane, which is nominated the critical plane. The approach has evolved from the work of Brown & Miller (1973) on multiaxial fatigue who first suggested the combined use of maximum shear strain range and tensile strain normal to the plane of maximum shear. The use of shear strain was justified by the observation that initiation tends to be a shear driven mechanism. The strain normal to a plain was employed due to its effect on propagating cracks.

Multiaxial fatigue is further complicated by the potential for non-proportional loading. Under proportional loading conditions the principal stresses remain in constant proportion to each other, and hence the angle of the principal axes remains constant throughout the fatigue cycle. Non-proportional or out-of-phase loading results in extra cyclic hardening due to the rotation of principal axes. Fatemi & Socie (1988) further developed the critical plane method by using normal stress instead of strain as the second parameter. This overcomes limitations of the Brown & Miller (1973) approach with respect to the increased damage associated with non-proportional loading.

The Fatemi-Socie (FS) parameter is an analogue of SWT for shear dominated failure. The FS and SWT parameters represent the most frequently applied parameters in fretting analysis:

$$FS = \frac{\Delta\gamma}{2}(1 + k\sigma_{\max}) = \frac{\tau_f'}{G}(2N_f)^b + \gamma_f'(2N_f)^c \qquad (2.15)$$

where k is a fitting parameter and $\Delta\gamma$ is the shear strain range over one cycle, G is the shear modulus, τ_f' is the fatigue shear stress coefficient, and γ_f' is the fatigue shear strain coefficient.

For most fatigue life situations, Fatemi & Socie (1988) have proposed the use of one of two multiaxial fatigue damage criteria, one for tensile cracking failure modes (e.g. Equation 2.14) and one for shear cracking failure modes (e.g. Equation 2.15). Such parameters should take account of both crack initiation and propagation. For shear cracking failure modes, the parameter should include shear strain amplitude for crack initiation, and maximum normal stress on the plane of maximum shear strain amplitude for crack propagation. For tensile cracking, the parameter should include maximum principal strain amplitude for initiation, and maximum normal stress on the plane of maximum principal strain amplitude for propagation.

Szolwinski & Farris (1996) were the first to suggest the critical plane method (with the SWT parameter) as a technique to deal with the multiaxial stress and strain cycles in fretting contacts.

2.4.4 Damage Models

Damage mechanics is usually a continuum approach which describes the degradation of material strength due to thermal and for mechanical loads. The principle centres on a damage parameter ω which for an undamaged material is 0 and for a failed material is 1 (Lemaitre, 1992). When applied to fatigue, ω is often related to the stress-strain cycles, via the constitutive equations. In its most complete form, damage mechanics is performed as part of a 'fully coupled' damage analysis, where material properties

such as Young.s modulus are altered based on loading history (e.g. Rashid et al, 2003). Frequently an 'uncoupled' analysis, which is significantly less complex than it fully coupled counterpart, is considered sufficient. In this case damage is not assumed to affect other material properties. A relatively common technique is to employ a fatigue parameter such as those discussed above as a cyclic damage measure (e.g. Fatemi & Socie, 1988). A damage accumulation rule is also required to relate cyclic damage to fatigue life. The most common damage accumulation rule is the linear damage rule first suggested independently by Palmgren (1924) and Miner (1945).

$$\omega = \sum_{i=1}^{N} \frac{n_i}{N_{fi}} \qquad (2.16)$$

where ω is the accumulated damage, n_i is the number of cycles experienced at loading cycle i, N_{fi} is the critical-plane SWT predicted number of cycles to failure at loading cycle i and N is the number of different load cycles experienced. In the Miner-Palmgren damage law damage is assumed to be independent of the order in which loads are applied. In practice this is not the case; proof stressing is a common technique for creating beneficial residual compressive stresses in pressure vessel to increase fatigue life (Fuchs & Stephens, 1980); conversely overstressing during early life can lead to crack nucleation that would not have formed at lower stress levels. Marco & Starkey (1954) state that damage accumulation is generally a non-linear interaction concerning both the nature of each individual loading cycle and the order in which different cycles are applied:

$$\omega = \sum_{i=1}^{N} \left(\frac{n_i}{N_{fi}} \right)^d \qquad (2.17)$$

However, the exponent *d* is typically difficult to determine and it is often not a constant; Jin et al (2003) found that for Ti-6Al-4V the value of *d* was dependent upon load level. Other non-linear damage rules have been proposed. Manson & Halford (1981) proposed the 'damage curve analysis' (DCA) method which proved difficult to apply and hence developed the 'Double linear damage rule' (DLDR) as an approximation to the former. However all non-linear rules appear to share the same problem; they rarely offer a sufficient increase in accuracy over the Miner-Palmgren rule to warrant the effort of determining the constants. As such the required material data for such models is rarely available from the literature.

Under variable loading conditions damage models also require cycle definition. In simple cases this can be determined from inspection. However, under random loading patterns this can become ambiguous. The most common algorithm for classifying such load cycles is the so called rain-flow counting method devised by Matsuishi & Endo (1968) for use in uniaxial loading. Figure 2.9 illustrates the concept, where the "rain flow" from one part of the loading spectrum to the next defines which cycle each part of the spectrum belongs to, breaking a complex loading regime into a number of different amplitude ranges which can be summed using the Miner-Palmgren damage law. Downing & Socie (1982) applied the method to biaxial loading via a critical plane implementation. One issue with the approach was in its application to compound parameters, where it was assumed that the loading was proportional; e.g. in the case of SWT, the stress 'channel' peak was assumed to occur at the same point in time as strain range 'channel' peak. The method has since been developed by others (e.g. Bannantine & Socie 1991, Langlais et al 2002) to address this issue. However, a specific channel must still be selected on which to base cycle definition, hence the method is not a well defined one.

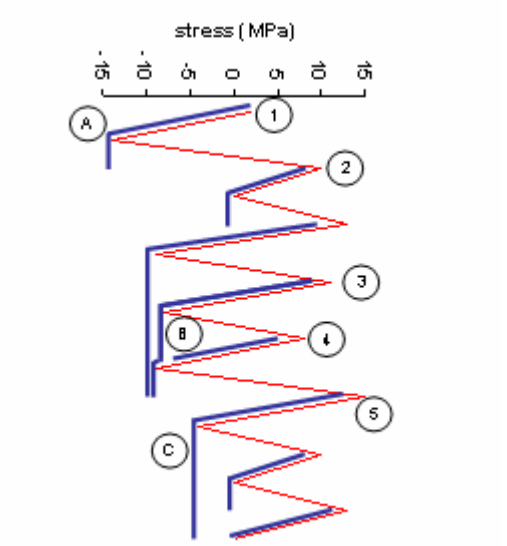

Figure 2.9. Rain-flow counting concept
(courtesy www.wikipedia.com)

2.4.5 Fracture Mechanics

Fracture mechanics is the study of the growth of cracks due to fatigue loading. The field initially presented an apparent analytical problem: in an elastic medium, infinite stresses occur at a sharp crack tip, implying that failure should result under very low load. Griffith (1921) considered the incremental growth of a crack from a thermodynamic viewpoint, stating that a crack would grow stably if the energy released by an increment in growth was equal to the energy required to form the new surfaces. Griffith also noted a material property which he termed the critical energy release rate G_{IC} which if exceeded led to unstable fracture. Figure 2.10 shows these stages in terms of the stress intensity factor (SIF) range at the crack tip and crack growth rate.

Linear elastic fracture mechanics (LEFM) using the stress intensity factor K to characterise the crack tip stress field. Under linear elastic conditions K and G are equivalent. Analytical SIFs are available for a range of different ideal geometries, they are generally in the form:

$$\Delta K = Q\Delta\sigma_{\infty}\sqrt{\pi l} \qquad (2.18)$$

where Q is a geometric form factor, $\Delta\sigma_{\infty}$ is stress remote from the crack and l is the length of the crack. In practical geometries Q is rarely available in closed form but truncated series approximations are available in the literature e.g. Rooke & Cartwright (1976), Murakami (1987), Anderson (1991). Figure 2.10 shows the typical relationship between SIF and crack growth rate in real materials.

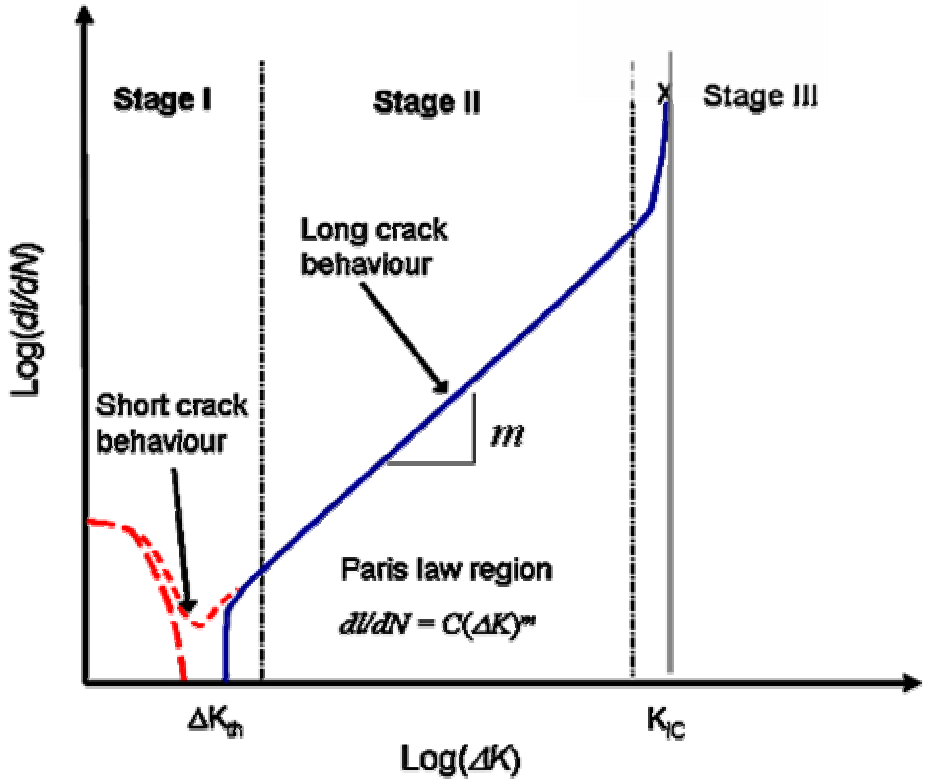

Figure 2.10. Schematic of typical crack growth behaviour

Paris & Erdogan (1963) were the first to observe the log-linear property of the majority of this curve, known as 'Stage II'growth. They proposed that crack growth in this region can be approximated by:

$$\frac{dl}{dN} = C(\Delta K)^{m} \qquad (2.19)$$

this relation has been embellished to give wider applicability to problems. The first modification improves fidelity at low ΔK values. At low ΔK values a threshold ΔK_{th} is displayed in many materials, below which no growth occurs. The following equations have been proposed in order to introduce asymptotic behaviour as ΔK tends to ΔK_{th}:

$$\frac{dl}{dN} = C(\Delta K - \Delta K_{th})^m \qquad (2.20)$$

$$\frac{dl}{dN} = C(\Delta K^m - \Delta K_{th}^m) \qquad (2.21)$$

Equation 2.20 was proposed by Donahue et al (1972) whereas Equation 2.21 was suggested by Klesnil & Lucas (1972).

The stress ratio R is the ratio between maximum and minimum loading conditions. i.e. $\sigma_{min}/\sigma_{max}$ can also be expressed through the ratio of the stress intensity at the crack tip i.e. $K_{min}/K_{max.}$ In most engineering materials the presence of negative stress intensity factors does not increase crack growth as the crack tip is shielded by closure of the crack faces. A negative stress intensity factor is non-physical, hence it is common to force K_{min} to zero if its calculated value is less than zero. Crack growth is also found to be dependent on R. High R ratios are typically found to accelerate crack growth for a given stress intensity factor range ΔK. A number of empirical relationships have been proposed to replicate this effect. Walker (1970) proposed such a model, which is commonly used to modify the Paris law for R-Ratio effects:

$$\frac{dl}{dN} = C_B\left(\frac{\Delta K^{m_b}}{(1-R)^{c_1}}\right) \qquad (2.22)$$

where C_b, m_b and c_1 are Paris type empirical material constants.

The LEFM approach is only valid when K sufficiently characterises the crack tip stress field, i.e. that the deformation is dominated by elastic stresses. If a plastic region is

created around the crack tip which has a radius comparable to the crack length, the assumption of small scale yielding no longer applies. This occurs at very short crack lengths and at very high load levels. Elastic-plastic fracture mechanics (EPFM) is concerned with this family of crack growth problems. At very short lengths cracks are observed to grow at much higher rates than would be predicted by Equation 2.16, as depicted in Figure 2.10. It is also found that these cracks propagate at stress intensity factors below the long-scale threshold ΔK_{th}. Figure 2.10 shows how these cracks can either arrest after the crack has grown some distance, or propagate and join the long crack growth curve, depending on the prevailing crack tip conditions.

There are a number of hypotheses regarding the difference between short and long crack behaviour. A short crack typically has a small stress intensity associated with it and therefore the stressed volume around the crack tip is also small. Therefore the growth of very short cracks is determined by perhaps one crystal, whereas a long crack will be elastically constrained by a larger number. Hence the long crack behaviour can more reliably be characterised by bulk material properties, where the short crack will exhibit much greater variability according to grain properties and orientations etc. (Anderson, 1991).

As the crack grows a plastic wake is formed. The residual stress in this wake has a tendency to close the crack. At very short lengths the wake is not sufficiently established to effect closure of the crack, and therefore short cracks do not benefit from the same level of shielding by the plastic wake as does a long crack.

Several workers have suggested crack growth laws for the short-crack problem (e.g Navarro & Del Los Rios (1987), Taylor (2002), El-Haddad et al (1979)). The models of Navarro & Del Los Rios and Taylor are focussed on modelling the retardation effect of microstructural barriers such as grain boundaries on the growth of

short cracks. The El-Haddad et al (1979) work proposed an empirical modification to the Paris-Erdogan law given in equation 2.16 to correct for short crack behaviour. They observed that at very short lengths a crack will grow at a rate equivalent to a crack that is some constant l_0 longer than the physical crack:

$$\Delta K = Q\Delta\sigma_{\infty}\sqrt{\pi(l+l_0)} \qquad (2.23)$$

where l_0 is a 'fictitious' or 'intrinsic' crack length which is found to correspond with the Kitagawa & Takahashi (1976) 'critical crack size' from threshold fatigue behaviour and is defined as follows:

$$l_0 = \frac{1}{\pi}\left(\frac{\Delta K_{th}}{\sigma_e}\right)^2 \qquad (2.21)$$

In terms of the El-Haddad concept, the physical interpretation of l_0 is yet to be satisfactorily explained, although Taylor (1999) has found that the parameter does bear significance when considering the size effect on the fatigue limits of both cracks and notches, generally l_0 is considered to be an empirical fitting parameter. However, the approach offers a very convenient method for approximating short crack behaviour, which approximates the prominent features of short cack growth behaviour (e.g. Taylor & O'Donnel, 1994, Dini et al, 2006).

Under general multiaxial conditions, the crack tip is subjected to both normal loading (Mode I) and shearing (Mode II & III), termed 'mixed mode' loading. Each loading mode has its own stress intensity factor which characterises the stress field for linear elastic materials. The presence of shearing modes has a tendency to make the crack turn. Erdogan & Sih (1963) proposed the maximum tensile stress (MTS) criterion, which stated that crack growth occurs in the direction of maximum hoop stress around the crack tip. Sih (1972) later offered the minimum strain energy density function (MSEDF) as an improved criterion. Both criteria are trigonometric functions of the

stress intensity factors, and both are commonly used as crack growth direction criterion in mixed mode fracture mechanics (e.g. Cissillino & Aliabadi (2004), Ko et al (2001)). Generally it is found that most of the proposed models predict relatively similar behaviour for brittle fracture, for example the MTS and MSEDF predict the cracking direction under pure mode II loading to be 70.5^{o} and 79.2^{o} respectively for ν=0.22 (Suresh 1998).

2.5 Fretting

2.5.1 General

Fretting occurs when small amplitude relative motion occurs between contacting components. The phenomenon can occur between non-metals, but is most frequently observed in metal on metal contacts, which is the focus of this work. Historically fretting has been categorised as occurring at relative displacements of up to around 300μm. Above this limit, the system is deemed as being 'reciprocating sliding', which is more fully understood than its fretting counterpart.

Fretting is a complex combination of sciences; tribology, contact mechanics and fatigue perspectives have been considered in fretting analysis. Collins and Macro (1964) cited fifty different variables which affect its behaviour. Dobromirksi (1992) later classified these into primary variables which have a direct effect, and secondary variables which operate indirectly by affecting the primary variables. The primary variables were cited as normal load, coefficient of friction and slip amplitude. However, even these 'primary' variables are found to be interdependent. For example, the COF and normal load will affect the slip distribution (Hills & Nowell, 1994), Jin & Mall (2002) and MColl et al (2003) observed that COF is dependent on normal load (Figure 2.11); an increase in normal load reduced the apparent COF.

Furthermore, COF is found to change with the number of fretting cycles e.g. (e.g. McColl et al, 2003). A typical evolution of COF with number of cycles is shown in Figure 2.11; at the start of a test the contact is contaminated with oils, water, oxides etc, thereby resulting in a low early COF, typically 0.1-0.2. As the surfaces wear the contaminants are dispersed allowing metal on metal contact; adhesion and asperity deformation become more prevalent. As wear progresses a debris layer is generally formed consisting of metal particles and their oxide products. The specific details of this layer such as chemistry and morphology, and hence its bulk material properties will depend on the loading conditions and environment (Godet et al, 1984)

A significant question regarding the friction behaviour of fretting systems still remains: Since the COF appears to be a function of several variables, it is likely that the COF varies both spatially across the contact and temporally. Dini & Nowell (2003) have developed an analytical model which predicts the slip zone coefficient based on macroscopic measurements. Experimentally this behaviour is difficult to capture due to inaccessibility of the region in question. The ability to measure variables such as COF and wear coefficient across the contact would provide valuable information on the tribo-system behaviour.

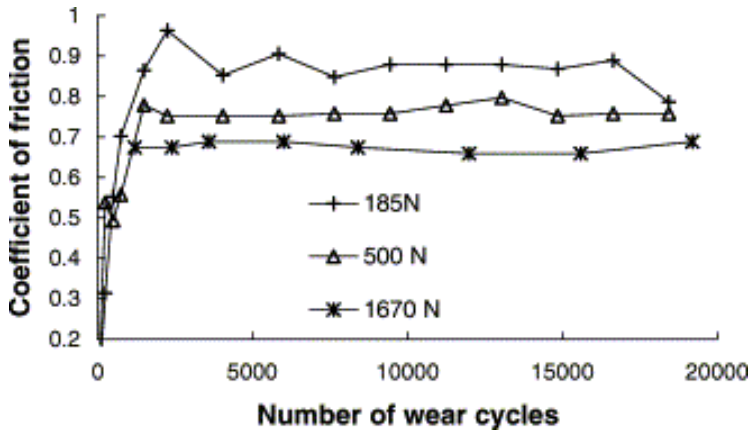

Figure 2.11. the effect of normal load and number of fretting cycles on the coefficient of friction (McColl et al, 2003)

Vingsbo & Soderberg (1988) reported a strong influence of slip amplitude on fretting fatigue life. The characteristic 'bath-tub' curve shown in Figure 2.12 displays a dependency on the slip regime prevailing at the contact interface. At low slip amplitudes the stick condition occurs, with very little relative motion. As slip amplitude is increased the partial slip state dominates and life is seen to reduce, typically by an order of magnitude. As the gross sliding state becomes established, fretting fatigue life rapidly recovers to levels seen in the stick state. The dominant damage mechanism appears to be dependent on slip regime; Fouvry et al (2004) offer a comprehensive outline of the characteristics of gross sliding and partial slip. Essentially, gross sliding gives high energy dissipation and high wear volumes, whereas partial slip tends to produce less energy dissipation and smaller wear volumes; however the latter is often accompanied by cracking, particularly at the stick-slip interface. It is generally observed that gross sliding tends to lead to infinite (or long) fatigue life and partial slip tends to lead to shorter fatigue life and component failure through cracking.

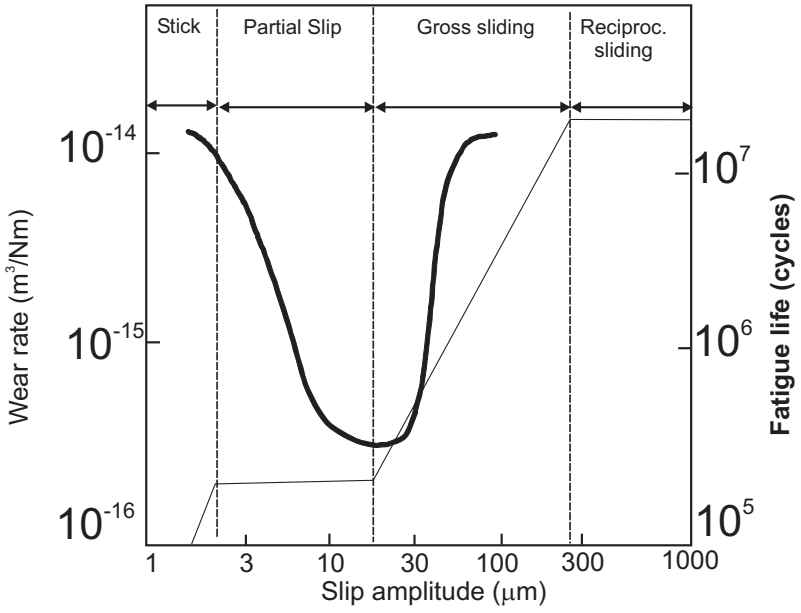

Figure 2.12. The effect of slip amplitude on a) fretting fatigue life (bold line) b) wear rate (thin line). (After Vingsbo & Soderberg, 1988)

There is also a coincidence of changes in wear rate and fatigue life shown in Figure 2.12. This has led to the hypothesis that the wear behaviour is instrumental in the relationship between slip amplitude and fatigue life. There is evidence that it is not simply the effect of surface damage induced by fretting wear that causes the reduction in life observed in fretting; there is a synergetic action when both fretting fatigue and fretting wear which results in a larger reduction in life than when specimens are pre-fretted and subsequently fatigue loaded. This is further evidence that the fretting problem should consider the two mechanisms in parallel.

Varenberg et al (2004) has pointed out the somewhat arbitrary nature of the boundary between fretting and reciprocating sliding occurring at 300μm. The actual transition will be dependent on the dimensional scale of the contact as well as other variables such as normal load, coefficient of friction etc. By applying Buckingham's Π-theorem, Varenberg proposed characterising the fretting regime by a dimensionless parameter termed the slip index. The slip index was demonstrated to be equally applicable to both nano-scale and macro-scale fretting tests. Varenberg generally defined fretting as "a relative cyclic motion between two surfaces, having a non-uniform distribution of local relative displacement at their contact."

Fretting fatigue often demonstrates failures under the contact itself (Figure 2.13). Most frequently observed under partial slip conditions, this can occur in both Hertzian contacts and punch on flat contacts (e.g. Jin & Mall, 2002, Nakazawa et al, 2003). Conventional applications of both LEFM and critical plane approaches tend to predict that the most damaging location is at the edge of contact. Fouvry et al (2004) introduced the concept of a threshold SWT value, above which cracking can occur. Although this allowed the prediction of cracking across the slip region, it also predicted cracking outside of the contact which is rarely observed.

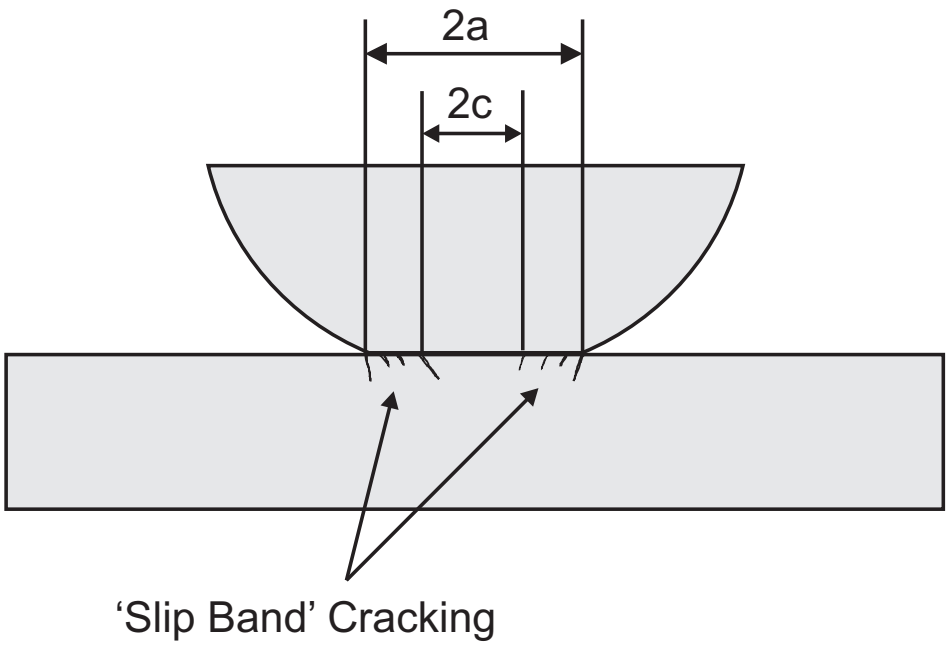

Figure 2.13. Schematic of the stick (dimensioned '2c') and slip regions (and cracking locations) associated with partial slip conditions .

2.5.2 Multiaxial fatigue parameters in fretting

As demonstrated in Figure 2.2, the cyclic stress state in the vicinity of the contact is multiaxial, owing to the non-linear nature of friction it is generally non-proportional. A number of researchers have applied other fatigue parameters to the fretting problem. The SWT and F-S parameters have been the most popular and generally the most successful (e.g. Sum et al, 2005, Araujo & Nowell, 2002, Fridrici et al, 2004) Other fatigue parameters such as Dang Van (Dang Van et al, 1989) have also been employed. In studies on T-6Al-4V, Jin & Mall (2004) found the MSSR parameter to be able to predict failure location, and cracking angle but not the effect of slip amplitude, in fact no fretting fatigue analysis has been able to predict the effect of slip amplitude on fretting fatigue life.

The high stress gradients present in fretting conditions can produce erroneous results when macroscopic fatigue parameters such as F-S and SWT are applied at the microscopic scale. Araujo & Nowell (2002) observed a pronounced size effect in

experiments on the fretting fatigue of both a 4%AlCu, and Ti-6Al-4V. Under nominally similar stress conditions, contact widths below a certain value were found to result in infinite life whereas larger contacts caused failures. Araujo & Nowell hypothesised that this size effect was similar to that observed in sharp notches, whereby a high stress must be applied over a sufficiently large area to initiate a fatigue crack. When they applied the F-S and SWT parameters to the analytical stress field they were unable to replicate this size effect: i.e. all tests were predicted to have finite life. However, when averaging the parameter over a certain 'process volume' both parameters were able to predict the experimental lives with good accuracy. In both the titanium and 4%AlCu, the length-scale of the process volume was found to be comparable with the size of the material microstructure.

The Dang Van parameter is distinct from most fatigue parameters as it is concerned with microscopic material behaviour rather than the macroscopic variables used by other correlations. However, the method only provides a finite/infinite life indication and is unable to predict a number of cycles to failure. Peridas et al (2003) have extended the method by comparing the criterion with more traditional approaches such as the Goodman method for uniaxial loading and the Sines criterion for biaxial loading. Thus a finite life prediction can be indirectly inferred from the Dang Van method.

Ruiz et al (1984) are the only authors to create a fretting only damage parameter. The parameter forms a product of shear stress, normal stress and slip amplitude. The method has been shown to give good prediction accuracy regarding the location of cracking under partial slip conditions, but has been shown by Lykins et al (2000) to give little correlation with the number of cycles to failure or whether infinite/finite life will occur.

2.5.3 Fracture mechanics in fretting

Fracture mechanics has been applied to the fretting problem in a variety of ways. Navarro et al (2006) have directly considered the growth of cracks under fretting induced stresses, resulting in accurate prediction of the relationship of between crack length and number of fretting cycles. The approach was novel in that it combined an initiation model, which bore similarities with Fouvry et al's (2004) SWT based cracking risk indicator, with fracture mechanics to model the propagation phase, furnishing a 'total-life' approach. The behaviour of the model in the nucleation and short crack phases did show some deficiencies, and the model lacked accuracy in this region. Navarro et al's fracture mechanics implementation was based on mode I growth on the basis that the mode I stress intensity factor K_I is much larger than K_{II}. However, further analysis led them to conclude that the crack path has significant impact on the propagation behaviour. By only considering mode I growth aspects, the crack was originally prescribed to grow along a straight path. However, if the crack path was prescribed to a take a path similar to that observed in their experiments, the prediction accuracy of their model was improved considerably. It follows that the mixed mode aspect is important in fretting crack growth.

Giannakopoulos et al (1998) suggested that the similarities in stress field created by a crack and a sharp edged contact can be used to draw an analogue commonly referred to as the crack like notch analogue (CLNA). The method has been developed by Conner et al (2004) to give a life prediction capability for both complete and incomplete contacts. The latter was achieved by considering an adhered contact, thus created the necessary singularity for the approach. The model was able to predict the finite life of complete and nearly complete contacts when compared to experimental

data to an accuracy of around $\pm 3N_f$. The prediction of incomplete contacts was also generally good, though some significant deviations were present (Figure 2.14)

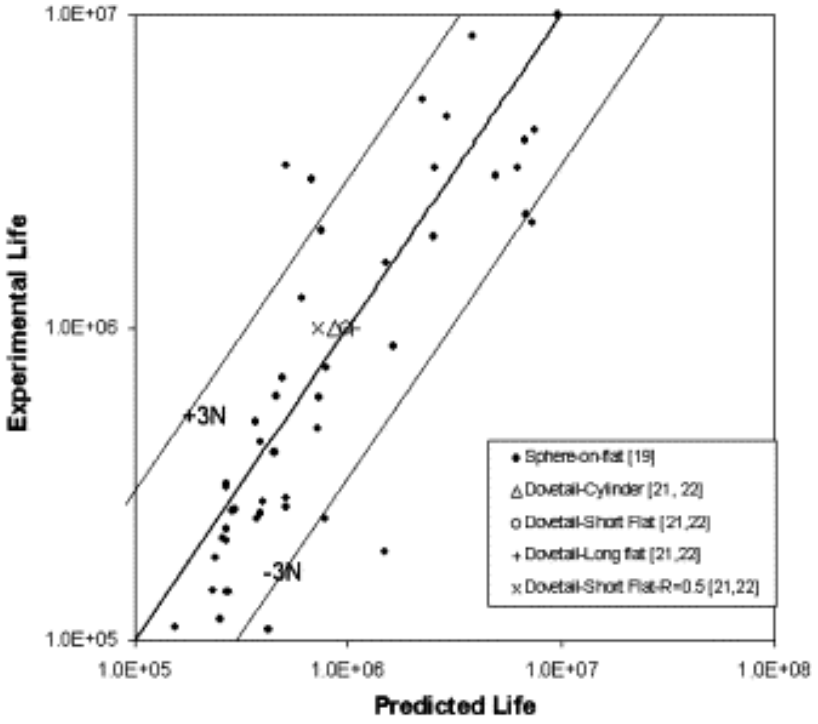

Figure 2.14. Comparison of experimental vs CLNA predicted lives (Connor et al, 2004)

Moobola et al (1997) also used a fracture mechanics approach, but rather than trying to model crack growth, the method focussed on predicting self arrest of cracks growing away from the contact stress field. They argued that in components operating at very high frequencies, such as gas turbine disc/blade contacts, infinite life is a requirement. By designing the component such that any cracks are naturally self arresting this requirement is guaranteed. The approach has been extended further by Dini et al (2006), and evaluated against a range of experimental fretting tests (Figure 2.15). The method showed good fidelity with experimental results, consistently predicting a finite or infinite (run-out) life for a range of fretting experiments. A potential limitation of the method is that it is a go/no-go indicator. Whilst this may be acceptable for components experiencing high cycle fatigue, it is of

limited use in analysing very highly stressed components where infinite life is not a practical possibility.

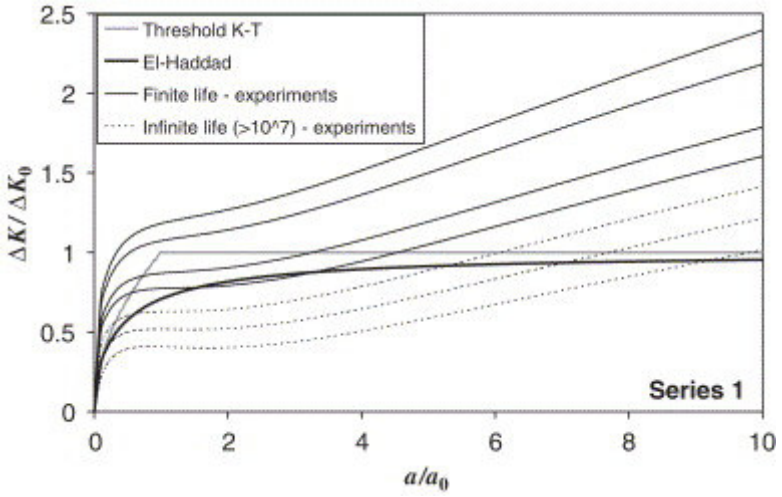

Figure 2.15 Dini et al's short crack based prediction of finite and infinite lives in fretting (Dini et al ,2006)

2.5.4 Numerical modelling of fretting contact

Due to the availability of closed form solutions for elastic half-space contacts, much of the analysis work has been based on this theory. However, the work is bounded by assumptions such as idealised material response, and half space geometries. With the availability of more powerful computers it has become possible to model fretting systems numerically. Boundary elements have been used in a few applications (e.g. McFarlane et al, 1999) though finite elements (FE) are the more popular owing to the greater availability of developed codes. In terms of real engineering components that experience fretting, the majority of modelling has concerned either spline couplings (e.g. Leen et al, 2003), or gas turbine blade/disc dovetail joints (e.g. Papinkos, 1998), railway axles (e.g. Ekberg, 2004) and riveted panels (e.g. Szolwinksi, 2000) have also been analysed using finite elements. Actual engineering assemblies provide a compelling argument in the choice of numerical techniques such as finite elements over analytical methods. Industry has a need for generic tools which can be directly

applied to general systems with increasing complexity. For example, Sum et al (2005) have analysed an experimental spline geometry regarding fretting performance under complex multiaxial load cycles and using elastic-plastic models. The FE model predicted that under large bending moments, a partial slip regime is created. The location of the stick-slip boundary was coincident with fretting fatigue cracks observed in experimental tests of a similar load case and geometry. Finite elements have also been applied to more simple cases such as 2D Hertzian contact (e.g. Sum et al, 2005, Lykins et al, 2000). The work by Sum et al showed that the finite element method showed an ability to capture the size effect of fretting fatigue, demonstrated earlier by Araujo & Nowell (2002). This is attributed to the fact that FE models essentially average the stress field over an elemental volume, which is similar to the volume averaging approach commonly adopted to explain such phenomena. When compared to similar analytical models such FE models generally show good fidelity. However, as with any numerical method, care must be taken to ensure convergence of the discretised problem. For example, Leen et al (2001) have shown that the assumed time increment used in a non-linear contact analysis can affect the slip distribution significantly.

2.5.5 Wear modelling in fretting

The application of wear modelling to fretting has received increasing attention. This attention has been justified by the observation that slip appears to be linked to fatigue life through wear behaviour. The earliest application to the fretting phenomenon was by Johansson (1994) who used a numerical implementation whereby the geometry was updated after a small wear increment. This was achieved by applying the Archard equation in a local context, based on shear traction and slip distributions across the

contact interface. Goryacheva et al (2001) presented an analytical formulation which was applied to the cylinder on flat geometry under partial slip conditions. The study found that in the slip regions wear occurred, owing to the relative movement. Conversely, in the stick region, no wear occurred. Hence the pressure initially distributed over the contact semi-width, was predicted to transfer to the stick region. Owing to the discontinuity in wear behaviour at the stick-slip boundary, a pressure peak was found to form at this interface. Using an asymptotic analysis, they found that singularities ultimately formed here. McColl et al (2003) also used an approach based on the Archard wear model, but implemented within an FE framework. The method was compared with experimental tests in the gross sliding regime, and found to give reasonable agreement with experimental wear scars (Figure 2.16)

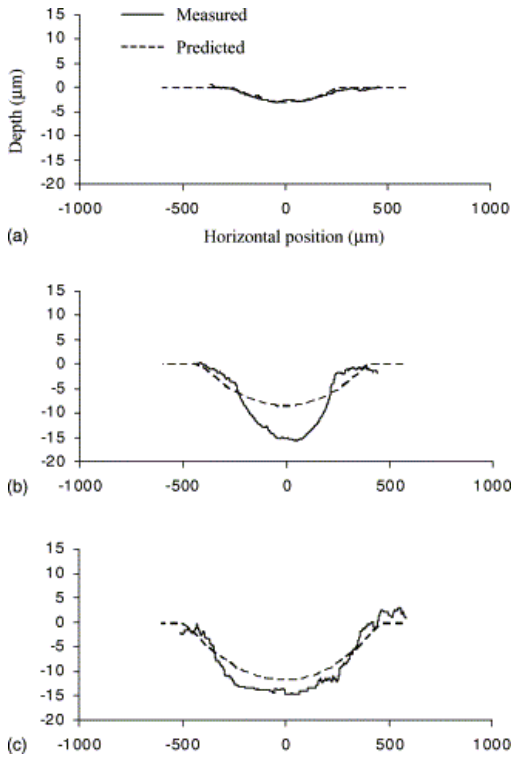

Figure 2.16. Comparison of Archard based fretting wear predictions and experimental wear scars at three increasing normal loads (McColl et al, 2003).

The method was then used to compare the wear behaviour under partial slip and gross sliding conditions by Ding et al (2004). It was shown that the predicted wear

behaviour of the two regimes is very different; partial slip was predicted to result in the characteristics predicted by Goryacheva et al (2001) whereas gross sliding was predicted to cause a significant reduction in peak contact pressure and a widening of the contact patch. Ding et al (2004) also studied the predicted effect of wear on the subsurface stress distributions. The partial slip simulations predicted a large increase in the shear stresses at the stick slip interface. This suggests a possible mechanism by which the cracking observed in the stick slip boundary could be explained.

Medina & Olver (2002) have applied an Archard based wear model to a boundary element analysis of a spline coupling; they found that the wear regions on the spline matched those on a corresponding experimental spline subject to rotating bending moment. However, no comparison was drawn between the wear depths predicted by the two methods. Ding et al (2006) have more recently applied the incremental method of McColl et al (2003) to predict the fretting wear of a spline coupling under torque load. The results show improved agreement with experimental observations over a previous wear predictions by Ratsimba et al (2004) which did not include the effect of geometry change.

Fouvry et al (1996) applied an Archard type relation, correlating the wear rate to the energy dissipated at the contact. They found that this method also showed good fidelity in the gross sliding regime of fretting. Despite being applied by a number of researchers, the Archard wear law remains unvalidated with respect to partial slip contacts. Qualitatively the approach appears to be correct in so far as both relative movement and normal load are required to cause wear: As mentioned, Johnson (1985) noted that wear was restricted to the slip annulus in a partial slip spherical contact. However it has not been proven that the wear volumes predicted by the method are accurate in the partial slip regime. McColl et al (2003) found that the

wear coefficient is dependent on variables such as normal load and stroke. Indeed, Archard stated that the law only applied to contacts in a state of equilibrium. The evolution of friction coefficient implies that the fretting contact is generally in a state of gradual change, rather than equilibrium. At the time of writing, the Archard wear law appears to be the only viable model for wear occurring at anything greater than the nanoscale.

Hattori et al (2000) investigated the effect of assumed distributions of wear of a punch on flat profile on the associated crack growth parameters in an unworn counter-body. This approach did not simulate the wear process incrementally. Furthermore, the approach did not investigate the effect of wear on nucleation behaviour, and was not able to predict the beneficial effect of gross sliding behaviour on the life, as demonstrated in Figure 2.12.

2.6 Summary of literature review

The fretting phenomenon is a complex mixture of sciences including tribology, fatigue and contact mechanics. Each of these perspectives has ramifications for the others, implying that fretting analysis requires a holistic approach that considers all three perspectives together. Generally it is found that this is not adopted; perhaps two of the three perspectives are considered in any given approach. The need for a more complete approach has been identified.

A modified version of the Archard wear equation has been applied to the fretting problem using both analytical and numerical frameworks. The approach has shown that the evolution of the contact due to material removal at the interface is significantly different depending on slip regime. Numerical implementations show

practical potential as they can be applied to complex geometries, and can be combined with other complex approaches such as material non-linearity etc if desired. Two fatigue model perspectives have found particular favour in fretting analysis; critical plane fatigue models and fracture mechanics. Critical plane approaches use correlations between variables such as stress or strain and the number of cycles to failure to allow prediction of fatigue lives under multiaxial loading conditions. Damage accumulation laws can be coupled with multiaxial techniques to provide a life prediction framework under variable loading conditions.

Fracture mechanics analysis has the advantage of explicitly considering the fretting induced stress field around a crack tip as it grows through the component.

There is a need to assess the effect of fretting wear on fretting fatigue behaviour. The literature review has shown a number of promising approaches that could be combined to provide a more general fretting model.

Chapter 3

Methodology Description

3.1 Overview

A method for linking critical plane fatigue models and wear modelling is described. The method, which is FE based to allow future application to more complex geometries, links critical plane life prediction and wear modelling via damage mechanics. The modelling framework employed throughout the thesis is described.

3.2 A new fretting fatigue modelling approach

The FE based wear simulation technique described by McColl et al (2003) and Ding et al (2004) has given a tantalising view of how fretting wear behaviour may explain a number of experimentally observed phenomena. As mentioned in the literature review, both fretting fatigue modelling and fretting wear modelling have been carried out in various forms by different researchers. A framework that quantitatively predicts the effect of fretting wear on fretting fatigue life of real components will help to give a better understanding of the two processes, particularly with regard to the impact of fretting wear on fretting fatigue behaviour. The methodology proposed here combines the FE based wear modelling approach of McColl et al (2003) with a critical plane lifing technique, such as that of Sum et al (2005) by employing a damage accumulation framework. The schematic in Figure 3.1 shows the basic methodology.

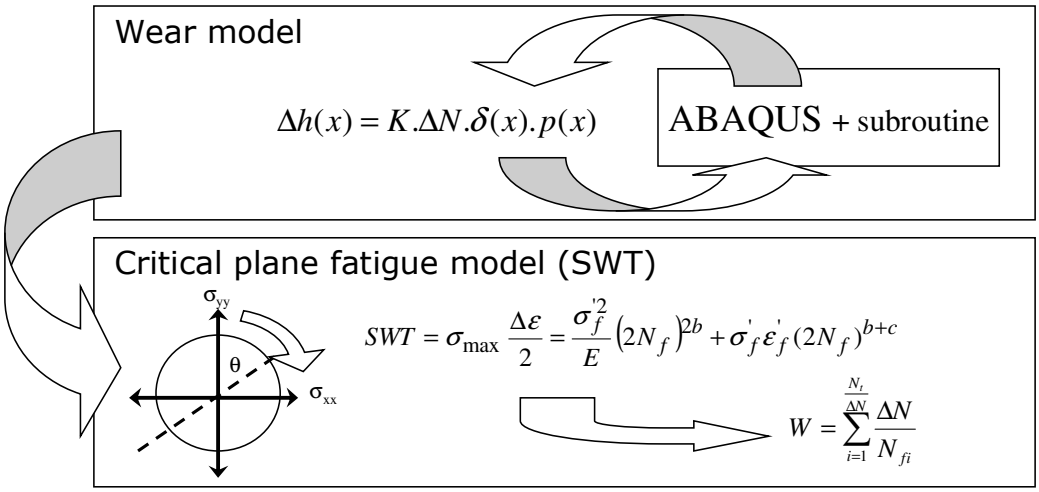

Figure 3.1. Schematic of the proposed methodology

Figure 3.2 gives a more detailed description of the processes. Initially an FE wear simulation is run, this allows the effect of wear on the evolution of stress and strain cycles to be captured. After this analysis has been performed, the fatigue damage associated with each sequential fretting cycle can be quantified via a multiaxial fatigue damage parameter. As wear is modifying the stress and strain cycles throughout the analysis, a damage accumulation framework is required such that the cumulative damage effect of each cycle can be monitored, and, upon reaching some failure criterion, a life prediction can be furnished.

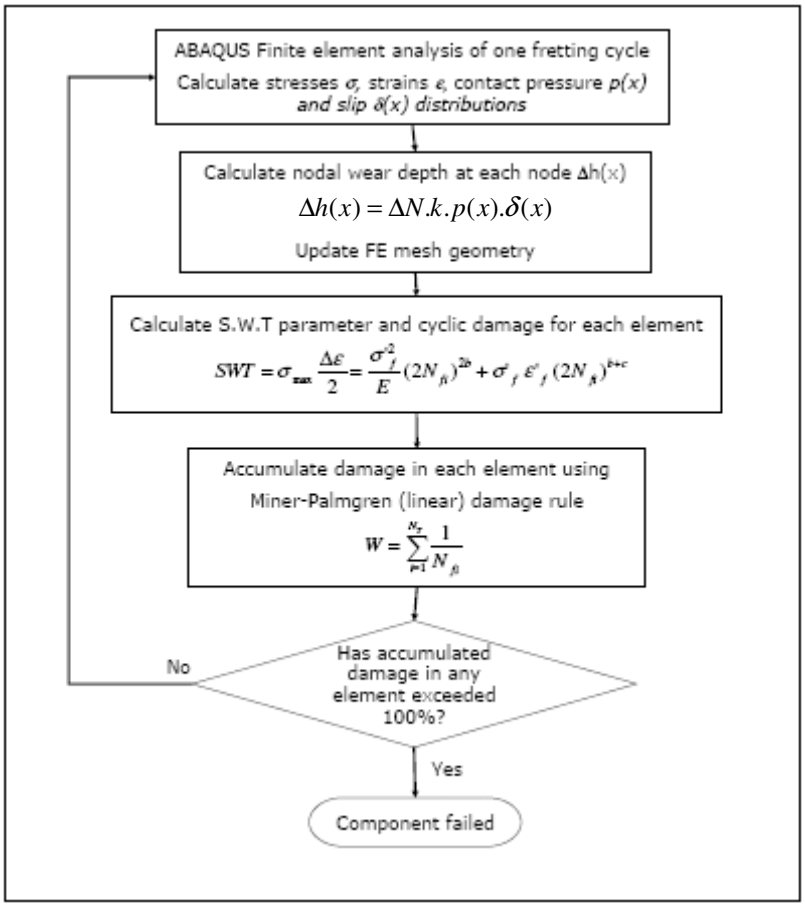

Figure 3.2. Flow chart of proposed combined fretting wear/fretting fatigue lifing methodology.

3.3 Wear model development

3.3.1 Introduction

The wear simulation technique developed here is similar to that implemented and validated by McColl et al. (2003), as also suggested by Medina & Olver (2002), which starts with the Archard equation, which is a commonly-used model for sliding wear damage:

$$\frac{V}{S} = K\frac{P}{H} \tag{3.1}$$

where V is the wear volume, S is the sliding distance, K is the wear coefficient, P is the normal load and H is the hardness of the material.

For a given point on one of the contacting surfaces, Equation (3.1) can be expressed as

$$\frac{h}{S} = k_l p \tag{3.2}$$

where h is the wear depth (mm), k_l is the dimensional local wear coefficient, defined as the wear per unit local slip per unit local contact pressure, and p is the contact pressure. The differential formulation of Equation (3.2) is

$$\frac{dh}{dS} = k_l p \tag{3.3}$$

McColl et al (2003) developed a numerical approach to simulate fretting wear using Equation (3.3). For a given contacting geometry, the initial distributions of contact pressure and relative slip between the contact surfaces are calculated by the finite element method.

The modified Archard equation is then applied as follows:

$$\Delta h(x,t) = k_l p(x,t)\delta(x,t) \tag{3.4}$$

where $\Delta h(x,t)$, $p(x,t)$ and $\delta(x,t)$ are the incremental wear depth, contact pressure, and relative slip at point x and time t, respectively.

Due to computational constraints it is not efficient to model each cycle explicitly. Instead, a cycle jumping technique is employed, similar to that described by Ding et al (2004), where the assumption is made that wear is constant over a small number of cycles. By multiplying the incremental wear by a cycle jumping factor ΔN, one FE cycle simulation is used to model the effect of ΔN actual wear cycles. Equation 3.4 becomes:

$$\Delta h(x,\tau) = \Delta N k_l p(x,\tau)\delta(x,\tau) \tag{3.5}$$

where τ is the time within one 'cycle' corresponding to ΔN wear cycles. The nodal wear depth for an incremental number of wear cycles is computed, permitting the modified geometry of the FE model to be determined. At the end of each converged increment, the incremental wear at each node on the contact surfaces is calculated for that increment, the node is then displaced by the calculated amount, normal to the local surface. Repeating this procedure incrementally, wear simulation can therefore be achieved. Unlike preceding works, the method is implemented here entirely within the ABAQUS code. The present implementation of Equation (3.5) is thus more accurate and efficient than that of Ding et al (2004) in the following aspects:

1. The spatial adjustment of the contact nodes is now achieved via a user subroutine called *UMESHMOTION* and within an adaptive meshing constraint (AMC) framework (HKS, 2005). This subroutine can be found in Appendix A1.

2. One implication of this is that, whereas previously the wear depth was calculated using the contact pressure for normal loading only and with an average relative slip over the tangential load cycle, now the incremental wear depth is calculated for each increment of the tangential load cycle (fretting cycle) using the associated 'current' values of both contact pressure and relative slip.

3. Whereas previously a separate analysis was needed for each cycle-jump, with an attendant unloading and re-loading of the normal load, the new implementation circumvents this, since the geometry modification is effected within the FE code itself.

4. Small cycle jumps give finer discretisation of the time domain helping to maintain stability and accuracy; larger jumps decrease the computational expense. Since the present implementation modifies the geometry incrementally throughout the

tangential cycle, it is more stable and hence much larger cycle jumps can be made before instability becomes an issue.

Due to the non-linear nature of contact analyses, it is necessary to discretise the time domain into a number of increments, such that loadings are applied incrementally. Leen et al (2001) reported that in frictional contact, the accuracy of the slip distribution is dependent upon the increment size chosen. As the Archard wear model uses slip as a principle variable, the accuracy of the wear model will in turn be dependent on the increment size selected. A sensitivity study on the effect of increment size upon aspects of solution accuracy is given in Appendix A2. The increment size selected was 50 increments per tangential load-step, i.e. 100 increments per cycle (see below).

3.3.2 Validation of the AMC approach

The new implementation has been successfully validated against the wear predictions of Ding et al (2004), which were in turn validated against measured wear scar data for a high strength CrMoV steel. The AMC approach has been validated for a fretting wear test, i.e. one where the fretting pad is loaded normally and experiences a cyclic tangential load against an otherwise unloaded flat specimen. For the results to be directly comparable, identical meshes were used (Fig. 3.3), and identical material models were used for the aero-engine Chromium-Molybdenum-Vanadium alloy steel designated S-CMV. Both the fretting pad and the specimen where heat treated according to the following process: heat at 940^{o}C for 45mins, followed by a room temperature oil quench and subsequent temper at 570^{o}C for 2 hours & 15 minutes, followed by an air cooling. Post heat treatment, the two components were finish

ground to a depth of 0.5mm. Finally the flat specimen was gas nitrided. The resulting surface hardness was 480HV and 900HV for the cylindrical and flat specimens respectively. - A Youngs' modulus of 206GPa, Poisson's ratio of 0.28 and linear elastic behaviour were assumed. McColl et al's wear coefficient k_f of 1×10^{-7}MPa^{-1} was used.

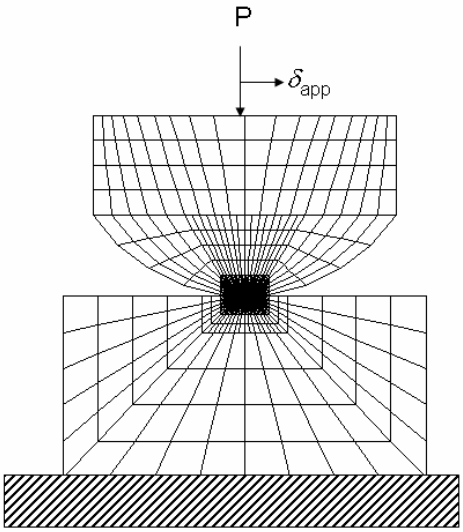

Figure 3.3. FE mesh (developed by McColl and co-workers (2003)) which was used for validation of AMC model

Both models were run for N=18,000 cycles, with applied slip amplitudes (δ_{app}) of 2.5 μm and 10 μm, allowing both partial slip and gross sliding conditions to be tested. The pressure distributions were used for comparison. Figure 3.4 & 3.5 show the pressure distributions reported by Ding et al (2004) as compared to those derived using the AMC technique. The two techniques give very similar results, with the only noticeable difference being at the edge of contact on the gross sliding case. Here the AMC technique shows slight peaks where the Ding method does not. This is attributed to the much larger cycle jumps used, resulting in a transient numerical 'roughness'. This was not considered an important discrepancy; the contact between

engineering materials is quite stiff, the contact pressure is therefore sensitive to small variations in the contact profile. McColl et al (2003) found that such artefacts affected solution stability rather than accuracy.

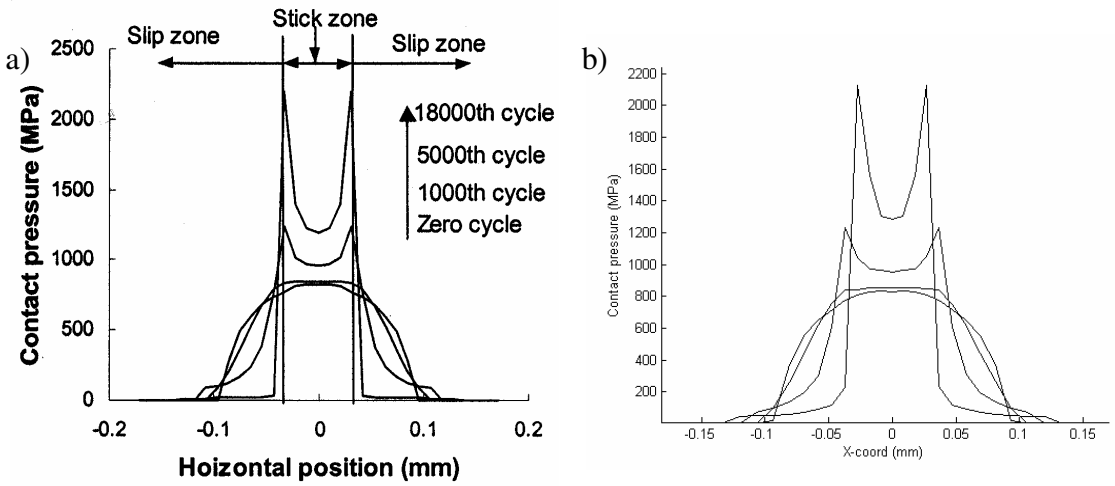

Figure 3.4. Pressure evolutions for the partial slip regime (δ_{app}=2.5 μm)
a) Ding et al (2004) wear model b) AMC version

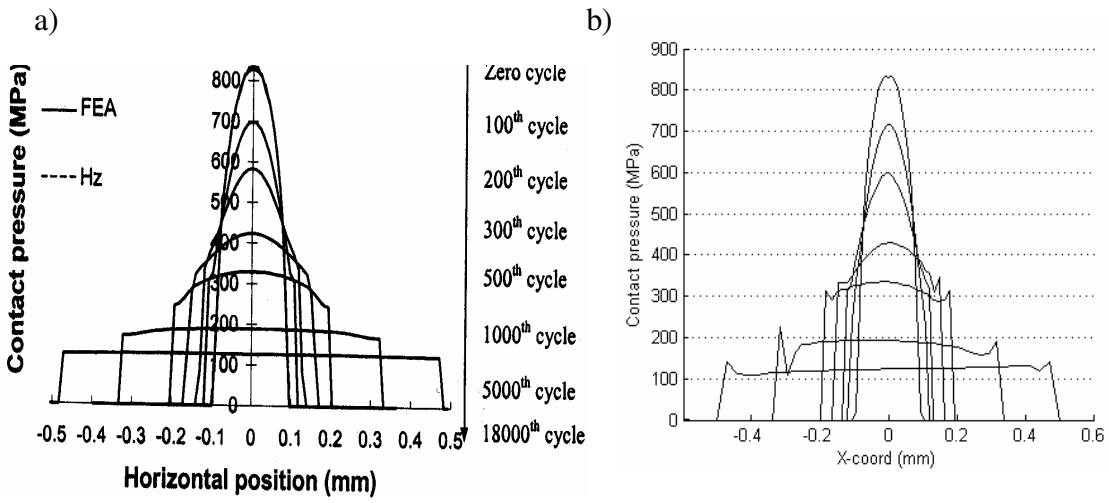

Figure 3.5. Pressure evolutions for gross sliding regime (δ_{app}=10 μm)
a) Ding et al (2004) wear model b) AMC version

In addition, a brief comparison against experimental observations has also been made, following a similar comparison made by McColl et al (2003). The case examined related to an experimental test, using the same geometry, and hence mesh as that outlined above. In this case a normal load of 185N, and a stroke, $\delta_{app,max}$-$\delta_{app,min}$, of

50 μm are applied. A wear coefficient of k=3x10^{-8}MPa^{-1} and a COF of μ = 0.9 are employed. These are consistent with those measured in the experiment for the loading conditions considered.

The resulting wear profile is in good agreement with the results of McColl et al in terms of both a) the numerical results, and b) the experimental results. Figure 3.5 shows the predicted evolution of the wear scar. The final scar dimension of 3 μm deep by 0.51 mm wide are both within 4% of those measured by McColl and co-workers, which is nearly identical to their numerical results.

The AMC technique is thus used hereafter in all wear modelling.

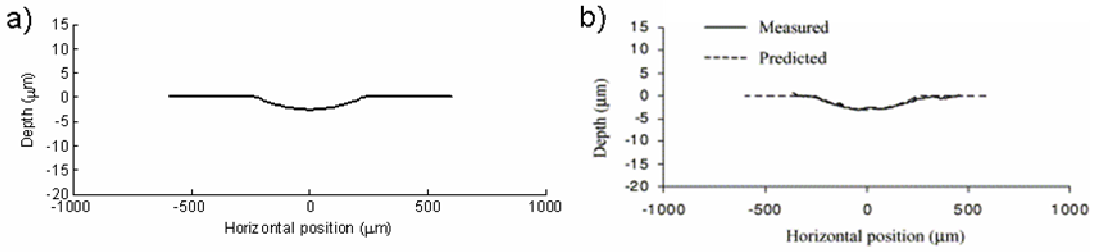

Figure 3.6. Comparison of wear scars a) AMC numerical model
b) experimental and numerical model after McColl et al (2003)

3.3.3 Friction model

Friction is a critical aspect of fretting fatigue modelling. The most common friction model employed is the well known Coulomb friction law which states that the maximum shear force which can be exerted by a contact is proportional to the normal load applied across the contact:

$$Q \leq \mu P \qquad (3.6)$$

If Q is less than μP, the contact experiences no net movement, if it exceeds μP, the contact will slide. The Coulomb friction model is a first order approximation of experimental observations that satisfies some of the characteristics of quasi-static behaviour. In this work, a further assumption is made: the Coulomb law is applied on a nodal basis, that is the shear traction at the i_{th} node is given by the inequality:

$$q_i \leq \mu p_i \qquad (3.7)$$

Hence the maximum transmittable shear stress at any point on the contact is assumed to be purely a function of the pressure at that point and the coefficient of friction.

Even in the relatively simple form of the Coulomb friction model, the discontinuous nature of friction implies that sophisticated solution is required in numerical routines such as finite elements. Two implementations are available in the ABAQUS code used in this work:

i) The penalty method

ii) Lagrange multiplier method

The penalty method allows a small 'elastic slip' to occur at surface points when the shear stress is less than the critical value for sliding thus improving the convergence behaviour of the contact model, particularly in mixed stick-slip cases such as fretting. The Lagrange multiplier method enforces exact sticking, however computational cost is increased convergence is typically slower. Fretting wear modelling requires accurate resolution of slip distributions. For this reason the Lagrange multiplier method is used to enforce Coulomb friction for all models in the present work.

3.4 Critical plane fatigue damage model

Multiaxial fatigue damage parameters provide an empirical correlation of fatigue performance in multiaxial stress states. As mentioned in Chapter 2, there is a vast array of different parameters that have been proposed. Generally, these parameters have been developed with a given material or loading condition in mind. Smith-Watson-Topper (SWT) (Smith et al, 1970) is generally accepted as being a reliable parameter in cases involving tensile cracking, i.e. relatively high strength materials under tensile dominated loading. Fatemi-Socie (FS) (Fatemi & Socie 1988) is often applied to cases where shear loading dominates failure, for example torsion loading. Fretting fatigue has had both parameters applied as a wide variety of characteristics can be exhibited by fretting failure. For example, shear cracking is typically noted near to the surface, yet after a short distance (typically a small number of grain diameters) the crack turns to grow perpendicular to the surface. Similarly with regards to loading both a high shear stress and high tensile stress can be witnessed. As a result both parameters have been shown to give quite similar results, with commendable accuracy in the partial slip regime. It should be noted that the methodology described here is independent of any specific fatigue parameter used. Any correlation requiring stress/strain data as input and giving a predicted number of cycles to failure as an output could be directly employed. Notable exceptions include the Ruiz (Ruiz et al, 1984) and Dang-Van (Dang Van et al, 1989) parameters as these do not furnish a number of cycles to failure.

Socie (1987) suggests that knowledge of the cracking behaviour for the material and loading state of interest allows selection of the most appropriate fatigue criterion. On this basis, Araujo and Nowell (2002) have suggested that the *SWT* parameter is

appropriate for fretting fatigue prediction of Ti-6Al-4V. SWT is employed in this description, although parameters such as FS could be substituted directly in its place. Critical plane implementations of multiaxial fatigue parameters address the fact that in a multiaxial stress state, the most damaging combination of stress and strain will not necessarily concur with the principal stress axis. This allows better treatment of out of phase loading and multiaxial scenarios (Socie, 1987). The SWT parameter is based on the combination of the Coffin-Manson low cycle fatigue equation, Basquin's high cycle fatigue equation and consideration of the peak stress to account for the mean stress effect, as follows:

$$SWT = \sigma_{\max} \frac{\Delta\varepsilon}{2} = \frac{\sigma_f'^2}{E}(2N_f)^{2b} + \sigma_f'\varepsilon_f'(2N_f)^{b+c} \tag{3.7}$$

where σ_{max} is the peak normal stress, $\Delta\varepsilon$ the maximum strain range within one fatigue cycle, σ_f' is the fatigue strength coefficient, E is Young's modulus, N_f is the number of cycles to crack initiation, b is the fatigue strength exponent, ε_f' is the fatigue ductility coefficient and c is the fatigue ductility exponent. By locating the plane on which the maximum SWT value occurs, a cyclic life and cracking direction can be deduced.

3.5 Combining fretting fatigue and fretting wear modelling

3.5.1 General

After the FE wear simulation has been completed for a particular loading combination, a set of stress and strain histories is available for the entire simulation length. Due to the occurrence of wear and the associated cycle by cycle change in stress and strain, the damage accumulated for each successive cycle will be different

to the last. A post-processing code is used which is based on the method of Sum et al (2005) in order to calculate the SWT parameter associated with each load cycle simulated and for each element in a specified region. As a critical plane implementation has been selected, the plane on which the damage parameter is maximum is required. This is achieved here by transforming the time histories for stress and strain onto planes at 5^{o} intervals over a 180^{o} range using the two-dimensional transformation equations for stress and strain.

$$\sigma_{\theta} = \frac{\sigma_{xx} + \sigma_{yy}}{2} + \frac{\sigma_{xx} - \sigma_{yy}}{2}\cos(2\theta) + \sigma_{12}\sin(2\theta) \tag{3.8}$$

$$\varepsilon_{\theta} = \frac{\varepsilon_{xx} + \varepsilon_{yy}}{2} + \frac{\varepsilon_{xx} - \varepsilon_{yy}}{2}\cos(2\theta) + \frac{\varepsilon_{12}}{2}\sin(2\theta) \tag{3.9}$$

Where σ_{θ} and ε_{θ} are the stress and strain respectively normal to the plane at angle θ to the x-y Cartesian coordinate frame.

The maximum normal stress σ_{max} with respect to time, and the corresponding strain range $\Delta\varepsilon$ are determined for each of the 36 planes in each element. $\Delta\varepsilon$ is the difference between the maximum and minimum values of strain normal to the candidate plane over the complete loading cycle. Thus, SWT values are thus obtained for each candidate plane in each element. These values are then employed to establish the maximum critical-plane SWT value with respect to plane orientation in each element, which in turn is used with Equation 3.7 to furnish a number of reversals to failure, $N_{f,}$ for the cycle under consideration

Figure 3.7 shows a flow chart of the process for calculating the critical plane fatigue damage from the wear simulation results.

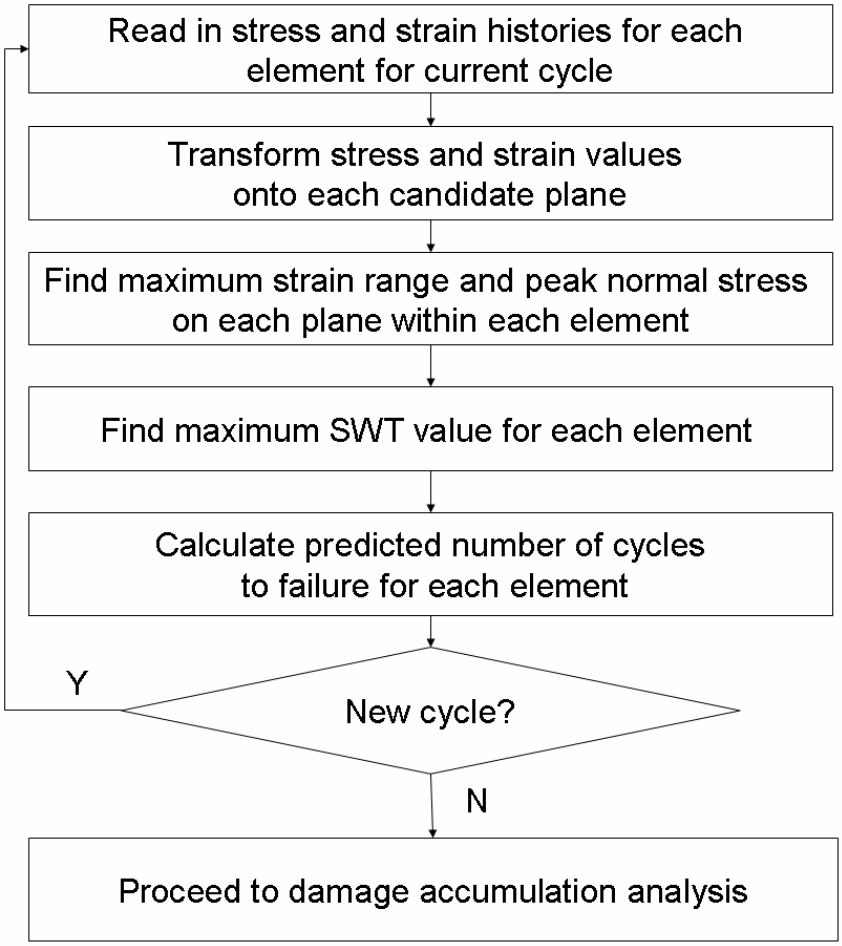

Figure 3.7. Flow chart showing the process for calculating the critical plane SWT value for wear simulations.

3.5.2 Damage accumulation framework

Following critical plane fatigue damage calculation, the cyclic fatigue damage at each element of interest is now known for each cycle analysed in the wear simulation. As the geometry removal effect of wear is altering the stresses from one cycle to the next, the cyclic SWT value only provides an instantaneous measure of rate of fatigue damage. In order to provide quantitative life predictions it is necessary to adopt a damage accumulation framework, such that the ongoing fatigue damage process can be monitored and related from one cycle to the next. The 'linear' or 'Miner-Palmgren'

(e.g. Miner, 1945) damage rule has been widely adopted in industry and requires no further material constants than those required for SWT calculations. In this application, the SWT correlation given in Equation 3.7 is used to provide a prediction of the number of cycles to failure N_{fi} for any fatigue cycle form *i,* experienced in any given element. The damage attributable to one application of *i* is defined by Miner-Palmgren (M-P) to be $1/N_{fi}$, the total damage sustained by n_i applications of cycle type *i* is found by multiplying the cyclic damage by the number of applied cycles, n_i/N_{fi}. The total damage sustained is then given by the summation of the damage caused by all applications of all cycle forms:

$$\omega = \sum_{i=1}^{N} \frac{n_i}{N_{fi}} \qquad (3.10$$

where ω is the accumulated damage, n_i is the number of cycles experienced at loading cycle *i*, N_{fi} is the critical-plane SWT predicted number of cycles to failure at loading cycle *i* (found using Equation 3.7) and *N* is the number of different types of load cycles experienced. Failure, defined here as the development of a 1 mm crack, is assumed to have occurred when ω reaches a value of 1. This assumption is made to maintain consistency with the failure criterion on which the material properties for Equation 3.7 are derived by Dowling (1998).

The adoption of the M-P rule is convenient in the absence of more detailed knowledge of material response. Currently there are no well established non-linear damage accumulation models applicable to multiaxial fatigue (Han et al, 2002). It is conceivable that an alternative damage accumulation relationship could be substituted in its place within the current framework. However, in the case of fretting wear, each cycle differs slightly from the next, therefore a damage rule that is able to provide a

continuous description of damage accumulation over a wide range of damage levels is necessary. The majority of non-linear damage rules are concerned with 'block loading' where discrete pre-determined loading levels are known. In order to implement these would require a large number of test data. In view of this, and the fact that the M-P rule has often been found to give comparable answers to more complex rules, M-P is adopted here.

When the cycle jumping technique described above is combined with Equation 3.10, the damage rule becomes:

$$\omega = \sum_{i=1}^{\frac{N_t}{\Delta N}} \frac{\Delta N}{N_{fi}} \tag{3.11}$$

3.5.3 Material point mesh

Due to the use of adaptive meshing to update the mesh on removal of material, specific elements and nodes are no longer linked uniquely to actual material points throughout the analysis, the mesh nodes will move with respect to their original location. Consequently, a 'material point mesh' (MPM) is created as the global reference for damage accumulation; the nodes of the MPM have fixed coordinates throughout the analysis. Cyclic damage is calculated at the centroid of each element, and linearly interpolated back to the MPM for accumulation. In this way, nodes on the MPM corresponding to removed material (due to wear) do not accumulate any further fatigue damage. Figure 3.8 shows this concept schematically.

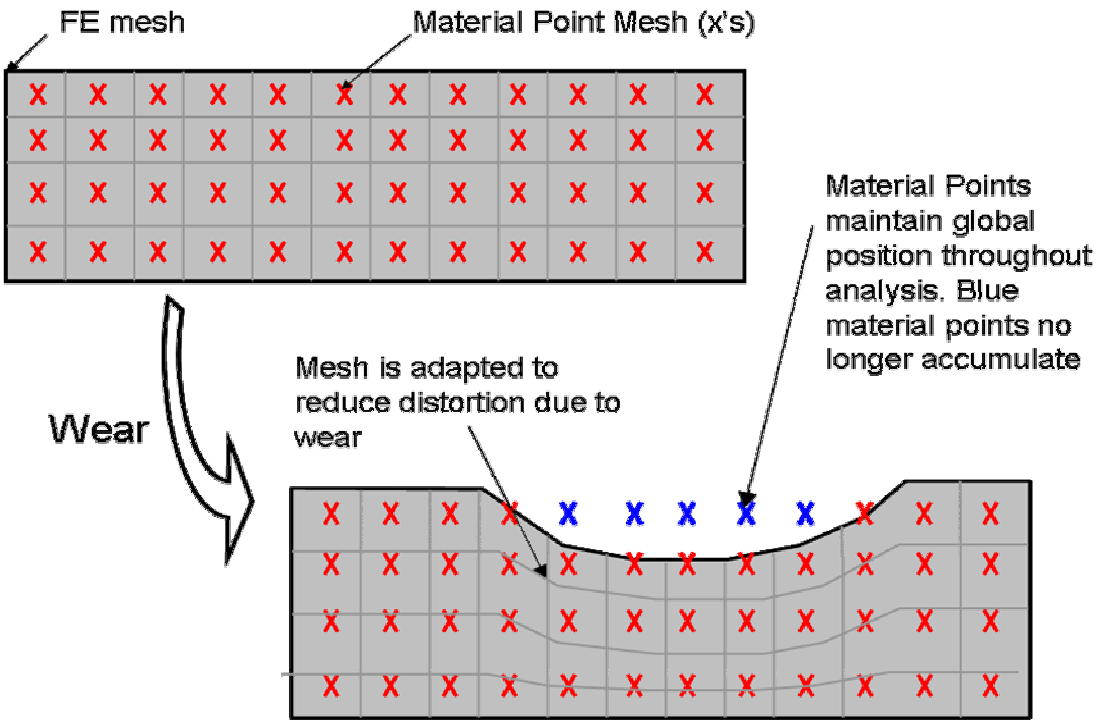

Figure 3.8. Schematic to show purpose of material point mesh for damage accumulation sites in presence of adaptive meshing

3.5.4 Damage anisotropy

As the stress state evolves due to wear, it is possible for the loading axis to change during fretting. Therefore the way in which damage on one plane relates to damage on other planes requires consideration. In general, damage can be an anisotropic phenomenon. That is to say that damage sustained in a given load direction may have a different effect on the fatigue endurance of other loading planes.

In this thesis damage is assumed to be isotropic. Therefore if a material sustains damage of 5% under one loading axis, and the axis then changes, the damage on this axis will also be 5%. Damage is always calculated based on the critical plane, maximum value, and is subsequently accumulated as a scalar quantity at each material mesh point. As such the isotropic assumption used here represents a conservative

assumption as the worst case loading conditions are summed together, irrespective of direction, from one cycle to the next. An alternative approach could involve accumulating damage on each of the 36 planes, giving a vector of damages for each material point. This is discussed further in Chapter 10

3.6 Numerical Aspects

The methodology described above is computationally demanding. Inevitably in such a complex problem, a number of approximations are necessary for an effective and efficient solution. Mesh dependency, time discretisation, and cycle jumping each have the potential to affect solution fidelity. Appendix A2 contains further details of sensitivity studies into these areas.

Chapter 4

Analysis of Hertzian Fretting Fatigue

4.1. Overview

The framework described in Chapter 3 is applied here to the cylinder on flat contact geometry subjected to displacement controlled tangential pad loading and bulk fatigue loads. The results show that the wear induced evolution of stresses is significant. The nature of this evolution differs depending on whether partial slip or gross sliding conditions pertain. This result is consistent with a number of experimental observations.

The differences in stress evolution due to slip regime are quantified to explain the experimentally observed dependence of fretting fatigue life on slip amplitude, which has not previously been done.

4.2. Model description

Figure 4.1 shows the specimen geometry and schematic test arrangement used, which corresponds to the experimental tests of Jin & Mall (2004) for a series of fretting fatigue tests. A pair of cylindrical (radius 50.8 mm) fretting pads are held in contact with a flat, uniaxially-loaded fatigue specimen. The material used in the experiments was a dual phase Ti-6Al-4V alloy which consists of ‘α’ hexagonal close packed and ‘β’ body centred cubic phases. The material was solution heat treated at 935^{o}C for 1.75 hrs, cooled in air and annealed at 700^{o}C for 2hrs in vacuum and cooled in argon.

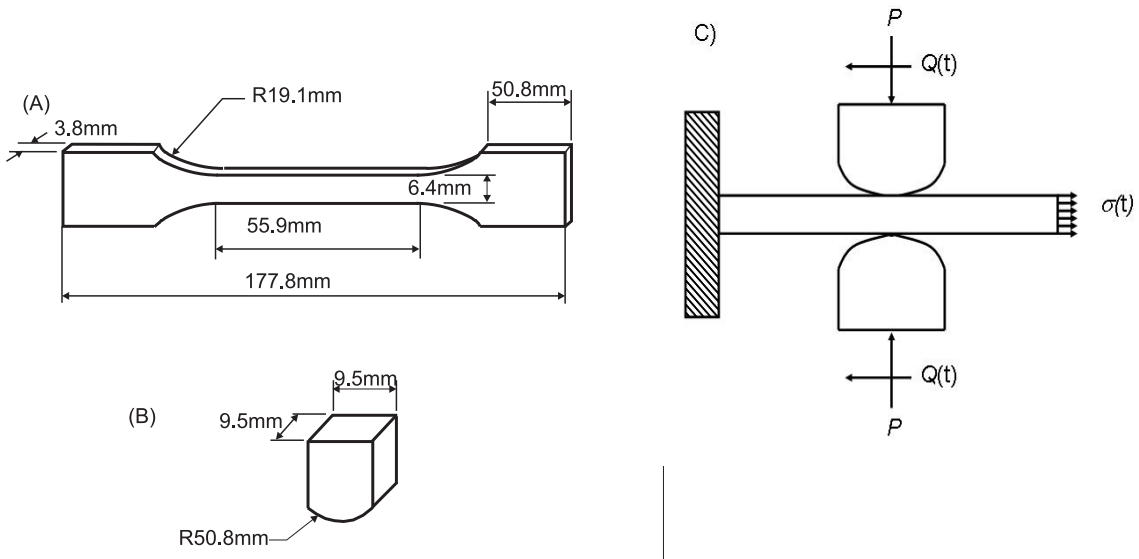

Figure 4.1. Schematic of (a) the fretting fatigue specimen,
(b) fretting pad and c) fretting fatigue test setup. After Jin & Mall (2004)

A symmetry plane parallel to the specimen axis is employed in the FE model so that only one pad needs to be modelled. A material model of Ti-6Al-4V with a Young's modulus of 126 MPa, a yield strength of 930 MPa and a Poisson's ratio of 0.32 was used. Table 4.1 shows the Smith-Watson-Topper fatigue constants used in the critical plane model.

Table 4.1: Fatigue properties for Ti-6Al-4V.

σ_f' (MPa)	b	ε_f'	c
2030	-0.104	0.841	-0.688

(The above data corresponds to a definition of crack initiation
as the development of a 1 mm crack (from Dowling, 1998)

4.3. Load history

The loading history is shown in Figure 4.2. In the first analysis step a normal load P of 208 N/mm (equivalent to 1334N applied to a 6.4mm wide specimen) is applied to the cylinder, resulting in a peak Hertzian contact pressure of 302 MPa, and a semi-width of 0.437mm, as indicated by Equations 2.1 and 2.3 respectively. In the next step

the specimen is loaded by a cyclic fatigue load $\sigma(t)$ with a maximum value σ_b of 550 MPa and a stress ratio R of 0.03. The pad is also loaded with a prescribed maximum displacement $\delta_{app,m}$, which is varied for each simulation to cover a range of slip amplitudes including partial slip through to gross sliding conditions. Note that $\delta_{app}(t)$ is the distance by which the top surface of the fretting pad is displaced relative to the global coordinate axis. The 'slip range' δ is the maximum slip observed on the contact surface over one cycle (Fig. 4.3). In these tests $\delta_{app,m}$ is less than the displacement due to specimen strain δ_ε caused by substrate fatigue loading. Therefore the instantaneous net shear force acts in the opposite direction to the applied displacement $\delta_{app}(t)$. To model the effect of wear, $\delta_{app}(t)$ and $\sigma(t)$ are applied cyclically in the FE model. Using the von Mises yield criterion, the macroscopic material behaviour is predicted to remain elastic throughout the predicted component life in all cases modelled.

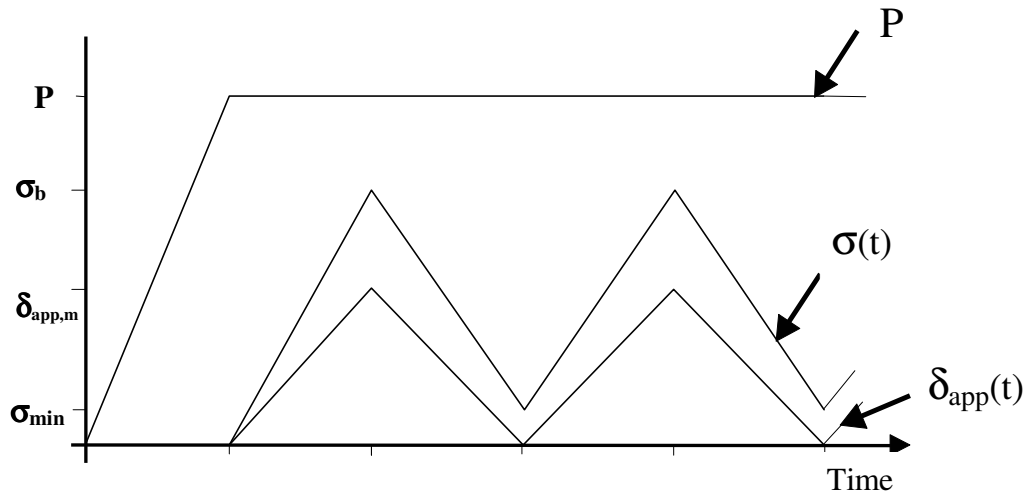

Figure 4.2. Normal load, tangential displacement and substrate fatigue stress histories implemented.

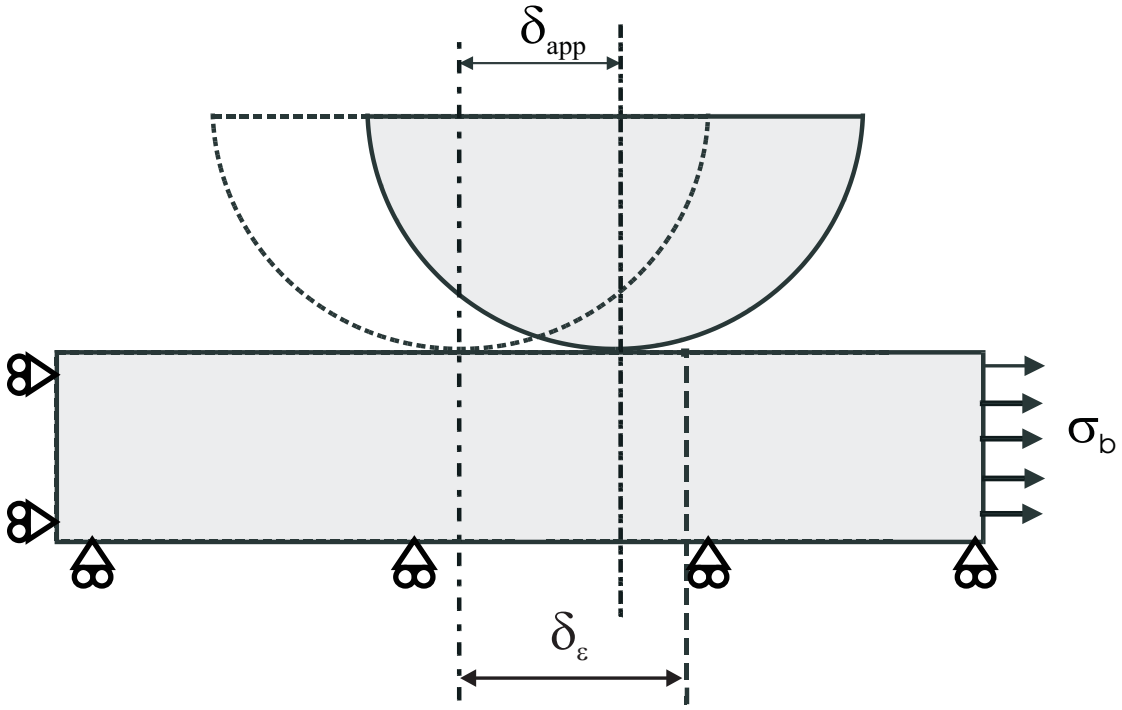

Figure 4.3. Relation between applied displacement, δ_{app} and displacement due to specimen strain δ_{ε}

4.4. Contact formulation

The Lagrange multiplier contact algorithm was used to strictly enforce the stick condition when the shear stress is less than the critical value according to the Coulomb friction law. In the fretting experiments, the coefficient of friction typically starts low, and rises to a higher value within the first few thousand cycles (Jin & Mall. 2004). Sabelkin & Mall (2006) have suggested that a constant COF value of 0.8 is representative for the tests studied here.

4.5. Validation of FE model against theory

Figure 4.4 shows the finite element meshes employed for the partial slip and gross sliding cases. Different meshes are employed due to the significantly different wear behaviour associated with the partial slip and gross sliding regimes. In gross sliding

cases it is found that the stress gradients are low, yet the growth in the contact width is potentially large, whereas in partial slip cases, the contact width change is relatively small yet the stress gradients can become quite large. Mesh 1 is targeted at partial slip cases (Fig. 4.4a), having a narrow refined contact region of 1.5 mm in width, while Mesh 2, used for gross sliding cases (Fig. 4.4b), has a wider refined region of 3.6 mm width. Both models use highly refined meshes (64 nodes) parallel and perpendicular to the contact surface (16 nodes) and both meshes share the same element depth of 16 μm at the surface. Multi-point constraints (HKS, 2004) are used to achieve a refined mesh towards the contact region with a coarse mesh away from the contact region, to reduce processing time. Matched meshes are used on the master and slave contact surfaces.

For SWT and damage accumulation purposes, a region 0.5mm deep into the specimen surface over the entire contact surface, i.e. 1.5 mm and 3.6 mm for Mesh 1 and Mesh 2 respectively, was monitored. That is all elements in this region had their SWT and cyclic damage levels calculated.

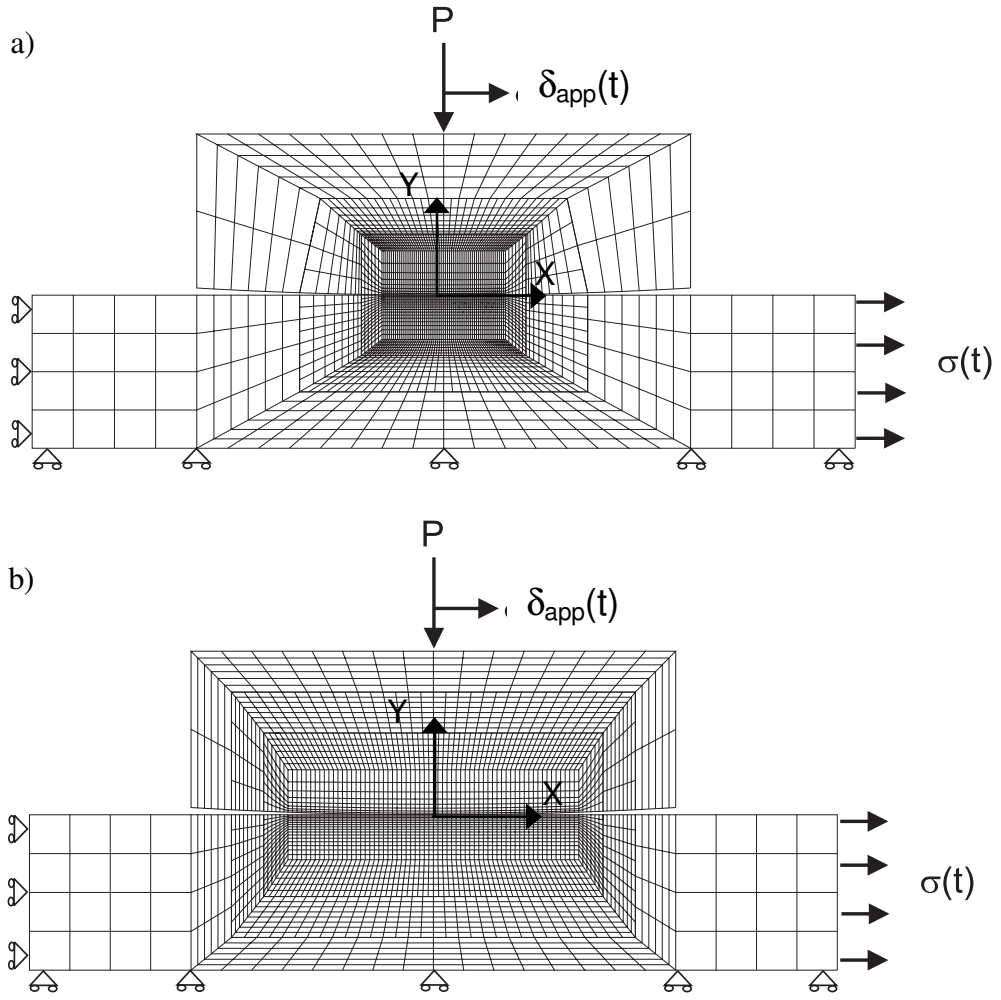

Figure 4.4. FE meshes of cylinder on flat geometry
a) 'Mesh 1' for partial slip analyses b) 'Mesh 2' for gross sliding cases

The FE model has been validated against theoretical models. The Hills & Nowell (1994) solution (Equations 2.5 and 2.8) provides a useful elastic half space derived comparison for partial slip conditions. Figure 4.5a shows that the FE-predicted shear traction distribution is in excellent agreement with the theoretical solution. The small differences are attributed to the elastic half-space assumption of the theoretical solution, which is not strictly satisfied since the contact semi-width of 0.437 mm is of comparable magnitude to the specimen thickness (1.9 mm). Figure 4.5b shows the

shear stress distribution at a depth of 8 μm into the contact surface for a gross sliding case (Mesh 2). This is compared with the elastic half space theoretical solution (e.g. Johnson, 1987). Although Mesh 2 is coarser than Mesh 1, Figure 4.5b shows that the resolution is adequate to capture the stress distributions under gross sliding conditions.

a)

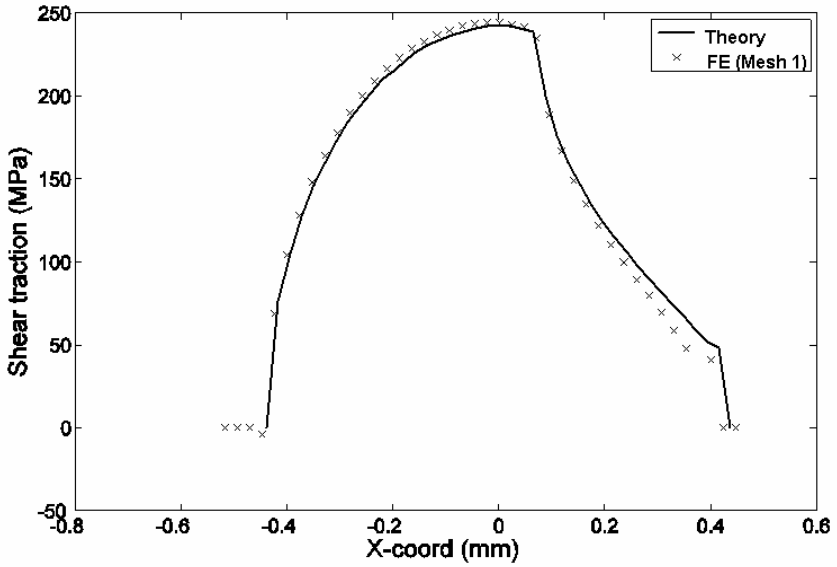

b)

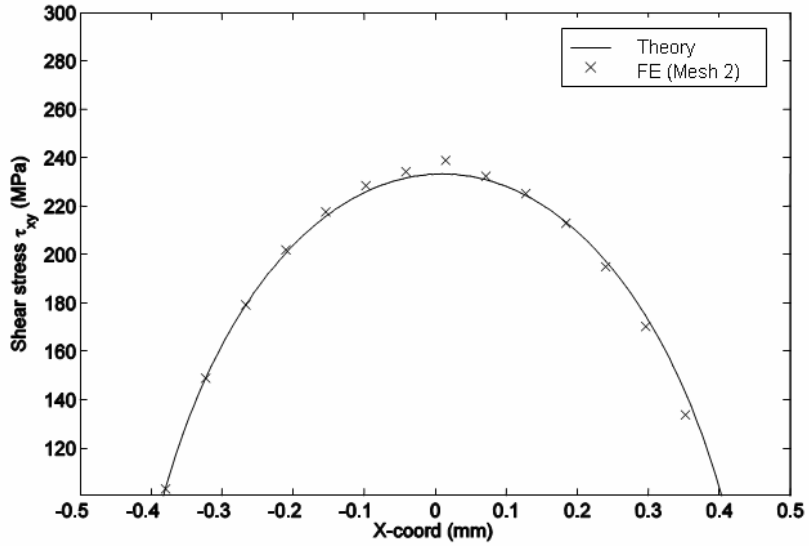

Figure 4.5 Comparison between FE predicted results and theoretical solutions for a) surface shear traction under partial slip (Q=140N) Hills and Nowell (1994), b) subsurface shear stress at a depth of 8μm under gross sliding (δ=4.7μm), Johnson (1987).

Comparison of slip values

It is a common observation that the measured slips from extensometer readings on fretting rigs are typically much bigger than theoretical models would suggest. Nishida et al (2003) observed with a scanning electron microscope that the interfacial slip was much smaller than the relative displacement measured by an extensometer close to the contact. It has also been pointed out by Jin & Mall (2004) that the FE-predicted and the experimental slip magnitudes associated with the transition from partial slip to gross sliding do not agree for these Ti-6Al-4V tests. The discrepancy has been attributed to elastic accommodation within the rig by Sabelkin & Mall (2005). The latter have conducted an FE study which included extra elastic accommodation to model rig compliance. It was concluded that the experimentally observed (global) 'relative slip range' was significantly larger than the actual slip at the surface. The relation between the global 'relative slip range' δ_{global} and the actual slip δ was concluded to be controlled by rig compliance and the COF. In order to estimate the local slip for wear coefficient determination here, the following relationship is employed:

$$\delta = \frac{\delta_{global}}{C_{rig} C_{COF}} \tag{4.1}$$

where C_{rig} is a constant which accounts for the effect of rig compliance and C_{COF} is a constant which accounts for the effect of COF. These constants have been determined from the data in Sabelkin & Mall (2005) as $C_{\text{rig}} = 10$ and $C_{\text{COF}} = 1.6$. Note that these variables are non dimensional fitting parameters to allow comparison between the FE model and experimental observations.

Derivation of wear coefficient

Direct calculation of the desired wear coefficient, k_l, requires knowledge of the local contact pressures and slips at a point on the contact surface. As these are not readily measurable, a modified form of Equation (3.2) was used to determine a bulk wear coefficient from the measured wear scar data of Magaziner et al (2004), as follows:

$$k = \frac{Ab}{2\delta N_t P} \tag{4.2}$$

where b is the specimen width and A is the cross sectional area of the wear scar, so that Ab is the estimated total volume of material worn. δ is the estimated relative slip range (via Equation 4.1) and N_t is the total number of fretting fatigue cycles endured.

In order to estimate the wear coefficient, it is necessary to employ wear scar data with a significant worn volume, which typically corresponds to gross sliding tests with large slip amplitudes. Consequently, the Ti-6Al-4V wear scar data employed here to estimate k, which has been published in Magaziner et al (2004) corresponds to a global slip value of 169 μm and a normal load of 601 N. The wear scar used is depicted in Figure 4.6. A graphical method has been employed, as described by McColl et al (2003), to estimate k and the resulting estimated value is 2.75×10^{-8} mm^3/Nmm.

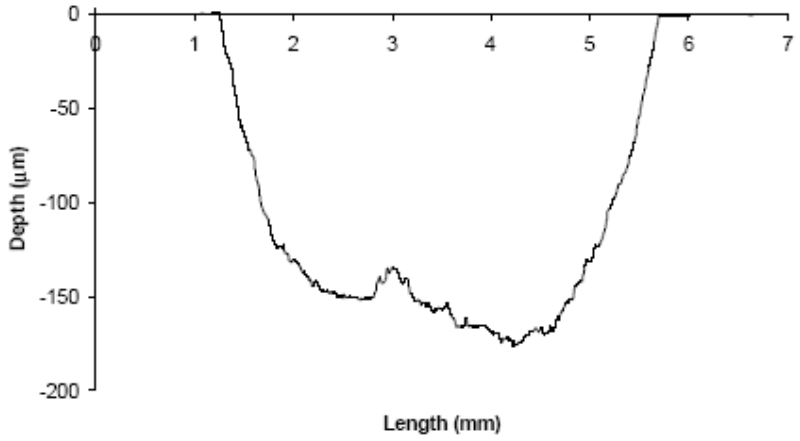

Figure 4.6. Wear scar used for derivation of wear coefficient
(δ_{global}=169 μm, P=601 N; from Magaziner et al, 2004)

4.6. Results

Effect of slip amplitude on life: neglecting wear

Figure 4.7 shows the predicted life as a function of slip amplitude without including the effects of material removal due to wear. In the partial slip domain, the predicted results show a significant effect of slip range. Specifically, the life reduces from about 130 000 cycles to about 14 000 cycles as the slip range is increased from 0.627 µm to the gross sliding threshold (~4.7 µm). However, once the gross sliding threshold condition is exceeded, the predicted life remains almost independent of slip range. Table 4.2 summarises the results from these analyses under the 'SWT without wear' columns.

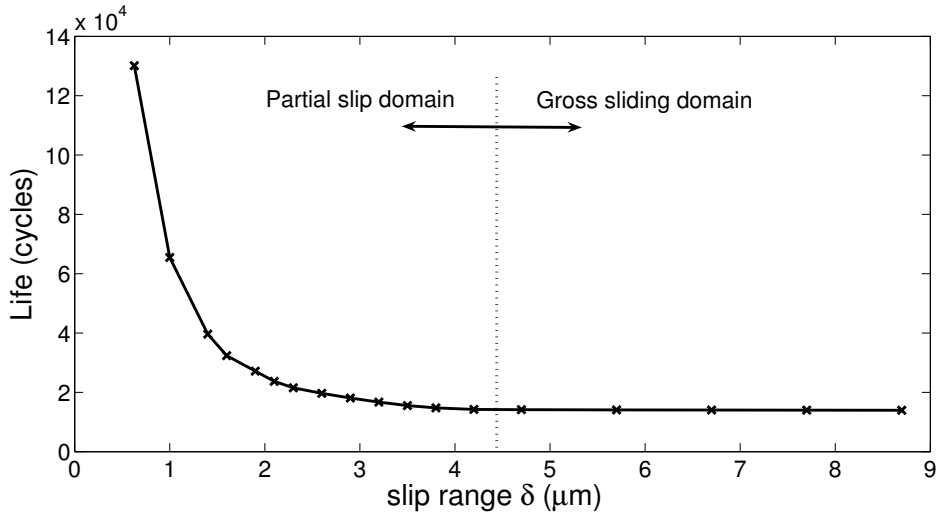

Figure 4.7. FE-based, critical-plane SWT prediction of fretting fatigue life as a function of slip amplitude, neglecting the effects of material removal due to fretting wear.

Table 4.2: FE based critical plane SWT life predictions
a) without effects of wear b) with effects of wear.

	a) SWT without wear				b) SWT with wear		
δ (μm)	SWT (MPa)	Angle (deg)	Predicted failure position (x/a)	Life (Cycles)	Final critical angle (degrees)	Final position of maximum damage (x/a)	Life (cycles)
8.7 (g.s.)	4.4056	-9	0.94	13955	-5	1.038	710534
7.7 (g.s.)	4.4013	-9	0.94	13985	-5	0.830	661243
6.7 (g.s.)	4.397	-9	0.94	14034	-5	0.830	632114
5.7 (g.s.)	4.3924	-10	0.94	14088	-20	0.208	364936
4.7 (g.s.)	4.3884	-10	0.94	14134	-20	0.208	37220
4.2 (p.s.)	4.381	-6	0.94	14221	-40	0.121	28790
3.8 (p.s.)	4.3366	-6	0.94	14758	-40	0.305	27812
3.5 (p.s.)	4.2768	-6	0.94	15527	-40	0.372	26107
3.2 (p.s.)	4.1935	-6	0.94	16694	-40	0.439	25418
2.9 (p.s.)	4.1056	-6	0.94	18063	-40	0.440	25611
2.6 (p.s.)	4.0139	-7	0.94	19662	-40	0.508	27239
2.3 (p.s.)	3.9199	-7	0.94	21510	-40	0.509	27206
2.1 (p.s.)	3.8226	-7	0.94	23685	-40	0.543	27058
1.9 (p.s.)	3.691	-8	0.94	27131	-40	0.644	28501
1.6 (p.s.)	3.5288	-8	0.94	32386	-40	0.645	31412
1.4 (p.s.)	3.3558	-8	0.94	39618	-40	0.712	38186
1.0 (p.s.)	2.9715	-9	0.94	65455	-40	0.714	95379
0.627 (p.s.)	2.5325	-10	0.94	130109	-40	0.829	175770

Note: g.s. = gross sliding; p.s. = partial slip.

The initial significant reduction in life with increasing slip range in partial slip can be explained by examining the predicted effect of slip amplitude on the shear traction distribution, which is shown in Fig. 4.8. The total shear force Q exerted on the specimen by the pad is given by the following integral:

$$Q = b\int_{-a}^{a} \tau(x)dx \tag{4.3}$$

where $\tau(x)$ is the shear traction at point x, b is the specimen width, and a is the contact semi-width. Until gross sliding is reached, increases in slip amplitude result in increasing shear force, as shown in Fig. 4.8, so that the trailing edge of contact stresses increase, thus reducing the predicted fatigue life. As slip is increased so that the gross sliding condition is passed ($Q=\mu P$), the shear force cannot increase any further so that the trailing edge stresses and hence predicted fatigue lifes are largely unaffected by further increases in slip. Jin and Mall (2004) found a similar trend using the modified shear stress range (MSSR) fatigue parameter.

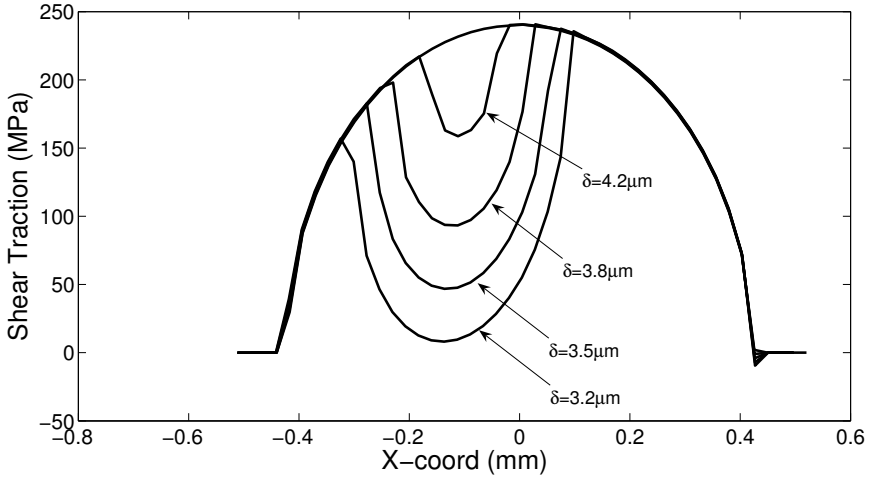

Figure 4.8. FE-predicted effect of slip amplitude on shear traction distribution.

Effect of wear: gross sliding

Figure 4.9 shows the evolving pressure distribution for the gross sliding case at the same instant in each cycle, namely when $\delta_{app}(t) = 0.5 \times \delta_{app,m}$. Clearly, the peak contact pressure reduces significantly with increasing number of fretting cycles. This general trend is similar to that reported by Ding et al (2004) for fretting wear tests, but in the present case the effect of a superimposed substrate fatigue load is included. In addition, the contact width increases by more than a factor of 2 over the first 150 000 cycles. These effects are due to the geometry of the specimen and pad becoming progressively more conforming with material removal. It is worth pointing out that the skewness of the pressure distribution is due to the asymmetry of the displacement and substrate fatigue loads at the instant for which these distributions are sampled. As found by Ding et al (2004), this evolution of contact pressure distribution under gross sliding conditions, where the shear traction is simply proportional to the contact pressure (via COF), leads to a reduction in the near trailing-edge peak tangential and shear stresses, which are the key stress components controlling multiaxial fatigue damage. Figure 4.10 shows how this directly translates to the evolution of the SWT parameter across the contact face, as a function of time. The values are plotted at the centroids of the first row of elements below the surface in the fatigue specimen which corresponds to a depth of 8 μm.

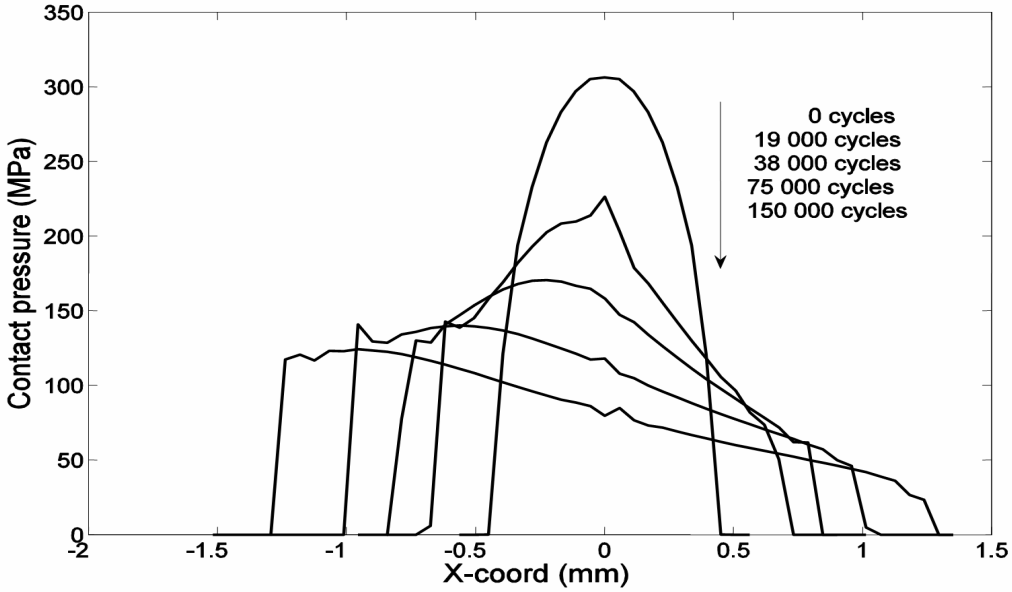

Figure 4.9. Predicted evolution of contact pressure distribution with wear under gross sliding conditions (δ= 8.7μm).

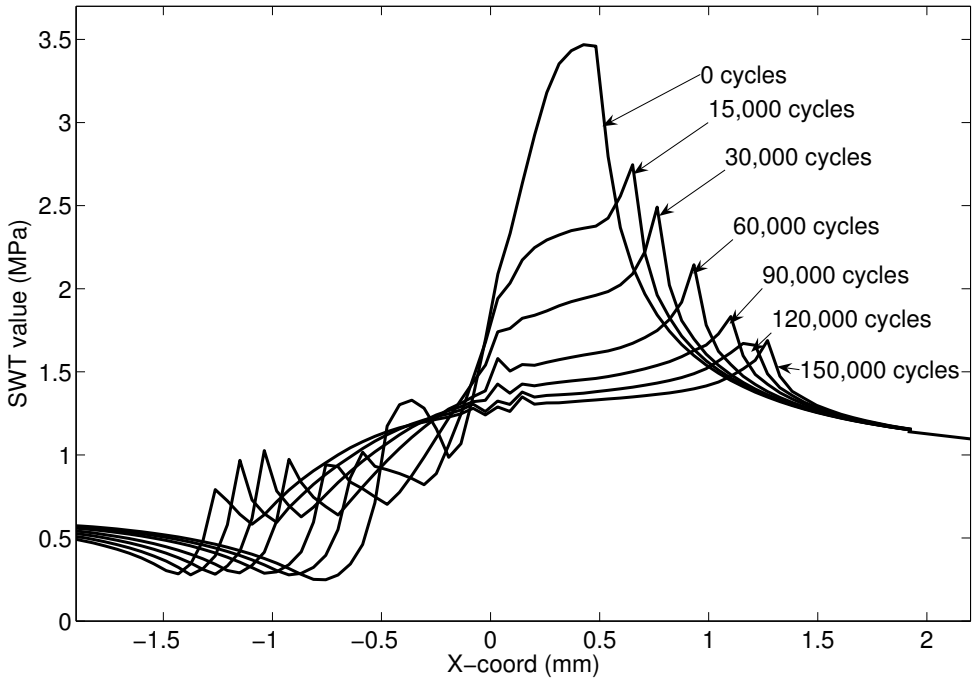

Figure 4.10. Evolution of the SWT parameter across the contact surface (δ=8.7μm)

Effect of wear: partial slip

Figure 4.11 shows the predicted evolution of contact pressure distribution for a partial slip case with δ=2.9 μm. Two key points to note about the results of Figure 4.11 are (i) the development of a local pressure peak at the trailing-edge stick-slip interface, which is also consistent with the predicted partial slip evolution of contact pressure presented by Ding et al (2004), and (ii) the fact that, in contrast to the gross sliding distributions, and except for the trailing edge slip zone, the contact pressure is not generally reducing with increasing cycles. In further contrast to the gross sliding results of Figure 4.9, the local pressure accentuation at the trailing edge stick-slip interface leads to a local accentuation in normal and shear stresses and, ultimately in the SWT value at this interface (Figure 4.12). For $\delta \leq 4.7\mu m$, i.e. the partial slip regime, failure is predicted to occur within the slip region, not at the contact edge.

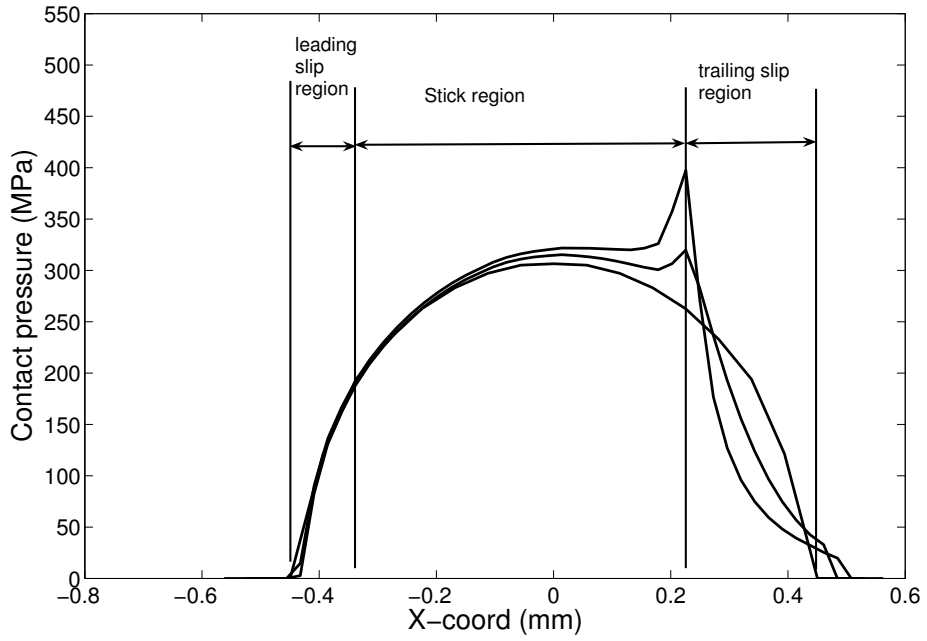

Figure 4.11. Pressure distribution evolution with wear for partial slip case (δ=2.8μm)

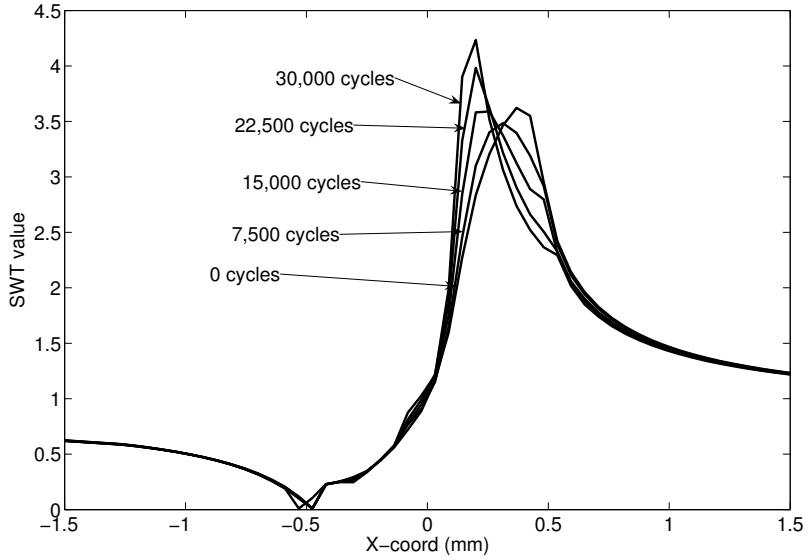

Figure 4.12. Evolution of the SWT parameter across the contact surface (δ=2.8μm)

Effect of slip amplitude on fatigue life: considering wear

Figure 4.13 shows two-dimensional contour plots of the accumulated damage ω for typical partial slip and gross sliding cases. The gross sliding results in Figure 4.13 are taken at 150 000 cycles, whereas the partial slip results are taken just before the predicted time of failure, at 25 000 cycles. The damage distributions show significant differences. The most obvious difference is the more localised nature of the partial slip predicted damage, as compared to the more widespread nature of the gross sliding distribution. The partial slip case reaches an ω value of 1 after only 25 000 cycles in this case, whereas after 150 000 cycles the gross sliding case has only reached about an ω value of 0.32. For gross sliding cases with slip ranges greater than 4.7 μm, insufficient computer memory is available for failure to be reached within the simulation period of 150 000 cycles. However, the evolution of SWT value follows an exponential-type decay which has essentially converged by 150 000 cycles for all cases examined here. Consequently, in cases of N_f >150 000 cycles, it was possible to

extrapolate, based on the SWT distributions obtained at N = 150 000 cycles, to infer the approximate number of cycles required to reach an accumulated ω value of 1 for each slip range considered.

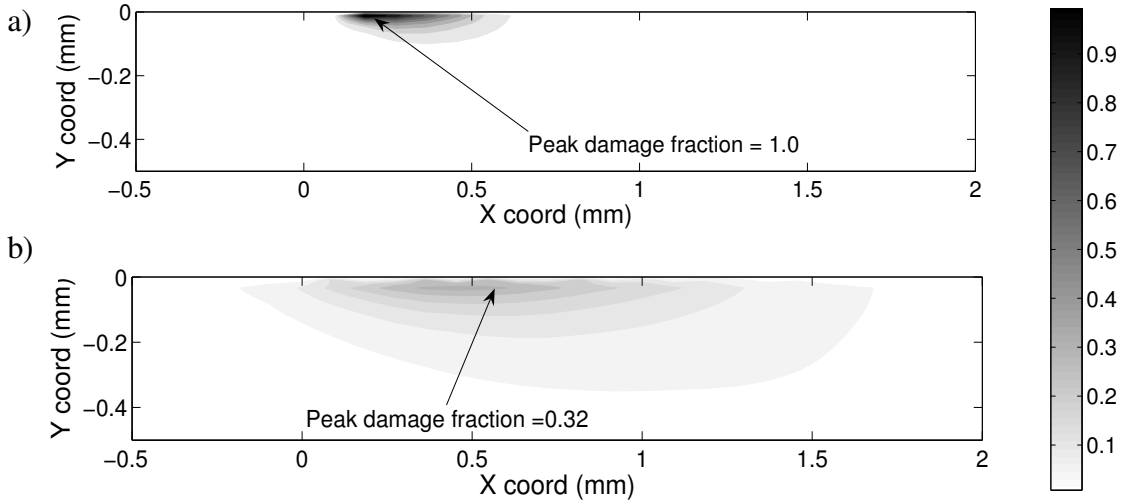

Figure 4.13. Predicted two-dimensional distributions of accumulated damage under the contact for:
a) partial slip case, at N = 25 000 cycles (δ = 2.9μm)
b) gross sliding case at N=150 000 cycles (δ = 8.7μm).

In summary, partial slip causes a transfer of pressure to the stick region, while the slip region is worn away and hence relieved of pressure. The result approaches a punch on flat contact with a pressure peak forming at the stick-slip interface. The implications of this on fatigue life are significant. Firstly, the trailing-edge stick-slip interface experiences a continually increasing and high level of cyclic damage. Secondly, in contrast to the gross sliding situation, where the damage is spread over an increasingly larger contact width, the partial slip situation leads to a focussing of damage accumulation at the trailing-edge stick-slip interface. The life predictions for the 'SWT with wear' analyses across the full range of slip ranges are given in Table 4.2, along with predicted failure angle and failure position. These predicted lives are

plotted in Figure 4.14 as a function of slip amplitude. In addition, the measured lives reported by Jin & Mall (2004) corresponding to the present FE analyses (using the local slip values defined by Equation 4.1) are also plotted in Figure 4.14 for comparative purposes.

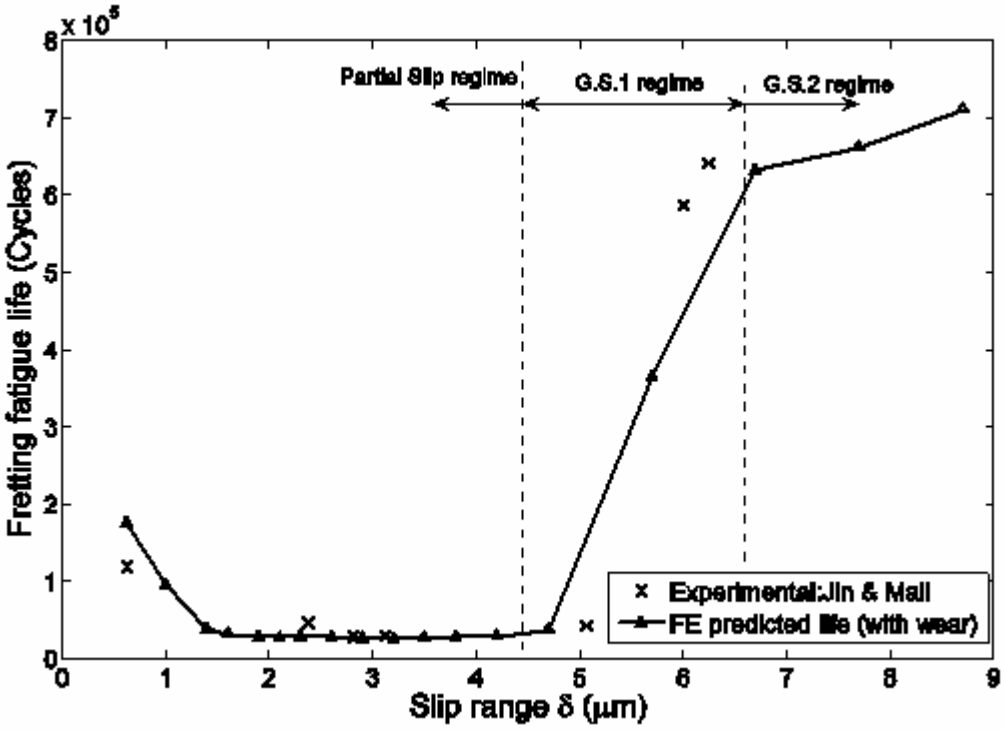

Figure 4.14. FE-predicted effect of slip amplitude on fretting fatigue life along with measured test data of Jin and Mall (2004) for the same series of tests.

Effect of coefficient of friction

A COF of 0.8 has been assumed in all cases discussed so far. Jin & Mall (2004) report that the measured COF varies from approximately 0.37 to 1.05, typically the early COF is low, rising to a stabilised state in the first 1000-75,000 cycles, depending on the slip regime. Figure 4.15 depicts the shear force histories for three experiments by Jin & Mall (2004).

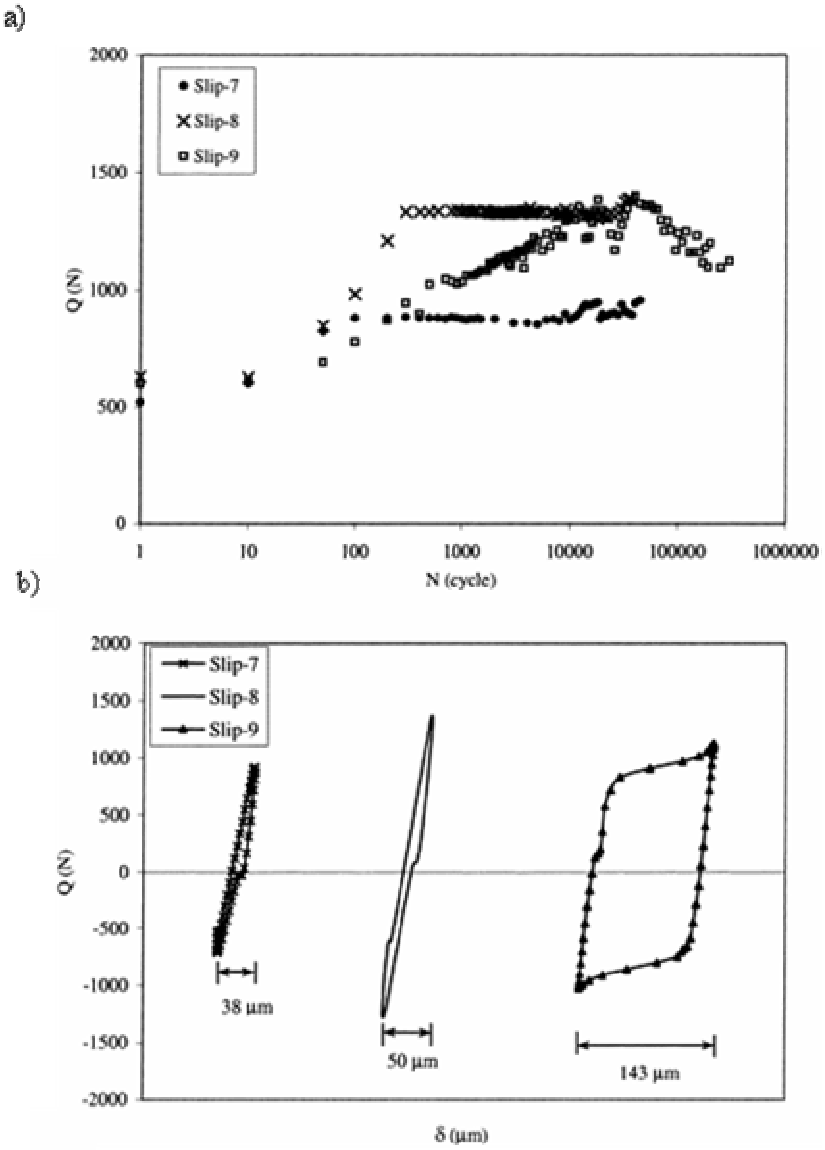

Figure 4.15. a) Example of shear force history for three different fretting tests. b) Associated hysteresis loops (Jin & Mall, 2004)

In the absence of a more refined friction model, the assumed value of $\mu = 0.8$ is intended to approximate the low starting coefficient of friction and the stabilised, higher value. In order to study the effect of the COF two values of δ_{app} have been studied, relating to the δ=8.7 μm, and δ=3.2 μm cases in Table 4.2. In this brief study, the $\delta_{app,m}$ of the model is kept constant for each case, whilst the COF is varied. It should be noted that although that the slip, δ, is a function of the COF, the two cases are referred to based on the δ value in Table 4.2 (i.e. the δ value given by the μ=0.8 case) All other parameters, including the wear coefficient are unaltered.

Figure 4.16 shows the effect of varying the COF on the predicted life. If wear is neglected, it is found that the fatigue life has an approximately log-linear relationship with the coefficient of friction. However, if wear is considered, a sigmoidal relationship is observed between friction coefficient and predicted fretting fatigue life. In both applied displacement cases, at extreme values of COF similar life predictions are obtained whether wear is neglected or considered. In between these extremes, a region is found where the 'wear analysis predicts a significantly longer life than that which neglects wear. As μ is increased further, a knee point is found, where the life is predicted to reduce rapidly, to a level similar to that predicted if wear is neglected. Figure 4.17 shows the effect of COF on the hysteresis loops for a sample of the cases shown in Figure 4.17.

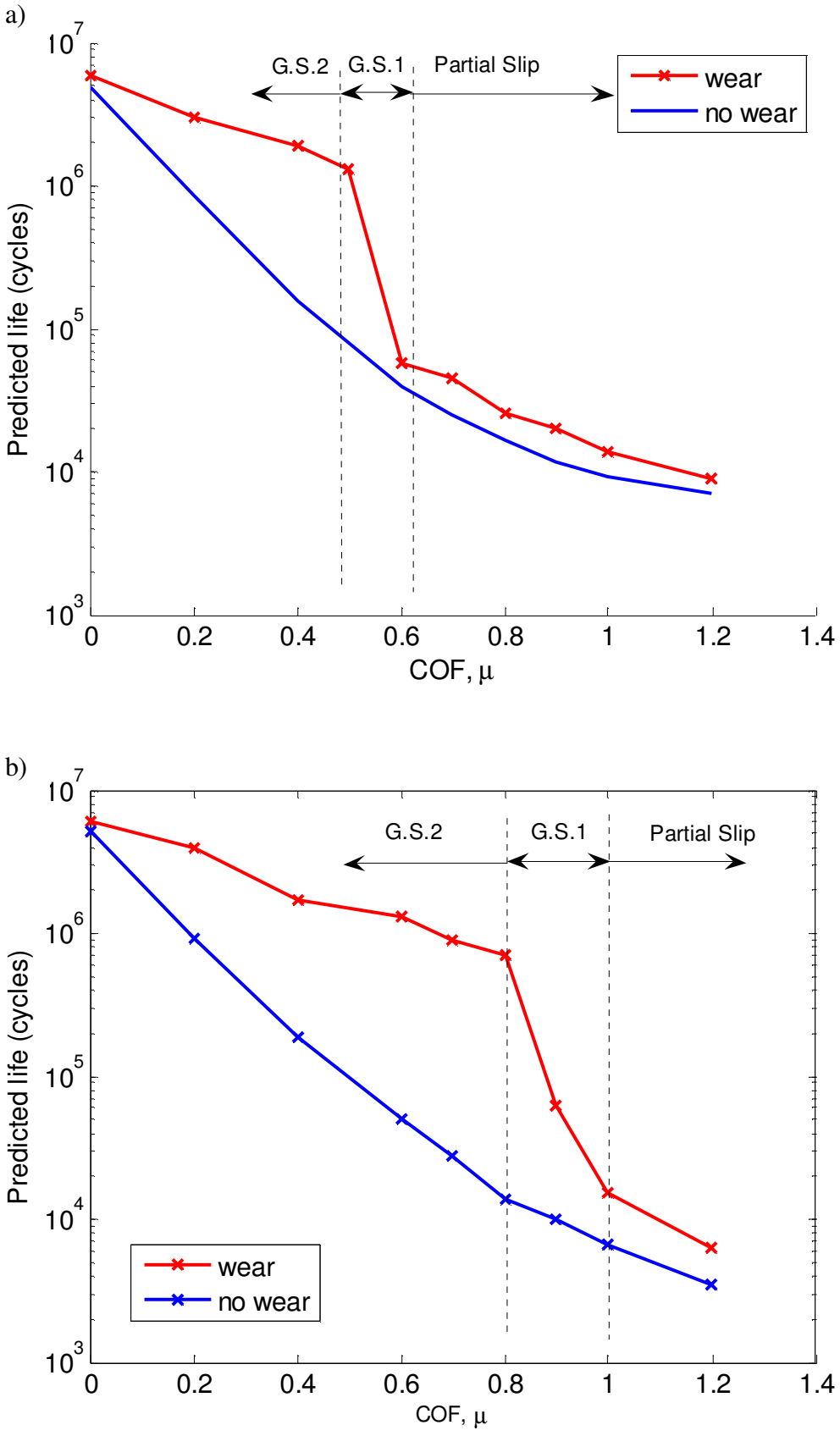

Figure 4.16. Effect of COF on predicted life
a) δ = 3.2 μm b) δ = 8.7 μm

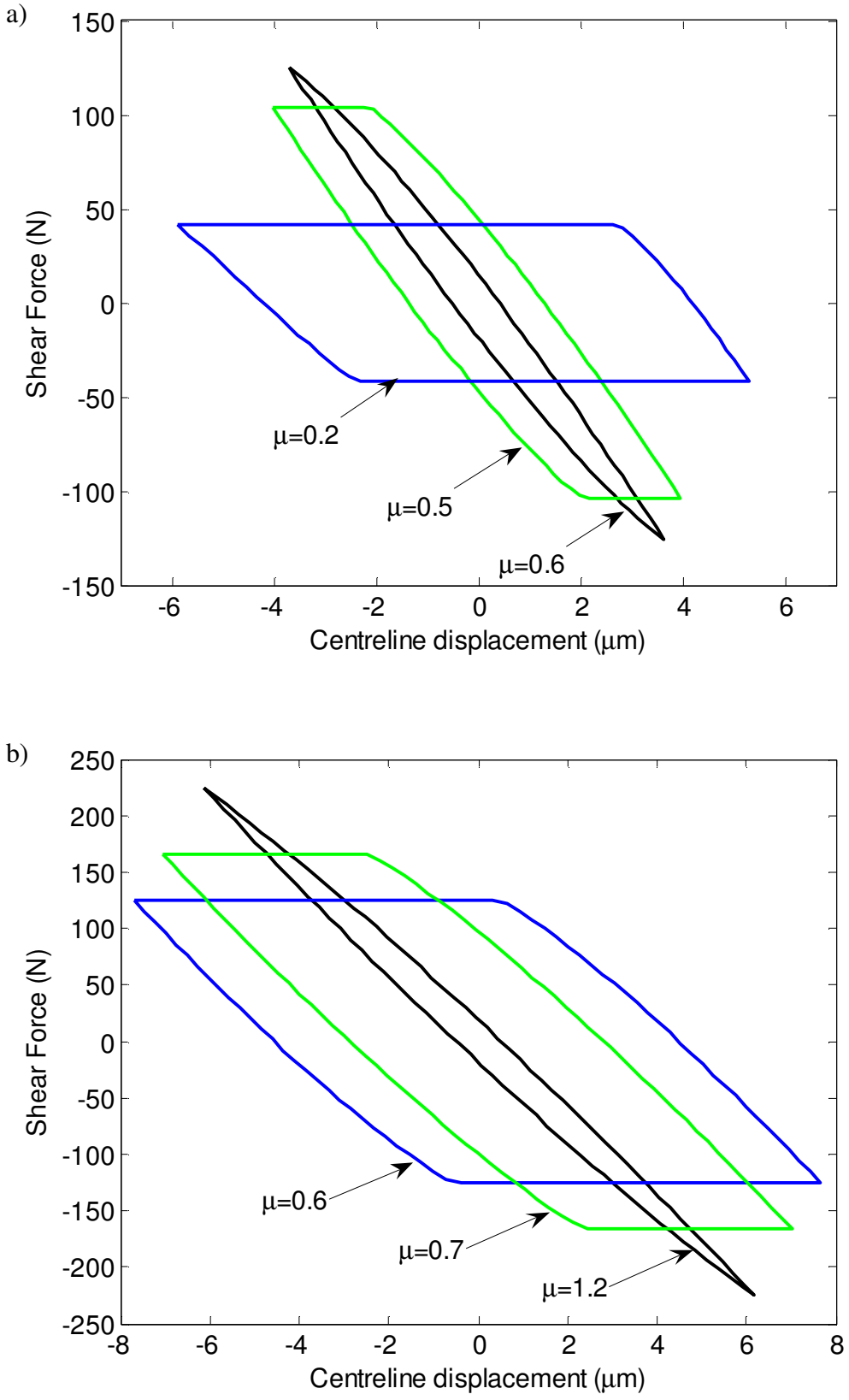

Figure 4.17. Effect of COF on cyclic hysteresis loops.
a) δ= 3.2 μm b) δ= 8.7 μm

4.7. Discussion of results

The effects of including wear (and the cumulative damage rule) in the calculation of fretting fatigue life can be summarised as follows, with reference to the results of Figures 4.7 and 4.14, in particular:

1. A significant increase in fatigue life is predicted in the gross sliding regime, particularly at higher slip ranges, although this increase starts to level off above a certain slip range. This increase can be directly attributed to (i) the reduction in peak contact pressure due to the material removal effect of gross sliding and the associated reduction of fatigue stresses and strains, and (ii) the fact that damage accumulation is not focussed on one location (Fig. 4.13). Both (i) and (ii) are direct consequences of the widening of the contact patch due to wear.

2. Within the partial slip regime, the location of maximum damage accumulation starts off near the edge of contact for small slip ranges (e.g. see δ = 0.627 μm in Table 2), due to the associated small slip zone size. However, with increasing slip range in the partial slip regime, this location moves steadily towards the stick-slip interface as the slip zone widens. There is a change in location of maximum damage accumulation once the partial slip/gross sliding threshold is crossed. In fact, the gross sliding regime can be split into two sub-regimes: one, denoted 'G.S.1', corresponds to small slip ranges (here δ = 4.7 and 5.7 μm) and the other, denoted 'G.S.2', corresponds to higher slip ranges (δ = 6.7, 7.7 and 8.7 μm). For G.S.1, the critical location is still near the centre of contact (x/a = 0.208) whereas for G.S.2 the critical location has returned to the edge of contact region (see Table 4.2).

3. The levelling off in fatigue life at higher slip ranges (G.S.2) can be attributed to a reducing benefit of stress redistribution due to material removal. Due to the nature of the cylindrical pad shape, the early evolution of the geometry brings the greatest benefit in stress redistribution, with a reducing rate of change of stress as wear proceeds. Consequently, gross sliding tends to produce conditions which converge over time. Figure 4.17 shows the predicted surface distribution of SWT for the G.S.2 regime cases at N=150 000 cycles. These cases show similar SWT distributions except for the slightly increased contact width. This shows that, from a fatigue point of view, the behaviour under gross sliding (above a certain slip range, in this case, somewhere between 5.7 μm and 6.7 μm) creates a stabilised state which is only a weak function of further increases in slip amplitude. In all such cases, the contact geometry evolves to a conforming contact with a uniform contact pressure. A key point here is that, for these cases, the fatigue life is dominated by this final stabilised state.

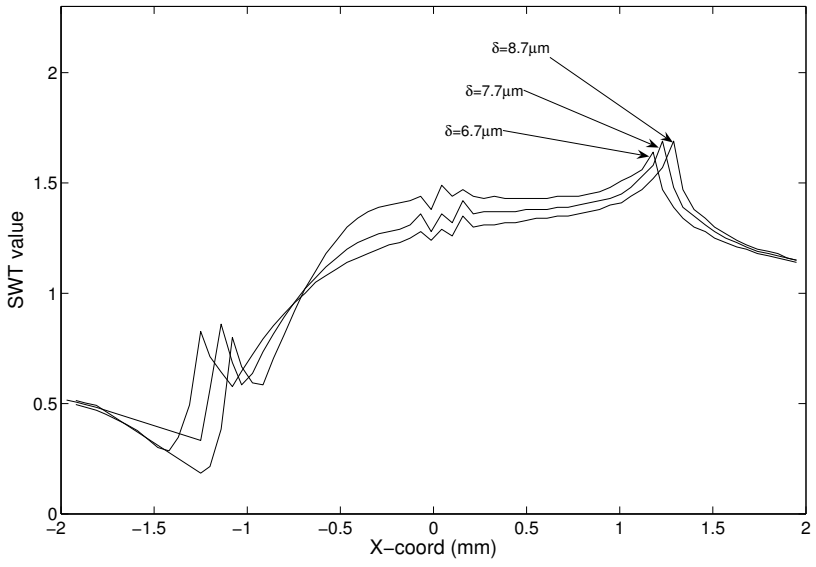

Figure 4.18. SWT distributions across the contact face
for the G.S.2 regime cases (150 000 cycles)

The transition gross sliding sub-regime G.S.1 (here δ = 4.7 to 6.7 μm) shows some affinities with partial slip behaviour (in terms of failure position and finite life). Figure 4.16 shows the predicted slip distributions for the three cases of partial slip, G.S.1 and G.S.2. In the G.S 1 sub-regime, the slip distribution bears a strong resemblance to the partial slip case, suggesting a similar wear rate distribution. For G.S.1 cases, the wear rate is still small enough that the rate of pressure and stress re-distribution is too slow to prevent the rate of damage accumulation reaching critical levels. As the slip amplitude is increased further, corresponding to the G.S.2 sub-regime, the contact slip, and hence the wear rate across the contact, are large enough to cause pressure and stress re-distribution before sufficient accumulation of damage to reduce the fatigue life due to fretting. This observation is consistent with Varenberg et al's (2004) definition of fretting, in that there is a large relative differential of displacement across the contact interface. This slip differential appears to be key to the wear mechanisms which govern the nature in which the contact tractions evolve. Further increases in applied displacement over those shown in Figure 4.18 reduces the relative differential further still until eventually a state of reciprocating sliding prevails.

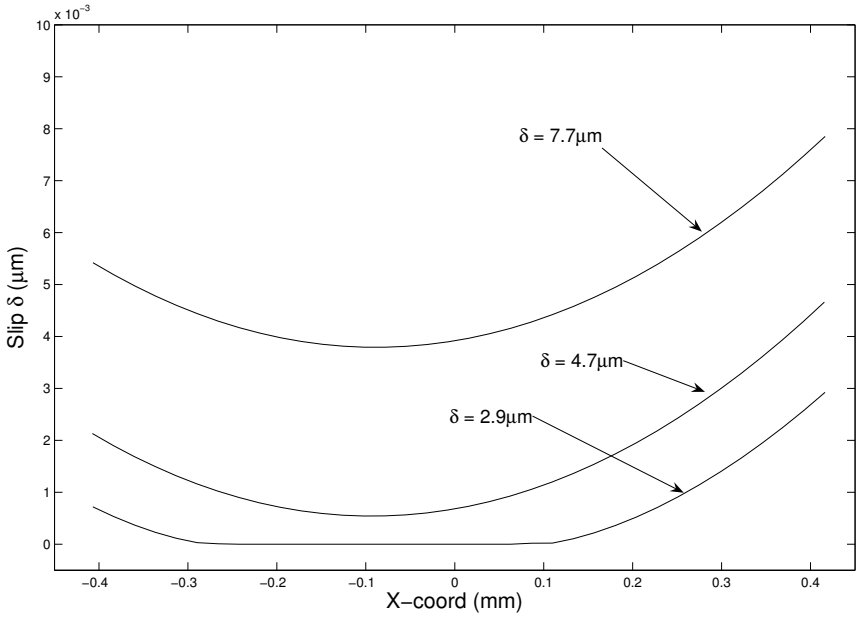

Figure 4.19. Slip distributions for the three slip regimes a) δ= 7.7 μm (G.S 2 regime) b) δ= 4.7 μm (G.S 1 regime) c) δ= 2.9 μm (Partial slip regime)

4. A comparatively small increase in fatigue life for the partial slip regime; this is simply due to the fact that even in partial slip cases, material removal initially has a beneficial effect in reducing the contact pressure at the critical location (trailing slip region, Figure 4.11) for the ideal Hertzian geometry. Even though the stresses and SWT values eventually increase significantly at the stick-slip interface with increasing wear, this takes some time to develop, and so in terms of overall life, wear is also predicted to give some benefit here (see Figure 4.12). The other key effect of wear in this case, as discussed below, is to shift the predicted failure location away from the contact edge to within the slip zone. These results also indicate why reasonably good (or at least mildly conservative) predictions of fretting fatigue life can be obtained for partial slip cases, even without including the effects of wear.

Clearly, the test data of Jin and Mall (2004) gives results which corroborate the FE-predicted effect of slip on fretting fatigue life, in particular the reduction of life

with increasing slip range in partial slip and the subsequent increase under gross sliding conditions. In addition, Table 4.2 shows that the predicted failure angle of 40^o under partial slip conditions gives better agreement with the experimental observations of ~43^o than the SWT predictions without wear (~7^o). The failure point prediction is also arguably more consistent with test data than the predictions without wear, whereby partial slip cracking is commonly observed across the slip zone, as predicted by the 'with wear' analyses. For partial slip conditions, the precise failure position within the slip region is found to be a function of the slip range. The principal reason for this behaviour is that the shear load affects the size of the stick zone, and hence where the pressure peak forms under partial slip conditions. Clearly the size of the stick zone and hence the predicted failure location will be affected by the value of COF assumed.

5. In all cases considered here the peak damage occurs at surface elements. This is due to the relatively high friction coefficient causing a significant stress concentration at the trailing edge. This is consistent with post mortem observations of Mall et al (2004) regarding similar tests. However it is foreseeable that failure could occur below the surface under different normal/shear load conditions, due to the high deviatoric stresses which are created subsurface under normal loading.

6. The predicted life has been shown to be strongly effected by the COF. Increasing the COF also increases shear traction and therefore, as might be expected, the predicted life is reduced. When wear is modelled, a range of COF values are found which result in a longer predicted life than that predicted if neglecting wear. The explanation for this behaviour is also related to the slip regime. Changing the friction coefficient affects two major fretting variables. Firstly, as mentioned, the shear force transmitted across the contact interface is altered. Secondly the slip

behaviour is changed. In both of the displacements considered, a critical COF μ_{crit} is found whereby small increases in the COF result in significant reductions in life. The value of μ_{crit} is found to be a function of δ_{app}. With reference to Figure 4.17, it is found that this critical coefficient of friction corresponds with the transition from gross sliding to partial slip. These observations are consistent with those outlined above with regard to the effect of slip amplitude as the mechanisms are essentially identical.

7. At both the extreme high and extreme low values of COF, the wear model life predictions are very similar to those predicted if wear is neglected. At high COF values, the slip is reduced and therefore so is wear, hence geometry evolution, and it effect on the stress field is significantly reduced. At vanishingly small COF values, the contact is no longer the critical region, as compressive stresses dominate here. Essentially the bulk fatigue load determines life at very low COF values, hence although significant wear is occurring, it has no effect on the predicted life.

4.8. Conclusions

This chapter has shown that the modelling approach described in Chapter 3 allows the effect of fretting wear upon fretting fatigue life to be quantified. The experimentally observed reduction of fatigue life with increasing slip under partial slip conditions and increase in fatigue life with increasing slip under gross sliding conditions has been captured using this technique.

The results corroborate the hypothesis that gross sliding in fretting fatigue can remove nucleating fatigue damage before propagation into cracks; the present methodology predicts that fatigue damage accumulated in the early cycles is worn away under

sliding conditions. However, it has also been demonstrated that the effect of pressure redistribution due to material removal is critical in that it reduces the risk of subsequent cracking.

There is a very definite competition between the damage modes at work. At low slip amplitudes prevalent cracking is indicated by high rates of fatigue damage and low lives. At large slip amplitudes, wear is the dominant damage mechanism, and the beneficial effects of the pressure redistribution and removal of damaged material increases the fatigue life significantly.

Chapter 5

Analysis of nearly complete fretting fatigue

5.1 Overview

In Chapter 4 the methodology of Chapter 3 was applied to a Hertzian cylinder on flat fretting geometry, which creates an incomplete contact. In this chapter the same methodology is applied to a rounded punch on flat fretting geometry which corresponds to a nearly complete contact configuration. By validating the method against both incomplete and complete contacts the method can be applied to physical geometries with greater confidence.

The effect of both slip amplitude and wear coefficient is investigated. The approach is able to predict the occurrence of failure at the stick slip interface, which is not possible using existing methods, as well as predicting the effect of slip amplitude.

5.2 Model Description

5.2.1 Test Geometry

Figure 5.1 shows the specimen geometry and schematic test arrangement modelled, corresponding to the experimental tests of Jin & Mall (2002). A pair of flat fretting pads with a nominal contact width of 4.45 mm and edge blend radii of 2.54 mm are held in contact with a flat, uniaxially-loaded fatigue specimen. The material used in the experiments was a dual phase Ti-6Al-4V alloy which consists of α (hexagonal close packed) and β (body centred cubic) phases. The material was

solution heat treated at 935°C for 1.75 hrs, cooled in air and annealed at 700°C for 2 hrs in a vacuum and cooled in argon. The material condition is nominally identical to that studied in Jin & Mall (2004) and Chapter 4; so the same material model is used, including the fatigue life constants (see Table 4.1)

5.2.2 FE model

A symmetry plane parallel to the specimen axis is employed in the FE model so that one pad is modelled (Fig. 5.2). The FE mesh created has graded refinement towards the edges of contact to improve the stress resolution in this region where high stress gradients can occur. The smallest element in the model is around 14 μm×9 μm.

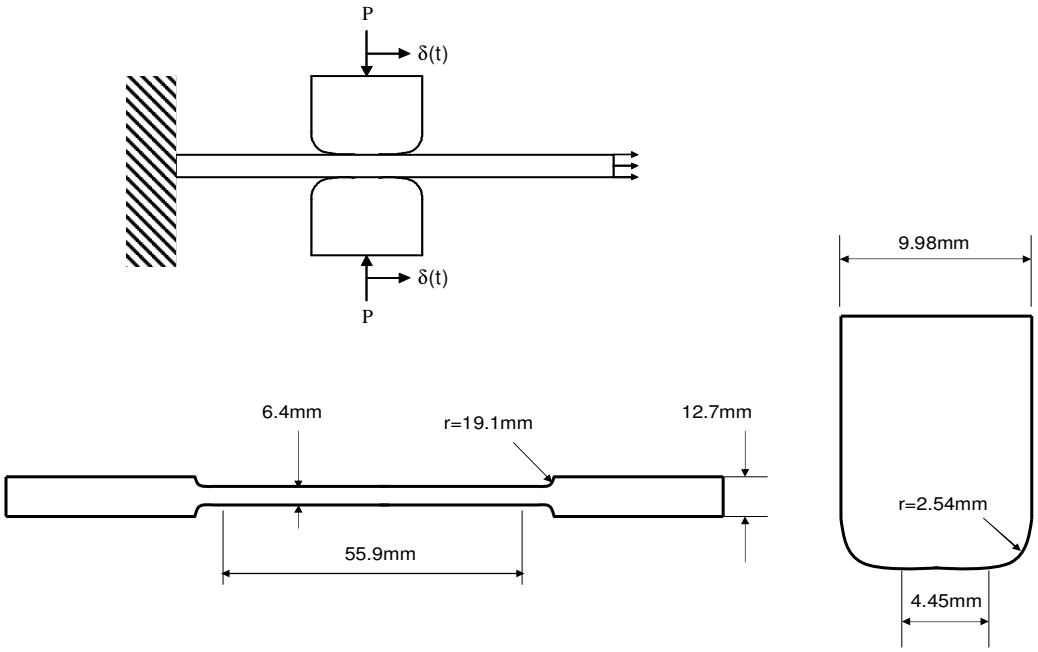

Figure 5.1. a) Experimental schematic b) Fretting fatigue specimen c) Fretting pad. After Jin & Mall (2002).

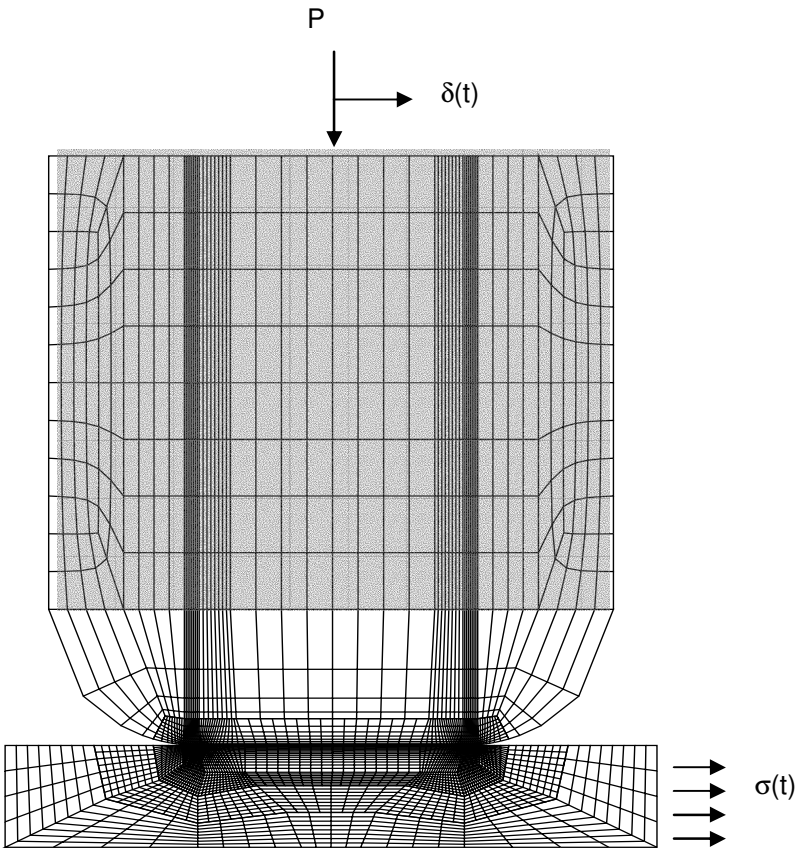

Figure 5.2. The FE mesh used for analyses.
Shaded section shows 'compliant section' used to represent rig compliance.

The constant curvature of the Hertzian geometry used in Chapter 4 allowed the fretting pad to be modelled to a height of only 2mm away from the contact surface as angular deflection of the pad did not cause significant variation in the contact pressure, this approach is not adequate in the present study. Due to the conforming nature of the contact and the relatively abrupt edge of contact, the influence of pad misalignment due to rig compliance was found to be an important factor (Sabelkin & Mall, 2005). In order to represent the flexibility of the experimental rig, the pad is modelled to a height of 11 mm away from the contact surface. Following the work of Sabelkin & Mall (2005) regarding the same experimental test equipment, the effect of rig compliance has been incorporated by setting the elastic modulus of

the extended section of the pad to a value of 55 GPa. The effect of the compliant section is discussed below, and further in Appendix A3. The top surface of the pad is prescribed to remain plane.

A similar friction formulation to that of Chapter 4 is used. A COF of 1.05 is taken as representative, based on the approximate stabilised dry sliding COF measured by Jin & Mall (2002).

Figure 4.3 shows the load cycle history for the first two load cycles. In the first analysis step a normal load P of 208 N/mm (equivalent to 1334 N for a 6.4 mm wide specimen) is applied to the fretting pad. In the next step the specimen is loaded by a cyclic fatigue load $\sigma(t)$ with a maximum value σ_{max} of 550 MPa and a stress ratio R of 0.03. The pad is also loaded with a prescribed maximum displacement δ_{app}, which is varied for each simulation to cover a range of slip amplitudes including partial slip through to gross sliding conditions. $\delta_{app}(t)$ and $\sigma(t)$ are applied cyclically in the FE model.

5.2.3 Variation of k

The cycle jumping technique described in Chapter 3, and employed in Chapter 4 is also used here, where the assumption is made that wear is constant over a certain number of cycles. The modified Archard equation given by Equation 3.5 shows that since k_1 and ΔN appear as a product on the right-hand side, this product can be represented as one constant k_{ref} which can be treated as a reference wear coefficient, as follows:

$$k\Delta N \equiv k_{ref} \tag{5.1}$$

so that Equation 3.5 can now be written as:

$$\Delta h(x,\tau) = k_{ref}\, p(x,\tau)\delta(x,\tau) \tag{5.2}$$

Subject to the assumption that the solution is approximately independent of the cycle jump size ΔN (See appendix A2) the effect of varying the wear coefficient k, within a reasonable range of values, can be investigated by varying the cycle jump size, as a post-processing exercise to a simulation using a fixed value of k_{ref}.

The benefit of this approach is that the evolution of contact pressures, slips, stresses and damage parameters can be presented in terms of a 'scalable' number of cycles, N^*, corresponding to the reference wear coefficient k_{ref}, which can be easily converted to specific numbers of cycles, N corresponding to arbitrary wear coefficient, k, as follows:

$$N = \frac{k_{ref}}{k} N^* \tag{5.3}$$

In the present study, a k_{ref} value of 4×10^{-5} MPa^{-1} has been employed, to expedite the wear simulations and thus reduce computational time.

5.3 Results and Discussion

5.3.1 Model validation and geometry study

In order to validate the results with respect to a theoretical solution, a sharp edged punch mesh was also developed. The theoretical solution is for a rigid punch normally loaded against an elastic half-space, as discussed in Chapter 2. The pressure distribution is singular as described by Equation 2.9. One of the objectives was to investigate the discrepancy between finite and elastic half space geometries. Three different variations on the sharp-edged punch geometry were compared, with a similar nominal contact width to that employed in the mesh shown in Figure 5.2. The meshes

used in these analyses are shown in Figure 5.3: 'SP-1' was designed to closely represent the theoretical situation, using a pseudo-rigid punch with a very high stiffness compared to the elastic specimen with which it contacted. This was achieved by setting the Youngs' modulus to 10^3 times higher than the specimen modulus. The elastic half-space was approximated by a specimen depth of 15 mm, which is approximately seven times the contact semi-width. 'SP-2' featured the same pseudo-rigid punch acting on a thin (1.9 mm) specimen like those used by Jin & Mall (2002). Finally an elastic punch on a thin specimen was analysed ('SP-3'). In each case a normal load of 208 N/mm is applied, equivalent to the 1334 N load on a 6.4 mm wide specimen as used by Jin & Mall (2002).

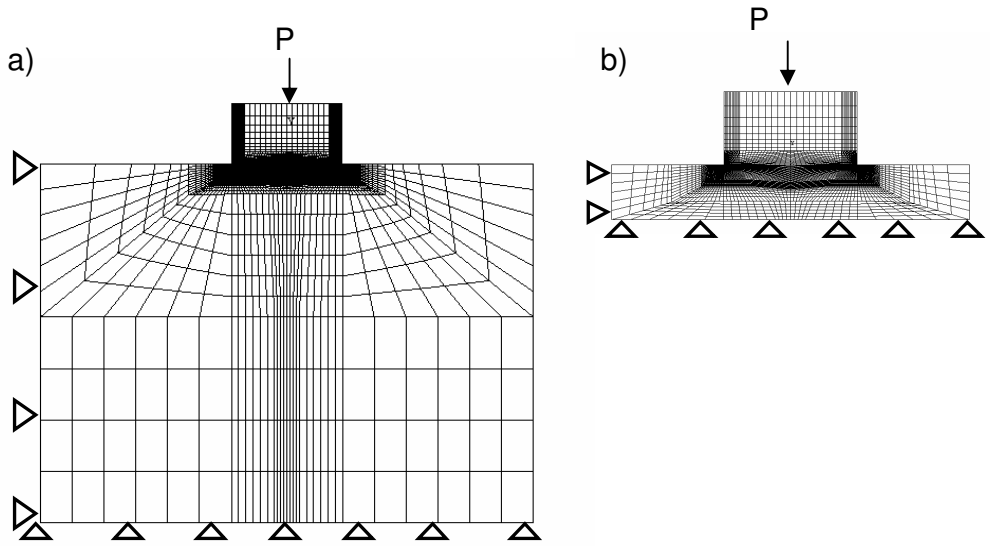

Figure 5.3. Sharp edged punch meshes

a) infinite half space approximation ('SP-1') b) finite thickness ('SP-2' & 'SP-3')

The pressure distributions are shown in Figure 5.4. SP-1 shows good agreement with the theoretical results. SP-2 & SP-3 highlight the importance of the assumptions concerning punch stiffness and specimen thickness: both thin specimen and finite modulus punch models tend to increase the load born by the centre portion, though a significant stress concentration persists at the edge of contact.

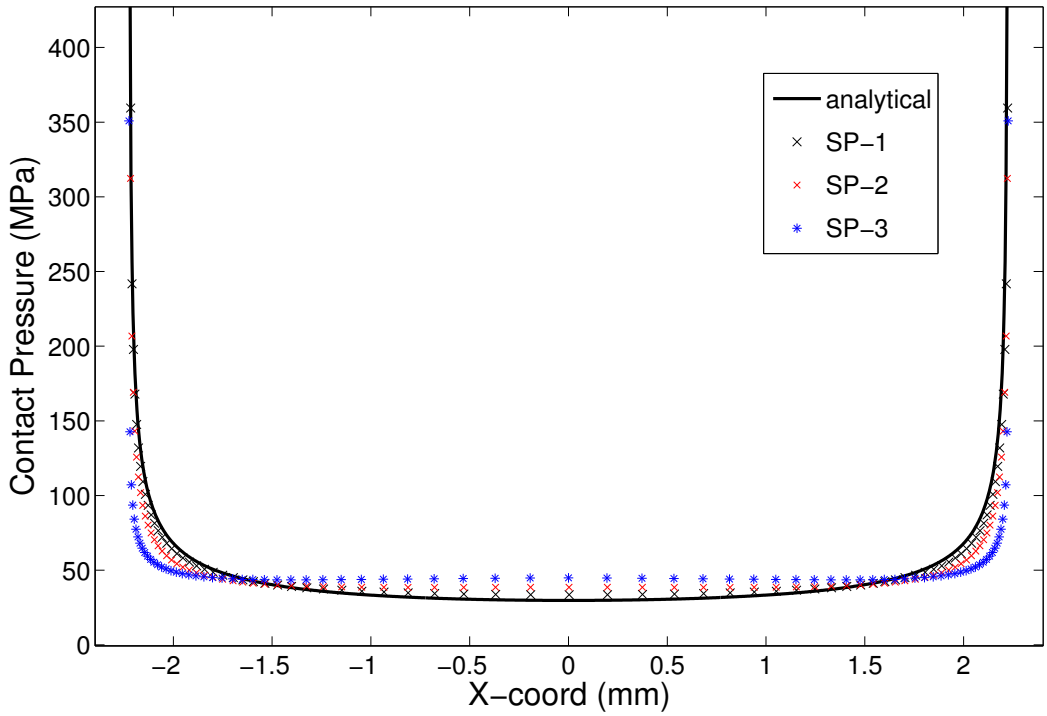

Figure 5.4. Pressure distributions for different sharp edged punch models
Compared to theoretical rigid punch

The 'nearly complete' nature of the rounded edge punch used by Jin & Mall (2002) is a further departure from the model described by Equation 2.9. Several variations on the nominal geometry shown in Figure 5.1 were created to study the effect of contact 'incompleteness'. This was achieved by modifying the mesh shown in Figure 5.2 by varying the width of the flat centre portion, and keeping the edge radii constant. In this way a full range of geometries between near-Hertzian and a wide punch on flat could be investigated, Figure 5.5 shows examples of two such meshes. Ciavarella & Macina (2003) reported similar finding in a study using an analytical technique. Figure 5.6 shows the effect of the '*a/b*' ratio on the pressure distribution across the contact face as determined by FE, note that here *a* is the width of the centre section (i.e. the unloaded contact width) and *b* is the width of the contact patch under full

normal load. The results are consistent with that of Ciavarella & Macina (2003), who adopted an analytical approach to a similar problem. The results also indicate that the rounded edge punch used by Jin & Mall (2003) gives a very similar pressure distribution to the sharp edged punch, as the *a/b* ratio for the normal load studied is 0.99. This implies that the conforming centre portion must be very narrow with respect to the edge radii to have a significant effect on the pressure distributions. In order to reduce the *a/b* ratio it is necessary to induce significant load redistribution onto the edge blend radii. In reducing the centre width, the mean contact pressure in increased, which causes greater elastic deformation and hence load redistribution. However, Figure 5.6 shows that in most practical applications, the addition of a blended radii is of limited merit, as typically the contact area will be a very weak function of normal load.

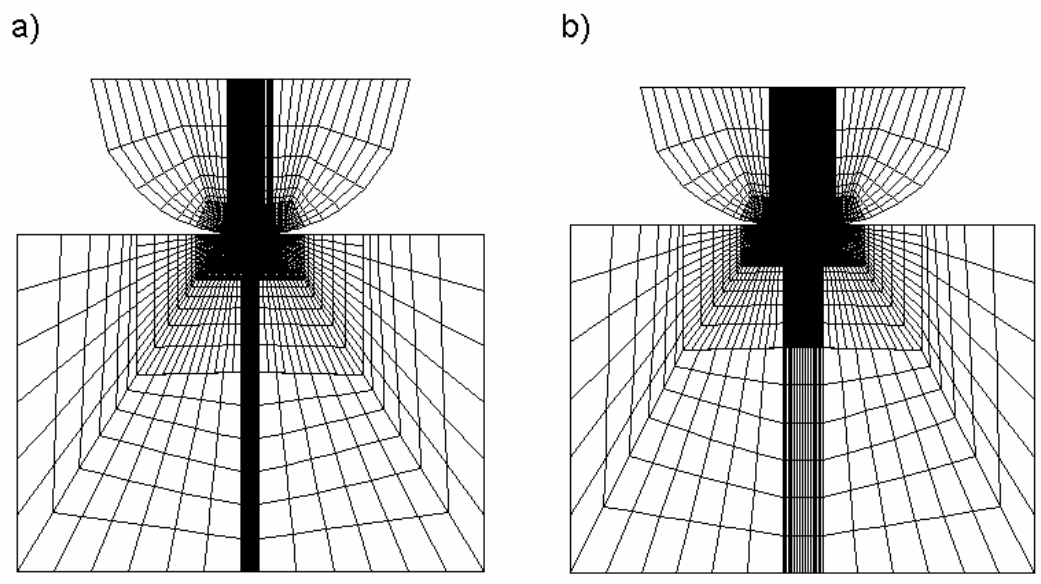

Figure 5.5. Two example meshes used in to study the effect of contact incompleteness a) centre width a = 0.25mm, a/b=0.6, b) centre width a = 0.325mm, a/b=0.833

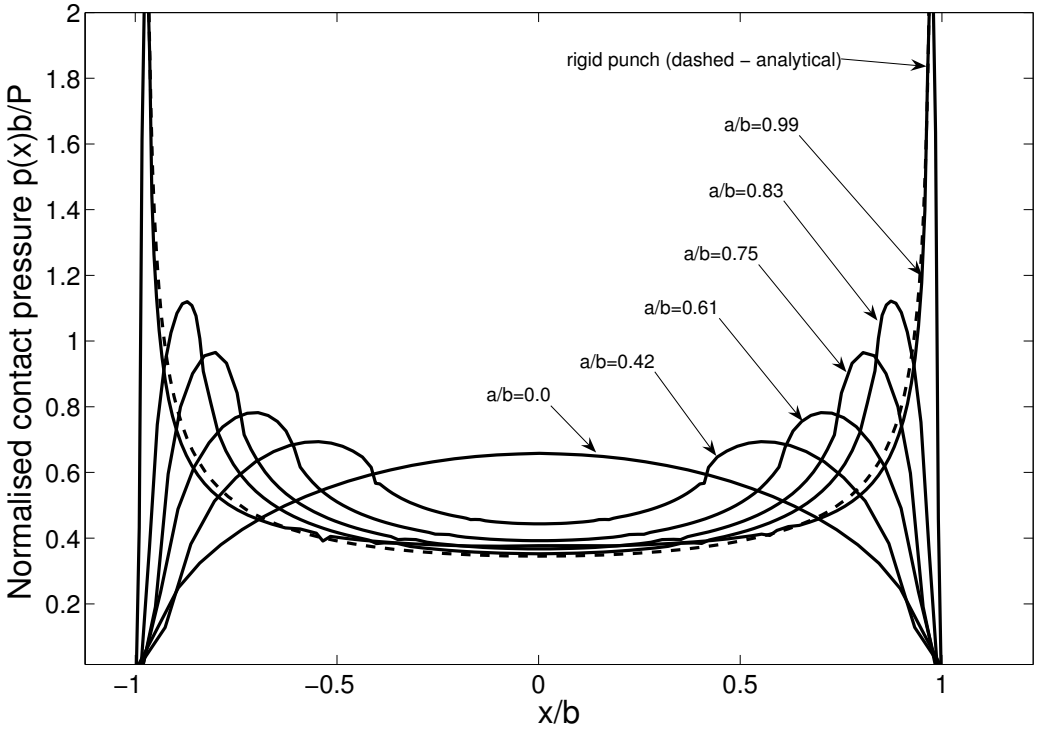

Figure 5.6. Effect of ratio of unloaded:loaded contact width (*a/b*) on pressure distribution.

5.3.2 Effect of rig compliance

The presence of a compliant section in the model creates an appreciable amount of load transfer throughout the fretting cycle as the pad is able to rotate under shear loading. At larger slip amplitudes, the shear force is large enough to cause sufficient deflection such that the trailing edge of the pad lifts free, whilst the leading edge is forced further into contact. This is illustrated in Figure 5.7, which shows the pressure distributions at maximum and minimum substrate fatigue stress for the $\delta_{app} = 40$ μm partial slip case. Whether or not the experimental rig displays this behaviour is not clear; however, it is interesting to note that the pad rotates in this manner, even though it is modelled with an encastre boundary condition and a compliant section modulus

(55 GPa) comparable to some engineering metals. This suggests that reducing the system stiffness has a detrimental effect on life by compromising contact alignment.

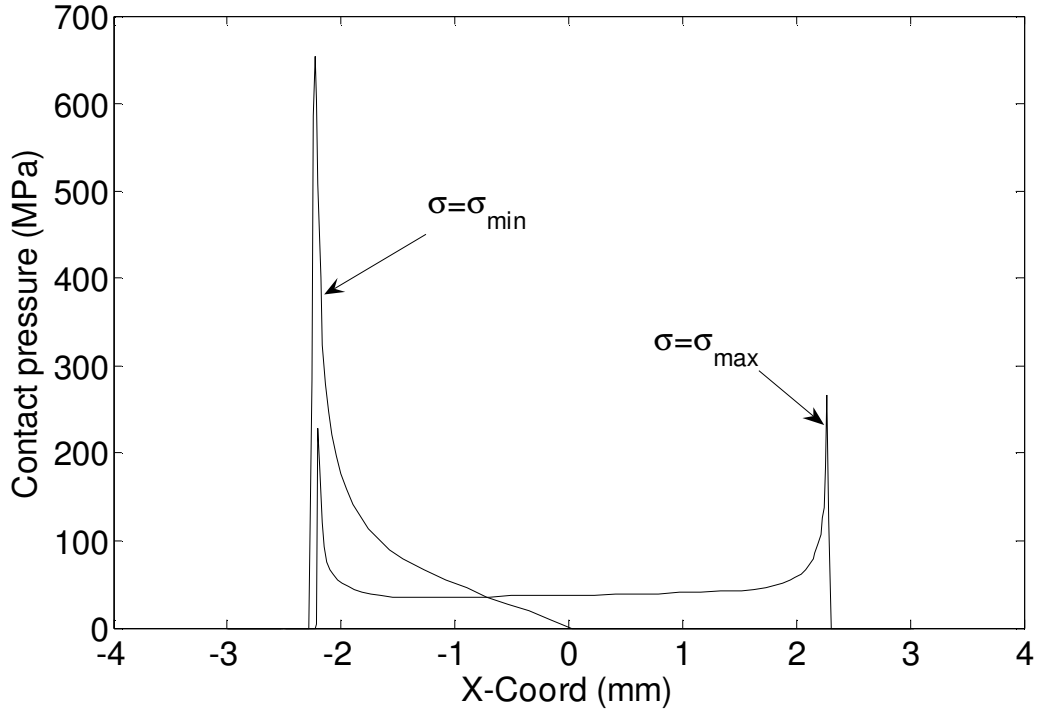

Figure 5.7. Contact pressure distributions for points of maximum and minimum fatigue stress, (δ_{app} = 40μm)

5.3.3 Effect of slip amplitude

The predicted effect of slip amplitude on fretting fatigue life is shown in Figure 5.8. If the effect of wear is neglected, a similar trend is observed as that found in Chapter 4, i.e. reducing life with increasing applied displacement. As δ_{app} is increased from zero the predicted life reduces as the shear force, and in turn the local fatigue stresses, increase. Note that the effect is less significant than was observed in the Hertzian case, as the high contact pressures found at the edge of contact create a significant stress concentration even in the absence of a tangential load. Figure 5.8b depicts the fretting fatigue life predictions according to the wear model, along with experimental test data for the same conditions as Jin & Mall (2002). The effect wear on fatigue life

is similar to that reported in Chapter 3 for the Hertzian fretting fatigue contact. Specifically, a minimum in life is predicted at the critical range of δ_{app} amplitudes corresponding to the transition from partial slip to gross sliding conditions (approximately $50\mu m \leq \delta_{app} \leq 85\ \mu m$), with comparatively long lives predicted as δ_{app} is either reduced or increased outside of this critical range. As mentioned above, at low (partial) slip amplitudes, the shear traction is reduced so that comparatively long lives are predicted. Additionally, as will be shown below, the action of wear over the edge of contact pressure concentrations is to amplify the increase in life at small applied displacements over those observed in Figure 5.8a. As such there is a significant beneficial effect of wear in all cases regardless of slip regime

At the onset of gross sliding, the shear tractions have saturated and a minimum in life is observed. However, as δ_{app} is increased still further the effect of wear is to increase fatigue life, as discussed in more detail below. The predictions show a good correlation with the relatively sparse experimental results.

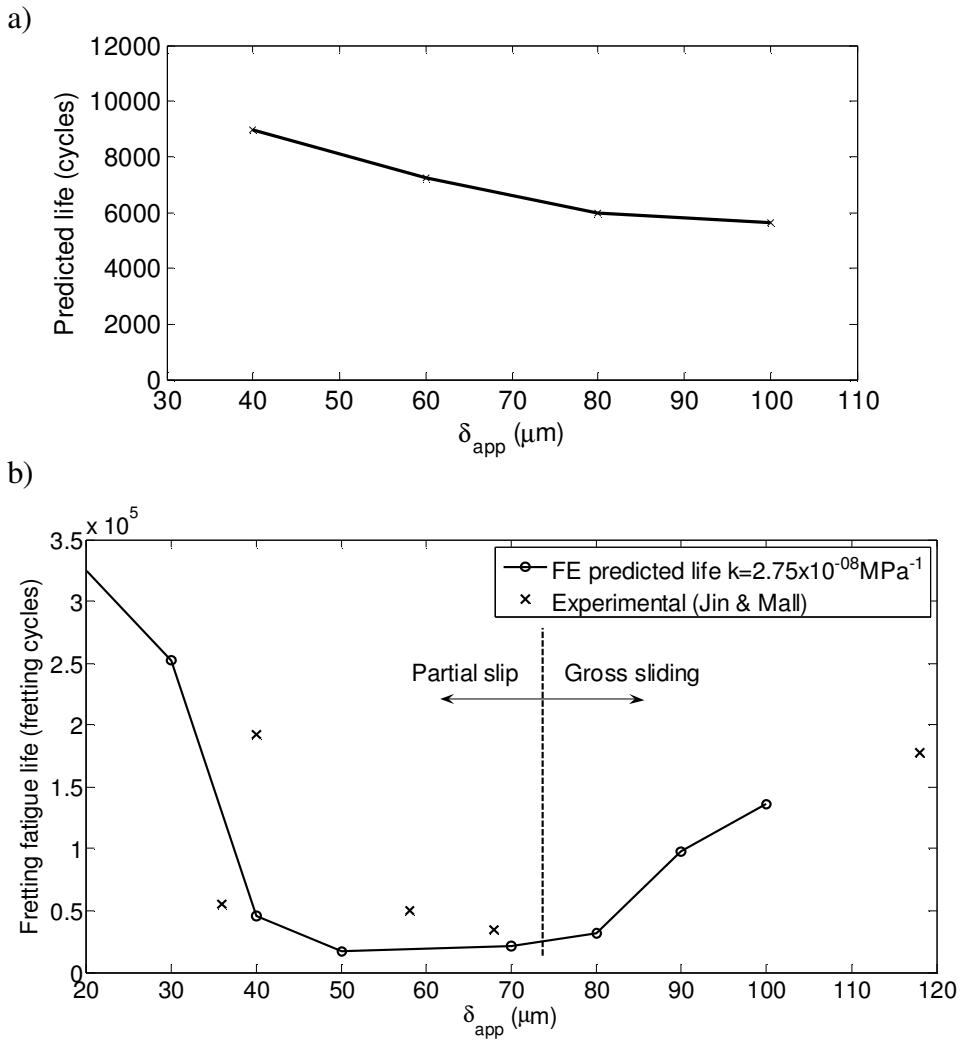

Figure 5.8. Prediction of fretting fatigue life at different slip amplitudes
a) without wear effects b) including wear effects

5.3.4 Effect of wear: Gross sliding

Figure 5.9 shows the effect of wear on the contact pressure distribution for a gross sliding case (δ_{app} = 90 μm). The two salient predicted effects of wear in this case are (i) the significant reduction in the edge of contact pressure peak and (ii) the significant increase in the contact area (and hence the load distribution area) by approximately 50%. Figure 5.10 shows the evolution of critical-plane SWT distribution across the

contact surface with increasing numbers of fretting cycles. For the unworn case and for early numbers of cycles, e.g. $N^* = 10$ (which corresponds to $N = 60{,}000$ cycles for $k = 2.75\times10^{-8}$ MPa^{-1}), there is a pronounced peak at the left-hand edge of contact (viz. the trailing edge at the instant of maximum substrate fatigue stress). However, it is clear that the predicted effect of wear here is to cause a dramatic reduction in the SWT value at this location. The associated rapid drop in cyclic fatigue damage is responsible for the increase in life observed at higher slip amplitudes in Figure 5.8. Failure is predicted at the trailing edge of contact for all gross sliding cases.

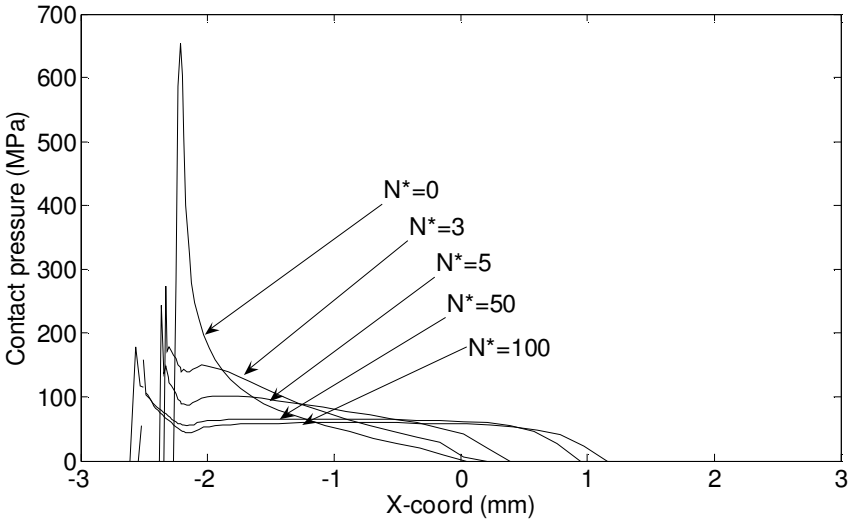

Figure 5.9. Evolution of contact pressure distribution for the δ_{app} = 90 μm gross sliding case. Note: for a typical value of $k = 2.75\times10^{-8}$MPa^{-1}, $N^* = 100$ corresponds to $N = 600{,}000$ cycles.

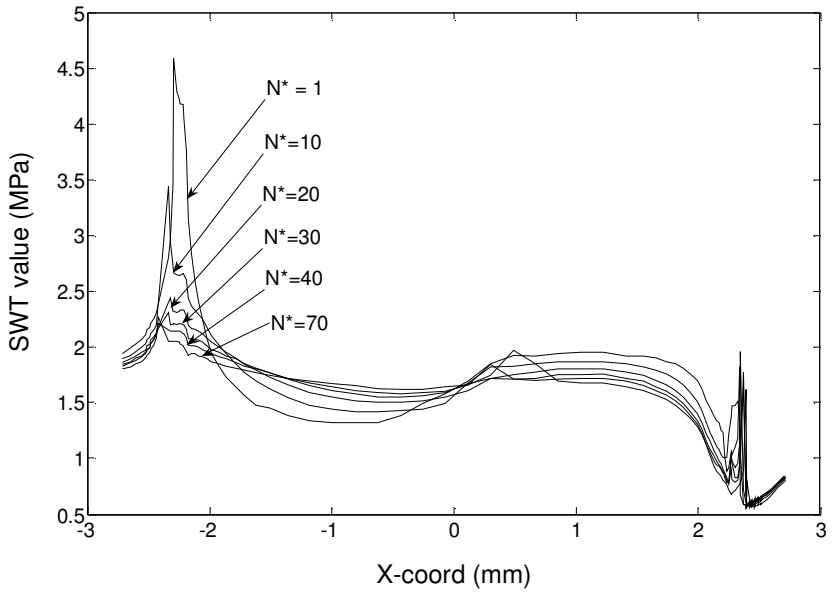

Figure 5.10. Evolution of SWT distribution across contact surface for the δ_{app} = 90μm gross sliding case. Note: for a typical value of $k = 2.75\times10^{-8}$ MPa^{-1}, $N^* = 70$ corresponds to N = 420,000 cycles.

5.3.5 Effect of wear: Partial slip

Figure 5.11 shows the predicted evolution of contact pressure distribution with increasing number of wear cycles for the δ_{app}= 40 μm partial slip case. As for the gross sliding case, wear is predicted to result in an initial beneficial effect in reducing the $N^* = 0$ edge of contact pressure peak. Thus, for $k = 2.75\times10^{-8}$ MPa^{-1}, for example, Figure 5.11 shows that the peak pressure value has dropped to about one quarter of its initial value after about 132,000 cycles ($N^* = 22$). For higher wear coefficients, this number of cycles will reduce proportionally, e.g. for $k = 2.75\times10^{-7}$ MPa^{-1}, the same attenuation will have occurred within about 13,200 cycles. However, a critical phenomenon of the partial slip case, as compared to the gross sliding case, is the development of a pressure peak well away from the contact edges as wear advances. It can be seen by comparing Figure 5.11 and Figure 5.12, (which shows the slip distribution for the δ_{app}= 40 μm case) that this pressure peak in fact develops at the stick-slip interface. The discontinuity between wear in the slip region and no wear in

the stick region generates a geometric and loading discontinuity which leads to a stress concentration, with load being gradually concentrated on the stick region.

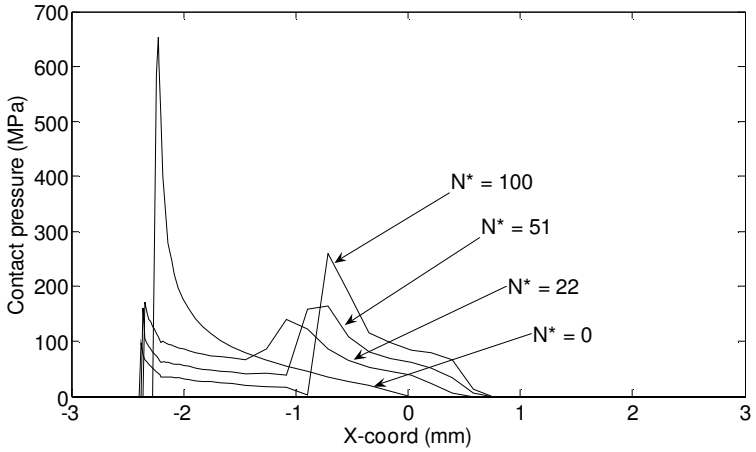

Figure 5.11. Evolution of contact pressure distribution with wear for the δ_{app} = 40 μm partial slip case. Note: for a typical value of $k = 2.75\times10^{-8}$ MPa^{-1}, $N^* = 100$ corresponds to 600,000 cycles.

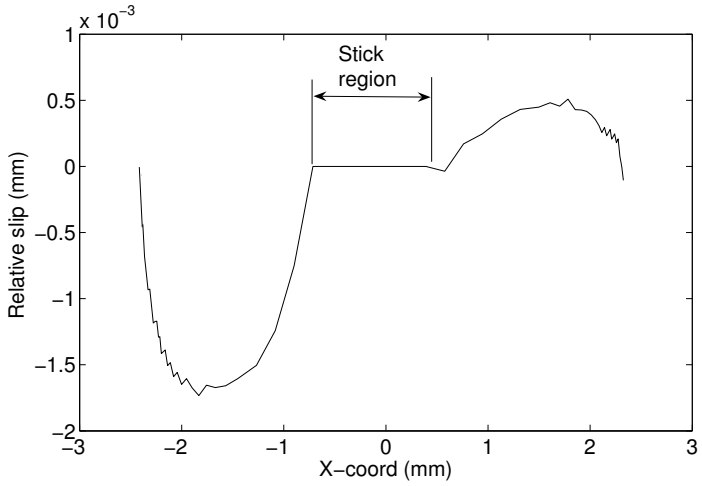

Figure 5.12. The $N^* = 100$ slip distribution for the δ_{app} = 40 μm partial slip case.

Note that in Figure 5.12 slip is only accumulated at regions in contact, hence relative movement occurring whilst parts of the interface are out of contact, e.g. due to the rig compliance effects discussed above, do not accumulate slip.

Figure 5.13 shows the predicted evolution of the SWT parameter across the contact surface for the latter partial slip case. Again, consistent with the attenuation in edge-of-contact pressure peak (and with the gross sliding case) during the early cycles, an

initial attenuation in edge-of-contact SWT value is predicted. However, the subsequent predicted development of the pressure peak at the stick-slip interface leads directly to an associated predicted increase in SWT value. The implication of this is that the issue of cracking location is predicted to become more complex for partial slip cases than for gross sliding; specifically, for partial slip cases, it is predicted that failure can occur at either the contact edge or the stick-slip interface, depending on the competition between rate of fatigue damage accumulation and wear-induced evolution of fretting stresses across the contact; as discussed below. This is consistent with the findings of Chapter 4; when wear is neglected, failure is predicted at the contact edge (setting k=0) whereas if wear effects are considered, failure was predicted at the stick-slip interface (setting k>0). Even though wear is predicted to reduce the edge of contact SWT peak for partial slip cases (as for gross sliding), this is offset by an accentuation of SWT at the stick-slip interface, which cannot be predicted by models which do not include the material removal effect of wear .

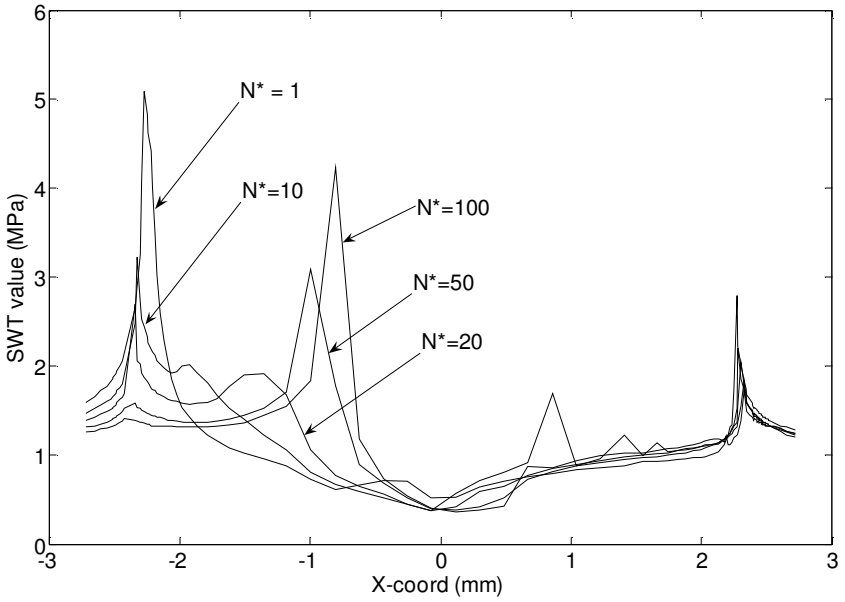

Figure 5.13. Evolution of SWT distribution across the contact surface for a partial slip case, δ_{app} = 40 μm. Note: for a typical value of $k = 2.75\times10^{-8}$ MPa^{-1}, N^* =100 relates to 600,000 cycles

5.3.6 Effect of wear coefficient on fretting fatigue behaviour

The aim of this thesis is to study the predicted interaction between wear and fatigue life; this can be easily investigated using the present methodology. For example, if we consider the evolution of contact pressure and SWT distributions of Figures 5.10 and 5.13, it can be seen that the time (N^*) at which the pressure peak and the associated SWT damage peak at the stick-slip interface starts to develop is dependent on the wear coefficient. If wear is retarded (i.e. by use of a low wear coefficient), the initial geometry and its associated pressure distribution (i.e. pressure and SWT peaks at either edge of contact) will dominate fatigue damage accumulation so that failure is predicted to occur at the contact edges. However, if wear evolves more rapidly (i.e. high wear coefficient), the pressure and SWT peaks at the edge of contact are reduced, but the stick-slip interface SWT peaks then dominate damage accumulation and hence failure is predicted at the stick-slip interface. The effect on predicted fatigue life of varying the wear coefficient is presented here for the partial slip case of $\delta_{app} = 40\ \mu$m. Figures 5.14 and 5.15 show the effect of k on predicted failure position and life, respectively. The failure position is found to switch from the edge of contact for $k < k_{crit} \approx 5.0\times10^{-8}$ MPa^{-1} to the stick-slip interface for $k \geq k_{crit} \approx 5.0\times10^{-8}$ MPa^{-1}. A comparison can be made with the experimental results of Jin & Mall (2002). It can be seen that the predicted failure point matches well with the observed cracking location on the micrograph. Referring to Figure 5.15, k is predicted to have relatively little effect on life for $k < 0.5\times k_{crit}$; the life is predicted to suddenly increase by a factor of about 5 as k approaches k_{crit}. Finally as k is increased further, for $k > k_{crit}$, the life is found to gradually decay back to approximately the same values as for $k < k_{crit}$. Jin & Mall (2002) have presented a wear scar for the partial slip case of the punch on flat geometry analysed here, which was observed to give stick-slip interface cracking.

A specific estimation of the wear coefficient of $k \approx 8\times10^{-7}$ MPa^{-1} has been obtained for this case, following the method outlined by McColl et al. (2003). The present analyses predict failure to occur at the stick-slip interface under partial slip conditions for this k value. It is worth pointing out that the value of k_{crit} will change for different fretting conditions, e.g. applied displacement, normal load, COF etc.

These results show that the interaction between fatigue and fretting wear is critical to the prediction of failure cause, location and number of cycles. Essentially, if the component can survive the initially severe loading conditions, viz. edge-of-contact pressure peaks and associated contact stress concentrations, so that wear-induced material removal can alter the pressure distribution, failure will occur at the stick-slip boundary, due to a completely different stress distribution to that given by the initial geometry.

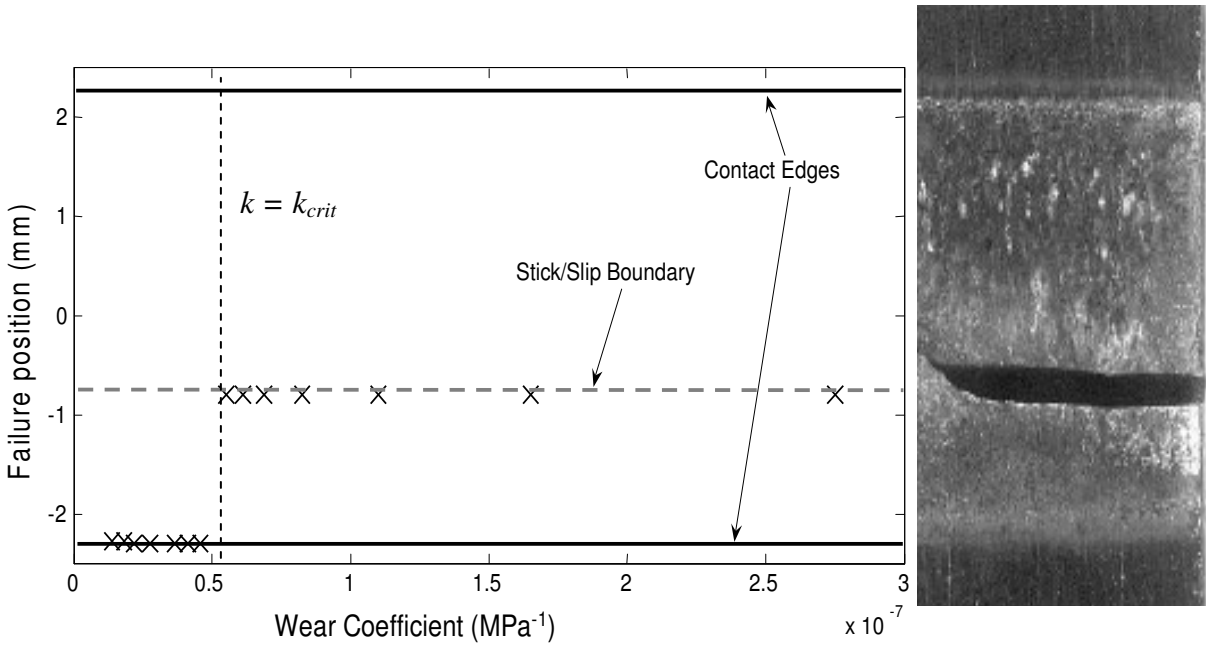

Figure 5.14. Effect of wear coefficient on predicted failure position (δ_{app} = 40μm). To the right is a wear scar micrograph from Jin & Mall (2002).

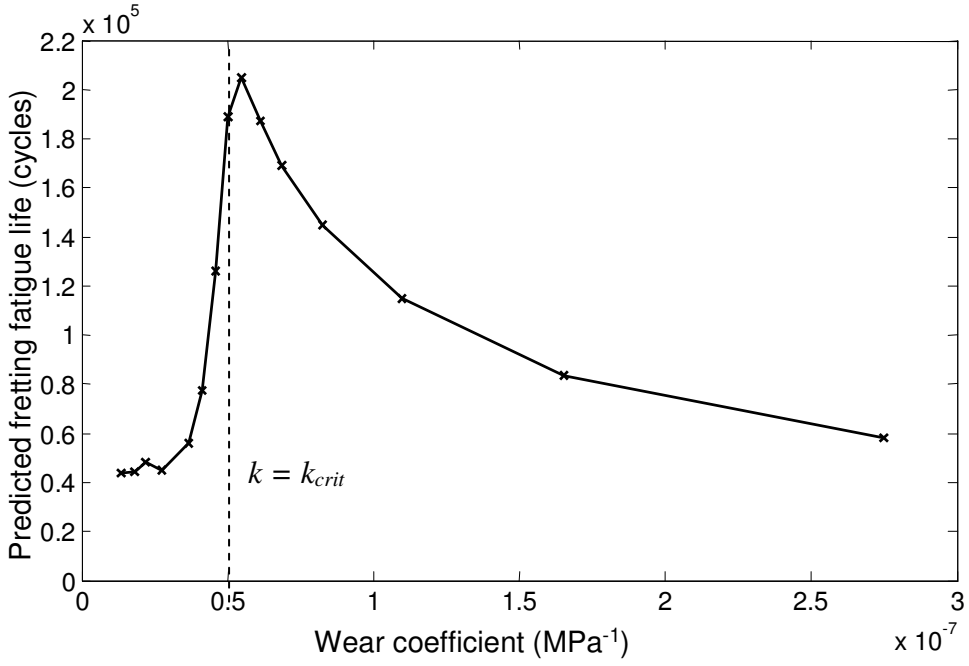

Figure 5.15. Effect of wear coefficient on predicted fretting fatigue life (δ_{app} = 40 μm partial slip case).

The reason for this peak in life at k_{crit} (Figure 5.15) lies in the material utilisation. Figure 5.16 shows the $\delta_{app} = 40\ \mu$m partial slip damage contour plots corresponding to failure ($\omega = 1$) for three values of wear coefficient, namely $k = 0.55 \times k_{crit}$ ($k = 2.75 \times 10^{-8}$ MPa^{-1}) $k \approx k_{crit,}$ ($k = 5.5 \times 10^{-8}$ MPa^{-1}) and $k = 1.6 \times k_{crit}$.($k = 8 \times 10^{-8}$ MPa^{-1}). In the $k = 0.55 \times k_{crit}$ case (Figure 5.16a) damage is highly localised at the trailing edge of contact. Conversely, in the $k = 1.6 \times k_{crit}$ case (Figure 5.16c), damage is highly localised to the stick/slip boundary. However, in the $k \approx k_{crit}$ case (Figure 5.16b), two regions of high damage are found, one near the edge of contact, and a second at the stick/slip interface. The material utilisation is high in this case because a greater amount of fatigue damage has been sustained by spreading it over a larger area. Figure 5.16 indicates that there is an optimum wear coefficient (k_{crit}) for maximum life under given fretting conditions. These results furthermore indicate that the present wear-fatigue methodology has the capability to model, and therefore ultimately design

for, commonly-observed phenomena from industrial practice such as 'bedding-in', whereby beneficial effects can be derived from using a mixed material combination with one wear-'soft' material and one wear-'hard' material. Note that the piecewise localised nature of the damage distribution in Figure 5.16 is due to the relatively coarse mesh employed towards the centre of the contact and the interpolation algorithm used, i.e. they are numerical artefacts.

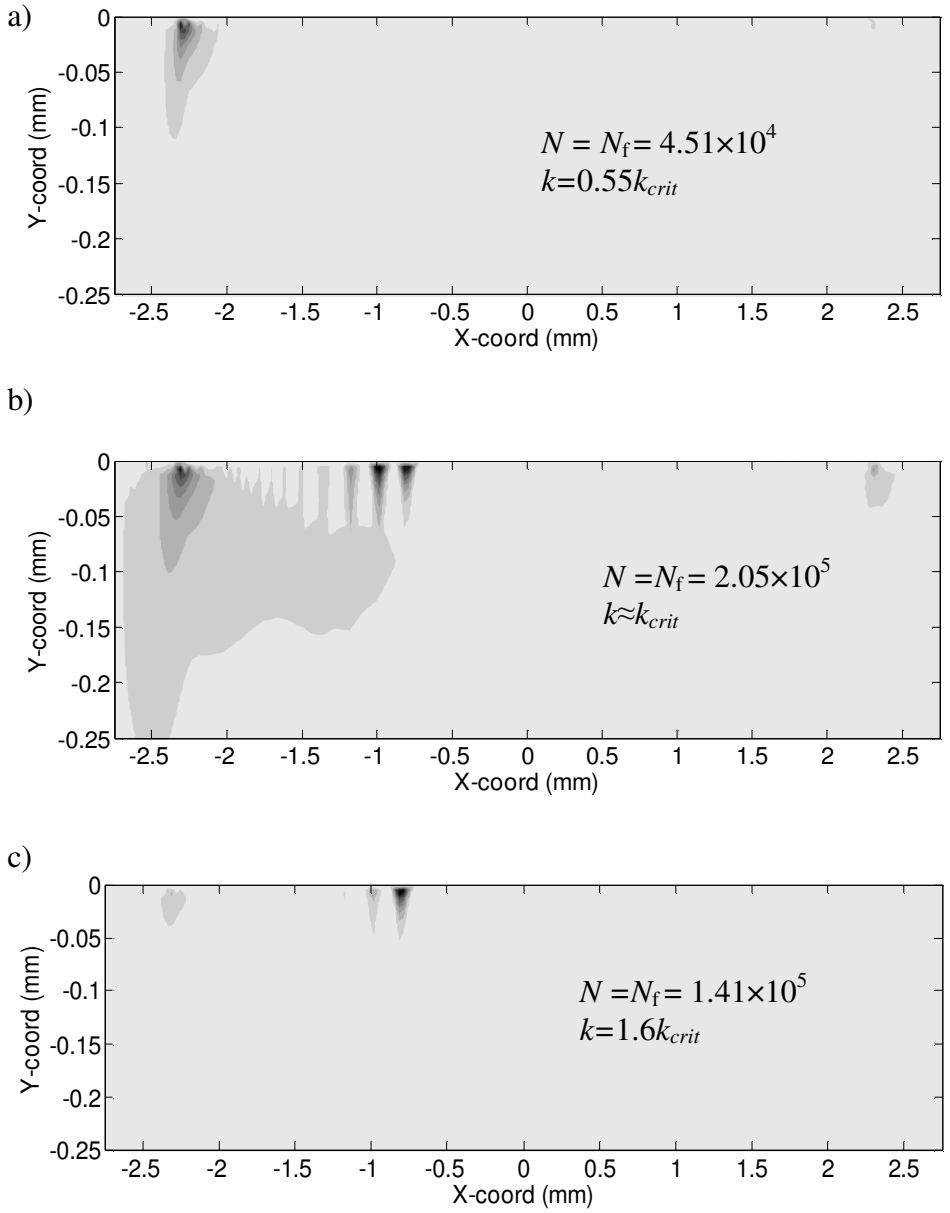

Figure 5.16. Showing the damage contours at failure (ω= 1) for different values of wear coefficient: a) $k = 2.75\times10^{-8}$ MPa^{-1} < k_{crit}; b) $k = 5.5\times10^{-8}$ MPa^{-1} ≈ k_{crit}; c) $k = 8\times10^{-8}$ MPa^{-1} > k_{crit}.

5.4 Conclusions

In this chapter, a finite element based method has been applied to predict and characterise the role of fretting wear on fretting fatigue for an almost complete contact fretting test configuration for Ti-6Al-4V, with comparisons against published test data from Mall and co-workers. The key findings are as follows:

- A significant effect of slip amplitude on fretting fatigue life was predicted, viz. a critical range of slip amplitude for minimum life corresponding broadly to the transition from partial slip to gross sliding, which is consistent with (i) a generally-accepted phenomenon of fretting fatigue and (ii) corresponding FE-based life predictions in the preceding chapter and test data for a Hertzian fretting test configuration.
- The life predictions were shown to exhibit good quantitative agreement with available test data in the region of minimum fatigue life.
- Prediction of failure position: It was shown that for gross sliding cases, failure is invariably predicted at the edge of contact, consistent with experimental observations. However, for partial slip cases, it was shown that due to the competition between wear rate and fatigue damage accumulation and the effects of edge-of-contact versus stick-slip interface SWT concentrations, failure location depended on the wear coefficient (for assumed constant fatigue properties). Thus, for low wear coefficients, partial slip failure is predicted at the edge-of-contact and for high wear coefficients at the stick-slip interface, with the sudden shift in position predicted at a single (critical) value of wear coefficient.
- The same critical value of wear coefficient was shown to give an optimum (maximum) partial slip fatigue life, for a given set of fatigue constants and

fretting conditions. This method provides a framework for designing for optimum fretting fatigue life.

- The work has demonstrated that prediction of fretting wear is a critical aspect for prediction of fretting fatigue and can have a major effect on the predicted evolution of stresses and damage parameters (e.g. SWT), and hence on predicted fatigue lives and failure position. This fundamental and important effect for fretting fatigue cannot be predicted by models which do not include the effects of material removal due to wear.

Chapter 6

A Combined Fracture Mechanics and Wear Modelling Method

6.1 Introduction

In the Chapters 4, 5 & 6 a total life approach was used to model the complete fatigue damage process. An alternative perspective of the fatigue phenomenon is given by fracture mechanics, where the crack growth is explicitly considered. This chapter describes the development of a method for investigating the effect of the fretting wear on crack growth in fretting systems. This fracture mechanics method is then combined with a modified version of the fatigue life approach developed in Chapter 3 to provide a framework which models initiation, the short crack phase and stage II crack growth separately, in the presence of a fretting wear modified stress field.

6.2 Damage tolerant approach

As mentioned in the literature review, a number of different approaches have been adopted in attempting to analyse the fretting fatigue phenomenon. Critical plane fatigue damage parameters and fracture mechanics techniques have proved to be relatively successful. In the preceding chapters, wear modelling was combined with multiaxial fatigue damage parameter lifing in the form of the SWT model. The following describes how a similar wear modelling method can be used to drive a fracture mechanics based fatigue model.

The stress gradients existing in fretting systems can be very high; in many cases the stresses at the surface are orders of magnitude higher than the bulk stress. This can give rise to phenomena such as crack self arrest. Crack self arrest is an attractive feature in fretting fatigue where nucleation is commonly unavoidable under the severe stresses and surface damage which are inevitable at the contact interface (Moobola et al, 1997). FDP methods cannot predict self-arrest, since they predict damage to continuously accumulate. However, a component that can be designed to create only self arresting cracks is inherently safe. Moobola et al (1997) state that to create self arrest in fretting, a relatively low fatigue load is required; indeed sometimes a bulk compressive load is required to suppress the action of contact stresses on crack growth. Of course, there will be some problems where highly stressed components are a necessity (e.g. due to space or mass limitations), so that it may not be possible to achieve self arrest anyway.

A number of investigators have applied fracture mechanics to fretting fatigue problems (e.g. Shkarayev & Mall, 2001, Munoz et al 2006). One benefit of this approach is that stress gradient effects can be directly addressed if crack growth is explicitly modelled, as in Shkarayev & Mall (2001). This is in contrast to damage accumulation approaches which base life prediction on the stress-strain behaviour at discrete points or regions in the material, ultimately selecting a critical point at which failure is predicted to occur. In Chapter 4 it was found that this point is at or near to the surface; the effect of the stress state away from the contact through which a crack grows was essentially neglected. Previous investigations into fretting have tended to concentrate on either crack nucleation or crack propagation. One notable exception is the work of Araujo and Nowell (2002) where an analytical approach was employed to

solve for both the nucleation life (to a 1 mm crack) and the propagation life (to failure).

In previous chapters no distinction has been made between crack nucleation and propagation; essentially the total life was predicted from the stress state and the associated cumulative fatigue damage at discrete points. Therefore, this chapter presents an FE-based fretting fatigue prediction methodology which combines the effects of cyclic wear simulation with crack nucleation and propagation prediction, including short crack growth prediction. The FE method has been adopted here as in previous chapters, to facilitate application to more complex geometries for engineering (e.g. aerospace) design.

The new methodology will facilitate prediction of the following key phenomena, which fractures mechanics, total life approaches and wear modelling could not themselves capture in isolation.

1) Crack self arrest
2) Dependence of fretting fatigue life on slip amplitude
3) Effect of wear on crack growth
4) Relative importance of nucleation and propagation behaviour.

The final point is particularly important to practical design as this defines the level of damage tolerance that a structure possesses. If the propagation period is short, then either a short inspection interval or a larger factor of safety must be employed. In aviation for example, many components are deemed critical to airframe safety and so their damage tolerance must be assessed as part of the certification process.

6.3 Methodology

Figure 6.1 shows a schematic representation of the proposed methodology, which combines wear modelling with crack nucleation and crack propagation prediction. The total fatigue life is defined as:

$$N_f = N_i + N_p \tag{6.1}$$

where N_i is the predicted number of cycles for nucleation of a short crack, typically about 10 μm depth, and N_p is the predicted number of cycles for this short crack to grow to failure, which is defined here as the number of cycles at which the crack length becomes equal to half the fatigue specimen depth. The wear analysis is used to determine the evolution of both contact and subsurface stress and strain data, which are used to determine the nucleation life N_i and location. A fracture mechanics sub-model is employed to simulate crack growth from the predicted nucleation site. As described below, both short and long crack growth are modelled. Surface tractions are applied to the sub-model which mimic the contact stresses that are predicted by the wear model. Hence the effect of wear on both nucleation and propagation can be investigated.

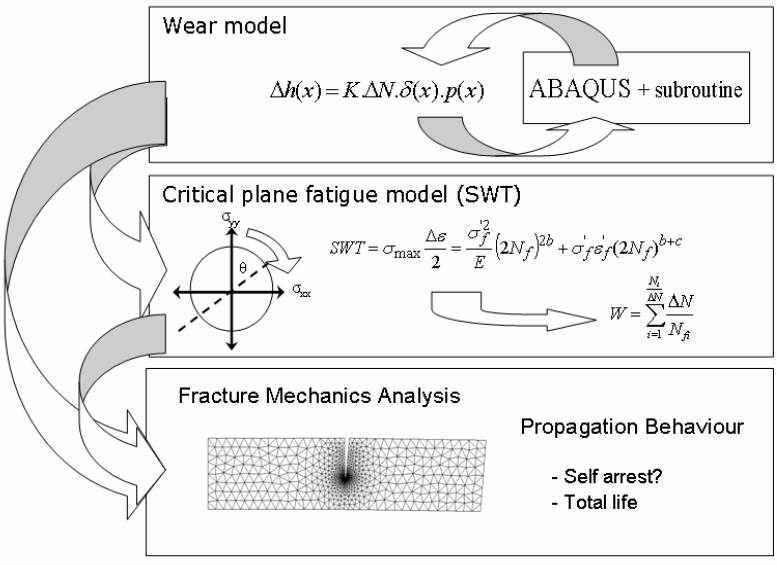

Figure 6.1. Schematic of wear-nucleation-propagation fretting fatigue methodology.

Nucleation life prediction

Direct modelling of the nucleation phase is difficult, although one possible approach is the application of polycrystal plasticity techniques, e.g. Goh et al (2001). However, this approach is computationally very intensive, particularly for application to industrial components and as a design tool. One objective of the present work is to develop a practical design tool for designing complex aeroengine components which experience fretting damage. Therefore nucleation is modelled using the critical-plane implementation of the SWT fatigue damage model and M-P damage accumulation framework adopted in previous chapters. The SWT parameter featured in Equation 3.7 is usually used to predict the total life of a component, i.e. for the crack length to reach a substantial length. This is related to the fact that the constants are defined using test specimens where the crack either causes failure or grows to a length of 1mm. Clearly there is an inconsistency in the use of Equation 3.7 for predicting nucleation of a 10 μm crack when the material parameters are defined based on the formation of a 1mm crack. This is discussed further below, where a method is presented to redress this inconsistency.

6.4 Crack growth

The assumption of small scale yielding is adopted in this method; hence the crack stress field is assumed to be determined primarily by the elastic stresses. The stress intensity factor K is used to characterise the crack tip stress field. There are a number of methods which can be used to assess K. Several methods have received research attention for use with numerical techniques. Two popular methods are investigated below; the contour integral method and the crack displacement correlation method.

A mixed mode cracj growth model is employed here, where stress intensity factors for both the opening mode (K_I) and the sliding mode (K_{II}) are assessed at each point throughout the fretting cycle, furnishing a maximum and minimum value for any given cycle analysed. The effective stress intensity factor range ΔK_{eff} is then found (Chen and Keer, 1991):

$$\Delta K_I = K_{I,\max} - K_{I,\min} \quad (\text{where } K_I \geq 0) \tag{6.2}$$

$$\Delta K_{II} = K_{II,\max} - K_{II,\min} \tag{6.3}$$

$$\Delta K_{eff} = \sqrt{\left(\Delta K_I^2 + \Delta K_{II}^2\right)} \tag{6.4}$$

The well-known Paris law can be used to correlate crack growth rate with stress intensity factor range (Paris & Erdogan, 1963). A range of developments have been suggested for the Paris crack growth law since its original conception to allow more general application. The version used here makes use of modifications which allow better description of near threshold- and short crack growth- behaviour. Cracks are found to self-arrest if the stress intensity factor range is below some critical threshold ΔK_{th}. Short cracks are often found to propagate at rates significantly higher than a long crack with an equivalent SIF. In addition short cracks can propagate at stress intensity factor ranges below the long crack threshold, ΔK_{th}. El Haddad et al. (1979) proposed that the growth of a short crack of length a can be described by analysing the crack as if it were actually of length $(l+l_0)$ so that:

$$\Delta K = Q\Delta\sigma_\infty\sqrt{\pi(l+l_0)} \tag{6.5}$$

where Q is the geometric form factor, $\Delta\sigma^\infty$ is the far field stress and b_0 is a 'fictitious' crack length which is found to correspond with the Kitagawa & Takahashi (1976) 'critical crack size' from threshold fatigue behaviour and is defined as follows:

$$l_0 = \frac{1}{\pi}\left(\frac{\Delta K_{th}}{\sigma_e}\right)^2 \qquad (6.6)$$

A range of different l_0 values between 10-60 μm have been suggested for Ti-6Al-4V at different stress ratios (Wallace & Neu, 2002). In this study the value of l_0 is taken as 20 μm, based on values of 133 MPa $mm^{1/2}$ and 569 MPa for ΔK_{th} and σ_e respectively, from Fadag et al (2007), following the approach used in Nicholas et al (2003). As a finite element formulation is used to determine the stress intensity factor, it is necessary to approximate the El-Haddad stress intensity factor $\Delta K_{eff,EH}$ as a perturbation of the FE determined value $\Delta K_{eff.}$, as follows:

$$\Delta K_{eff,EH} = \Delta K_{eff}\sqrt{\frac{l+l_0}{l}} \qquad (6.7)$$

This approach means that the effective threshold SIF below l_o increases linearly with increasing (short) crack length. The crack growth law used in this study is thus formulated:

$$\frac{dl}{dN} = C\left(\left(\Delta K_{eff}\sqrt{\frac{l+l_0}{l}}\right)^m - K_{th}^m\right) \qquad (6.8)$$

where $\frac{dl}{dN}$ is the cyclic growth rate, C and m are the Paris constants. In a study specifically aimed at comparatively assessing a number of different approaches for modelling short and long crack growth in fretting fatigue, Navarro et al. (2006) concluded that Equation 6.8 gave the best correlation with measured life, compared with a number of alternative crack growth laws for fretting fatigue of Al-7075.

The values of the Paris constants C and m employed here are: $C = 1.25\times10^{-11}$ MPa.$^{-2.59}$mm$^{-0.295}$ and $m = 2.59$ (Araujo & Nowell, 2002). ΔK_{th} is taken as 133 MPa$\sqrt{}$mm (Shkarayev & Mall, 2001).

Under the multiaxial stress state created by fretting loads it is possible for cracks to change direction. A number of different criteria have been suggested in the literature. The approach used here is the Sih (1972) minimum strain energy density function. For two-dimensional problems the strain energy density function S is given by:

$$S = c_{11}K_I^2 + c_{12}K_I K_{II} + c_{22}K_{II}^2 \tag{6.9}$$

where:

$$c_{11} = \frac{1}{16\pi G}(3 - 4\nu - \cos\theta)(1 + \cos\theta) \tag{6.10}$$

$$c_{12} = \frac{1}{8\pi G}\sin\theta.(\cos\theta - 1 + 2\nu) \tag{6.11}$$

$$c_{22} = \frac{1}{16\pi G}(4(1-\nu)(\cos\theta - 1 + 2\nu)(1 - \cos\theta) + (3\cos\theta - 1)(1 + \cos\theta)) \tag{6.12}$$

with θ as the angle between the existing crack propagation direction and the new propagation direction, ν is Poisson's ratio, taken here as 0.32, and G is the shear modulus. θ is selected such that S forms a local minimum. If more than one minimum occurs within the domain $-\pi < \theta < \pi$, the minima chosen is that which gives the maximum absolute value of S (Sih, 1985). The values of K_I and K_{II} employed here in Equation 6.9 are the values observed whilst K_I is at a maximum each cycle. However, it should be noted that under the non-proportional loading conditions, which occur during contact, the maximum values of K_I and K_{II} may occur at different points during the cycle, making propagation direction more difficult to define.

6.5 Finite element modelling

6.5.1 Global-sub model approach

A global-sub model approach is employed to solve the crack propagation problem in the presence of wear-induced geometry modification. Figure 6.2 shows the global model and crack growth sub-model of the fretting fatigue test arrangement, as discussed in more detail in Chapters 3 and 4. The time histories of contact pressure $p(x,t)$ and shear traction $q(x,t)$ are calculated using the global model over N_t fretting cycles, along with crack nucleation data for input to the SWT critical plane calculations. $p(x,t)$ and $q(x,t)$ are then passed to the sub-model and crack growth is simulated over N_t fretting cycles. Figure 6.3 shows a more detailed flowchart of the methodology, which has been automated via a MATLAB program, created to drive the crack growth analysis, in conjunction with ABAQUS. An entirely new model is created for each crack growth increment.

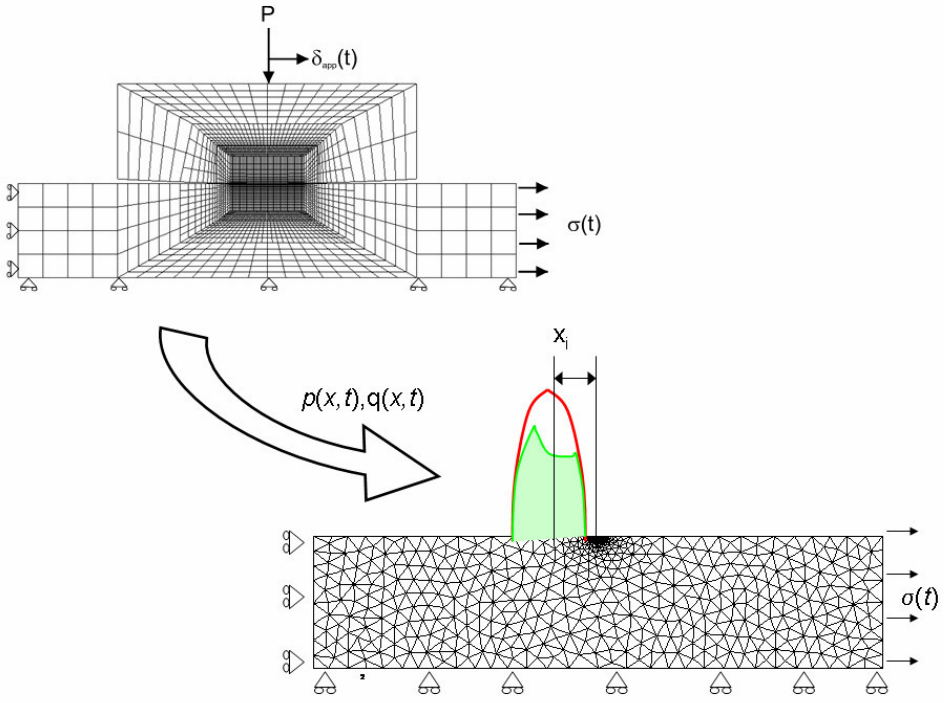

Figure 6.2. Schematic showing transfer of traction data from global wear model to crack submodel.

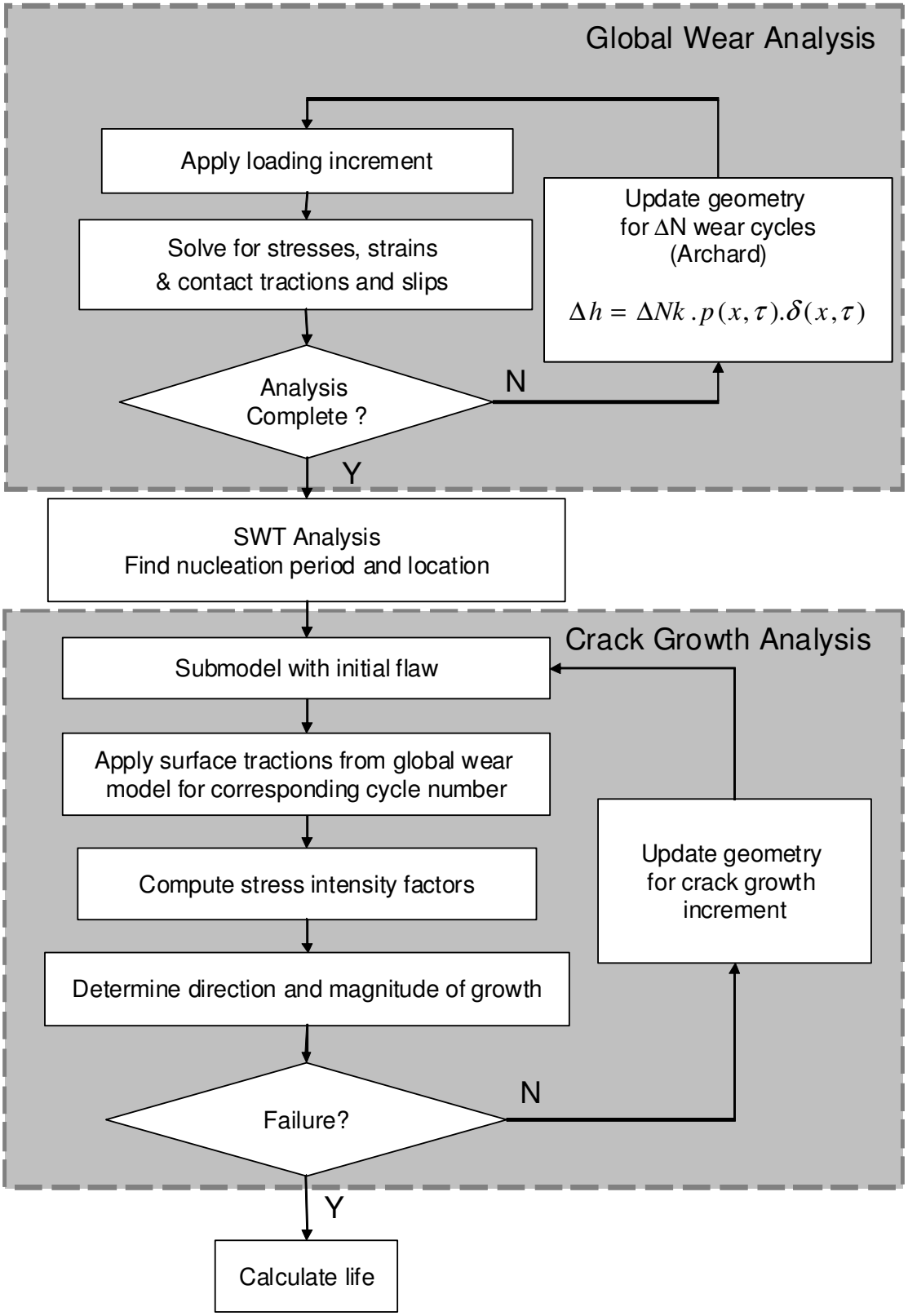

Figure 6.3. Flow chart for computational sequence for submodel analysis.

6.5.2 *Mesh generation*

As suggested in Figure 6.3, a new model is created for each incremental crack growth analysis, whereby the geometry is updated for crack growth, and the traction distributions are modified according to the wear model. The ability to mesh an arbitrary geometry is necessary in order to automate the crack model. Although Shkarayev & Mall (2001) used quadrilateral elements in their crack growth study, triangular elements have been selected for this study as they are more general, offering the ability to mesh any geometry. The meshes are generated using the DistMesh Matlab suite (Persson & Strang, 2004). This is an open source MatLab toolbox for meshing general 2D geometries. The method employs the well known Delaunay algorithm for triangulation. The method has been found to create high quality meshes of complex geometries by using a force-equilibrium method to perturb meshes to achieve low distortion levels. However, this program only creates first order (linear) elements which give unacceptably high stress errors. Modifications to this code where made to allow mid-side nodes to be inserted to create a quadratic triangular mesh, improving stress solution accuracy significantly.

6.5.3 Stress intensity factor determination

Crack displacement correlation method

This method relies on the correlation of displacement of the crack with the stress intensity factors K_I and K_{II} via the following equations. The approach is attractive in FE as the method is based on displacement, the primary variable, so that the level of mesh refinement required is reduced over methods based on stress.

When using FE, it is found that the best correlation is obtained from nodes a short distance away from the crack tip, avoiding errors associated with the singular region. However, the method was found to offer a high degree of scatter when only a small number of elements are present along the crack. When the crack is short, very small elements had to be used to maintain accuracy, resulting in large elements counts to avoid element distortion. These findings are consistent with those of Anderson (1991).

$$K_I = \frac{E}{(4-3\nu)(1+\nu)} \lim_{r\to 0}\left[u_I \sqrt{\frac{2\pi}{r}} \right] \tag{6.15}$$

$$K_{II} = \frac{E}{(4-3\nu)(1+\nu)} \lim_{r\to 0}\left[u_{II} \sqrt{\frac{2\pi}{r}} \right] \tag{6.16}$$

where u_{I} and u_{II} are the displacements in the mode I and mode II directions respectively.

Contour integral method

The contour integral method has become one of the preferred methods for evaluating crack tip parameters such as K in FE. The method takes advantage of the path independent qualities of contour integrals. The method is energy based, and therefore insensitive to mesh refinement.

ABAQUS has developed the contour integral method as a standard function within the code. The principal contour integral evaluated is the J-Integral (Rice, 1968). Conceptually, J is a path independent line integral around the crack tip which defines the energy release rate for both linear and non-linear material response (Figure 6.4).

For 2D plane strain, linear elastic behaviour, as is assumed in this work, J and K are directly related via:

$$J = \frac{K_I^2(1-\nu^2)}{E} + \frac{K_{II}^2(1-\nu^2)}{E} = \int_{\Gamma} \left(wn_i - \sigma_{ij} n_j u_{ij} \right) ds \tag{6.15}$$

Where w is the strain energy density, $\underline{n}$ is the outward unit vector normal to the contour surface Γ, and s is the arc length along the contour, $\underline{u}$ is the displacement vector, and $\underline{\sigma}$ is the traction vector

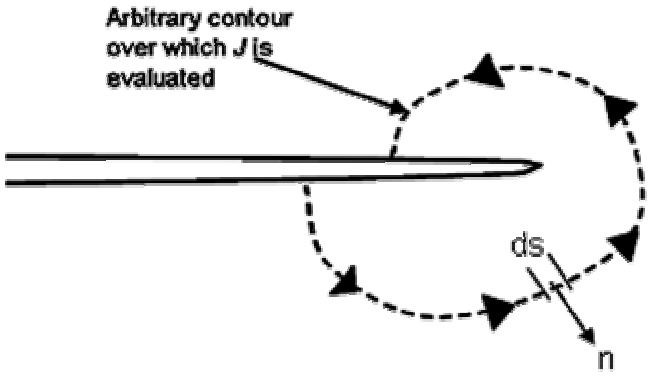

Figure 6.4. J as a path independent contour integral

The ABAQUS code evaluates J around a number of rings of elements around the crack tip. The interaction integral method of Shih & Asaro (1988) is then employed to extract the stress intensity factors K_{I} and K_{II} for further analysis. As will be shown later, this method offers good accuracy when compared to a variety of benchmark solutions and as such is adopted for all fracture mechanics results presented here.

The contour evaluation facility in ABAQUS is only available for quadrilateral elements; to this end, a method has been developed in which a rosette of quadrilateral elements is implanted at the crack tip to enable crack tip parameter evaluation (Figure 6.5). For the rosette elements a quadratic quadrilateral formulation is used. The elements sharing the crack tip node are degenerate; the three nodes along the

element edge at the crack tip are collapsed onto the crack tip and tied to give equal displacement. In addition, a quarter-point node spacing is applied to the mid-side nodes to modify the element shape function. This provides the correct $1/\sqrt{r}$ strain singularity for LEFM (Anderson, 1991). Figures 6.6 and 6.7 show that this approach gives very good agreement with the theoretical and boundary element derived benchmark solutions from the literature, for a range of slanted cracks in SENT specimens under plain fatigue (Rooke & Cartwright, 1976, Anderson, 1991).

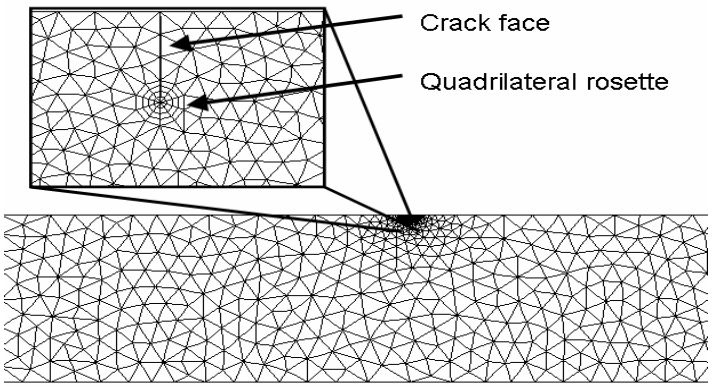

Figure 6.5. An example mesh showing initial 10 μm surface defect and detail of rosette of quadrilateral elements around the crack tip.

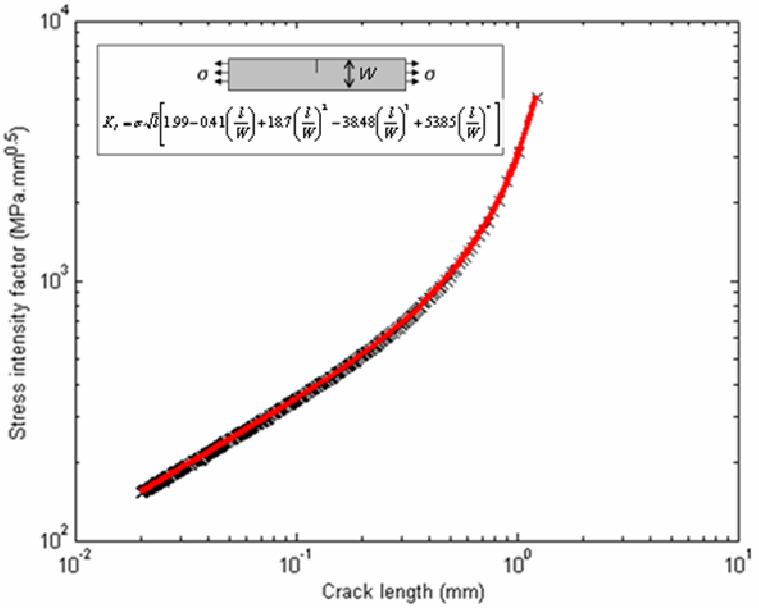

Figure 6.6. Comparison of theoretical (Anderson, 1991) and FE based predictions of crack propagation in SENT specimen for transverse crack (plain fatigue).

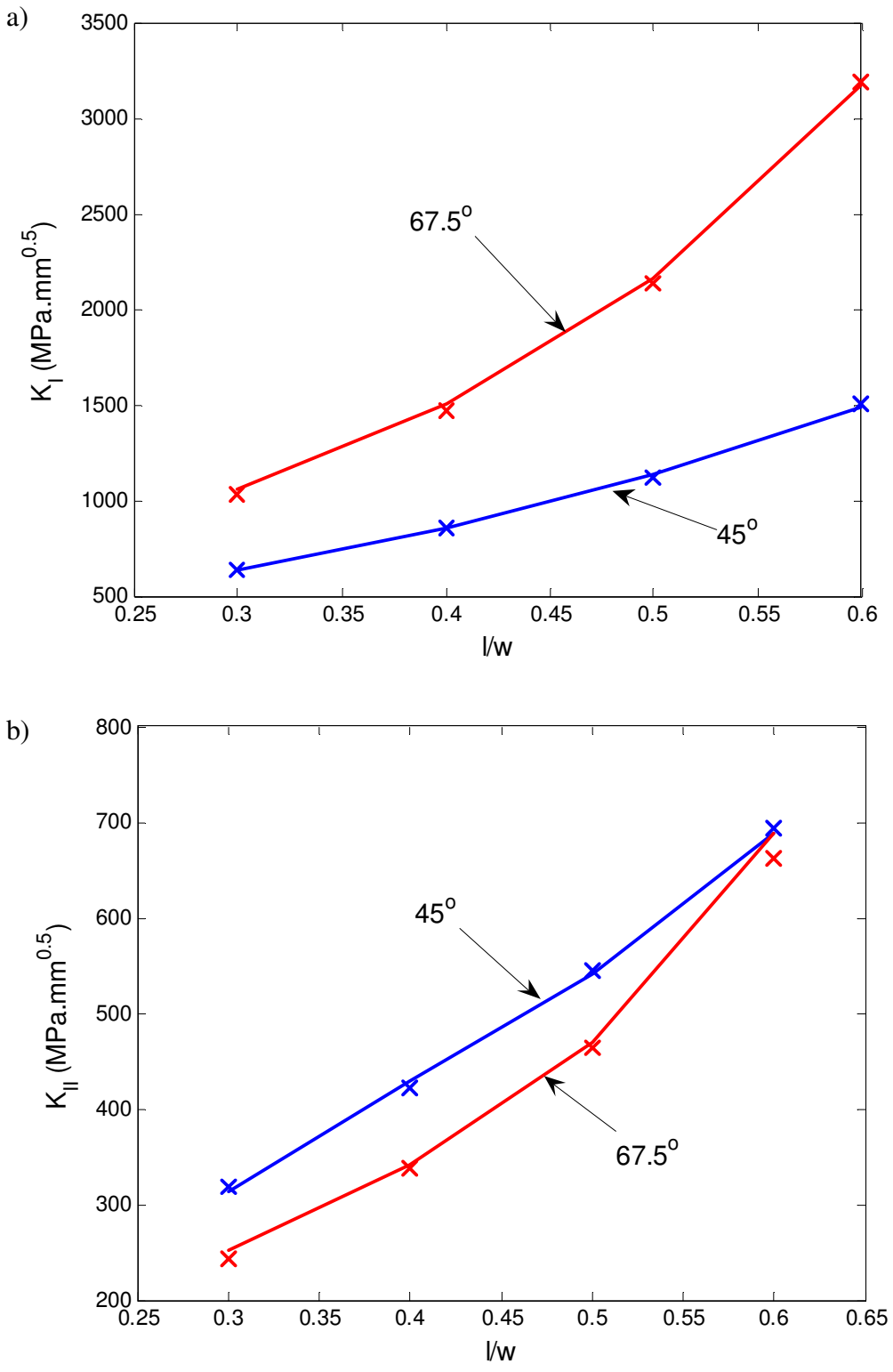

Figure 6.7. Comparison of benchmark solution (Rook and Cartwright 1976) and FE based solutions for SIF for slanted (angle shown is angle of crack to specimen surface) cracks in SENT specimens for:. (a) Mode I and (b) Mode II.
(Note: curves show benchmark solution, crosses show authors' FE data).

6.6 Combining critical plane and LEFM approaches

Table 3.1 shows the Ti-6Al-4V SWT constants available from Dowling (1998), which have been derived from fatigue tests where failure is defined as the occurrence of a 1 mm crack. However, the length scales of damage relevant to crack nucleation in this chapter are significantly shorter than this; specifically, a crack is assumed to have nucleated here (i.e. $\omega = 1$) when it has reached a depth of 10 μm. The element depth at the surface is 16 μm, so that the centroid, where damage is monitored, is at 8 µm depth. This was considered sufficiently close to 10 µm to assume a 10 μm crack. Hence a modified set of fatigue constants is derived corresponding to 10 μm nucleation. The SWT equation is based on the combination of the Basquin high cycle fatigue (HCF) equation, for stress to life relation, and the Coffin-Manson low cycle fatigue (LCF) equation, for plastic strain to life relation, as follows, respectively:

$$\frac{\Delta\sigma}{2} = \sigma_f'\left(2N_f\right)^b \tag{6.16}$$

$$\frac{\Delta\varepsilon_p}{2} = \varepsilon_f'\left(2N_f\right)^c \tag{6.17}$$

with consideration of the peak stress to account for the mean stress effect. Due to the adoption of LEFM it was more consistent to modify only the Basquin constants as they relate to the elastic stress range, whereas the Coffin-Manson equation is concerned with LCF and plastic behaviour.

The approach adopted here is as follows:

1. Establish N_f across the 300 MPa to 500 MPa range of stress amplitudes, corresponding to a 1 mm crack length, using the Basquin constants of Table 6.1.

2. Estimate N_p, the numbers of cycles for a 10 μm crack to grow to 1 mm, for a series of stress levels across the range 300 MPa to 500 MPa, using LEFM with the El-Haddad correction for short crack growth, using the solution for a semi-elliptical surface crack in a round bar under tension from Murakami (1987)

$$K_I = F_I \sigma \sqrt{a} \tag{6.18}$$

where F_I is taken to correspond to the position of maximum SIF along the crack-front.

3. Calculate $N_i = N_f - N_p$ across the same range of stress amplitude levels and hence obtain the new Basquin constants corresponding to a 10 μm crack.

Table 6.1 shows the resulting modified Basquin constants and Figure 6.8 shows the 10 μm nucleation and the 1 mm crack stress-life curves.

Table 6.1. Estimated Basquin constants corresponding to 10 μm crack nucleation in Ti-6Al-4V.

σ_f' (MPa)	b
1817.2	-0.0978

6.7 Contact stress evolution treatment

The impact of wear on fretting fatigue crack growth is studied here through the effect of evolving stresses on propagation. In the cases studied here the crack propagation rate is significantly higher than the wear rate, so that the reduction in length of a crack due to wear is negligible. The stress evolution aspect of wear is investigated by updating the sub-model boundary tractions *p(x,t)* and *q(x,t)* derived from the global

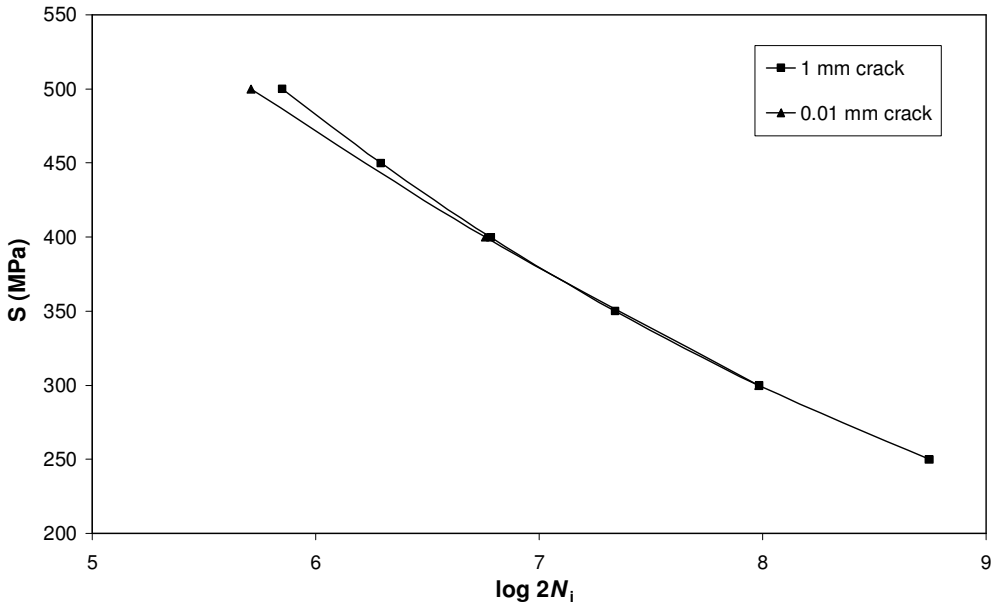

Figure 6.8 Comparison of Basquin stress-life curves corresponding to nucleation of a 10 μm crack and development of 1 mm crack.

model wear analysis. As the same computational constraints exist here as were identified in Chapters 3 and 4, a ΔN of 1500 cycles has been utilised within the wear modelling routine. However the forward prediction method used in the crack propagation simulation requires a much smaller cycle jump size, e.g. 100 cycles. Consequently, a linear interpolation scheme was implemented to determine the pressure and shear traction distributions for the crack growth cycle jumps, which are intermediate to the wear cycle jump $p(x,t)$ and $q(x,t)$ data available from the global wear model. Otherwise, the approach adopted follows that described in Chapter 3.

Chapter 7

Effect of wear on crack growth behaviour

7.1 Introduction

The fracture mechanics based methodology described in Chapter 6 is applied here to the cylinder on flat geometry studied in Chapter 4. The results are compared with the total life results of Chapter 4. In addition the effect of wear on propagation behaviour is studied more generally. The effect of slip regime on crack growth is also studied. Finally, the method is used to investigate the implications of bulk fatigue load on crack arrest behaviour under wear conditions.

7.2 Results

7.2.1 Comparison with test data

Figure 7.1 shows the effect of slip $\delta_{app,m}$ on fretting fatigue life, as obtained from: (i) the present methodology (referred to as 'wear-nucleation-propagation'), which separately predicts nucleation of a 10 μm crack and propagation of that crack to specimen half-depth, including the effects of geometry evolution due to wear, (ii) previous life predictions from Chapter 4 (referred to as 'wear-SWT total life'), which did not distinguish between nucleation and propagation, but did include the effects of geometry removal due to wear and predicted life to a 1 mm crack, (iii) the predicted life to nucleation of a 10 μm crack (referred to as 'wear-nucleation') including the effects of geometry evolutions due to wear and (iv) the measured lives from the work

of Jin & Mall (2004). Note that, as in Chapter 4, a relationship between global and local slip has been assumed, as defined by Equation 4.1, to address the issue of rig compliance. Again, as in Chapter 4, due to two slightly different apparatus being used in Jin & Mall (2004), only those results obtained using a constant normal load are considered here as this matches the boundary condition used in the FE model more closely.

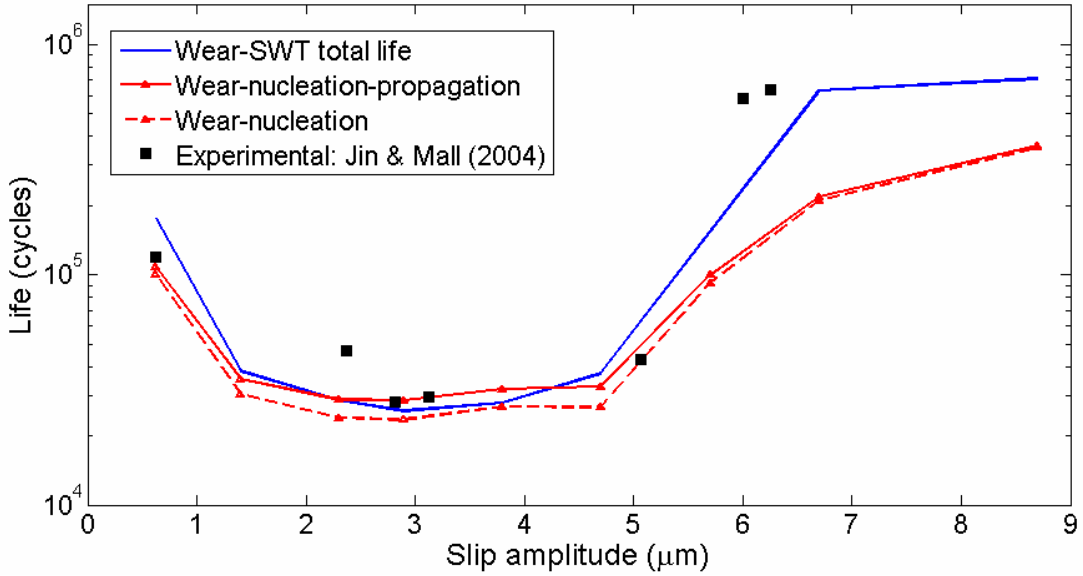

Figure 7.1. Comparison of predicted fretting fatigue life as a function of local slip amplitude, δ, against test data of Jin & Mall (2004), including results of 'wear-nucleation-propagation' method, along with 'wear-nucleation' and 'wear-SWT total life' method reported in Chapter 4.

7.2.2 Effect of nucleation period

The combined nucleation-propagation predictions of Figure 7.1 are predicated on the assumption of an initially perfect material, with no inherent flaws, so that the nucleation life is defined as the number of fatigue cycles from zero (initial) damage to a damage level equivalent to a 10 μm crack. However, real materials will not be perfect but will have initial flaws and weaknesses which can be modelled as initial damage. One of the benefits of the present approach is the ability to separate the nucleation and propagation lives, so that the nucleation life can be varied to simulate

different numbers of cycles to nucleation. As the contact stresses continuously evolve due to material removal effects, the crack propagation life will be affected by the assumed (or calculated) nucleation life. Therefore the effect on subsequent fretting fatigue crack propagation of varying N_i is investigated here; this can be thought of as considering different degrees of inherent damage, so that for $N_i = 0$, for example, the material is assumed to already have a 10 μm crack present, whereas for $N_i = 10000$, the assumption is that the 10 μm crack has occurred after 10000 cycles, viz. the nucleation response of the material has been varied accordingly, or alternatively, inherent damage in the material is assumed so that the additional number of cycles required for a 10 μm crack is $N_i = 10000$. Thus, for $N_i = 0$, the crack is assumed to have nucleated immediately and initially grows under the influence of the unworn surface tractions, whereas if $N_i = 10000$, the initial flaw grows in a worn contact stress field relating to the 10000th cycle.

Two δ values have been studied, one corresponding to an interfacial slip δ of 8.7 μm and another corresponding to $\delta = 2.9$ μm. The FE-predicted contact slip distributions corresponding to both of these cases are shown in Figure 4.15, where it is clear that the $\delta = 2.9$ μm case gives rise to a central stick region from about x = -0.027 mm to about x = 0.1 mm, with non-zero slip elsewhere reaching a maximum value of about 2.9 μm at one contact edge (x is distance from the centre of contact). In contrast, the $\delta = 8.7$ μm case gave no stick region, but still gave a significantly non-uniform distribution of contact slip, again reaching a maximum value of about 8.7 μm at one contact edge. Both cases have the same normal load as studied in Chapter 4, giving an initial contact semi-width, $a_0 = 440\mu$m

Figure 7.2 shows the predicted effect of varying N_i on the subsequent crack propagation under gross sliding conditions with the initiation site x_i at the edge of contact (x_i/a_0=1.02). If nucleation is assumed to occur instantly the propagation period is 4300 cycles whereas if nucleation is judged to have occurred at 1×10^5 cycles, the propagation period is 7600 cycles. This is longer than that found in the plain fatigue case of the same bulk stress load. Figure 7.3 shows that towards the final stage of propagation, the presence of the contact slows growth appreciably compared to the plain fatigue case. This is attributed to the widening of the contact width with wear, such that the crack is eventually under the contact and experiencing compressive stresses over an increasing portion of the loading cycle. It is important to note that the propagation period is small in comparison with the total life (~1%). This indicates that in this case, the nucleation period is the more important consideration in terms of fretting fatigue life prediction.

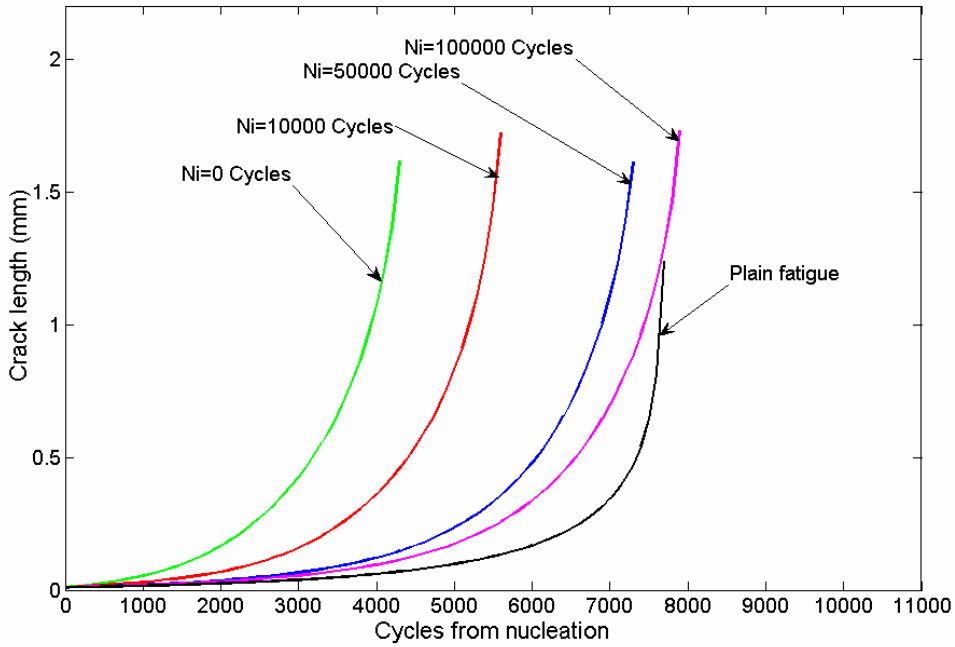

Figure 7.2. Predicted effect of nucleation time on the gross sliding propagation behaviour (x_i/a_0 = 1.02).

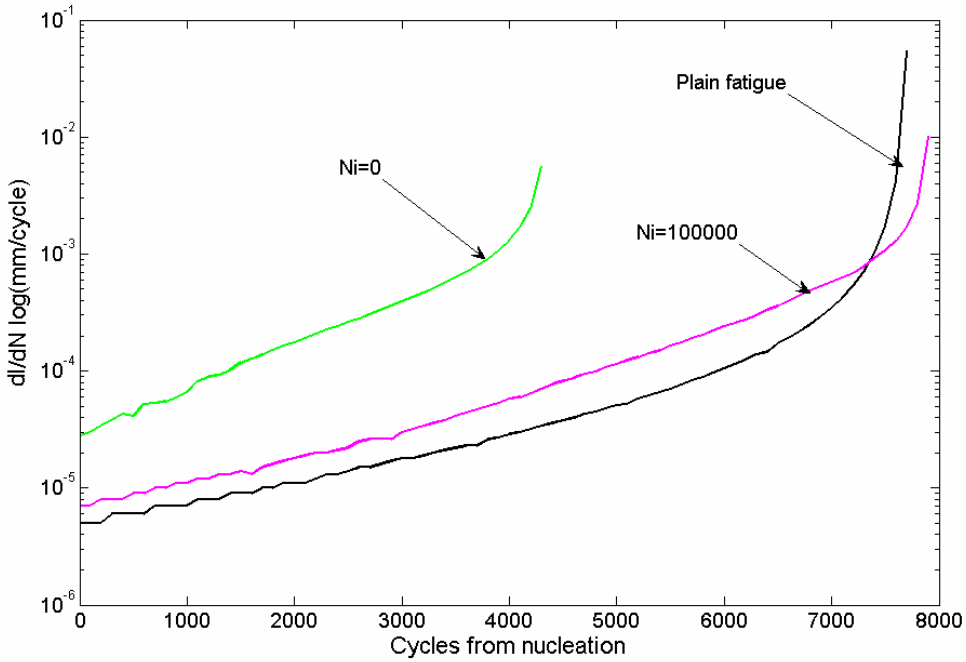

Figure 7.3. Comparison of predicted gross sliding crack propagation rates with different nucleation periods (x_i/a_0 = 1.02) against plain fatigue growth prediction.

Figure 7.4 shows the predicted effect of N_i for the partial slip case, for two different assumed nucleation locations, namely the stick-slip interface (x_i/a_0=0.57) and the edge of contact (x_i/a_0=1.02), while Figure 7.5 shows the relationship between propagation life, N_p, and initiation location x_i for different assumed N_i values for the partial slip case. If the nucleation period is assumed to be negligible, i.e. N_i=0, the propagation life is observed to be a relatively strong function of the nucleation location, with the edge of contact found to provide the most rapid propagation. However, as wear damage is allowed to advance by increasing the assumed nucleation period, the propagation life is found to become a much weaker function of nucleation location, i.e. propagation in the slip region has been accelerated significantly by wear, specifically the development of the stick-slip interface pressure peak. Conversely the effect of wear at the edge of contact is to retard propagation slightly, which is also consistent with the reducing pressure at the initial contact edge. Under partial slip

conditions wear creates a wider region over which cracking could be expected, which helps to explain why cracking is often observed at multiple points along the slip region in tests.

a)

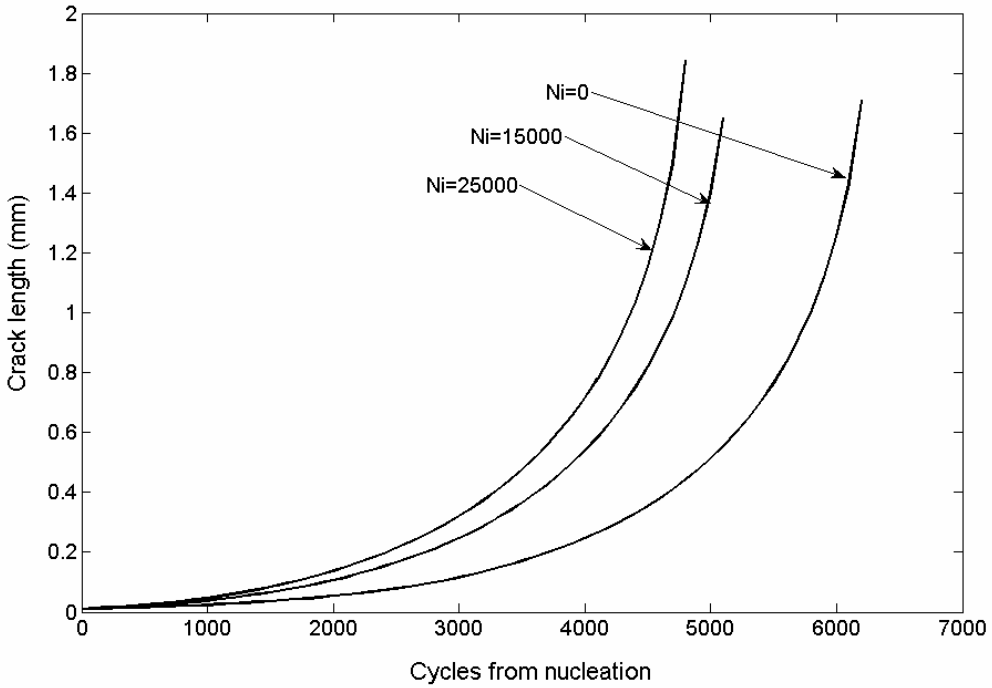

b)

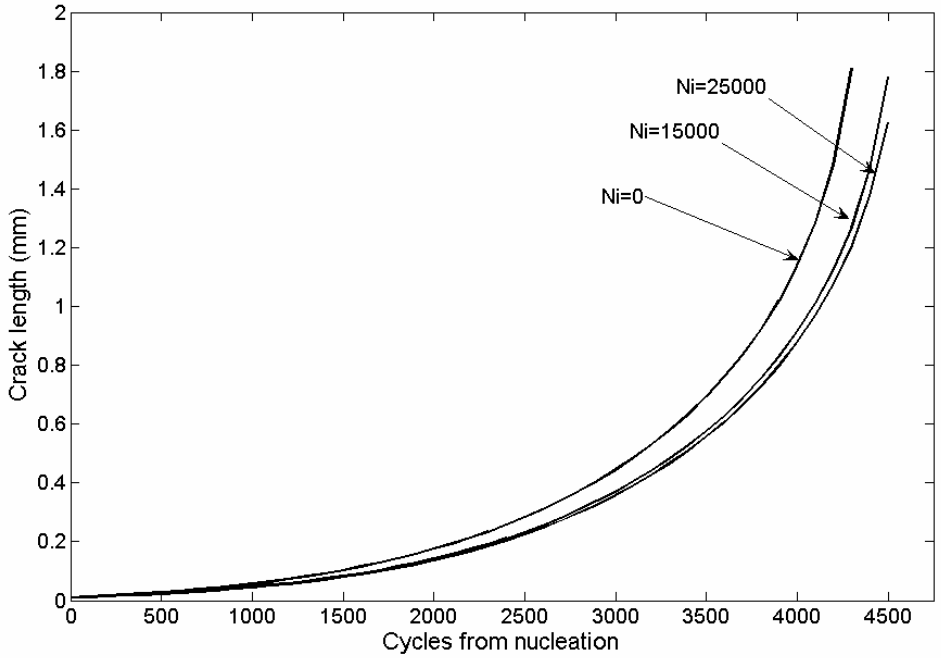

Figure 7.4. The predicted effect of varying the nucleation period upon partial slip propagation behaviour for two different cracking locations:
a) x_i/a_0=0.57 (stick slip boundary),b) x_i/a_0=1.02 (contact edge).

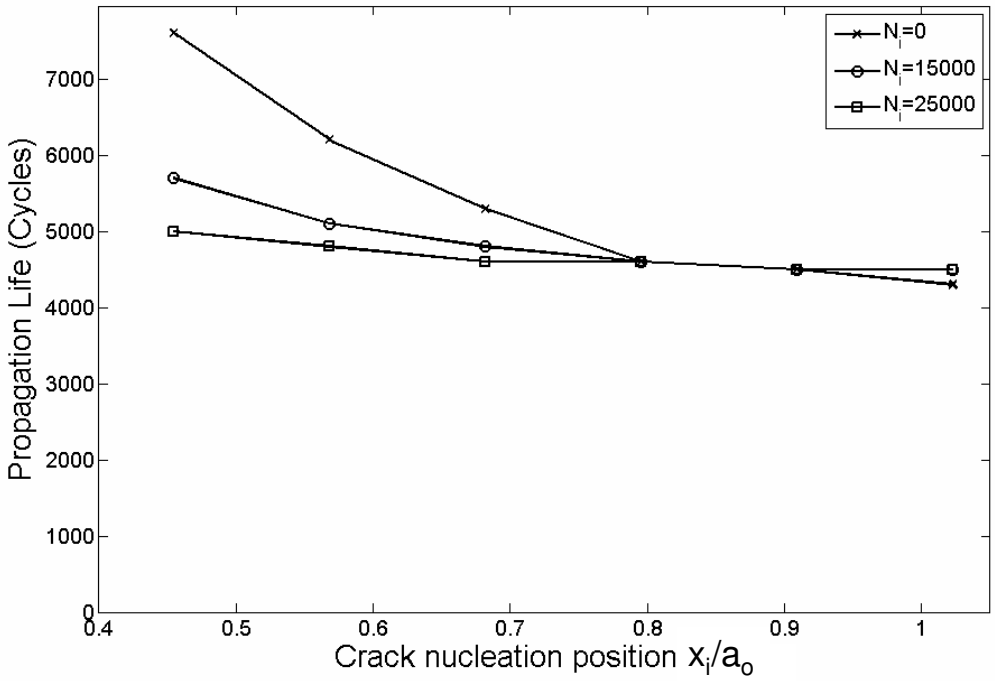

Figure 7.5. Partial slip predicted crack propagation life as a function of crack nucleation position.

7.2.3 Effect of bulk stress: crack arrest

In the experimental work of Jin & Mall (2004) a relatively high bulk fatigue load of 550 MPa is used. The results presented here suggest that under these high stress conditions the majority of the fatigue life is spent in the initiation phase. The phenomenon of crack arrest arises when the stress intensity at the crack tip drops below the threshold value for growth (Eq. 6.8). This can occur either due to the crack having grown into a lower stress region or due to the stresses on the crack tip reducing due to stress redistribution. The sub-modelling approach adopted for the crack propagation analysis obtains the evolving contact tractions from the global model, which explicitly models the geometry removal due to wear. It is therefore possible to decouple the evolving contact tractions $p(x,t)$ and $q(x,t)$ from the bulk fatigue stress $\sigma(t)$, to explore the effect of varying the bulk stress under a given surface traction evolution.

In order to investigate this effect and thereby illustrate some key fretting fatigue phenomena, a wear-induced contact stress evolution associated with a 550 MPa peak bulk fatigue load, is employed with two slip amplitudes; $\delta_{app,m} = 8.7$ μm (gross sliding) and $\delta_{app,m} = 4.2$ μm (partial slip). Each case is studied with a varying bulk fatigue stress applied to the sub-model crack propagation analysis. The propagation behaviour is then investigated using 'with wear' and 'without wear' analyses. The 'without wear' analyses use the unworn pressure distribution, whereas the 'with wear' analyses use the evolving surface tractions, as predicted by the global model. For each case the crack is placed at the point of maximum damage as predicted by the nucleation model. For the gross sliding case this is at the edge of contact and for the partial slip case it is at the edge of contact for the 'without wear' analyses and at the stick-slip interface ($x_i/a_0 = 0.121$) for the 'with wear' analyses.

Table 7.1 summarises the results of the gross sliding cases. Generally wear has the predicted effect of slowing crack growth compared to when wear is neglected; this is demonstrated at the 200 MPa fatigue load. However, if the fatigue load (σ_b) is dropped to 100 MPa, the role of wear becomes critical in failure prediction; Figure 7.6 shows the predicted crack growth curves for the 'with wear' and 'without wear' assumptions. The 'without wear' assumption predicts that the crack propagates to failure, whereas the 'with wear' assumption causes sufficient attenuation of stresses that the crack is predicted to arrest at a length of 26 μm after 1.3×10^4 cycles, having grown out of the most highly stressed region, local to the contact surface. If σ_b is reduced to zero it is found that both assumptions lead to predictions of no crack growth.

Table 7.1. Effect of bulk stress on gross sliding case results.

Bulk stress level (MPa)		final length (mm)	comments
0	with wear	0.01	no growth
	no wear	0.01	no growth
100	with wear	0.026	arrested 13 000 cycles
	no wear	1.8 (failed)	failed 115 000 cycles
200	with wear	1.8 (failed)	failed 40 000 cycles
	no wear	1.8 (failed)	failed 35 000 cycles

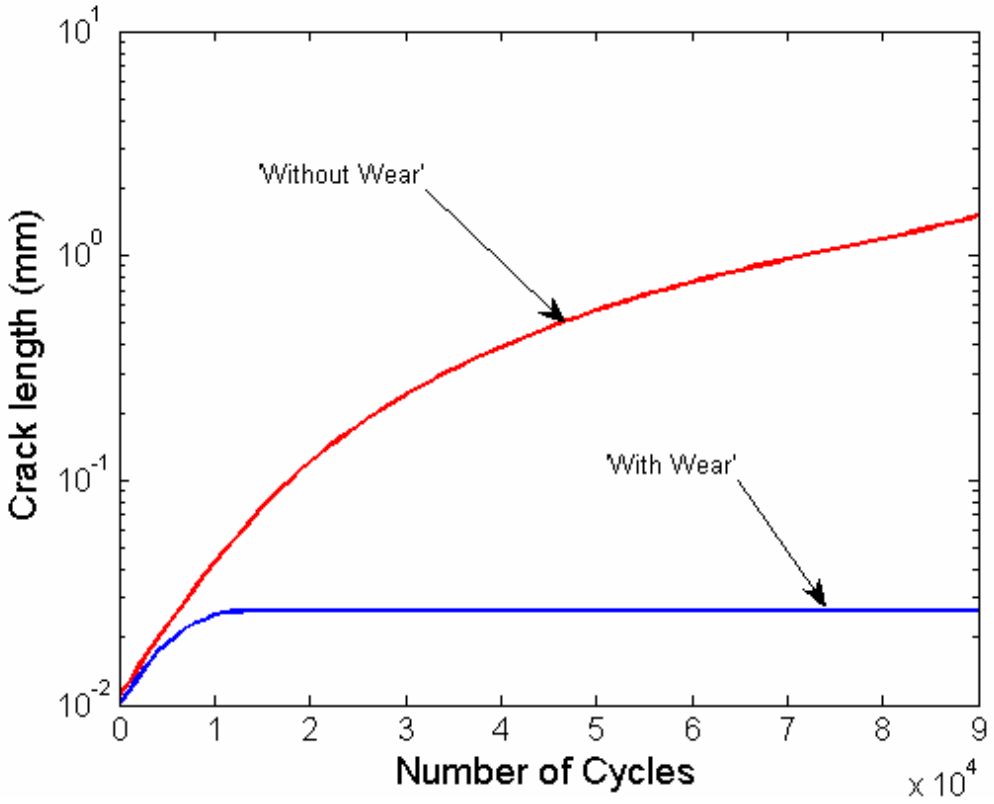

Figure 7.6. Comparing 'with wear' and 'without wear' predictions of crack length versus number of cycles for gross sliding case with $\delta_{app,m} = 8.7$ μm and $\sigma_b = 100$ MPa.

Table 7.2 shows the results of the partial slip cases. In the 0 MPa case, neither the 'with wear' nor 'without wear' analyses predict failure. However, Figure 7.7 shows that the 'with wear' analysis predicts that the crack is initially dormant, until about 4×10^4 cycles, at which point the contact stresses have evolved to a condition which is favourable for crack growth, after which the crack grows to a length of about 0.8 mm,

at which point it arrests, due to it having grown out of the fretting fatigue contact stress field. When the bulk stress is increased to 50 MPa, the 'no wear' analysis predicts no growth, i.e. infinite life. However, as shown in Figure 7.8, the 'with wear' analysis predicts that although crack growth is relatively slow, the pressure peak which develops at the stick-slip interface is enough to drive the crack through to failure. At the higher stress level of 100 MPa, both analyses predict failure; after 1.51×10^5 cycles for the 'without wear' model, and after 1.06×10^5 cycles for the 'with wear' model.

Table 7.2. Effect of bulk stress on partial slip case results.

Bulk stress level (MPa)	Analysis Type	final length (mm)	comments
0	with wear	0.8	reactivated 30 000 cycles, arrested 400 000 cycles
	no wear	0.01	no growth
50	with wear	1.8 (failed)	Reactivated 30 000 cycles, failed 364 000 cycles
	no wear	0.01	no growth
100	with wear	1.8 (failed)	failed 151 000 cycles
	no wear	1.8 (failed)	failed 106 000 cycles

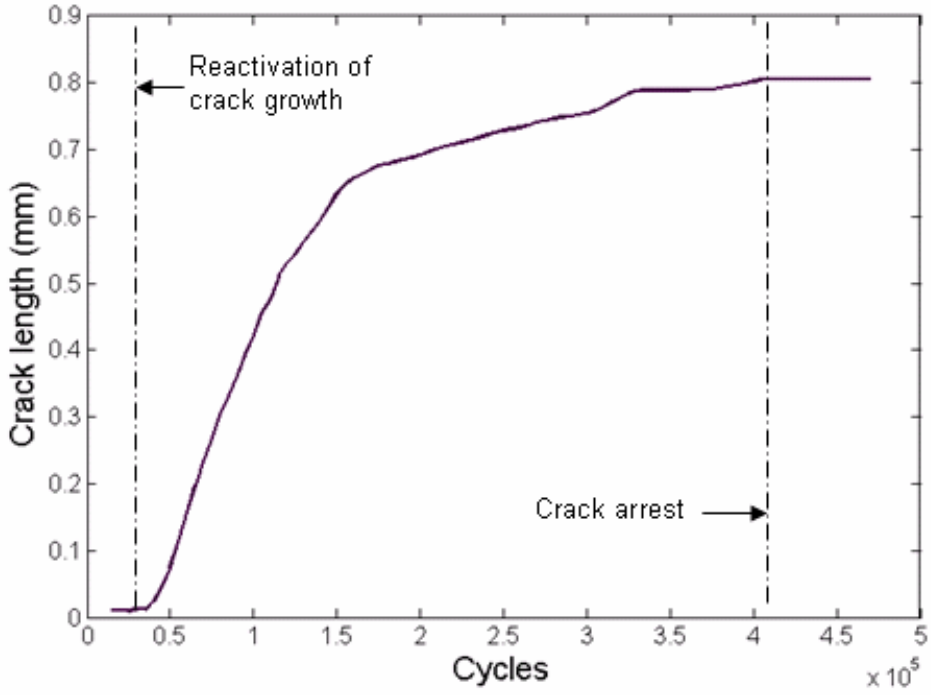

Figure 7.7. 'With wear' predicted crack growth curve for $\delta_{app,m} = 4.2$ μm, partial slip case with $\sigma_b = 0$ MPa.

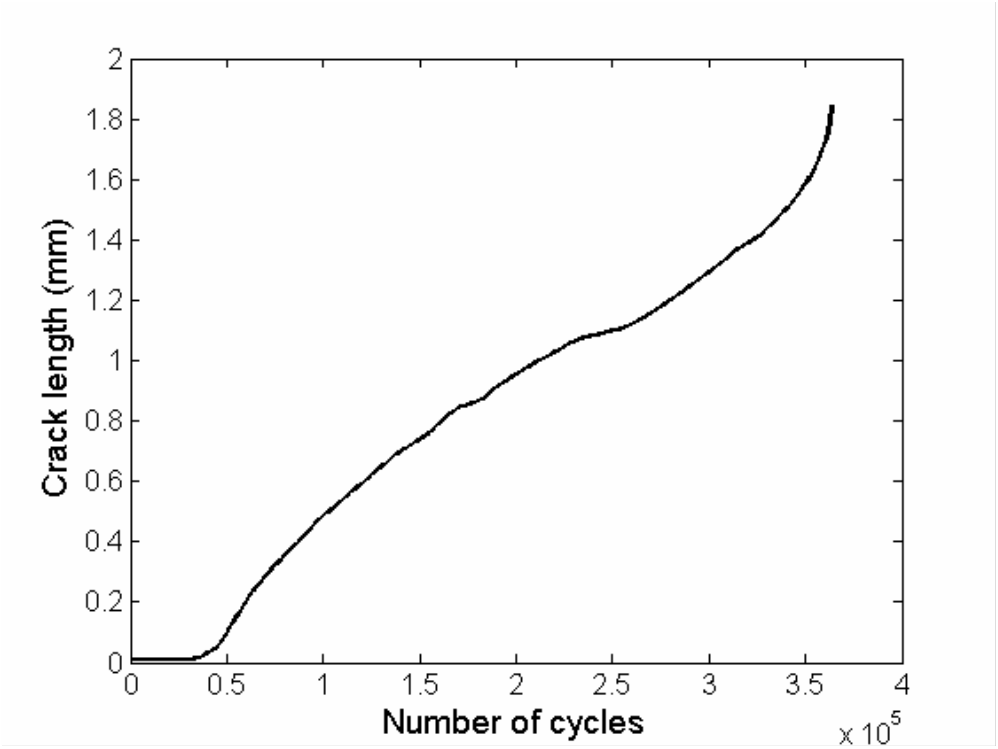

Figure 7.8. 'With wear' predicted crack growth curve for $\delta_{app,m} = 4.2$ μm partial slip case with $\sigma_b = 50$ MPa.

7.3 Discussion

In the experimental cases modelled, the predicted propagation lives are short when compared to the total expected life, and they are similar for both gross sliding and partial slip, even though the stress gradients are significantly steeper and the peak stresses are higher for the worn partial slip cases. In the gross sliding cases the propagation life is typically only around 1-2% of the fatigue life. The rapid propagation of fatigue cracks under this loading regime is consistent with the plain fatigue results: simple 2D theoretical predictions of crack propagation life show that reducing the fatigue load from 550 MPa to 250 MPa would increase life from 7500 to 80000 cycles for a similar single-edge notched tension (SENT) geometry. In contrast, for the partial slip cases and the low life, low slip gross sliding cases, the predicted propagation life forms a greater proportion of the total life, e.g. up to about 20% for a slip of about 3.5 μm. Recent work on crack growth prediction in Ti-6Al-4V for

fretting fatigue by Fadag et al (2007), without considering the effects of wear, has analysed the proportion of crack propagation as a function of load and assumed initial crack length, for both flat and cylindrical fretting pad geometries. It was shown that, for the intermediate and high cycle regimes (with N_f greater than about 10^5 cycles), predicted propagation life formed only a small part of total life (less than 10%). This was reported to be in agreement with experimental observations from Lykins et al (2001) where the initiation and propagation proportions were estimated from post-mortem microscopic observations of striations. Clearly, these latter results are consistent with the predicted propagation proportions of Figure 7.1.

Figure 7.1 shows that the wear-nucleation-propagation methodology predicts the same general trend with respect to slip amplitude as the wear-SWT total life results of Chapter 4, and the experimental data; specifically, a critical range of slip amplitudes is predicted corresponding to the partial slip regime, which results in short fatigue lives. However, some differences are apparent between the results of the present methodology and those of the wear-SWT total life approach. In the partial slip region, the wear-nucleation-propagation method predicts longer life, and hence is more accurate, than the wear-SWT total life method, whereas in the gross sliding region, the converse is true.

Figures 7.2 and 7.4 indicate that the propagation period is less sensitive to slip amplitude than the initiation period. Figure 7.1 ('wear-nucleation' curve) shows that initiation life can vary by an order of magnitude with slip amplitude, whereas the maximum variation in propagation life is only around a factor of 2.0. In the partial slip regime the reduction in initiation life through the adoption of short scale constants is more than offset by the associated propagation life, so that the wear-nucleation-propagation methodology predicts longer life than the wear-SWT total life approach.

In the gross sliding regime, the propagation life is small with respect to the reduction in nucleation life caused by the use of short scale fatigue parameters. Hence, under gross sliding conditions, the wear-nucleation-propagation methodology results in a smaller predicted life than the wear-SWT total life approach. One plausible explanation is that the 10 μm nucleation life is under-predicted, e.g. due to the simplifying assumptions made in Section 6.6, and this, compounded with the sensitivity of predicted nucleation life to slip amplitude, results in the differences observed in Figure 7.1.

It is also worth pointing out a number of other related issues, as follows:

- The Coffin-Manson terms have not been modified in the process of identifying the 'short-scale' SWT constants. The 10 μm nucleation life may thus be underestimated, since the high cycle fatigue crack propagation behaviour is thus assumed to apply across the full range of stress levels.

- Crack closure and mean stress effects are not included in the crack propagation model; this will also contribute to differences between the wear-SWT total life and the wear-nucleation-propagation life.

- The sub-model (crack propagation) analyses of this thesis, do not explicitly model the change of geometry associated with wear, but only the associated (global model) predicted surface traction evolution. Consequently, the predicted (sub-model) surface stress evolution with fretting cycles will be slightly in error.

- The use of a symmetry assumption means that it is assumed that there are two cracks growing at the same time from both sides of the specimen. This is not unreasonable when the cracks are short, since multiple crack initiation sites are typical of fretting experiments, but as the cracks become longer, e.g. within linear

elastic fracture mechanics regime, this assumption may become less realistic, since typically only one dominant crack grows to failure. However, comparison of SENT and double-edge notched tension (DENT) SIF expressions suggests that for short cracks, $l/W < 0.05$, the symmetry assumption will lead to a slightly over-estimated (about 2%) SIF, which will in turn lead to a slightly underestimated propagation life (by about 3%).

In summary, the wear-total life approach gives better correlation with the test data for the higher slip amplitudes (gross sliding) whereas the wear-nucleation-propagation approach gives better correlation for the lower slip amplitudes (partial slip). There are several works in the literature where reasonable life predictions have been achieved considering only the propagation period, i.e. neglecting the nucleation period completely (e.g. Navarro et al, 2006). However, the present work shows that the adoption of a propagation-only prediction model can lead to significant inaccuracies. The balance between nucleation and propagation periods is dependent not only on the prevailing loading conditions, but also on the way in which the local stresses evolve with time.

The bulk stress study shows how critical it is to consider the wear and propagation aspects of fretting modelling. Under gross sliding, it is found that the attenuation of stresses due to wear can result in crack arrest whereas the 'without wear' analysis would not predict the beneficial self arrest condition: the attenuation of stresses due to wear is sufficient to stop the crack at a short length. Figure 7.9 shows that initially the crack tip has sufficient stress intensity to drive propagation, but the reduction in contact pressure due to the gross sliding condition causes the crack to arrest.

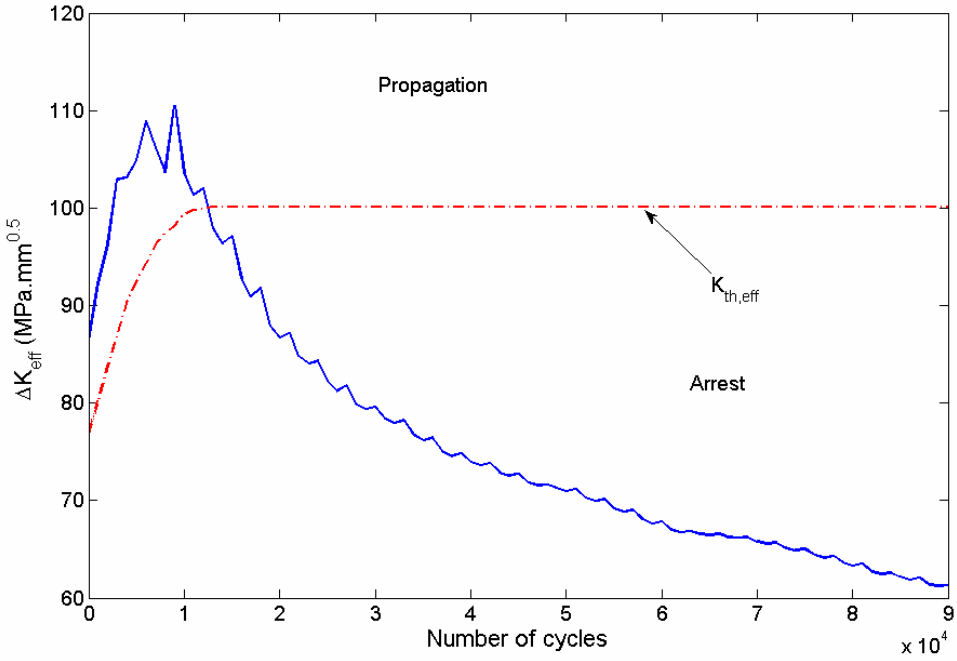

Figure 7.9. Comparison of 'with wear' predicted ΔK_{eff} history with threshold envelope, for $\delta_{\text{app,m}}$ = 8.7 μm gross sliding with σ_{b} = 100 MPa.

The threshold envelope $\Delta K_{\text{th,eff}}$ depicted is bounded by the line:

$$K_{th,eff} = K_{th}\sqrt{\frac{l}{l+l_0}} \tag{7.1}$$

This shows the value of ΔK_{eff} at which crack growth will occur at the current crack length, demonstrating a reduction in the threshold value at short crack lengths.

The partial slip cases of Table 7.2 highlight that it would be incorrect to assume that neglecting wear just results in more conservative estimates for life when compared to an equivalent 'no-wear' analysis.

The predicted effects of wear are complex. Depending on the slip distribution across the surface, and the substrate stress, not only is accelerated or retarded failure predicted, but different predictions with respect to finite or infinite life are obtained. Figure 7.10 shows the qualitative occurrence of these wear-induced phenomena in terms of δ and σ_{b} on a fretting map.

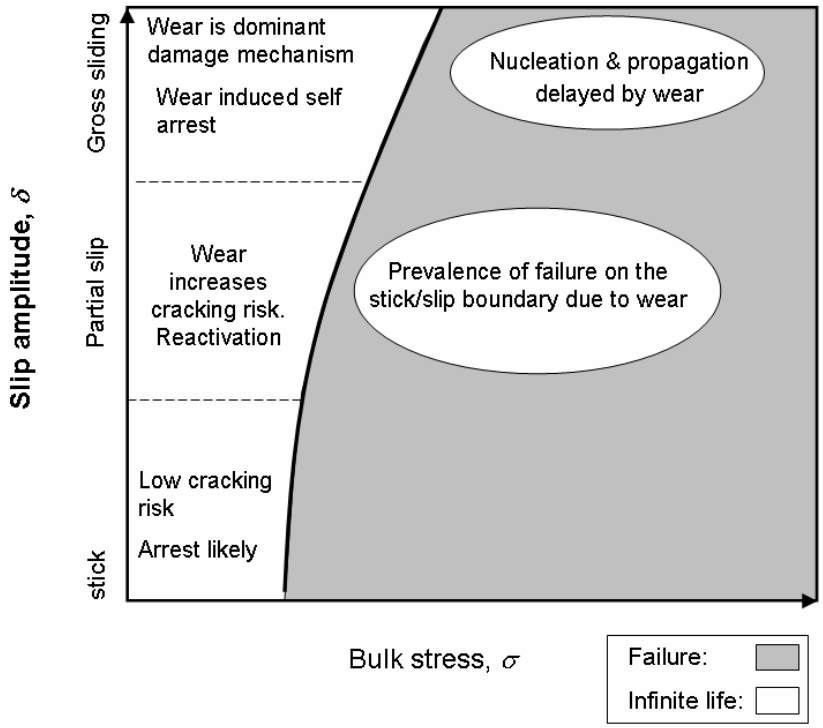

Figure 7.10. Fretting map indicating the various wear induced phenomena and their relation to slip and bulk stress level.

7.4 Conclusions

The wear-nucleation-propagation model presented here is the first attempt, to the author's knowledge, to address the interaction between crack growth and wear effects in a finite element context. The chapter has presented a study of the effects of wear on fretting fatigue crack propagation (and nucleation). The results show that the propagation of fretting fatigue cracks can be strongly affected by changes in the contact stress distributions which can be caused by wear. The conclusions are as follows:

- It is shown that the model captures the key effect of a minimum predicted fretting fatigue life with respect to a certain range of slip (or displacement) amplitude. This phenomenon has not been captured by other methodologies, excluding the work shown in previous chapters. Furthermore, the inclusion of

crack propagation effects with the wear-nucleation approach leads to improved life prediction accuracy in the critical range of slip (minimum life), where the propagation life is predicted to form up to 20% of total life.

- The evolution of contact stress under partial slip conditions increases the rate of propagation of cracks in the slip zone to levels similar to those at the edge of contact, thus reproducing the experimentally-observed phenomenon of cracking within the slip zone, as well as at the contact edge. This is in contrast with models that neglect wear, which predict the highest propagation rates at the edge of contact.

- For the loading conditions considered, the study of propagation in isolation does not give an accurate indication of total fatigue life. It is shown that nucleation can be a significant, even dominant, component of total life.

- A method has been suggested for deriving a set of short-scale (nucleation) SWT fatigue constants, by combining fracture mechanics with traditional long-scale SWT constants, to allow a more meaningful application of multiaxial fatigue damage models to problems involving high stress gradients, as found in contact fatigue.

- It is shown that different loading combinations of the same initial geometry can produce markedly different relative contributions of propagation and nucleation to total life. However, the notion that the distinction between nucleation and propagation aspects of life can be neglected has merit under certain conditions.

- The complex interaction between wear and fatigue has been highlighted by analyses using lower bulk fatigue loads:

- The wear resulting from gross sliding can cause self arrest in a case in which a 'without wear' analysis would predict crack propagation and component failure
- Partial slip can result in a dormant crack propagating from the stick-slip boundary to cause failure. Critically, similar loading conditions used in a 'without wear' analysis predicted that the crack tip loading remains below the threshold SIF, indicating infinite life.

Chapter 8

Fretting analysis of a tapered rotor joint

8.1 Overview

The methods developed in this thesis have been developed as practical engineering analysis tools for future application in real fretting problems. In this chapter the method is used to analyse and predict the fretting performance of a novel type of rotor joint.

8.2 Torque couplings

8.2.1 Taper couplings

Tapers are often used to provide location in engineering structures. Dovetail and fir tree roots are used in turbine/disc assemblies in gas turbine engines. Many applications use the mechanical advantage of the wedge action to induce a force in one direction due to the application of a force in an orthogonal direction.

The taper coupling has been employed for decades in the machine tool industry, most notably as the 'Morse taper' (Figure 8.1) for machine tool chuck location, where there is a need to accurately locate two parts concentrically whilst allowing transmission of torque, and demounting. These same requirements apply to a number of couplings within gas turbines, additionally the joint must provide a high level of repeatability to ensure balancing requirements are met.

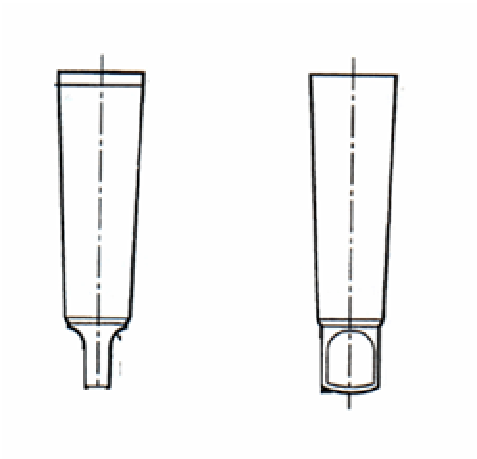

Figure 8.1. The Morse taper, an example of a taper joint used to transmit torque

Currently these roles are often fulfilled by curvic couplings, which have splined faces across which torque is transmitted. Whilst curvic couplings fulfil the performance requirements mentioned above, they are costly to manufacture and present a number of maintenance issues. A novel design of taper coupling has been conceived which, in principal, is capable of replacing some curvic coupling applications. However, as a highly loaded contact the taper coupling may be prone to fretting. This chapter shows an example application of the previously developed fretting wear analysis which was used in the early appraisal of the joint design concept.

8.2.2 Conic Coupling

Figure 8.2 shows the design concept of the novel conic coupling. Whereas the curvic joint that it is intended to replace relies on normal contact pressure to transmit torque directly, the conic joint generates its torque capacity by the wedge effect of two concentric cones which in turn can generate a shear traction for torque transmission

As there is no positive drive location, and torque capacity is related to the diameter of the friction surfaces, the conic coupling is suited to relatively low torque applications

requiring relatively large diameter couplings, such as those found in the high pressure rotor parts of gas turbines.

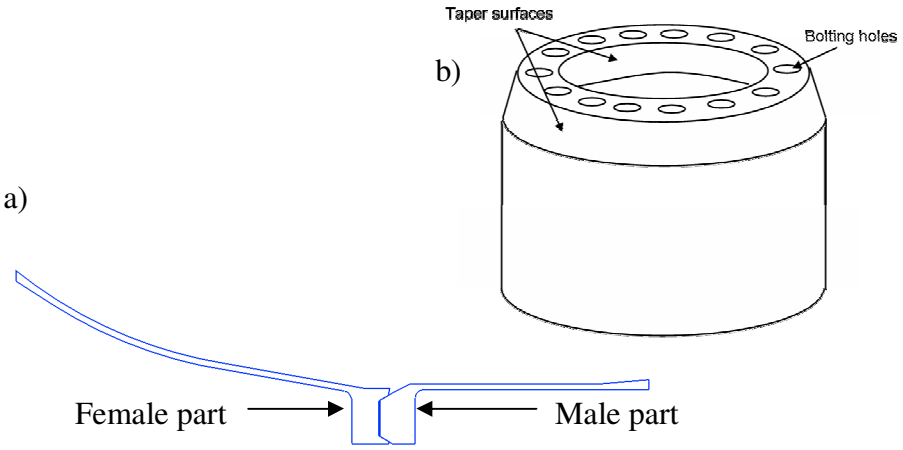

Figure 8.2. a) Simplified cross section of conic joint
b) Basic geometry of male conic coupling

8.3 Model description

As a separate part of this investigation a 3D sector model was created by a third party (Figure 8.3). This model was used to investigate bolting behaviour and torque carrying capability of the conic coupling. However, due to the computationally intensive nature of the wear modelling approach developed in this thesis, it was not feasible to model fretting wear behaviour of the joint in 3D.

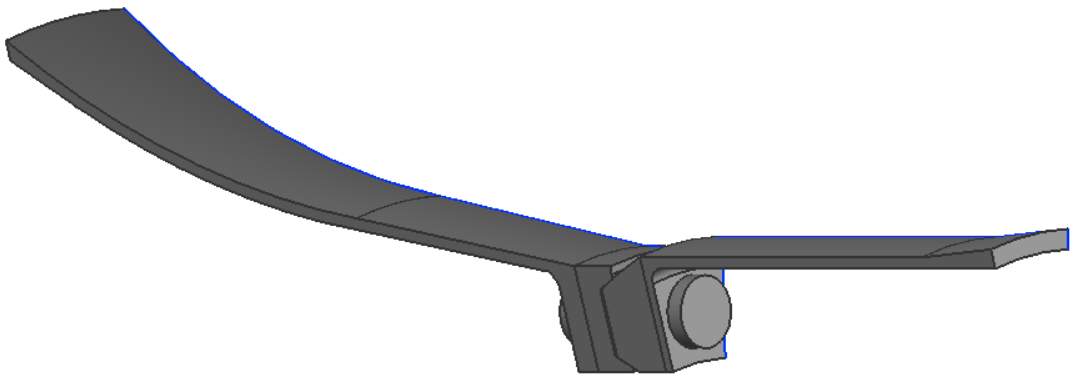

Figure 8.3 Third Party 3D sector model

In order to simplify the model It was necessary to reduce the problem size both in terms of element dimensionality and load case complexity.

2D axisymmetric elements allow 2D representations of axisymmetric structures, subjected to axisymmetric loads, such as torque and axial load. Fourier elements offer the ability to model non-axisymmetric loads such as bending. However, non linearity such as contact is not compatible with the Fourier element formulation. Studies by Leen et al (2002) have shown that a principal cause of fretting fatigue failure in spline couplings is the presence of rotating bending moments such as those caused by gyroscopic manoeuvre loads. Here, the assumption is made that bending loads are the prime cause of fretting and only these loads are modelled.

In order to model the effect of bending on the contact performance of the joint an approximation to the bending load was devised. A plane strain formulation is used in conjunction with the assumption that the bending load is reacted purely as a variation in the load forcing the coupling together. In addition a symmetry plane was enforced along the bolt centreline, as such it was necessary to model only one quarter of a cross section of the joint. This allowed a model with an acceptable number of elements to be created, whilst maintaining a fine mesh in the regions where a stress concentration was expected at the edge of contact (Figure 8.4).

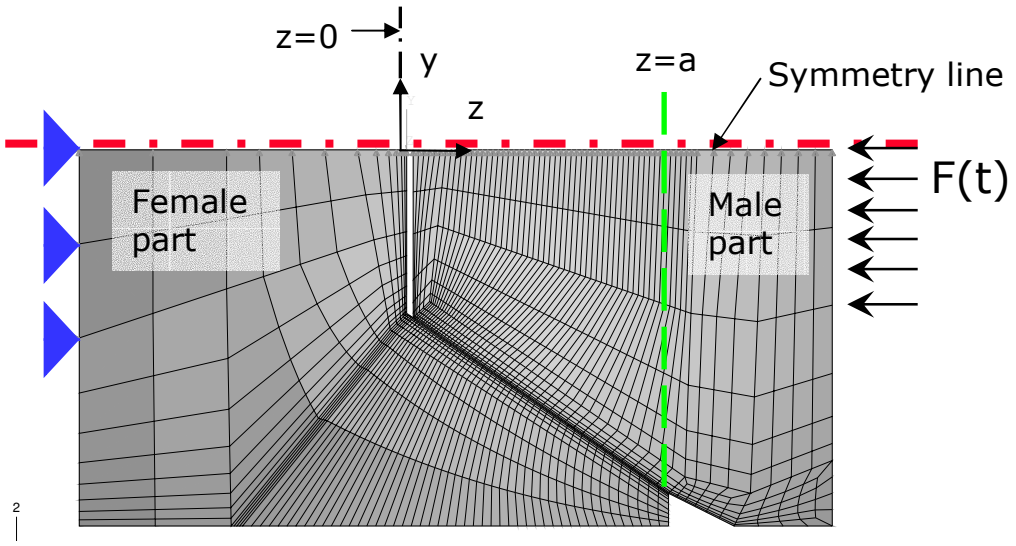

Figure 8.4. 2D Approximate model used for fretting analysis.

Providing that this model is representative of the contact conditions at the joint, it should provide an adequate approximation of the fretting behaviour of the conic coupling. Figure 8.5 shows a comparison of the pressure distribution for both the 3D sector & 2D representation under a bolting clamp load. This shows that the 2D model is representative of the contact conditions arising from normal loads. The 2D model also shows improved resolution of the contact stresses over the 3D sector model due to the finer mesh.

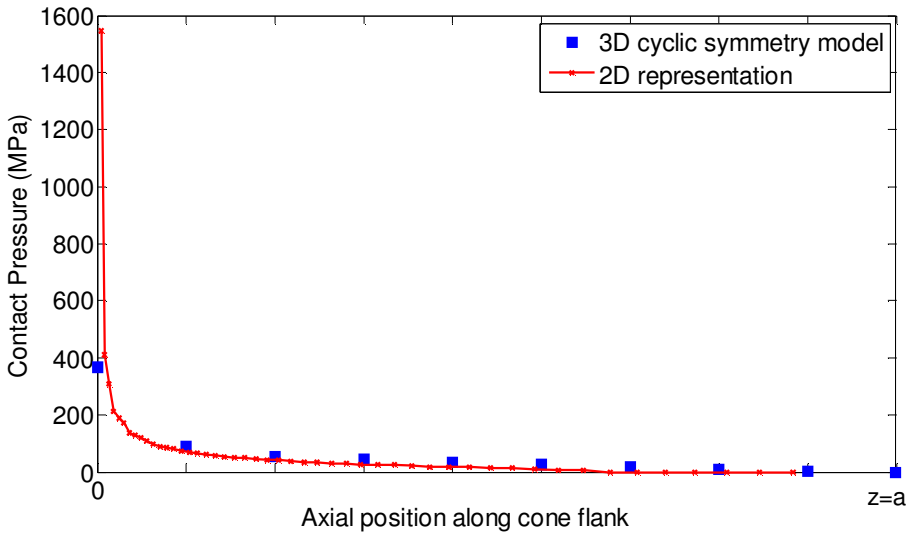

Figure 8.5. Comparison of 3D and 2D models under bolting clamp load

There are two major loading components that can be considered by this model: axial load and bending load. The axial load is a superposition of the clamping force, F_{cl}, produced by the bolts and the gas separation load F_g, caused by the aerodynamic forces which act to separate the compressor and turbine. The bending moment B_m is principally due to pitch/yaw manoeuvres which create gyroscopic couples. If the joint is axially short and at relatively large diameter, this bending moment will approximately be reacted as an axial force variation F_m which creates a couple over the joint

Each of these load components occur at different principal frequencies. F_{cl} is applied on engine build and hence does not fluctuate significantly during the life of the engine between builds, assuming that joint separation does not occur, The gas separation forces will principally vary from 0-F_g-0 once per flight. B_m is induced once per revolution of the HP spool whilst in manoeuvre and hence occurs at much higher frequency than either F_g or F_{cl}. The exact number of bending moment cycles is dependent on manoeuvre occurrence and therefore must be estimated. Here a value of 500 bending cycles is assumed per flight. Figure 8.6 shows the loading history assumed.

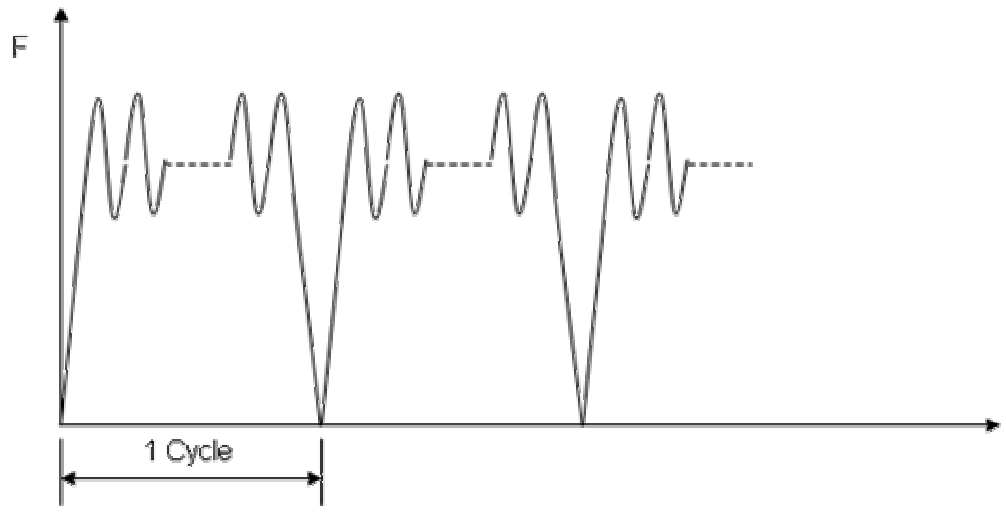

Figure 8.6. Loading history for fretting study

8.4 Results

8.4.1 Fretting wear study

As the intention of this study was to study the impact of bending moment on fretting, other loads such as thermal, centrifugal body forces and torque were neglected. This assumption entailed that the stress state within any given element is not correct and so the fatigue lifing aspect of the fretting fatigue modelling tool could not be utilised. Instead, the fretting wear behaviour of the joint was modelled to provide insight as to the possible stress evolution which might be created due to fretting wear. By using the experience of previous chapters, it is possible to infer whether the wear kinetics are likely to be detrimental, and therefore warrant further investigation. Although not universally applicable, such a method increases the usefulness of the approach, particularly as a initial investigation tool

Figure 8.7 shows the evolution of the contact pressure distribution after 4.5×10^6 cycles, which is significantly longer than the expected number of cycles required for the application being assessed. Figure 8.8 shows the evolving slip distribution. The discontinuity in the slip distribution coincides with the region of the flank that is lifting out of contact. Importantly, this is not in the high contact pressure region, instead the wear occurring at the tip of the male part results in load shedding onto the less highly loaded region. This is distinct from the partial slip cases noted in Chapter 2 where the load transfer was onto the highly loaded regions. This implies that the action of fretting is likely to improve the surface traction distributions from a fatigue aspect; essentially fretting wear will act as a ‘bedding in’ process. Additionally it appears that the fretting fatigue performance will be adequately described by the performance of the unworn geometry, mitigating the need for a wear analysis of the 3D geometry.

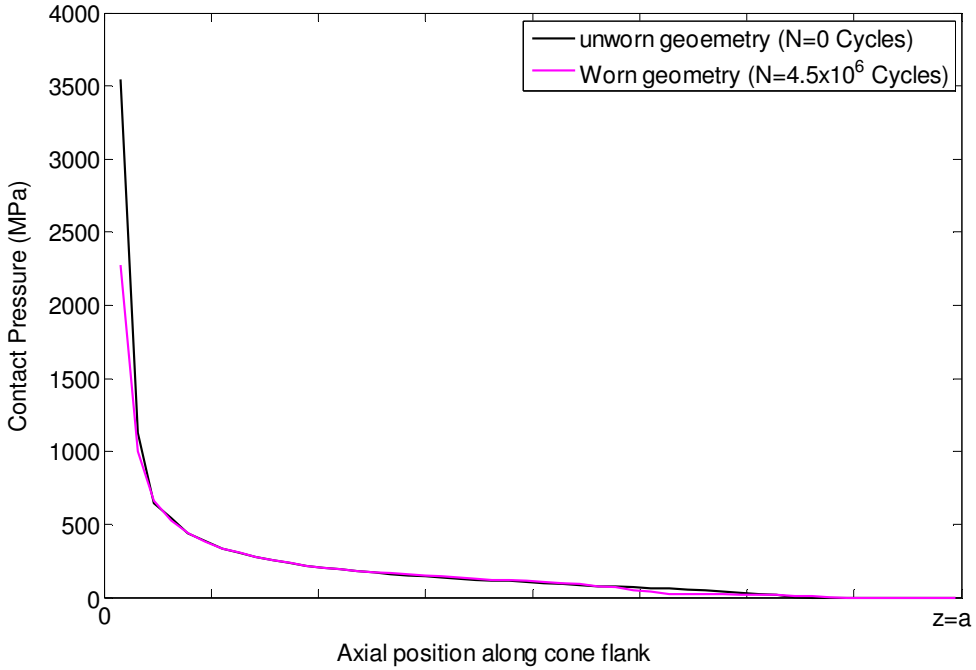

Figure 8.7. Effect of fretting on contact pressure distributions

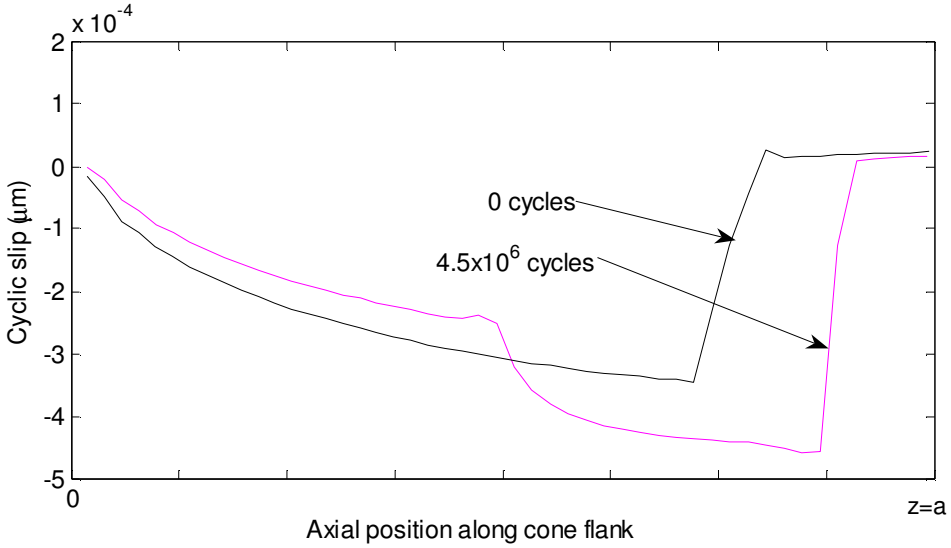

Figure 8.8. Evolution of slip distribution due to wear.

8.4.2 Design optimisation

Figures 8.5 and 8.7 show two important characteristics:

1) A contact pressure peak at the front of engagement (x=0mm)
2) A region of zero contact due to lift off (7mm>x>8mm)

These features are both caused by deflection of the female 'jaws'. The concept of 'barrelling' is common in spline couplings, where small amounts of material are removed from the tooth flank to improve the contact pressure distribution. This is known to reduce the contact stress concentration on the spline tooth flank, increasing its load carrying capacity considerably. A similar concept was devised for the conic joint such that the high pressure region was initially brought out of contact to reduce the concentration in this region (Figure 8.9). The deflection of the female jaws would then result in a more evenly distributed contact pressure.

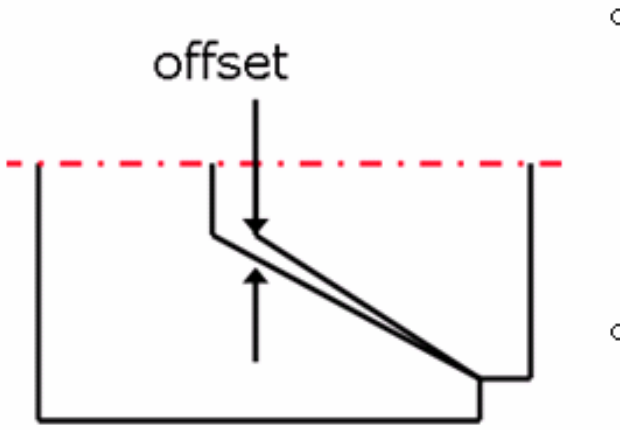

Figure 8.9. 'Barrelling' concept applied to conic coupling as a taper angle offset.

Figure 8.10 shows the effect of mismatches of varying size between the cone taper angles. As the mismatch is increased the contact pressure is shifted toward the rear of the joint. Eventually lift-off is caused at the front of the conic surface. However, this

is distinct from that shown in Figure 8.5 and 8.7 as the edge of contact pressure peak is significantly reduced. This is attributed to the female parts jaw being relatively compliant at their tips, yet stiff at their root. Figure 8.10 implies that this 'barrelling' method is relatively robust against manufacturing tolerance etc.

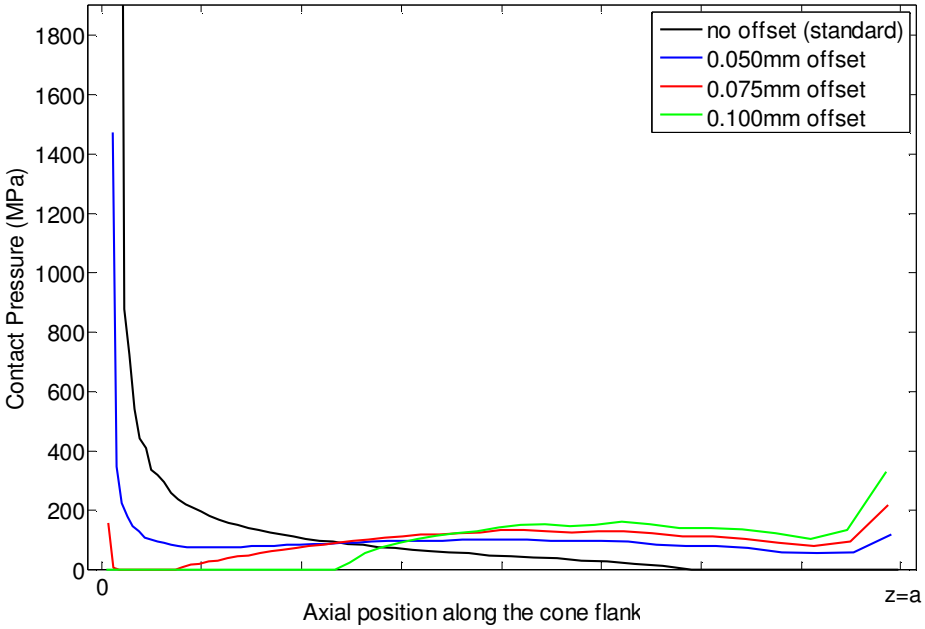

Figure 8.10. Pressure distributions for different levels of offset.

Effect of coefficient of friction on offset requirements

Figure 8.11 shows the effect of coefficient of friction on pressure distribution. The shear traction generated by friction tends to close the female jaws around the male. This is opposite to the effect of the normal load *F(t)*, which tends to spread the jaws. It follows then, that the offset required for low friction conditions will be larger than that which is optimum for high friction conditions. Given that under fretting conditions, the COF can vary by a significant amount, it is clear than the offset must be designed with this is mind. As mentioned, the pressure distribution associated with too large an offset is less detrimental than too little. Hence, the offset should be

designed such that a steady pressure distribution is obtained under the lowest expected friction conditions. Any increase in the COF of friction will tend to shift the pressure distribution towards the end of the female jaws, rather than creating a pressure peak at the male tip.

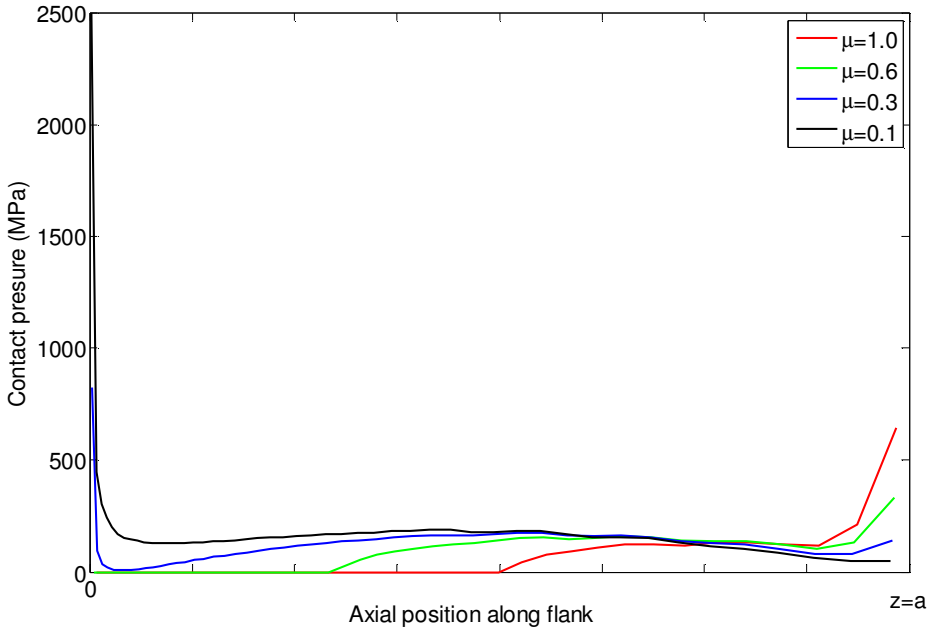

Figure 8.11. Pressure distributions for different coefficients of friction. (Offset=0.1mm for all cases)

8.5 Conclusions

A brief study into the contact performance of a novel type of rotor joint has been given. By approximating the geometry to a 2D representation, the fretting behaviour has been assessed under bending and axial loads. Investigations into the contact behaviour have indicated that a potential improvement could be made by introducing a small angular offset between the two taper parts.

Chapter 9

Conclusions

9.1 Conclusions

This thesis has presented a methodology that allows the effect of fretting wear on fretting fatigue to be quantified. Two different fatigue perspectives have been considered: one based on strain-life multiaxial fatigue relationships, and the other on fracture mechanics. The two techniques were also combined to create a method which modelled the nucleation and crack propagation stages separately. Both approaches used the Archard wear equation to model the material removal aspect of wear, the Coulomb friction law to model interfacial shear stress behaviour and both methods were implemented using finite elements. The methods help to explain a number of key phenomena on the interaction between fretting wear and fretting fatigue not previously treated numerically.

The multiaxial fatigue parameter approach showed the ability to predict the effect of slip amplitude on fretting fatigue life. This is the first such methodology to predict this effect. The method was validated against experimental results for two different contact geometries, the cylinder-on-flat and the punch on flat. The simulation results showed good correlation with the experimental results published independently by Jin & Mall (2002, 2004). The studied cases included both nearly complete and incomplete contact types.

In both cases the contrast between gross sliding and partial slip has been highlighted: whereas gross sliding causes an attenuation in stress which results in an increase in

fatigue life, the partial slip cases showed that the pressure concentration at the stick/slip boundary are magnified by wear, increasing damage at this location such that failure occurs here rather than at the edge of contact which is commonly predicted in more conventional studies. The occurrence of cracking across the slip region and particularly on the stick/slip boundary has been noted in a number of experimental studies.

A study into the effect of wear coefficient in the punch-on-flat case showed that the effect of wear can cause markedly different failure characteristics particularly in terms of the failure position. At higher assumed wear coefficient values, the predicted failure location was predicted with good accuracy. Again, to the authors knowledge, this phenomenon had not previously been quantified. The method also indicated that an optimum wear coefficient may exist for a partial slip contact which distributes damage more evenly within the component, extending life before failure.

The fracture mechanics method showed particular advantage in modelling crack arrest behaviour, providing a powerful advantage over the total life method which cannot predict such behaviour. The study indicates that it is not suitable to use fracture mechanics in isolation as a life prediction tool, as nucleation appears to be a significant fraction of total life in some cases, particularly those with high bulk stress levels as studied here. To this end the two methods were combined. The strain-life based method was modified to predict the time to nucleation, and the fracture mechanics method was used to predict the propagation from the site and time indicated by the said nucleation model. This method showed improved accuracy in the partial slip regime over the ‘SWT only’ method featured in early chapters, but under-predicted life at higher slip amplitudes. This is attributed to necessary simplifications assumed whilst formulating the nucleation model.

The numerical nature of the methodologies was adopted with the specific aim of analysing complex geometries such as curvic and spline couplings. The methods developed will improve the ability to predict the service life of such components which may be subject to fretting fatigue. This will help reduce reliance on costly, time consuming experimental testing. A preliminary analysis of a new type of torque carrying joint has shown the application of the method to a real engineering assembly. In this case the method was used to gain confidence that the coupling is not likely to be subject to fretting wear or fretting fatigue issues. This analysis highlights a powerful aspect of the methods; they can be applied to help 'map' the operating parameters which would be likely to lead to fretting fatigue or fretting wear operating conditions. This will aid engineers in avoiding this potentially dangerous operating regime.

Chapter 10

Recommendations and further work

10.1 Overview

Fretting fatigue is a complex phenomenon. This thesis has developed methods which can predict some experimental observations which have not previously been predicted for the fretting fatigue process. A number of assumptions were inevitably required and the resulting predictive tool is thus necessarily a simplification of the actual process. This chapter discusses potential areas of further work which were not addressed in the thesis.

10.2 Method improvements

The predictive tools presented in the thesis can be categorised into three main groups:

i) Tribology Model

ii) Fatigue Model

iii) Damage accumulation Model

10.2.1 Tribology Model

The Coulomb friction and Archard wear models are key elements of the approach adopted. They are relatively simple, which has some merit in terms of ease of application. However it is known that the coefficients of both friction and wear are not constant (e.g. Ding, 2003).

10.2.2 Friction Model Improvements

It is possible to implement a model which includes a variation in COF with numbers of cycles and future work should address this. For example, Cheikh et al (2007) have recently presented a kinematic-isotropic friction model. This work uses an analogy with the idealised hardening mechanisms from plasticity theory to capture the experimental observations of how COF varies within each cycles, and from cycle to cycle.

A further enhancement whereby the COF is able to vary across the contact surface according to variables such as contact pressure and slip would be more complex to implement due to reduced solution stability; however, some workers have had some success e.g. Naboulsi & Nicholas (2003) allowed μ to be a function of contact pressure and slip within an FE approach.

Another issue with the Coulomb implementation assumed is that the maximum shear stress is assumed to be a linear function of the normal load. In reality a shear stress limit will exist which will be related to shearing failure of the interface.

10.2.3 Wear Model Improvements

The wear coefficient under fretting conditions depends on stroke, normal load and number of cycles, and thus presumably also on local slip and contact pressure. Future work should address these aspects. Furthermore there is the issue of determination of local wear coefficient, which presents a more significant experimental challenge.

As an intermediate improvement the Archard equation may take the form of a map for the wear coefficient which correlates k with normal load, slip amplitude and number of cycles for example. This would induce only a slight increase in computational

requirements whilst improving the generality of the solution. This would give the advantage of allowing more complex cycle combinations than those considered here to be analysed. By undertaking a series of relatively simple fretting wear tests the tribological behaviour of a given material combination, under given environmental conditions could be mapped out. Molinari et al (2001) used this approach to allow the wear coefficient to vary with temperature for plain sliding conditions, allowing the modelling of both low speed and high speed conditions.

Fretting has been found to be a three body wear process, that is the tribological behaviour of the system is not only dependent on the two contacting bodies but also the tribo-layer that is created between them. (Godet et al, 1984, Halliday & Hirst, 1956). The analysis approach presented here has neglected the effect of the third body. Work by Ding et al (2007) sought to address this issue with respect to fretting wear behaviour, with the effect of improving the quality of predictions obtained by the wear model. Applying the approach to a fatigue system is a natural progression, although somewhat more complicated. The third body is a mixture of many different substances (parent material, oxides, lubricant and other contaminants) that has both solid and fluid like characteristics. The behaviour of this layer will determine how the loads are transmitted across the interface, and thus will affect the fatigue behaviour of the contact.

Molecular dynamics offers the promise of being able to model the interactions at the surface, by capturing the mechanistic behaviour of the contact to predict the wear and friction characteristics at a fundamental level. However the computing power required to apply this method to real engineering problems is currently prohibitive.

10.3 Fatigue Model

10.3.1 General

Clearly, the critical-plane SWT is just one among many available multiaxial fatigue damage parameters. For different materials and applications, and arguably for the same ones, alternative damage parameters may be more appropriate.

Multiaxial fatigue parameters are empirical fatigue correlations. The steep stress gradients associated with the small size of the critically stressed volumes that can occur in fretting fatigue can cause problems for these approaches. Crystal plasticity theory explicitly models the response of individual crystals. Using a small number of material constants it is possible to accurately model the plastic cyclic behaviour of each individual grain in the material. A further stage of sophistication is shown by the field of dislocation modelling. In this approach the movement and coalescence of dislocations in the crystal structure of grains is modelled. These approaches are attractive for their generality; however, they require very significant computational resource even to model small regions of material, and cannot currently be applied to engineering scale components.

10.3.2 Damage accumulation assumption

In general, damage is an anisotropic phenomenon. This is due to a number of factors such as basic material anisotropy, strain hardening/softening effects etc. Physically, damage is the degradation of material due to micro-void growth occurring under thermal or fatigue loading.

The isotropic damage model employed in this work is generally a conservative predictor compared to the anisotropic version. In the case where the critical plane

does not alter, the anisotropic analogue will predict equal damage evolution on this plane as the isotropic model, as the cyclic damage sustained on any given plane must, by definition, be less than or equal to that calculated on the critical plane. Life predictions made using the isotropic model will be shorter, the degree by which will depend on the evolution of the stress state biaxiality throughout the analysis. From a practical viewpoint the anisotropic damage model is somewhat less computationally efficient than its isotropic counterpart as damage must be calculated and stored on 36 different planes over a potentially large number of elements and loading cycles. The level of damage anisotropy will probably vary from one material to another. Therefore application of these advanced models will require an in-depth understanding of a materials response to multiaxial loading

10.4 Other areas of application

The methodologies presented employ several empirical parameters that are obtained from experimental tests, such as fretting wear tests, fatigue tests, crack growth tests etc. Examples of these include coefficient of friction, wear coefficient, SWT constants, Paris constants and the short crack growth threshold. This is advantageous in the sense that this type of data is often readily available, but nonetheless, it means that the methodologies are not purely theoretical tools for fretting fatigue prediction, i.e. they are approximations to physical behaviour observed under certain conditions. It should be pointed out that the empirical parameters used in the models may be affected by normal load, material properties, surface roughness, operating environment etc. Application to other materials and geometries will require consideration of these effects.

10.4.1 Engineering assemblies

The method has shown good potential for predicting some of the critical aspects of fretting fatigue when compared to experimental observations. The tool has been developed for practical use in analysing real engineering assemblies. At the time of writing sufficient computational resource was not available to apply the method to more complex geometries than those studied. As computer speeds and memory capacities increase the prospect of applying the methods to the analysis of complex geometries will become a reality. This should allow a better understanding of how fretting affects such components and hence allow improved design.

10.4.2 Materials

The majority of this work concentrated on contact between Ti-6Al-4V on Ti-6Al-4V. The chemical interaction between components has only been dealt with in terms of the effect of wear on contact pressure. It is foreseeable that in other material combinations this may not be a suitable assumption. Hutson et al (2006) and Lee et al (2004) conducted a series of experiments for fretting contact of aluminium, nickel and titanium alloys on Ti-6Al-4V specimens. The study found that generally the fatigue behaviour of the specimen was unaffected by changing the pad material, with the exception that fatigue endurance under certain loading conditions with the Nickel pad was slightly improved. Importantly they found that under the partial slip conditions considered, the use of multiaxial fatigue parameters such as SWT were able to describe the fatigue behaviour adequately. This indicates that the models described here should be applicable to other material combinations. However, this will require validation.

10.4.3 Coatings

Coatings have become a popular method for reducing wear, and are increasingly popular for fretting applications. However these coatings usually carry some penalty on fatigue life. The methods described here should, with modifications, be applicable to coatings also. Failure of the coating is dependent not only upon surface wear but also delamination and cracking due to substrate/coating compatibility induced strains. Wear modelling should be particularly useful in the analysis of coatings as relatively small wear depths can result in the coating being penetrated. The ability to accurately predict the life of both the coating and the substrate component will be critical for the successful design of these components.

Appendix A1

Abaqus Subroutine

A1.1 Overview

This appendix details the ABAQUS subroutine developed in order to allow fretting wear modelling to be carried out within the ABAQUS environment. Detailed information on the inputs and outputs can be found in HKS (2005). The program is written to comply with the FORTRAN 90 standard.

A1.2 Code

```
      SUBROUTINE UMESHMOTION(UREF,ULOCAL,NODE,NNDOF,
     &           LNODETYPE,ALOCAL,NDIM,TIME,DTIME,PNEWDT,
     &           KSTEP,KINC,KMESHSWEEP,JMATYP,JGVBLOCK)
C
      INCLUDE 'ABA_PARAM.INC'

C
      !standard UMESHMOTION array variables
      DIMENSION ULOCAL(NDIM),JELEMLIST(100000)
      DIMENSION ALOCAL(NDIM,100000),TIME(2)
      DIMENSION JMATYP(100000),JGVBLOCK(100000)
C
C!!!!!!! Variables defined by JJM !!!!!!!!!
          !generic program control variables
          INTEGER::flag1,cnt1
          !flag to designate as a master node (1) or slave (0)
          INTEGER::master
          ! contact pressure, shear, slip, opening, xcoord, ycoord, and slip over the
          increment at node currently being !considered
          REAL::CPRESS,CSHEAR,CSLIP,COPEN,XCOORD,YCOORD,INCSLIP
          ! interpolation values (pressure&slip) for closest slaves and the associated
          !gradients
          REAL::CPRESS_R,CPRESS_L,INCSLIP_R,INCSLIP_L,grad_pr,grad_sl
          !array to hold variables passed from abaqus utilities
          DIMENSION ARRAY(15)
          !these variables are used in the HKS tyre wear simulation
          INTEGER::LOCNUM,NELEMMAX
          CHARACTER::PARTNAME
          !wear distance computed for current node
          REAL::W_dist
          !minimum Xcoord error between current node and closest slave found so far
          REAL::X_error, Y_error

        common/wear/
     &    ilastnode,  !holds the last node that was visited
     &  ilastnode2,
     &    isclock,  !counts how many slave nodes have been recorded
     &    imclock,  !counts how many master nodes have been recorded
        !the dimension of these arrays needs to be larger than the number of contact
        !nodes
     &  snodes(2000),  !record of all slave node numbers
     &  imnodes(2000),  !record of all master node numbers
     &  oldslip(2000),  !records the slip from the last incremnt for each slave node
```

```
&    tempslip(2000), !records the slips for this increment (continually updated
&    spress(2000),  !records the contact pressures for all slaves
&    sxcrd(2000),   !records the x coordinates for all slaves
&    sycrd(2000),   !records the y coordinates for all slaves
&    sincslip(2000),!records the slip over the increment for all slaves
    !acts as a lookup table between the
    !global node numbers and the above arrays
    !therefore size needs to be bigger than the number of nodes in the model.
&    slavereg(100000),
&    imasterreg(100000)

  !!!!!! INITIALISE DATASETS  !!!!!!!!!!!!!!!!!!!!!!!!!!!!!!!!!!!!!!!!!!!!
  !initialise flag1 to 0, this allows entry to the do while loops
  flag1=0
  cnt1=1
  !assume node is a slave as initial guess
  master=0
  !initialise some variables used for interpolating
  !use a number which is exact but not realistic (for checking later)
  CPRESS_L=0
  CPRESS_R=0
  INCSLIP_L=0
  INCSLIP_R=0
  X_L=1.001*XCOORD
  X_R=0.999*XCOORD
  !maximum allowed incremental nodal movement before increment is abandoned
  h_crit=0.001
  !these were copied from HKS tire wear simulation
  NELEMMAX = 500
  NELEMS = NELEMMAX

 !open external datafiles
  OPEN(unit=16,file='c:\temp\ContactOut_slave.txt',status='unknown')
  OPEN(unit=17,file='c:\temp\DummyNodes.txt',status='unknown')
  OPEN(unit=18,file='c:\temp\ContactOut_mast.txt',status='unknown')

  !update node logger
  ilastnode=NODE

  !!!!!!!!!!!ABAQUS SUBROUTINES FOR RETRIEVING DATA!!!!!!!!!!!!!!!!!
  !this is needed so that the element values can be averaged to the nodes
  CALL GETNODETOELEMCONN(NODE,NELEMS,JELEMLIST,JELEMTYPE,
$     JRCD,JGVBLOCK)
  LOCNUM = 0
 JRCD = 0
 PARTNAME = ' '

  !GET NODE VARIABLES using abaqus utilities::
  !contact stresses
  CALL GETVRMAVGATNODE(NODE,'CSTRESS',ARRAY,JRCD,
&                      JELEMLIST,NELEMS,JMATYP,JGVBLOCK)
  CPRESS = ARRAY(1)
  CSHEAR = ARRAY(2)
  !contact displacements
  CALL GETVRMAVGATNODE(NODE,'CDISP',ARRAY,JRCD,
&                      JELEMLIST,NELEMS,JMATYP,JGVBLOCK)
  CSLIP = ARRAY(2)
  COPEN = ARRAY(1)
  !coordinates
  CALL GETVRN(NODE,'COORD',ARRAY,JRCD,JGVBLOCK,LTRN)
  XCOORD=ARRAY(1)
  YCOORD=ARRAY(2)
  flag1=0

  !loop to identify master nodes
  IF((CPRESS==0).AND.(COPEN==0))THEN
    !this state is impossible for a slave node, so designate as a master
    master=1
    IF(imasterreg(NODE)==0)THEN
      WRITE(18,*)'found a new master',NODE
          imclock=imclock+1 !click on counter for next unrecorded slave
          imnodes(imclock)=NODE
      !store the element number that relates to the snode,spress etc
          !array for use a a lookup
          imasterreg(NODE)=imclock
    END IF
```

```
ELSE !slave node so input new contact data
  !check that this has been noted as a slave in external arrays
   IF(slavereg(NODE)==0)THEN
        isclock=isclock+1 !click on counter for next unrecorded slave
        snodes(isclock)=NODE
     !store the element number that relates to the snode,spress etc
        !array for use a a lookup
        slavereg(NODE)=isclock
   END IF
   !have new contact data for this node (slave) so update its data
   spress(slavereg(NODE))=CPRESS
   sxcrd(slavereg(NODE))=XCOORD
   sycrd(slavereg(NODE))=YCOORD
   !update temporary slip log for current increment
   tempslip(slavereg(NODE))=CSLIP
   INCSLIP=CSLIP-oldslip(slavereg(NODE))
 END IF

 !define an initial positional 'error' between current master node
 !and a 'close' slave node, basically this is a large number
 !(wrt element size on the contact surface)
 X_error_R=1
 X_error_L=1
 !initialise indicators to show whether slave nodes have been
 !located close to the master (one for each side) (i.e. switch off)
 L_flag=0
 R_flag=0

 !set up a loop to link master to slave node
 IF(master==1)THEN
   !master node: so need to find the 2 slave nodes beside it
   !go through each slave node in turn
   DO cnt1=1,isclock
     !check which side of the master node this slave node is on
        IF(sxcrd(cnt1).GT.XCOORD)THEN
       !this slave is on the right hand side of NODE
          IF(ABS(XCOORD-sxcrd(cnt1))<X_error_R)THEN
            !read in new closest RH slave node data
            CPRESS_R=spress(cnt1)
            !new incremntal slip
            INCSLIP_R=tempslip(cnt1)-oldslip(cnt1)
        X_R=sxcrd(cnt1)
        !update new error between slave and node
        X_error_R=ABS(XCOORD-sxcrd(cnt1))
       !trip flag to show that a value has been recorded for RH slave match
               R_flag=1
          END IF
     ELSE !this slave must be on the LH side of this master
       IF(ABS(XCOORD-sxcrd(cnt1))<X_error_L)THEN
            !read in new closest LH slave node data
            CPRESS_L=spress(cnt1)
            !new incremntal slip
            INCSLIP_L=tempslip(cnt1)-oldslip(cnt1)
        X_L=sxcrd(cnt1)
        !update new error between slave and node
        X_error_L=ABS(XCOORD-sxcrd(cnt1))
        !trip flag to show that a value has bee recorded for LH slave match
               L_flag=1
         END IF
       END IF
   END DO
  !output the matched slaves to the screen

   !may not have got two slave matches for master (e.g. at ends of slave
   !surface)
   !therefore include logic for all possible events
   IF(R_flag==0)THEN
     !only matched on the left side, so use this data
     CPRESS=CPRESS_L
     INCSLIP=INCSLIP_L
   END IF
   IF(L_flag==0)THEN
     !only matched on the right side, so use this data
     CPRESS=CPRESS_R
     INCSLIP=INCSLIP_R
   END IF
```

```
    IF(L_flag==0.AND.R_flag==0)THEN
      !no match found, reset to zero
          CPRESS=0
      INCSLIP=0
    END IF
    IF(L_flag==1.AND.R_flag==1)THEN
      !have match for two slaves, therefore can interpolate
     grad_pr=(CPRESS_R-CPRESS_L)/(X_R-X_L) !gradient of press wrt X
      CPRESS=CPRESS_L+grad_pr*(XCOORD-X_L) !interp. pressure at master node
      grad_sl=(INCSLIP_R-INCSLIP_L)/(X_R-X_L) !gradient of slip wrt X
      INCSLIP=INCSLIP_L+grad_sl*(XCOORD-X_L) !interp. slip at master node
    END IF
 END IF

  !calculate the wear distance for this node
  !note UREF is passed from the input (.INP) file
  W_dist=(CPRESS)*ABS(INCSLIP)*UREF

  !suppress mesh movement during the first step (normal loading)
  IF(KSTEP==1)THEN
    W_dist=0
  END IF

  !compute new nodal coordinate to next worn position
  ULOCAL(2)=ULOCAL(2)-W_dist

  !check to see if convergence control is needed (i.e to reign back in wear
  !instability
  IF (W_dist.GT.h_crit) THEN
    !save the old increment
    PNEWDT_0=PNEWDT
    !Find out the fraction by which we are over
    !suggest the increment to be a little smaller than that idicated by the limit
    !(assuming linearity - extrapolate back)
    PNEWDT_1=0.99*h_crit/W_dist
    IF(PNEWDT_1.LT.PNEWDT_0)THEN
      !this increment will now be abandoned by abaqus, it will restart at a
      !smaller increment change
      PNEWDT=PNEWDT_1
      !record incremnt adjustment in msg file
      WRITE (7,*) 'CHANGING TIME INCREMENT FROM ',PNEWDT_0
      WRITE (7,*) 'TO ',PNEWDT
     WRITE (7,*) 'BASED ON NODE ',NODE
    END IF
 END IF

  !print contact conditions if its a slave node
  IF(master==0)THEN
    WRITE(18,1000),NODE,CPRESS,CSHEAR,master,oldslip(slavereg(NODE)),
&                INCSLIP,W_dist,XCOORD,YCOORD
  ELSE IF(master==1)THEN
    WRITE(16,1000),NODE,CPRESS,CSHEAR,master,oldslip(slavereg(NODE)),
&                INCSLIP,W_dist,XCOORD,YCOORD
  END IF
    !need to write some coordinate positions for the SWT analysis to define the
    !morphology of slave surface. We only write this data at beginning of every
    !loadstep
  IF(KINC==1)THEN
    IF(snodes(1)==NODE)THEN
      WRITE(17,*),'LOADSTEP',KSTEP
   END IF
    WRITE(17,*),'0 ','0',XCOORD,YCOORD
  END IF
 !END IF

 !the old slip data should only be updated after all master nodes have been dealt
  !with in this increment. In this way, we will not update information before the
  !masters
  !have been moved. Slaves are not sensitive to this issue as they always have a
  !new contact data to enter.

  !IF(NODE==imnodes(imclock))THEN
  IF(NODE==1)THEN
    !reset the incremental slip values for the new increment
    DO cnt1=1,isclock
  oldslip(cnt1)=tempslip(cnt1)
```

```
          END DO
          !write header for increment in slave contact output
          IF(master==1)THEN
                WRITE(16,*),'LOADSTEP',KSTEP,'INCREMENT ',KINC
            WRITE(16,*),ilastnode, isclock
            WRITE(16,*),'NODE  CPRESS  CSHEAR  COPEN  CSLIP  XCOORD YCOORD'
          !now write header for increment in master contact_out
            WRITE(18,*),'LOADSTEP',KSTEP,'INCREMENT ',KINC
            WRITE(18,*),ilastnode, isclock
            WRITE(18,*),'NODE  CPRESS  CSHEAR  COPEN  CSLIP  XCOORD YCOORD'
        !  END IF
        END IF
        ilastnode2=NODE

        !format statements
        !contact/wear output to the data file
1000  FORMAT(i5,1x,e13.6,1x,e13.6,1x,i3,1x,e13.6,
     &                      1x,e13.6,1x,e13.6,1x,e13.6,1x,e13.6)

2000  FORMAT(i5,1x,e13.6,1x,e13.6,1x,e13.6,1x,e13.6,1x,e13.6)


      RETURN
      END
```

Appendix A2

Verification of Numerical Aspects

A2.1 Overview

The numerical modelling employed in this work is an approximate technique based on a number of assumptions. The accuracy of the model is based on the validity of these assumptions. This appendix presents the checks that were made regarding some of these assumptions. The validations presented here are all based on the Hertzian model employed in Chapter 4, where further information on the model can be found.

A2.2 Effect of cycle jumping

Cycle jumping essentially assumes that the cyclic wear over a number of cycles is approximately constant. Therefore the wear over a similar number of cycles ΔN can be approximated by multiplying the wear over one cycle by ΔN. The technique significantly reduces the computational expense of wear modelling. In the past, cycle jumping has been used to good effect, e.g. McColl et al (2003). In that work, the principal limitation to cycle jumping related to solution stability such that the contact solution could not be solved if too large a cycle jump was used. As mentioned in Chapter 3, the Adaptive Meshing Constraint (AMC) technique used in the present work is significantly more stable, so that larger cycle jumps can be used with little impact on stability. It is therefore necessary to reassess the limitations of cycle jump size with respect to the AMC technique. Furthermore the use of a critical plane fatigue model in conjunction with cycle jumping implies that the fatigue model may also be affected by the ΔN value employed.

Effect of ΔN on wear model solution

McColl et al (2003) found that the maximum cycle jump size was controlled by the maximum wear depth per fretting cycle analysed. In their implementation they found ~0.06mm/cycle to be the practical maximum, with the limiting factor being computational stability due a 'rough' surface being created. This 'rough' surface was a numerical feature and resulted in lack of convergence to the contact solution. In the cases studied, this resulted in maximum permissible cycle jump sizes in the order of 30 to 100. The AMC technique is more stable than the method employed by McColl et al (2003). The Hertzian geometry studied in Chapter 4 has been analysed using ΔN values of up to 1 500 000; although convergence is slowed somewhat at these extreme values, a solution is still achieved. The improved stability is owed to the fact that the geometric perturbation of the wear model is implemented at the end of each increment, rather than once per cycle, hence in the models studied in this thesis the geometry is updated (in the cases studied in this work) 100 times per cycle as compared to once per cycle in the case of McColl et al (2003). Hence the numerical roughness mentioned is more difficult to create. However, this implies that solution accuracy is likely to be the limiting factor when using A.M.C. rather than solution stability.

Figure A2.1 compares the wear depth at several time points using different cycle jump sizes for a gross sliding case (δ= 8.7mm). The effect of ΔN on the wear solution accuracy is found to be acceptable up to quite large values. The same is found to be true for partial slip cases, as shown by Figure A2.2. In this case pressure distribution is shown, which is also a good indicator of convergence as the pressure distribution is sensitive to the contact profile. There is slightly more dependence on ΔN than in the gross sliding case. This is due to the more complicated slip distribution: wear rate

varies across the contact surface to a greater degree in the partial slip case. Convergence was judged to be satisfactory however

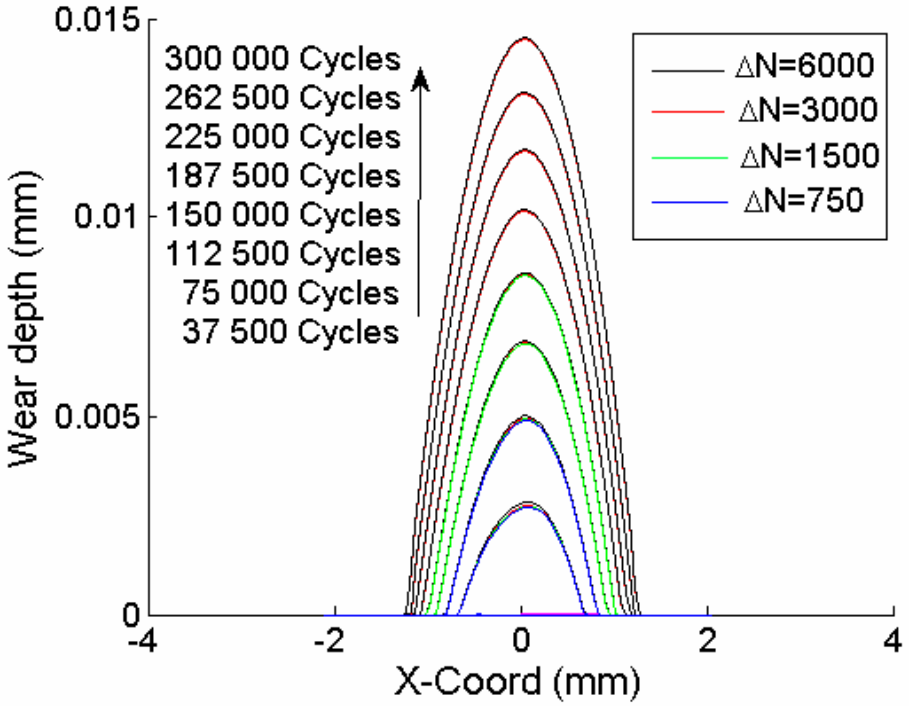

Figure A2.1 Wear depths at points throughout the wear simulation for different ΔN values (Mesh 2, δ = 8.7μm)

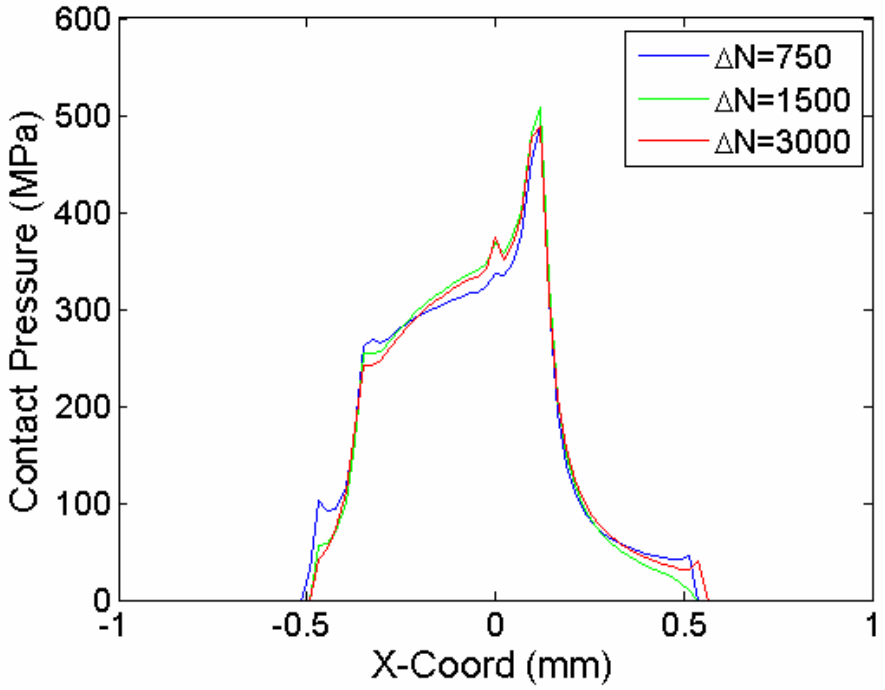

Figure A2.2. Pressure distribution after simulated 75,000 cycles. (Mesh 1, δ=2.6μm)

A drawback of the AMC method is that the entire analysis is run as one 'job', i.e. the input deck for each cycle being analysed must be loaded into the computer memory, which means that memory is the primary constraint on problem size. Current 32-bit architecture has an upper limit of 2^{32} i.e. only 4GB of memory can be addressed by the machine. As such, the AMC method is quite limited for high cycle analysis on 32-bit computers. Methods of circumventing this limit, such as running serial analyses were attempted though this was subject to the same stability issues as found by McColl et al. (2003) & Ding et al (2004). In all analyses in this thesis, the maximum simulation length was around N^*=100, i.e. 100 fretting cycles could be modelled in total. 64-bit machines which are becoming more widely available will remove this 'glass ceiling', however the present work is subject to the 32-bit imposed limit.

If a small cycle jump size is utilised, the total number of 'real' cycles that can be modelled is therefore small. For example in Figure A2.1, in the case of ΔN=750, only 75,000 cycles could be analysed, if ΔN=1500, 150,000 cycles can be analysed and so on. In the ΔN=6000 case, 600 000 cycles were analysed, though only the first 300 000 cycles are depicted for clarity.

Effect of ΔN on fatigue model solution

The use of a fatigue damage model in conjunction with the wear model means that the assumption of cycle jumping must also be employed within the fatigue model. This is borne out in Equation 3.9. The relative insensitivity of the wear model solution to cycle jump size implies that the stress solution is also unlikely to be very sensitive to ΔN also. Figure A2.3 confirms this. The SWT parameter value which is used to calculate fatigue life is found to be quite insensitive to ΔN over the range considered.

However it is worth noting that the fidelity at the beginning of the analysis is compromised when using high ΔN values (Figure A2.4). This can be attributed to the fact that the SWT parameter is evaluated over the first cycle, which, due to the incremental updating of the geometry, actually represents a multiple of geometries relating to the first ΔN cycles. The result is that the SWT parameter evaluated over the first analysis cycle is actually some kind of average for the first ΔN cycles. As such, the fatigue model will be affected by the ΔN value assumed. Although not employed here, either a small ΔN value could used over the first simulated N^* cycles, or some form of 'back extrapolation' method could be used to reduce this effect if required. It is important to consider that the extent of this effect will essentially be governed by how quickly the geometry changes throughout the analysis, which will be affected not only by the ΔN used, but also by the wear coefficient, the slip amplitude, the contact pressure, and the way in which these parameters change with wear. Faster changes will require finer discretisation of the time domain, e.g smaller ΔN.

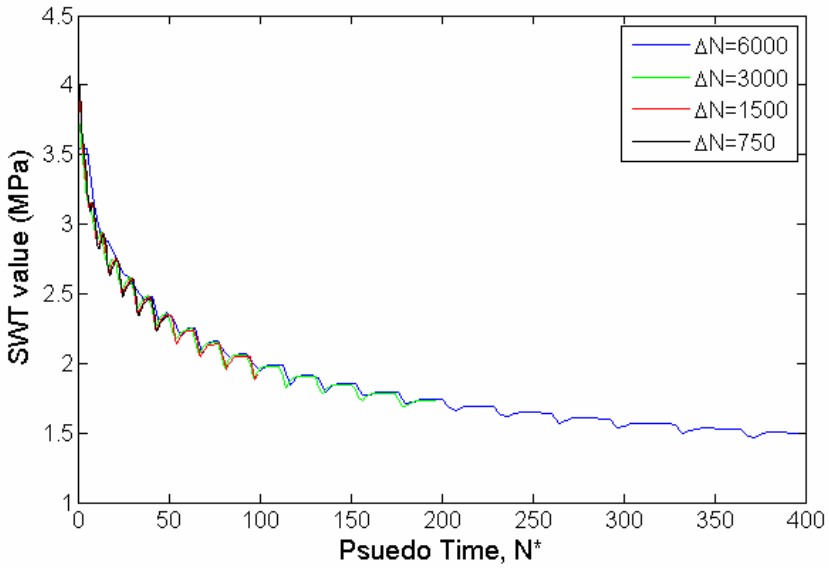

Figure A2.3. Evolution of peak SWT value with number of cycles (Mesh 2, δ=8.7μm, Gross sliding)

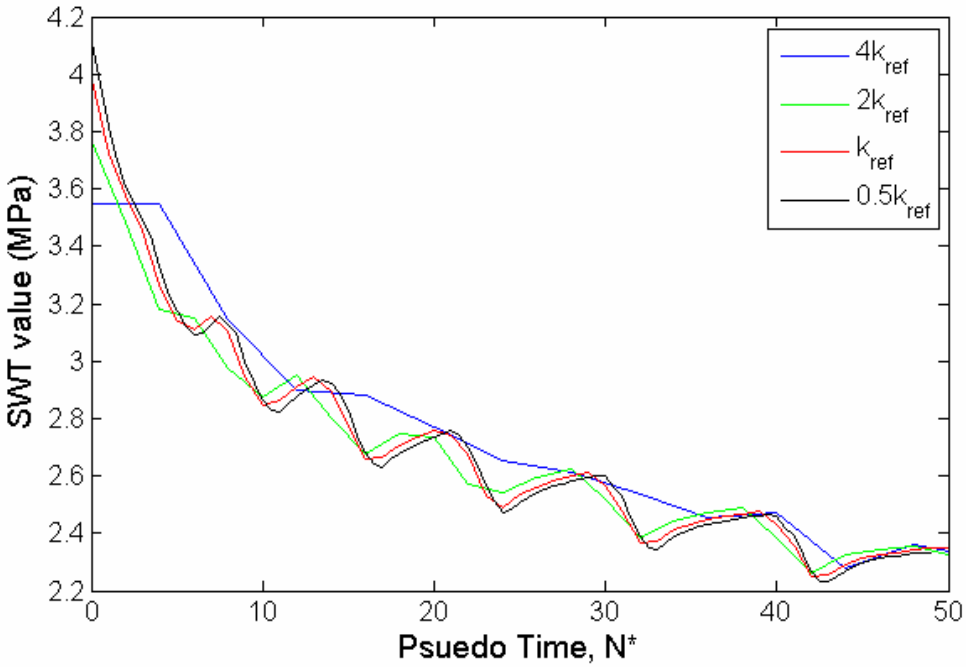

Figure A2.4. Initial evolution of peak SWT value with number of cycles, (Mesh 2, δ=8.7μm)

A2.3 Effect of increment size

In the FE analysis of non-linear systems solution is reached by breaking each load step down into smaller increments. By gradually increasing each load non-linearities (such as contact behaviour) can be captured more accurately than a linear perturbation analysis would allow. The number of increments used within a step governs the discretisation of the time domain. It has been shown by Leen et al (2001) that the solution of slip distribution by FE is sensitive to time incrementation. Referring to Equation 3.3 it is clear that any errors will tend to propagate throughout the analysis potentially causing significant discrepancies in the fatigue life prediction. Figure 2.5 shows the solution for slip distributions using nominally identical modelling conditions with two different increment sizes. The coarse incrementation is 10 increments per fretting cycle, the fine one is 100 increments per fretting cycle. We find that a relatively small dependency of the wear profile on increment size is shown.

The effect on the evolution of the SWT parameter is found to propagate slightly (Figure A2.6). The use of the Lagrange multiplier method in enforcing exact sticking is likely to be limiting this dependency. However, in all analyses an increment size of 100 increments per fretting cycle is used to limit this effect.

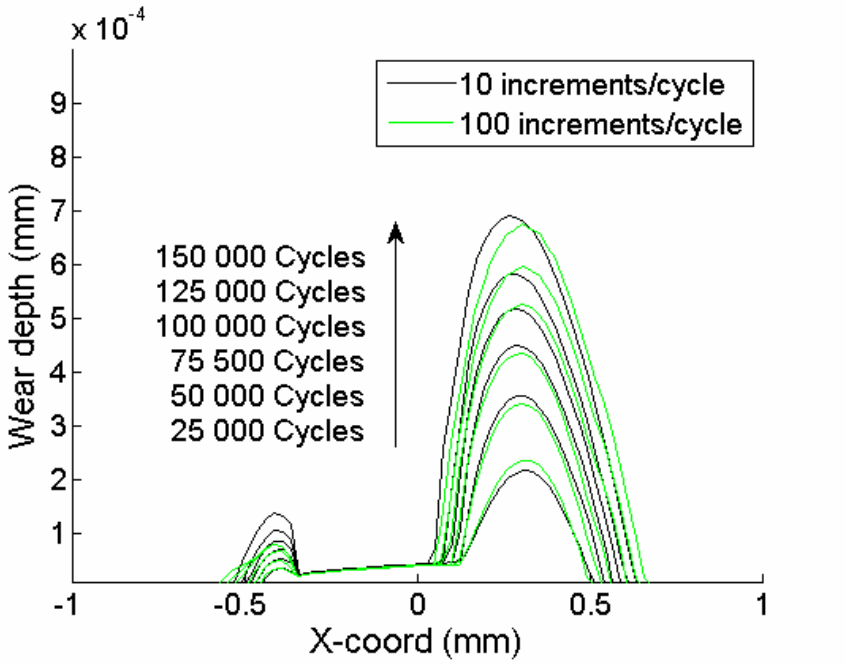

Figure A2.5. Dependence of wear profile on increment size adopted.
(Mesh 1, δ=2.6μm)

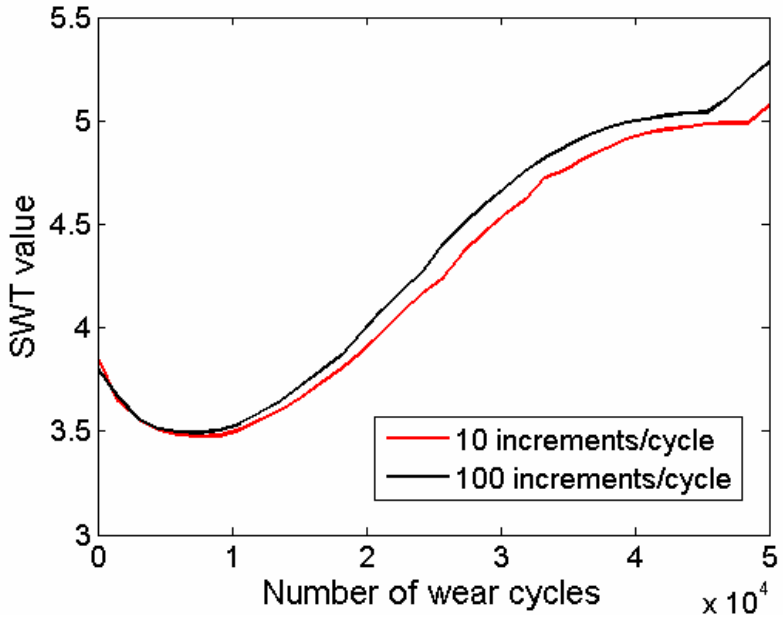

Figure A2.6. Propagation of errors in peak SWT value due to increment size adopted.
(Mesh 1, δ=2.7μm)

An interesting feature of Figure A2.4 and Figure A2.6 is the discontinuous nature of the SWT evolution. This feature is caused by the discrete nature of finite elements. The discontinuous points relate to the time point at which the critical element changes. Figure A2.7 shows the traces of SWT parameter over time for all of the critical elements in a partial slip case (δ=2.8 μm). Figure A2.8 shows the equivalent plot for gross sliding case (δ=8.7 μm). It is seen that as the stress distribution evolves each critical element passes through a peak value, before dropping away, and ultimately being replaced as the critical location as another element experiences increasing stresses and strains. The frequency of occurrence of the discontinuities is related to the mesh density. The effect of mesh refinement on the SWT fatigue model is discussed below.

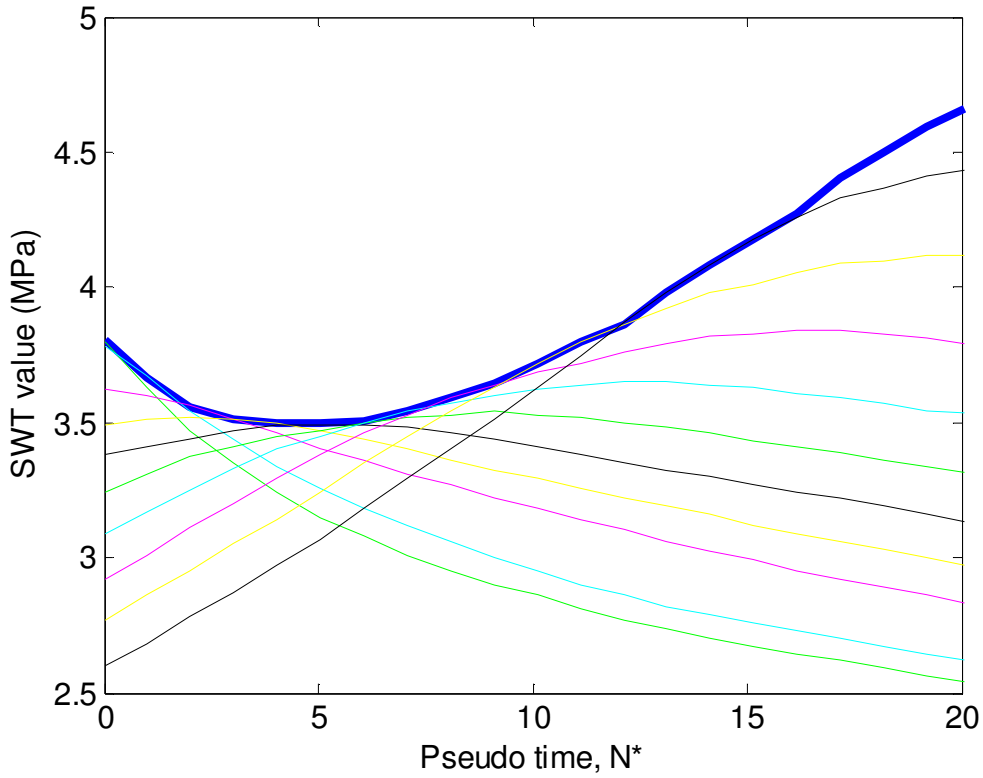

Figure A2.7. SWT trace for all critical elements, gross sliding case (δ=2.9μm). Note that thick line is global maximum, thin line shows trace for a given element

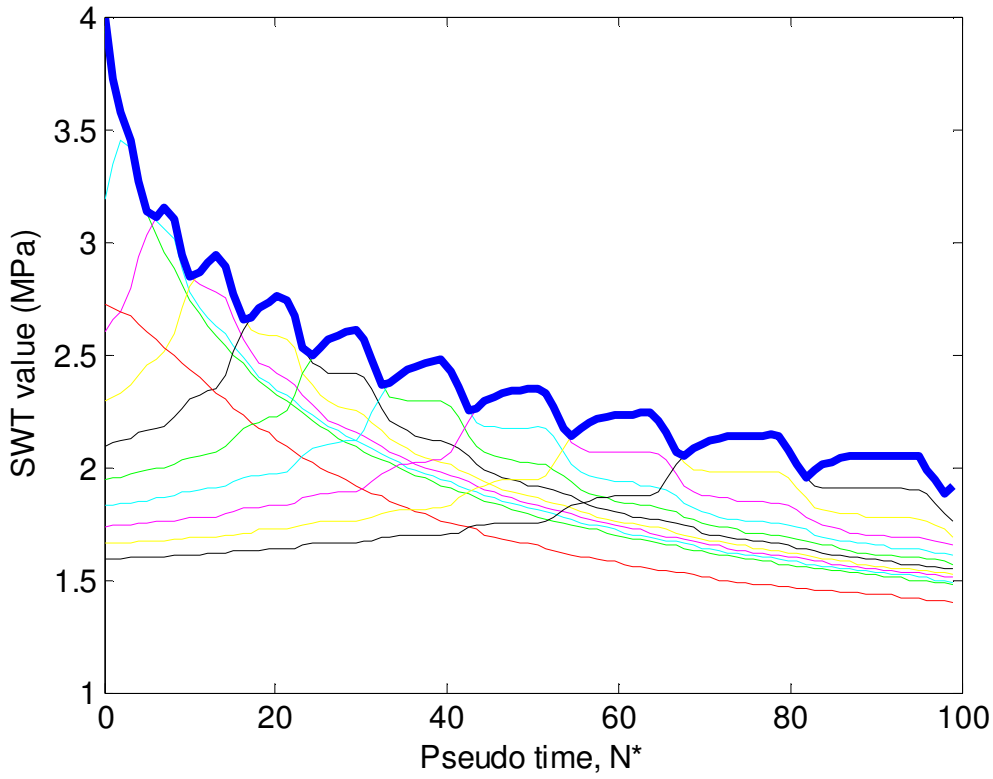

Figure A2.8. SWT trace for all critical elements, gross sliding case (δ=8.7μm). Note that thick line is global maximum, thin line shows trace for a given element

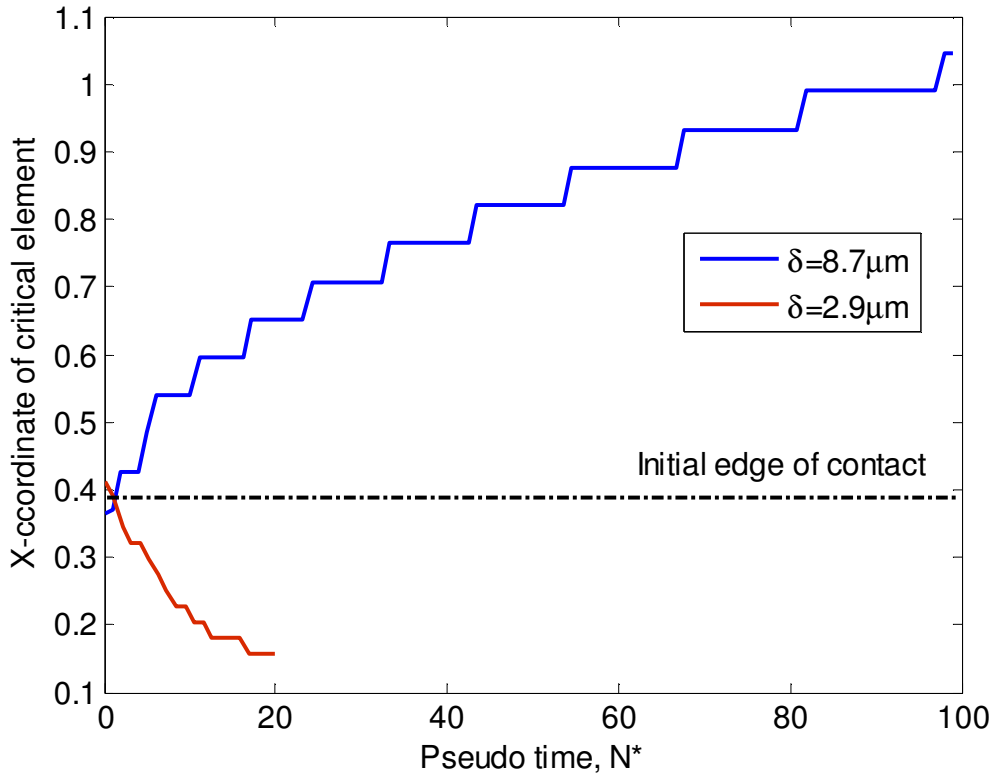

Figure A2.9. Location of critical (peak SWT) element with increasing wear

A2.4 Mesh refinement

The refinement required in an FE mesh must be balanced against the computational resource available. Wear modelling is a particularly numerically intensive activity due to the repetitive, though non-linear, nature. However this means that efficient use of elements brings substantial reductions in computational expense. For this reason the meshes employed are made as efficient as possible. The meshes have been checked against relevant theoretical results in Chapter 4 and 5 and show excellent agreement with them.

In addition, a mesh convergence study was conducted with respect to the SWT lifing model. It is well documented that finite element solutions for stress and strain are mesh dependent. As such the SWT parameter is susceptible to mesh dependency also. The three meshes studied are depicted in Figure A2.10.

The first two are 'Mesh 1' and 'Mesh 2' in Chapter 4. The region containing contact elements is refined to provide better resolution where high stress gradients are expected. Mesh 1 has contact elements over a width of 1.5mm, with the contact surface element dimension being 23μm, and an element depth of 15.7μm.

The contact width increase due to wear is far greater in the gross sliding cases. Therefore Mesh 2 has an increased potential contact width at 3.6mm. Given the computational constraints discussed above, it was necessary to maintain the total element count, hence, Meshes 1 and 2 are topologically identical; in Mesh 2 the contact surface element dimension is therefore increased to 56μm. The surface element size going into the specimen part is 15.7μm in both Mesh 1 and 2. Mesh 3 is an additional mesh which is similar in terms of contact width to Mesh 2, with the edge node spacing doubled at all points. This results in Mesh 3 having a contact surface

element dimension of 113μm, and a depth into the surface of 31μm. The models are compared for both a gross sliding case (δ=8.7μm), and a partial slip case (δ=2.9μm). The loading cycle is identical to that studied in Chapter 4. To provide a back to back comparison across the slip range, no wear was considered in this study.

Figure A2.11 shows effect of mesh density on the SWT solution for the two cases. In the gross sliding case, Mesh 3 is found to under-predict the SWT value by approximately 11% compared to the value predicted by Mesh 1. Mesh 2 is found to under predict the SWT value by a smaller margin of 3.8%.

In the partial slip case error imposed by the larger element size of Meshes 3 and 2 is increased to 13% and 4.8% respectively. The partial slip case presents a more challenging stress field to model via finite elements as the shear traction distribution is non-continuous, hence a larger relative error is observed in this case.

The nature of a typical S-N curve is such that small changes in stress results in large changes in life. Figure A2.12 depicts the effect of element size on the life prediction. The relative errors are increased due to the sensitivity of life to SWT value. This is particularly noticeable in the partial case, where the error on life is found to be 71% for Mesh 3 and 20% for Mesh 2. The gross sliding case shows reduced errors, with Mesh 3 and Mesh 2 under-predicting life by 54% and 15% respectively. Although these errors are quite large, when compared to the experimental scatter that occurs in fatigue testing they are relatively small; generally an error band of $\pm 2N_f$ is considered typical at any point on the life curve.

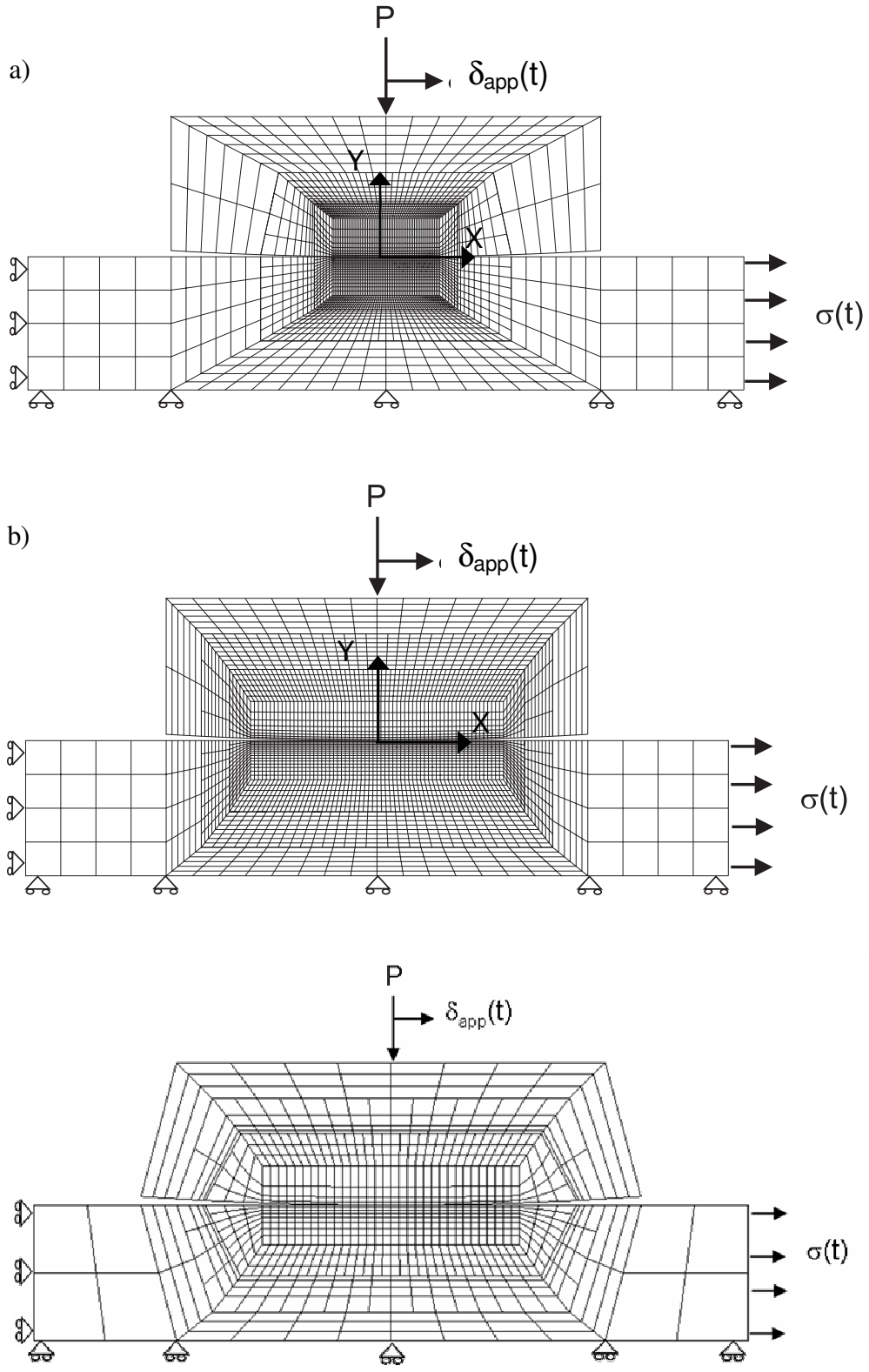

Figure A2.10. Meshes used in convergence study:
a) Mesh 1 b) Mesh 2 c) Mesh 3

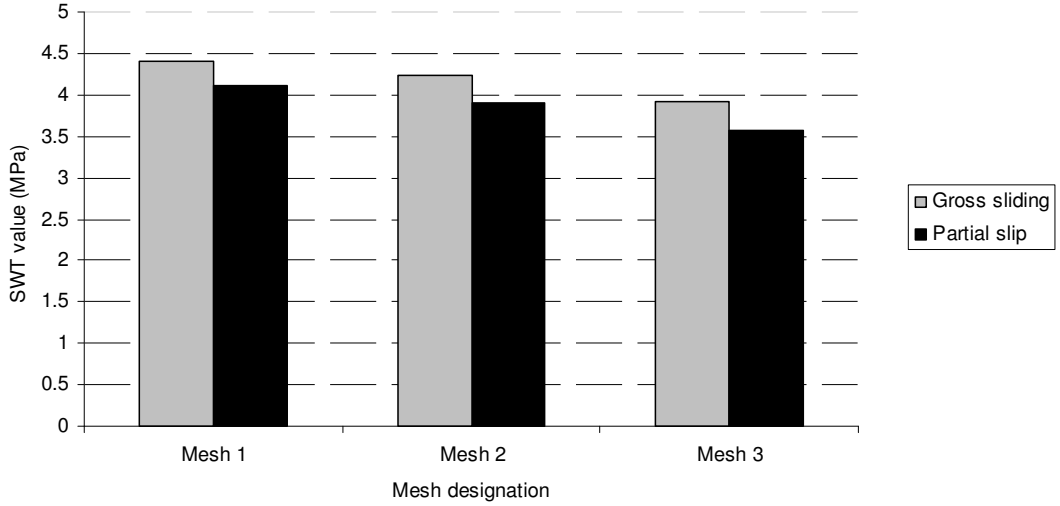

Figure A2.11. Effect of mesh on SWT value.

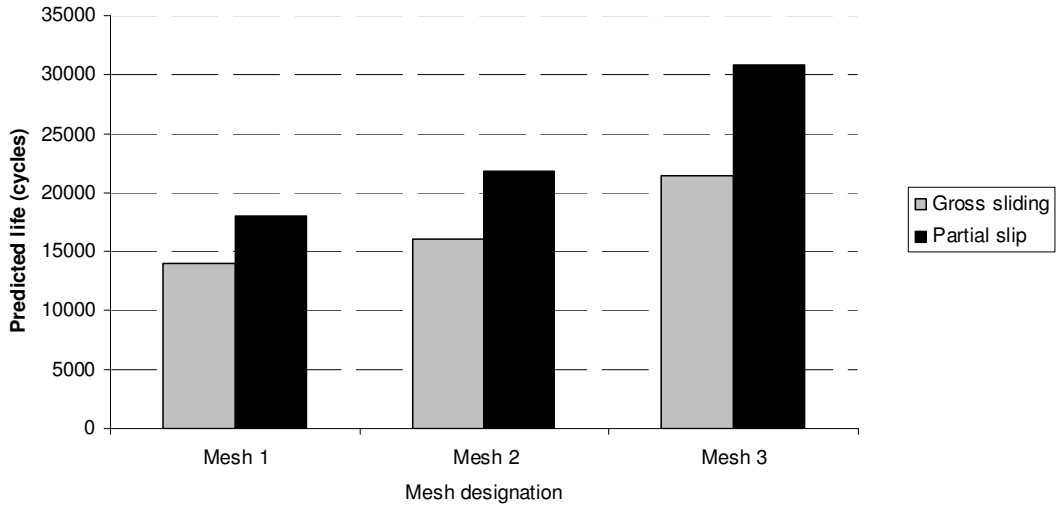

Figure A2.12. Effect of mesh on life prediction

Given the need for reduced element count with application to the wear model, it was concluded that the errors posed by Mesh 2 were acceptable for the gross sliding cases, where a significant growth of contact patch is expected, and the extra contact width is beneficial. In the partial slip cases this potential for growth is not required, hence a finer mesh can be created in the contact region, with improved life prediction

accuracy. Comparison with Mesh 3 indicates that an extended simulation period cannot reliably be achieved by reducing the number of elements in the model.

As 64bit architecture becomes more readily available, a further assessment should be undertaken to quantify the effect of mesh density on the fretting fatigue life predictions.

A2.5 Stress reporting location

Stress FE analyses use force and displacements as the primary solving variables. The stresses are derived from these values and are calculated at the integration points (Fig. A2.13). Generally, finite element codes can report the stresses at a range of positions within the element, typically:

- Integration points
- Averaged at nodes
- Averaged at the centroid

In order to assess which reporting position gave the most reliable results for stresses in a contact analysis, the stresses for a Hertzian FE contact analysis (i.e. normal load only) were compared with those from the theoretical solution. In each case the closest subsurface node/integration point/centroid to the surface was compared with the Hertzian stress distributions at the same depth. Only linear elements are considered here as these are known to give superior contact performance to their quadrilateral counterparts, which are prone to produce contact pressure fluctuations (HKS 2005).

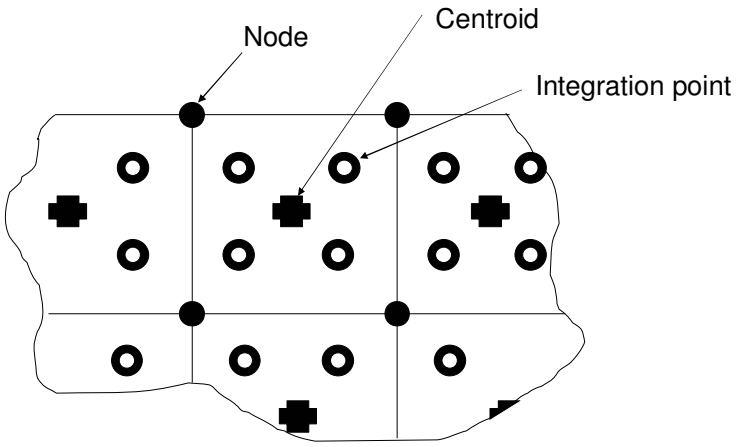

Figure A2.13. A typical first order, two dimensional, quadrilateral, finite element. The reporting locations offered within the ABAQUS^{tm} FE code are labelled

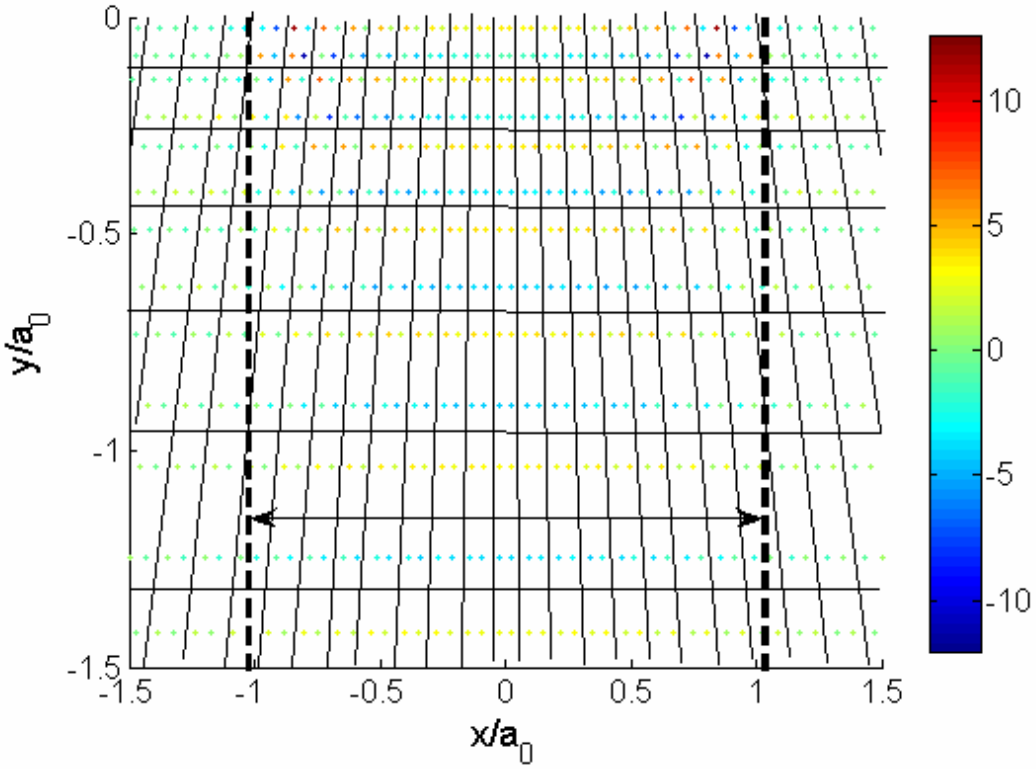

Figure A2.14 percentage error to the Hertzian solution for σ_{yy}.
The contact width is marked with dashed lines.
Note the symmetric characteristic of the error within each element

Figure A2.14 indicates that the integration points provide a 'noisy' collection of data. There is a symmetric characteristic to the relative error to the Hertzian solution within each element. Typically the upper integration points were found to over predict the Hertzian solution, whereas the lower points under-predicted it. Note also that the peak stress error is found at the edges of contact, which are known to be the critical location for fretting fatigue failure. Given the high stress gradients present in contact modelling, the use of extrapolation (as required when requesting nodal averaged values at the surface) is likely to generate erroneous data. In contrast, the centroidal values were found to offer very good agreement with the Hertzian theory, as they averaged the errors noted in Figure A2.14. For this reason the centroidal values of stress and strain are used throughout this thesis.

Appendix A3

Effect of rig compliance

A3.1 Overview

In Chapter 5 the rounded edge punch on flat geometry was found to be more sensitive to the pad holding conditions than the cylinder on flat geometry modelled in chapter 4. it was necessary to model the effect of rig compliance in order to capture the load transfer from one side of the fretting pad to the other during the fretting cycle. This appendix reports aspects of this behaviour not included in Chapter 5.

A3.2 Initial geometry

Initially the mesh used to model the experimental geometry of Jin & Mall (2002) was similar in extents to that used in Chapter 4; the pad geometry was extended a short distance away from the contact interface, to reduce the immediate impact of the boundary condition applied to the upper surface of the pad, as shown in Figure A3.1. i.e the compliant section indicated in Figure 5.2 was not present. In all other respects, the models are identical.

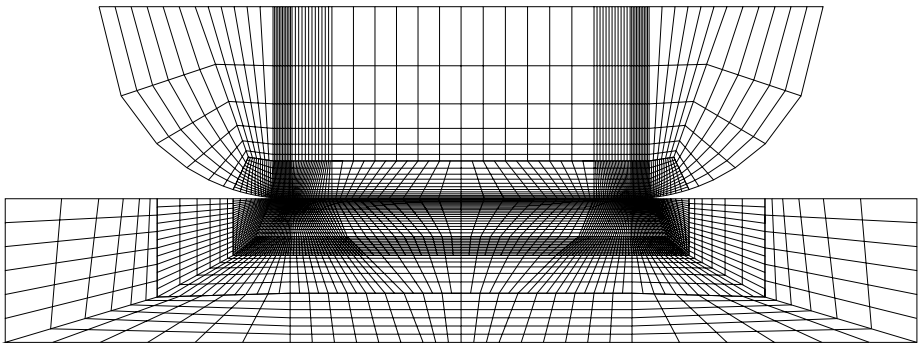

Figure A3.1. Initial mesh used to study the rounded edged punch on flat geometry of Jin & Mall (2002). Note the absence of the compliant section used in Chapter 5

A typical partial slip distribution for this model is given in Figure A3.2. There are several important features in the slip distribution. Firstly a partial slip state can be created, where a stick region is formed, bounded by two slip regions which extend to the edges of contact. Secondly, the sliding direction is reversed in either slip zone.

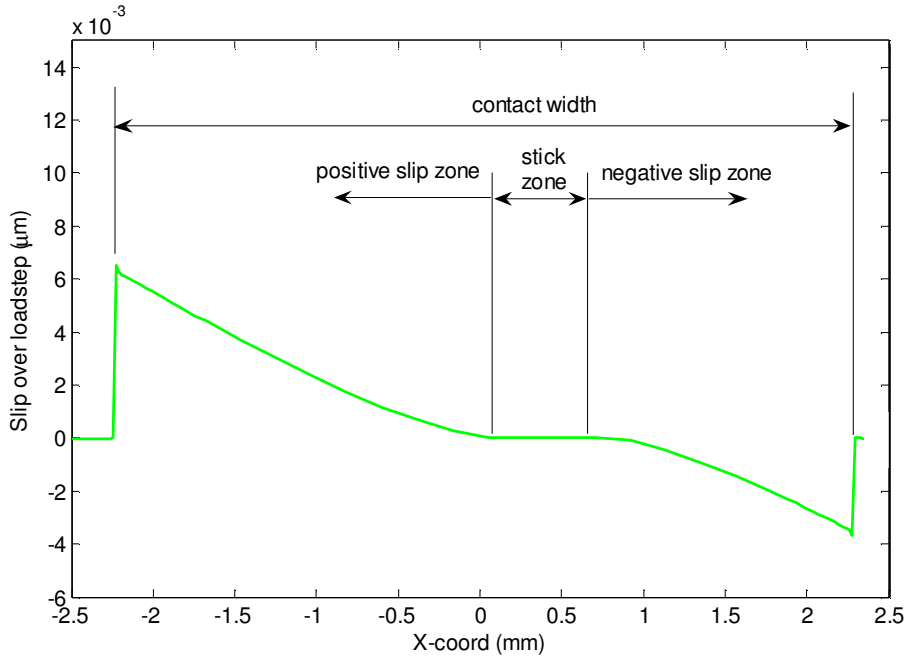

Figure 3.2.. A typical slip distribution for punch on flat (δ_{app}=25μm)

These features are explained by the presence of a substrate fatigue load, which creates a strain, and therefore a displacement field in the specimen. Hence there is a tendency to create relative motion across the contact interface. In the stick region friction is able to suppress any relative motion. However, in the slip region the shear traction generated is above the friction limit and therefore relative motion occurs. As the specimen is being stretched the relative motion is such that all points on the specimen are moving away from the centre of the stick zone. Hence a slip, and shear traction reversal exists across the stick zone. The effect of the applied displacement on the slip distribution is shown in Figure A3.3. The location of the stick zone is found to be a function of applied displacement. The stick region is essentially located in the region where the displacement fields of the pad and the specimen are most closely matched. Hence the location of the stick region is a function of the applied pad displacement and the applied substrate fatigue load. Figure A3.4 shows the shear traction distributions associated with Figure A3.3. In the partial slip cases the shear traction is found to reverse across the stick zone, hence a positive shear traction peak is observed at the left hand side, whilst it's negative counterpart is observed at the right hand side. In the gross sliding case (δ_{app}=50 μm) no stick zone is present and therefore no reversal in the shear traction direction occurs.

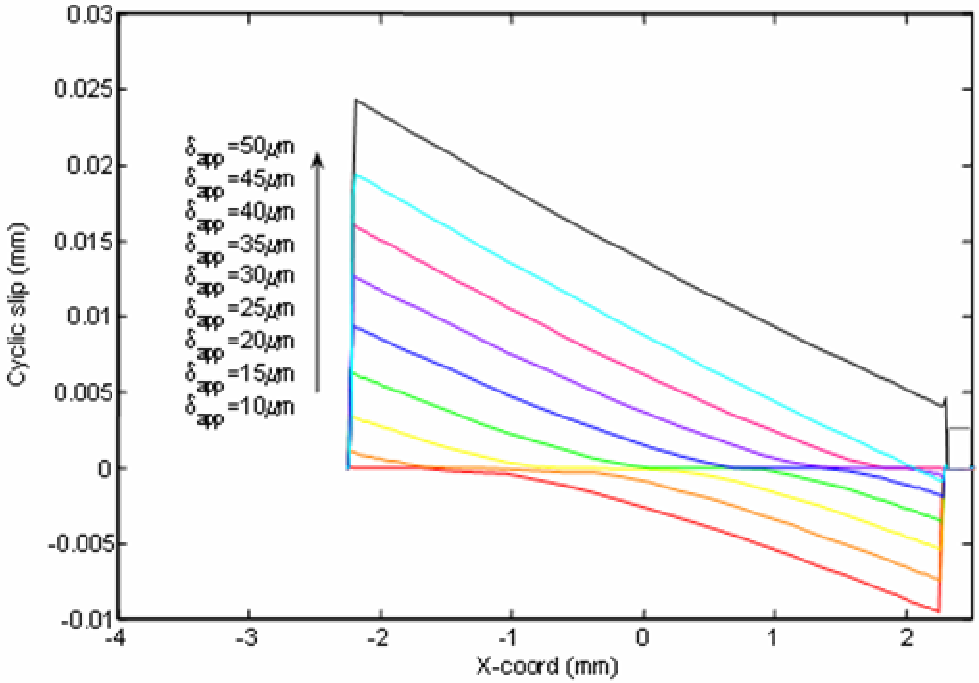

Figure A3.3. Effect of applied displacement on slip distribution

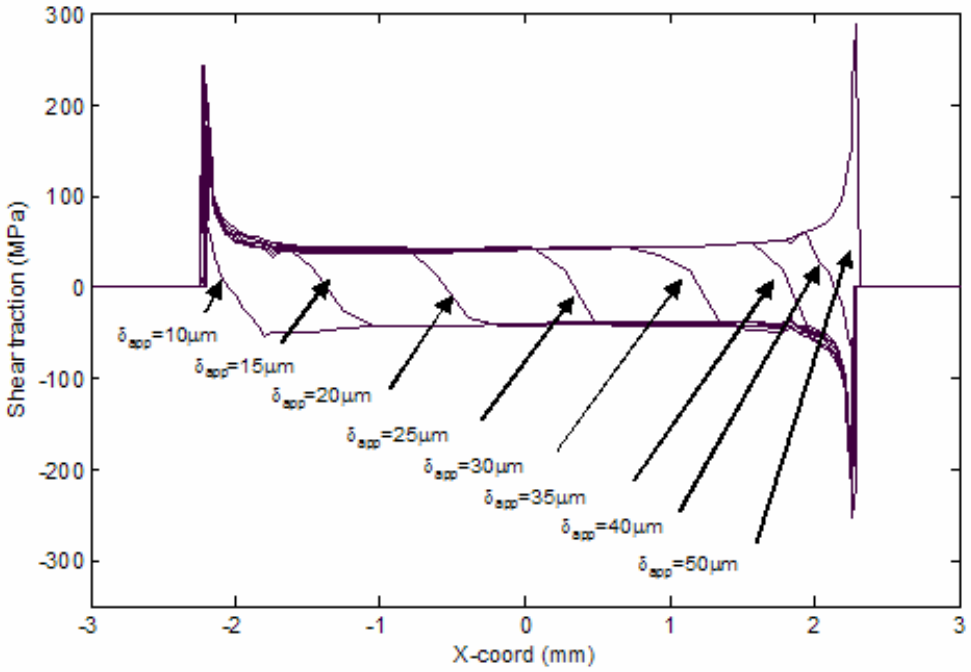

Figure A3.4. Effect of δ_{app} on shear traction distribution

As shown in Chapter 5, the addition of the compliant section complicates the behaviour of the contact as regions of the contact are found to open during parts of the cycle. Hence it is clearer to look at the 'short' model to understand the basic effect of δ_{app} on the contact behaviour.

Selection of the correct modulus in the compliant section strictly requires knowledge of a number of rig variables. However, the focus of Chapter 5 was not to accurately model the rig of Jin & Mall (2002), but rather to demonstrated the effect of wear and slip amplitude on the fatigue life of a nearly complete contact. To this end, the compliance of the section was 'tuned', for one applied displacement (δ_{app} = 35 μm), to give a life commensurate with those of the experiment, i.e. around 60 000 cycles. Figure A3.5 shows the effect of different compliances in the predicted fretting fatigue life as predicted by the wear model.

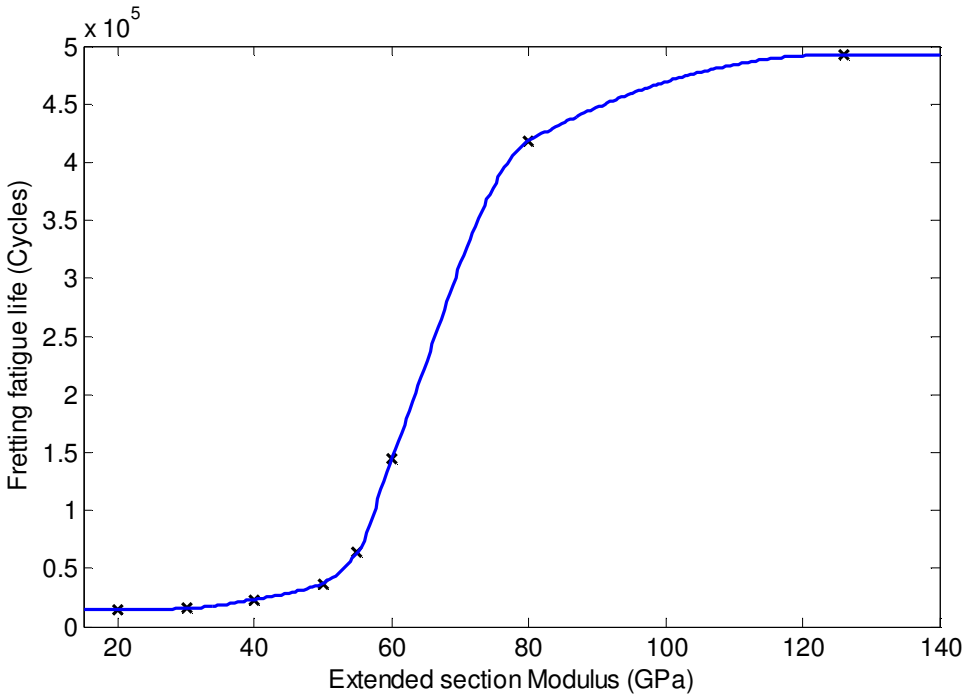

Figure A3.5. Predicted effect of compliant section modulus on fretting fatigue life (δ_{app} = 35μm)

The relationship between the modulus of the compliant section and the predicted life is found to be sigmoidal. At extreme values the predicted life is relatively insensitive to further changes in compliant section modulus. This is attributed to the diminishing effect on load redistribution at these extremes. However, in the intermediate region the life is sensitive o the compliant section modulus. This shows that the effect of rig 'scenery' can be very strong.

Appendix A3

Effect of rig compliance

A3.1 Overview

In Chapter 5 the rounded edge punch on flat geometry was found to be more sensitive to the pad holding conditions than the cylinder on flat geometry modelled in chapter 4. it was necessary to model the effect of rig compliance in order to capture the load transfer from one side of the fretting pad to the other during the fretting cycle. This appendix reports aspects of this behaviour not included in Chapter 5.

A3.2 Initial geometry

Initially the mesh used to model the experimental geometry of Jin & Mall (2002) was similar in extents to that used in Chapter 4; the pad geometry was extended a short distance away from the contact interface, to reduce the immediate impact of the boundary condition applied to the upper surface of the pad, as shown in Figure A3.1. i.e the compliant section indicated in Figure 5.2 was not present. In all other respects, the models are identical.

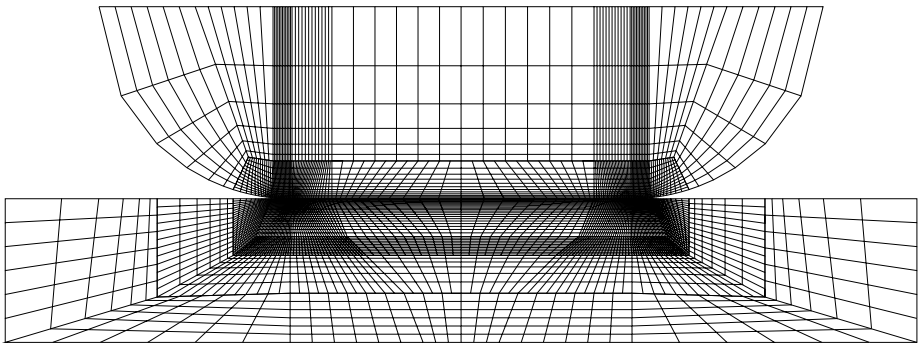

Figure A3.1. Initial mesh used to study the rounded edged punch on flat geometry of Jin & Mall (2002). Note the absence of the compliant section used in Chapter 5

A typical partial slip distribution for this model is given in Figure A3.2. There are several important features in the slip distribution. Firstly a partial slip state can be created, where a stick region is formed, bounded by two slip regions which extend to the edges of contact. Secondly, the sliding direction is reversed in either slip zone.

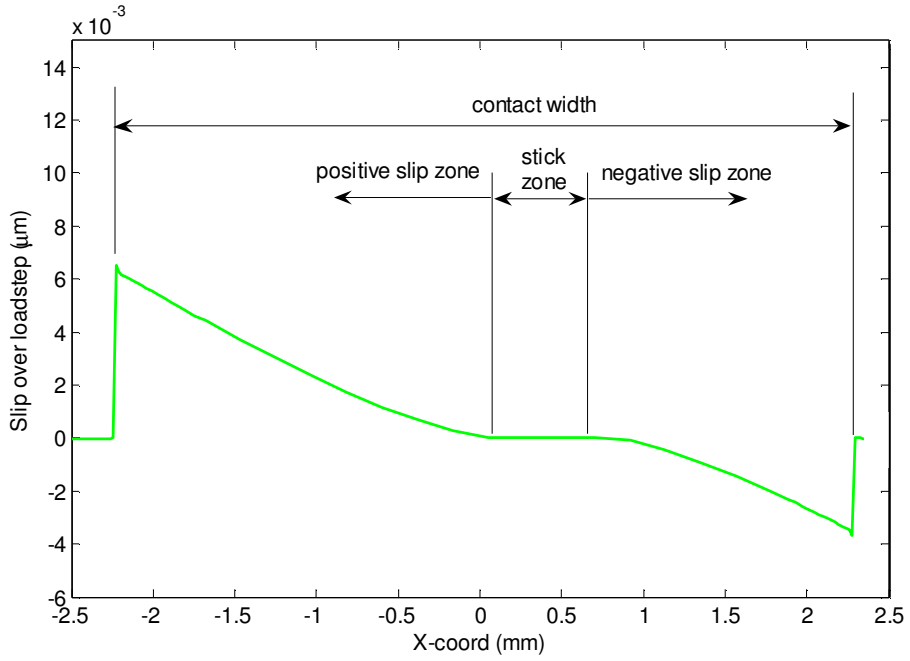

Figure 3.2.. A typical slip distribution for punch on flat (δ_{app}=25μm)

These features are explained by the presence of a substrate fatigue load, which creates a strain, and therefore a displacement field in the specimen. Hence there is a tendency to create relative motion across the contact interface. In the stick region friction is able to suppress any relative motion. However, in the slip region the shear traction generated is above the friction limit and therefore relative motion occurs. As the specimen is being stretched the relative motion is such that all points on the specimen are moving away from the centre of the stick zone. Hence a slip, and shear traction reversal exists across the stick zone. The effect of the applied displacement on the slip distribution is shown in Figure A3.3. The location of the stick zone is found to be a function of applied displacement. The stick region is essentially located in the region where the displacement fields of the pad and the specimen are most closely matched. Hence the location of the stick region is a function of the applied pad displacement and the applied substrate fatigue load. Figure A3.4 shows the shear traction distributions associated with Figure A3.3. In the partial slip cases the shear traction is found to reverse across the stick zone, hence a positive shear traction peak is observed at the left hand side, whilst it's negative counterpart is observed at the right hand side. In the gross sliding case (δ_{app}=50 μm) no stick zone is present and therefore no reversal in the shear traction direction occurs.

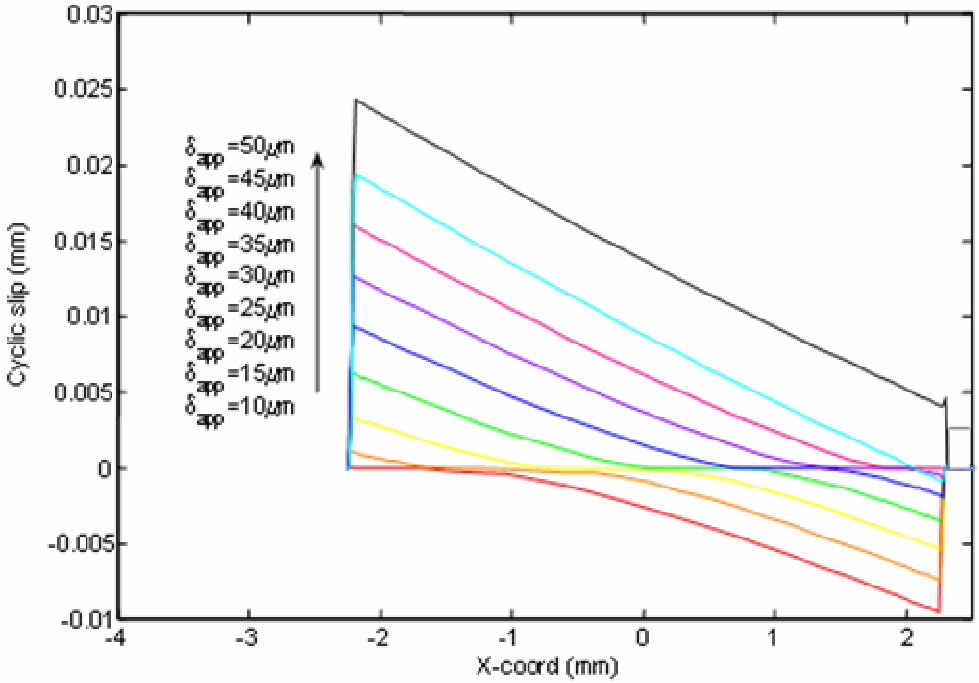

Figure A3.3. Effect of applied displacement on slip distribution

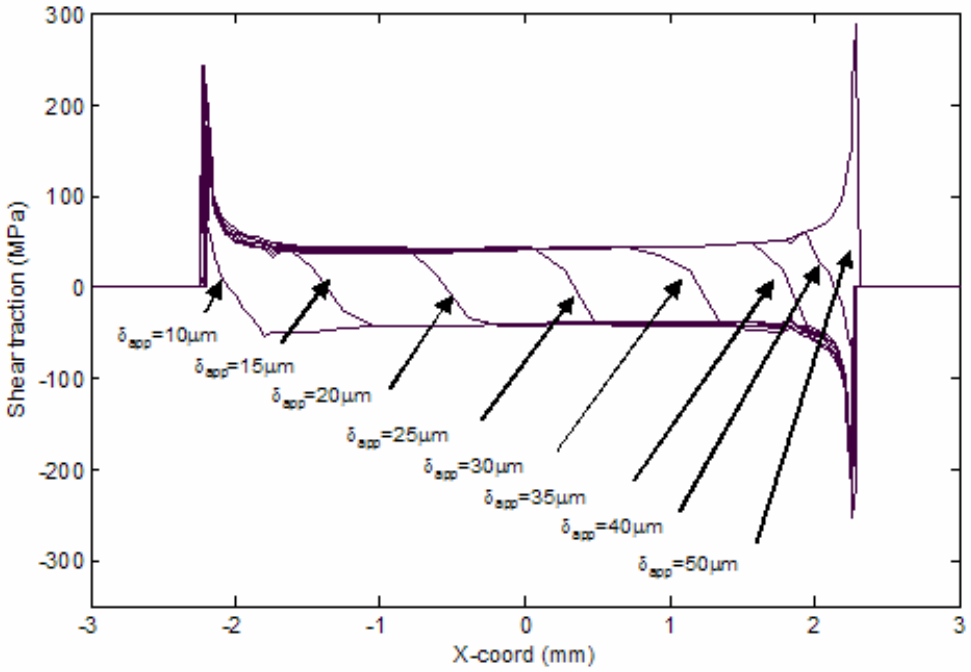

Figure A3.4. Effect of δ_{app} on shear traction distribution

As shown in Chapter 5, the addition of the compliant section complicates the behaviour of the contact as regions of the contact are found to open during parts of the cycle. Hence it is clearer to look at the 'short' model to understand the basic effect of δ_{app} on the contact behaviour.

Selection of the correct modulus in the compliant section strictly requires knowledge of a number of rig variables. However, the focus of Chapter 5 was not to accurately model the rig of Jin & Mall (2002), but rather to demonstrated the effect of wear and slip amplitude on the fatigue life of a nearly complete contact. To this end, the compliance of the section was 'tuned', for one applied displacement (δ_{app} = 35 μm), to give a life commensurate with those of the experiment, i.e. around 60 000 cycles. Figure A3.5 shows the effect of different compliances in the predicted fretting fatigue life as predicted by the wear model.

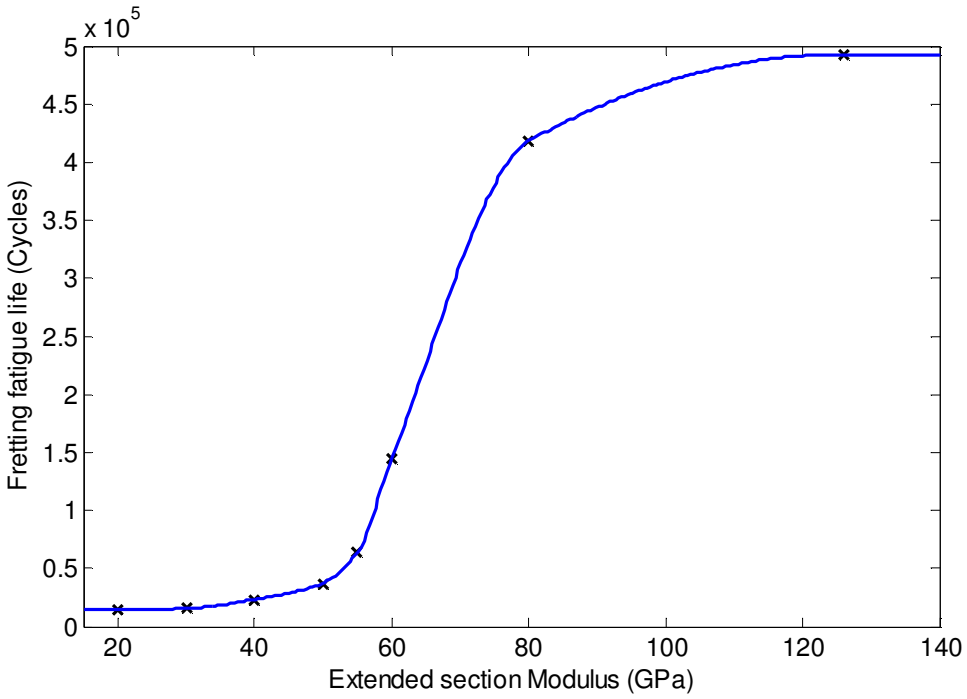

Figure A3.5. Predicted effect of compliant section modulus on fretting fatigue life (δ_{app} = 35μm)

The relationship between the modulus of the compliant section and the predicted life is found to be sigmoidal. At extreme values the predicted life is relatively insensitive to further changes in compliant section modulus. This is attributed to the diminishing effect on load redistribution at these extremes. However, in the intermediate region the life is sensitive o the compliant section modulus. This shows that the effect of rig 'scenery' can be very strong.